Flow Control for Loads Control

Al-Battal, Nader

Award date:
2019

Awarding institution:
University of Bath

Flow Control for Loads Control

Nader Hassan Al-Battal

A thesis submitted for the degree of Doctor of Philosophy

University of Bath

Department of Mechanical Engineering

Nov 2018

Copyright

Abstract

During gust encounters and turbulence aircraft are subject to extreme loads that dictate the structural requirements. Amelioration of these loads would allow reduced structural weight and therefore greater efficiency. Flow control is used for controlling the extreme loads at the fluid-structure interface. Two versions of the jet flap, normal and upstream blowing from the upper surface are studied under steady state conditions to illustrate the effectiveness of these devices at mitigating lift loads. The upstream blowing jet flap is further investigated through periodic and transient activation to demonstrate the feasibility for controlling transient gust encounters. These measurements include force, pressure and Particle Image Velocimetry measurements at a Reynolds number of 660,000 for a NACA 0012 airfoil.

For the steady-state measurements the jet strength was quantified using volumetric flow rate coefficient, C_Q to facilitate comparison between the two deflection angles. A range of volumetric flow rate coefficients up to C_Q = 0.44% were studied for a range of angles of attack $0° \leq \alpha \leq 20°$ for five chordwise locations. It was observed that normal blowing at x_J/c = 0.95 induces a change in lift of ΔC_L = -0.15 for the maximum flow rate coefficient. Locations further forward produce a negligible change in lift coefficient. Upstream blowing is significantly more effective and capable of mitigating lift at all the chordwise locations investigated by up to ΔC_L = -0.33. Upstream blowing encourages the shear layer to deflect upwards creating a greater adverse pressure gradient on the upper surface. As expected, increasing volumetric flow rate coefficient increases the magnitude of the change in lift for all cases studied. Locations near the trailing edge are preferable for low angles of attack; locations near the leading edge are preferable for high angles of attack, as greater lift reduction is obtained.

The unsteady periodic measurements encompassed a range of reduced frequencies, $0 \leq k \leq 0.471$ comparable to gusts on civil aircraft with jet momentum coefficients up to C_μ = 0.032 for three chordwise locations: x_J/c = 0.08, 0.60 & 0.95. As expected, with increasing frequency the amplitude of the unsteady lift decreases and the phase lag increases. The leading edge location, x_J/c = 0.08, experiences large phase lags, with a phase difference of φ = -98° for k = 0.079 at α = 13°; hence trailing edge jets are preferred for faster lift response.

The unsteady transient measurements consider the same locations with jet flap deployed in a square wave profile switching from C_μ = 0 to C_μ = 0.016 and back. The stepped increase in jet velocity incites a gradual movement in the separation point on the upper surface. Jets closer to the trailing edge remain more responsive with transient cases; at α = 10°, steady state lift is attained with τ = 8 for x_J/c = 0.95, while this delay extends to τ = 20 for x_J/c = 0.08.

Acknowledgements

I would like to express my gratitude towards my supervisors, Ismet Gursul and David Cleaver, for their continuous support and invaluable advice throughout my PhD. I would also like to extend this gratitude to the industrial supervisors from Airbus UK, Dr. Thomas Wilson, Steve Spurway and Maurizio Pardi.

I would like to acknowledge the technical advice and support given by the staff at the University of Bath, Steve Thomas, Ian Trussler, Steve Coombes, Colin Brain and Vijay Rajput.

I would like to acknowledge everyone at the office for their support and humour over the years.

I am grateful for the support of my family, particularly my mother who has made countless sacrifices. I am also grateful for the friends I consider my 'family'; Neuni for her constant humour and distractions, and my friends back in London.

Table of Contents

List of Figures

Nomenclature

α	=	angle of attack
α_0	=	angle of attack for zero lift
α_R	=	reference angle of attack
b	=	span
c	=	chord length
c_e	=	chord of ellipse
C_L	=	lift coefficient
$C_{L\alpha}$	=	lift curve slope
C_{Lmax}	=	maximum lift coefficient
C_{Lmin}	=	maximum lift coefficient
C_{Loff}	=	blowing off lift coefficient
C_{Lon}	=	blowing on lift coefficient
C_{Lmean}	=	mean lift coefficient
C_Q	=	volumetric flow rate coefficient
c_R	=	root chord length
c_T	=	tip chord length
C_U	=	uniformity coefficient
C_μ	=	momentum coefficient
$C_{\mu max}$	=	maximum momentum coefficient
ΔC_L	=	change in lift coefficient relative to baseline
δ	=	deflection angle
f	=	frequency
F_g	=	flight profile alleviation factor
h_J	=	slot width
H	=	gust gradient
$\bar{I}_j$	=	phase averaged jet momentum flux

k	=	reduced frequency
κ	=	normalised time constant
K_g	=	gust alleviation factor
L	=	gust wavelength
Λ	=	sweep angle
M	=	Mach number
Δn	=	incremental load factor
φ	=	phase angle
ρ_J	=	density of jet air
ρ_∞	=	density of freestream flow
Re	=	Reynolds number
s	=	span
S	=	wing area
Str	=	Strouhal number
T	=	time
τ	=	convective time
U_{mean}	=	mean jet velocity
U_{ds}	=	design/maximum gust velocity
U_g	=	gust velocity
U_J	=	jet velocity
U_r	=	resultant velocity
U_∞	=	freestream velocity
μ_g	=	mass ratio parameter
μ_∞	=	dynamic viscosity
V_e	=	true airspeed in knots
W	=	aircraft weight
x_J	=	location of jet

Chapter 1 : Introduction

As the world becomes increasingly connected and emerging markets continue to grow, aircraft manufacturers are compelled to meet the increased passenger demand as well as reduce emissions. Currently, the aviation industry accounts for approximately 2.3% of the global man-made carbon dioxide emissions [1]. However, with air traffic expected to grow by two-fold before 2031 [2], it is necessary for the industry to limit its carbon footprint and avoid any growth in emissions. Significant gains in technology over the past 35 years have led to a reduction in fuel consumption of 60% for civil aircraft [3], however, regulations such as Flightpath 2050 aim to further reduce greenhouse emissions of aircraft [4]. This stipulates carbon dioxide emissions must be reduced by 75% before the year 2050, in comparison to the levels experienced in 2000. The combination of environmental and financial drivers means airlines will demand more efficient aircraft to adhere to new regulations. In order to successfully achieve this target, aircraft and engine manufacturers will need to pursue optimisation in areas such as airframes, aerodynamics and propulsion to improve efficiency, alongside improvements in manufacture, maintenance and operations to reduce costs.

A potential area for optimising aircraft efficiency is flow control technology. Aircraft are subjected to greater loads during gust encounters or when performing manoeuvres. Such extreme loads determine the structural integrity of the wing required [5]. However, an increase in structural integrity will ultimately demand an increased structural weight which will be detrimental to the aircraft fuel efficiency. Effective alleviation of these loads will therefore lead to a reduction in structural weight of the wing [6]. Optimised load alleviation techniques have been suggested to mitigate fuel consumption by as much as 11% [7].

Gusts are an unsteady aerodynamic phenomenon and can reach high frequencies. As such, gust load alleviation systems must be capable of responding to high frequency gusts. When considering an aircraft at cruise speed encountering a maximum gust frequency of 20 Hz, the reduced frequency as defined with Eq. [1.1], can reach k = 0.75. Reduced frequencies above k > 0.2 are considered highly unsteady [8], whereas quasi-steady and unsteady frequencies are characterised by k < 0.05 and 0.05 < k < 0.2, respectively.

$$k = \frac{\omega c}{2U_\infty} = \frac{\pi f c}{U_\infty} \qquad [1.1]$$

Frequencies of this magnitude require powerful hydraulic systems for conventional control surfaces in order to be capable of a fast response. However, this in turn adds greater mass to the aircraft wing structure. Current control surfaces used to reduce gust loads, which comprise of ailerons and spoilers, are large and sized for manoeuvres. Therefore giving them a large inertia, with typical

deflection rates reached between 35-40°/s [9]. Their poor frequency response also means their effectiveness at reducing wing-root bending moment depreciates for gusts at higher speeds [10].

An effective flow control technology would need to be able to reduce large loads, be fast acting and retain a high frequency response. This frequency response would need to exceed that of current control surfaces, in order to nullify the need for additional structural weight. One potential form of flow control technology is fluidic actuator. These fluidic actuators can be fast acting and possess a high frequency bandwidth, but require their frequency response to be further investigated. Despite being fast acting, their effectiveness may depreciate with increasing frequency when at cruise.

In this project, the jet flap is proposed as a fast acting actuator and will be investigated in terms of its lift reduction capability and frequency response. Although this current study is looking at the jet flap on a fundamental level, its potential to be implemented on a commercial aircraft will also be considered, requiring experimental parameters to be scaled to cruise conditions. The research questions to be addressed are:

1. What is the effect of the chordwise location on the airfoil upper surface on the lift reduction capability and how is this affected by angle of attack?
2. Does the effectiveness of the jet flap for lift reduction vary with jet deflection angle?
3. What is the relationship between blowing strength and lift reduction?
4. What is the relationship between lift reduction and reduced frequency for periodic deployment? How is this affected by chordwise locations and angle of attack?
5. For sudden jet deployment, how does the aerodynamic response vary with chordwise location and angle of attack?
6. How do the results scale to civil aircraft cruise conditions?

Chapter 2 : Literature Review

2.0 Summary

This section provides an overview of gust load definitions and the types of gusts an aircraft may be subjected to. Current gust load alleviation techniques used on aircraft are discussed, with their effectiveness under unsteady state conditions also reviewed. Potential light weight solutions to the gust load problem are reviewed, with a main focus on jet flaps. The jet flap is proposed as an alternative to current gust load alleviation technology. An overview of various types of jet flaps under differing situations is outlined. Unsteady jets are discussed because of the similarities with pulsed jets and synthetic jets, although these may have different objectives (e.g. separation control, etc). Finally, an overview of the airfoil utilised for jet flap consideration, NACA 0012, is provided to legitimise its use within this project.

2.1 Gust Load Definitions

A discrete gust represents a disturbance in the atmosphere through an irregular velocity profile, whereas continuous turbulence is deemed to be a succession of discrete gusts, as shown in Fig. 2.1. Turbulence can occur from a number of natural events due to convection or clean air, which include the following [11,12]:

Convection

- Thunderstorms – can produce extreme levels of turbulence.
- Cumulus clouds – the cotton looking cloud can produce varying levels of turbulence.
- Heat convection – convection over heated land is capable of engendering a disturbance.

Clean Air

- Jet streams – the wind shear from fast moving streams is responsible for 60% of turbulence reports related to clean air.
- Earth's boundary layer – wind shear caused by wind over ground.
- Mountains – tops of mountains can produce large eddies.

Discrete gusts or continuous turbulence are typically separated into three categories; vertical gusts, lateral gusts and head-on gusts. Vertical gusts present the greatest risk to the aircraft structure, in particular upward gusts. Such vertical gusts incite a change in the effective angle of attack $\Delta\alpha_{eff}$, which causes large lift forces and pitching moments. As a result, the aircraft will experience a plunging acceleration that translates the entire aircraft. Lateral gusts will require the aircraft to yaw, in order to reduce the effect of the gust and reach stability. Head-on gusts produce a similar plunging

motion to that of vertical gusts, but act about the centre of gravity, causing the pitching motion to vary from vertical gusts.

The effective change in angle of attack caused by a vertical gust can be illustrated through a quasi-steady approximation as shown in Fig. 2.2. Introducing a vertical gust with a velocity, U_g, to an aircraft travelling forward at freestream velocity, U_∞, will produce a resultant velocity, U_r. As such, this change in angle of attack will nevertheless create a change in lift, which can be determined using:

$$\Delta L = \frac{1}{2}\rho U_\infty S U_g C_{L\alpha} \quad [2.1]$$

The series of gusts during turbulent encounters will continuously create changes in lift. Such regular changes in loading will ultimately create large changes in wing root bending moments. It is therefore pertinent to decompose continuous turbulence loads to understand the effect on the aircraft, and ensure sufficient safety factor [11]. The decomposition of turbulence into smaller discrete gusts allows one to predict the response of the aircraft.

2.1.1 Discrete Gusts

Prior to the 1930s, gust load analysis was disregarded. It was only once aircraft began to fly at greater speeds, thereby enhancing gust loads subjected on to the aircraft, that it became relevant. Earliest representations of the discrete gust include the 'sharp-edge gust' first proposed by Wilson [13]. The original sharp-edge gust follows a square wave profile in vertical velocity, so that the aircraft is subjected to a temporal change to the maximum gust velocity, U_g. Therefore, the sharp-edge gust solely reflects the loads acting on the aircraft, and not any plunging motion [11]. The expected incremental change in load, Δn, incited by the gust could be calculated by dividing Eq. [2.1] with the aircraft weight, to produce Eq. [2.2]. Experimental investigations have shown that the immediate alleviation of sharp-edge gusts is infeasible due to slow flap displacement [14]. The addition of a motion and lag factor was later included by the Federal Aviation Regulations [11]. The factor alters the gust to follow a linear ramp profile, which extends the distance to which the gust reaches the maximum gust velocity U_{ds} after a gust gradient distance, H.

Further amendments to gust load predictions were carried out in the early 1950s, as Pratt [15] demonstrated a formula for a gust based on a 1 – cosine shape was more suitable than a linear ramp shape. Gust loads were considered as additional mass, compelling the formula to depend on a mass ratio parameter, μ_g, see Eq. [2.3] [11]. The formula was consequently incorporated in the Civil Aviation Regulations (CAR) in 1956 [11], and was first utilised for the design of the early Boeing 737 aircraft [16].

$$\Delta n = K_g \frac{U_{ds} V_e C_{L\alpha} S}{498W} \quad [2.2]$$

Where V_e is the true airspeed in knots, and 498 considers the sea-level air density and converts velocity from knots to fps. The gust alleviation factor, K_g is:

$$K_g = \frac{0.88\mu_g}{5.3 + \mu_g} \quad [2.3]$$

$$\mu_g = \frac{2W}{C_{L\alpha} S c \rho g} \quad [2.4]$$

Simplification of a large continuous turbulence sequence is achieved with discretisation, to determine the length of each individual gust, as shown by Hoblit [11], Fig. 2.3. The fundamental shape of the discrete gust is taken as the 1 – cosine gust, and is defined in European Aviation Safety Agency (EASA) Certification Specifications Part 25 (CS-25.341) [17] as Eq. [2.5] below. The conditions state that designers must consider the aircraft experiencing a symmetric vertical gust.

$$U = \frac{U_{ds}}{2}\left[1 - \cos\left(\frac{\pi s}{H}\right)\right] \quad [2.5]$$

The gust gradient, H, is defined as the lateral distance until the amplitude of the gust, with criteria in CS-25 stating an appropriate amount of gust gradients between 9 m to 107 m must be considered. The distance of which the aircraft has travelled within the gust length is defined as s. The design gust velocity U_{ds} is defined below as:

$$U_{ds} = U_{ref} F_g \left(H/_{350}\right)^{1/6} \quad [2.6]$$

The reference gust velocity, U_{ref}, refers to velocities at various altitudes. The flight profile alleviation factor, F_g, scales with altitude to reach unity at the highest working altitude for the aircraft, and is dependent on the ratio between maximum landing and take-off weights.

2.1.2 Continuous Gusts

Continuous turbulence subjects the aircraft to unsteady characteristics and therefore the dynamic response must be considered. Atmospheric turbulence spectrum was originally expressed by von Kármán [18] as a power spectral density, defined in a simpler form as Eq. [2.7]. Similarly, the Dryden spectrum, shown in Eq. [2.8], gained interest for isotropic turbulence analysis [19], and was originally suggested by Liepmann [20] for gust load analysis. However, CS-25 criteria request the use of the von Kármán spectrum during design.

$$\Phi(\Omega) = \sigma_w^2 \frac{L}{\pi} \frac{1 + \frac{8}{3}(1.339L\Omega)^2}{[1 + (1.339L\Omega)^2]^{11/6}} \quad [2.7]$$

$$\Phi(\Omega) = \sigma_w^2 \frac{2L}{\pi} \frac{1}{[1 + \mathrm{L}^2\Omega^2]^2} \quad [2.8]$$

The wavelength of the continuous turbulence is defined in CS-25 [17] as 2,500 ft (762m) and the frequency is given by Ω, rad/m. The point at which the PSD curve begins to reduce is determined by the wavelength L. The root mean square (rms) value, σ_w, represents the fluctuations of gust velocity about a mean value. This value is normalised for calculation of power spectral density in CS-25. The square root of the area under the PSD output curve from Eqs. [2.7 & 2.8], gives the rms value. The response to the isotropic turbulence spectrum is determined as the Frequency Response Function, or transfer function [11]. The output of this determination includes aeroelastic characteristics involving wing root bending moments and torsions.

Following the start of the PSD decline, a comparison of the two spectrums illustrates the reduction follows differing gradients. The von Kármán PSD follows a -5/3 slope, while the Dryden PSD follows a -2 slope. It is due to these exponents that the von Kármán spectrum engenders a more appropriate calculation of gust velocities, due to its closeness to a typical gust velocity psd [11, 21].

2.2 Flow control

Flow control can be used to produce desirable changes in the flow structure including the prevention of flow separation or transition delay. Ultimately, such alterations could produce benefits in the form of lift enhancement or drag reduction, consequently enhancing the performance of the aircraft [22]. Although, any performance improvement also has to consider a number of further factors including: ease of implementation, maintenance, weight penalty and design costs [23]. Furthermore, several implications may arise whilst pursuing a particular change. As shown in Fig. 2.4, flow reattachment along the airfoil surface will augment the lift being produced but this will correspond to an increase in induced drag. However, the rewards of flow control are evident when the benefits of increased lift outweigh any drag penalty.

Two divisions of flow control known as ‘passive’ and ‘active’ work to produce changes in the flowfield in differing ways. Passive flow control performs without the need for a direct energy input. Passive vortex generators fall into this category, as the vortices they shed mitigate the wake size [24]. However, the additional VG surface increases skin-friction drag, and therefore the benefit of increase lift and reduced pressure drag associated with the diminishing flow separation must supersede this additional profile drag.

Active flow control is more suitable for dynamic situations, where an actuator may be deactivated or retracted when not needed to avoid negative effects. The categorisation of active flow control is shown in Fig. 2.5. In order to cope with high frequency disturbances an aircraft may encounter, it is desirable for the actuator to possess a high-bandwidth [25]. As such, bandwidth becomes highly important within closed-loop systems [26]. In addition to bandwidth, the actuator must have a high gain so as to remain sensitive to any changes in flow and have little lag. As such, an ideal actuator would possess both a high-bandwidth and a high gain, however, achieving both characteristics is a challenge. Despite the trade-offs associated with gain-bandwidth, the benefits of flow control are clearly apparent, and as it will be shown in section 2.2.1, current flow control strategies on aircraft will be reviewed.

2.2.1 Current Gust Load Control

Successful control of gust loads with fast acting control surfaces allows for reduced structural weight. Although research for gust load control started earlier, a series of disturbing events in the Middle East including the Yom Kippur war, which incited the Arab oil embargo enforced by OPEC in the early 1970s, resulted in a six-fold increase in the price of oil [27] compelling aircraft manufacturers to pursue efforts to reduce structural weight so as to improve fuel efficiency [28]. In 1975, the Lockheed-Georgia Company incorporated a Gust Load Alleviation (GLA) system on the military aircraft C-5A, which saw the use of outboard ailerons, elevators and accelerometers [29]. Flight tests with C-5A saw the wing root bending moments approximately halve during gust encounters. The system used an accelerometer on the wing to determine the effective change in angle of attack incited by the gust. This would then be used to produce a damping function for the actuators to counter the gust. The success of the C-5A permitted Lockheed California Company to transfer their technology to commercial aircraft. The active load alleviation system was installed on the Tristar L-1011 during the 1980s, making the aircraft the first commercial plane to include ailerons for GLA [30]. The installation of outboard ailerons forced the wing to have its span enlarged which ultimately contributed to a reduction in fuel expenditure of 3%. The system on the Tristar L-1011 saw a lag response for ailerons of 90° for gusts between 1-2Hz [31].

Implementation of a gust load alleviation system incorporating ailerons, spoilers and elevators was studied for the Airbus A300, and was shown to potentially mitigate gust loads significantly [31]. Although the Airbus A310 aircraft had gust load alleviation control surfaces on the wing, ailerons were not applied to initial iterations of the aircraft [32]. However, outboard ailerons were eventually made active for the A320 in the late 1980s, making the A320 the first European commissioned aircraft to incorporate full GLA control surfaces. The system compensated for the lag of the actuator by locating the accelerometers ahead of the wings, along the fuselage. This gives the hydraulic actuators adequate time to respond and prevent early deployment which may give rise to

aerodynamic flutter [32], for deforming flexible wings. It was shown with the A320, spoilers had a greater influence on inboard bending moment whilst ailerons are preferred for influencing bending moment between the midspan and wing tip. The eventual outcome of the new system showed that the A320 was capable of relieving wing root bending moment produced during unsteady wind encounters by 15% [32]. Modern aircraft have certainly evolved since the days of aircraft with early iterations of gust load alleviation systems. Detection of atmospheric disturbances ahead of the aircraft to create a feedforward input provides control surfaces with additional time to respond and therefore optimises load reduction. UV Doppler Lidar systems have been shown to provide a forward detection range of 50m, which translates to a lead time of 300 ms for control surfaces to perform on an Airbus A340, enough time for ailerons to deflect up to 15° [33], see Fig. 2.6. Furthermore, the Airbus A380 utilises fast acting sensors to allow control surfaces to physically respond within a fifth of a second from the point of gust detection [34].

2.2.1.1 Spoilers

Spoilers are typically positioned along the upper surface of the wing, see Fig. 2.7a. The spoiler resembles a flat plate, which is rotated to promote separation. This separation creates a reduction in the lift-to-drag ratio. This is beneficial for instances where a loss in lift is required, such as during upward gust encounters or upon landing approach.

Larger deflection angles produce greater changes in lift, as they reduce suction ahead of the spoiler to a larger effect [35, 36]. However, Consigny *et al.* [35] found lift to remain relatively constant until the spoiler was sufficiently inclined to prevent separated flow downstream of the spoiler from reattaching. These findings are corroborated by Maskell [37], who observed lower deflection angles risk a negative pressure gradient emerging after a separated region, hence diminishing the effect of the spoiler to significantly alter lift as greatly as larger deflections do. McLachlan *et al.* [38] showed a further loss of lift of $\Delta C_L \approx$ -0.5 can be achieved by increasing the deflection angle from δ = 30° to 60° at α = 0°. Kim and Rho [39] showed as the spoiler increases in deflection angle, the pressure along the upper surface downstream of the spoiler becomes less negative, indicating a loss of lift. The greater deflection angle causes the spoiler to protrude further into the global freestream, which incites a reduction in shedding frequency [39]. Although, the ability to change lift to a larger extent is desirable for a control surface, consideration for a spoiler-trailing edge flap combination must be taken. The ability for flow to reattach along the surface allows the potential to utilise a trailing edge flap to further manipulate the flow.

The effect of spoiler location on lift was studied by Maskell [37]. For a given deflection angle of δ = 40° at α = 4°, it was shown that placing the spoiler at x/c = 0.4 failed to reattach flow along the surface, unlike the spoiler at x/c = 0.2. This resulted in a greater change of lift of ΔC_L =

0.238. Croom *et al.* [40] suggested spoilers must be positioned further downstream on swept wings, to achieve analogous results to spoilers on unswept wings.

Experimental studies from McLachlan *et al.* [36] showed the deflection angle to have no effect on the gradient of the lift curve, but reduces lift by ΔC_L = -0.5 for a deflection angle of $\delta = 30°$. The spoiler becomes ineffective beyond stall angle, as separation initiates upstream of the spoiler location. In addition, it was shown that vortex shedding frequency is dependent on the deflection angle, therefore, larger angles were correlated to smaller Strouhal numbers.

When undergoing unsteady deployment Consigny *et al.* [35] found low spoiler angles continued to be ineffective at separating the flow downstream of the spoiler. This is due to the extent of the separated region being proportional to the spoiler height [41]. However, when considering the effect of excitation, the amplitude in change in lift coefficient became smaller with larger reduced frequencies, accompanied by greater phase delays. The lag associated with large frequencies means the force is not expected to reach that of the steady state [42]. The deployment of the spoiler incites a vortex at the spoiler-tip similar in nature to that of a dynamic stall vortex. The vorticity from this spoiler tip vortex is enhanced with greater reduced frequencies. This is due to the oscillating spoiler enhancing the ability to mix flow between flow either side of the shear layer. As such, the development of this vortex is dependent on the frequency and is decoupled from the oscillatory movement of the spoiler. Costes *et al.* [43] experimentally investigated an oscillating spoiler located at x/c = 0.67 and observed that lower deflection angles produce greater force variation than larger deflection angles; unsteady force variation with $\delta = 5°$ is greater than twice the amplitude observed at $\delta = 10°$. Despite the low deflection angle, there remains a substantial phase delay.

As the spoiler returns to the inactive baseline case, behaviour behind the spoiler varies with excitation. Aft of the spoiler, the size of the wake is dependent on the frequency. At sufficiently large frequencies, the flow behind the spoiler fails to reattach. As the baseline case is attained, the wake region is shed away from the upper surface. Below this threshold frequency, flow will reattach to the surface [42].

The ability of the spoiler to reduce lift was found to be dependent on the reduced frequency of the spoiler [39]. Kim and Rho [39] showed oscillating at a reduced frequency of k = 0.5 was found to reduce mean lift by $\Delta C_L \approx$ - 0.06. Furthermore, oscillating the spoiler at a frequency two times greater than the Strouhal frequency at $\delta = 10°$, saw the change in lift increase by approximately 50%.

A dynamic stall vortex is present during rapid deployment. However, this vortex is attributed to a significant force reversal [44]. The amplitude of the force reversal associated with this vortex from the spoiler is reduced with spoiler location when placed closer towards the trailing edge, which is also accompanied with a faster response to deployment [44]. The maximum amplitude for this

force reversal is attributed to the separated region, formed by the initial spoiler tip vortex, closing at the trailing edge. Negative lift change is obtained when the counterrotating vortex formed by the trailing edge incites this bubble to burst, causing the separated region to develop and expand. Therefore, to minimise the effects from the dynamic stall vortex caused by spoiler deployment, generating a vortex in the opposing manner is required. Choi *et al.* [44] show that placing a small slot between the airfoil surface and the spoiler negates the initial lift rise observed during rapid deployment.

Transient deployment of the spoiler up to $\delta = 20°$ saw unfavourable behaviour [35]. Lift initially increased for half the time required to reach steady state value, before beginning to reduce, as shown in Fig. 2.7b.

2.2.1.2 Trailing Edge Flaps/Ailerons

Lift can be varied through a control surface at the trailing edge, known as a plain flap [45]. The trailing edge flap encompasses the aft portion of the airfoil and is a form of high lift device due to its ability to augment lift beyond the value for a 'clean' airfoil through downwards deflection. This positive deflection can be considered as an effective increase in airfoil camber [46]. Their primary purpose is to reduce the landing speed of the aircraft to provide a safer approach to the runway. When the flap is activated upwards instead, a negative camber is realised creating lift reduction. When placed on the outboard section of the wing, the ailerons can mitigate bending moment by displacing the loading centre towards the fuselage, see Fig. 2.8a.

With steady state experiments, it has been shown that increasing the flap deflection angle downwards further increases the loading on the wing [43]. While upward deflection angles cause a reduction in lift, with pitching moment increasing [47]. Despite changes in lift values, the gradient of the lift curve remains constant regardless of the deflection angle until stall [48]. Lift augmentation is attributed to larger suction pressures on the upper surface, but large suction peaks are also observed at the hinge line of the flap when deflected [47]. Although the trailing edge flap can still produce a change in lift in the post-stall region, greater deflection angles create a more severe drop in lift at the stall angle [47]. The change in lift is dependent on the chordwise extent of the flap. Larger flap sizes have been shown to create larger changes in lift [47, 49]. Jacobs & Pinkerton [47] determined a difference of lift coefficient $\Delta C_L \approx$ - 0.30 between a flap length of 0.10c and 0.20c at a deflection angle of $\delta = -50°$.

When the trailing edge flap is compared to an upstream spoiler, it retains a faster response for sinusoidal motion profiles [43]. Costes *et al.* [43] observed the unsteady flap to produce similar forces with low reduced frequencies below $k \leq 0.5$. However, the change in lift increases with frequencies near unity ($k = 1$). This is contrary to the observations of Bak *et al.* [48], who note that

the amplitude decreases with frequency, therefore reducing the range in lift coefficient change to the steady state. When this change in lift is represented with hysteresis loops, a greater frequency excitation causes a horizontal shift in a clockwise direction. When oscillating the aileron in a sinusoidal pattern, the range of lift coefficient change becomes smaller with angle of attack; at a low angle of attack of α = 4.6°, saw a change in lift coefficient of $C_L - C_{Loff} \approx 0.11$, as this rises to α = 19°, the change in lift coefficient reduces to $C_L - C_{Loff} \approx 0.04$, for a fixed reduced frequency of k = 0.082. The oscillating trailing flap was numerically investigated by Leishman [50] using a state-space model based on Wagner's function, showed at low Mach numbers the deflection of the flap acts with a phase lead with reduced frequencies above k = 0.5.

A fast acting sensor is crucial to achieving effective lift reduction, as Buhl *et al.* [51] shows a later deployment of a trailing edge flap reduces the ability to decrease gust loads. It is preferred to incorporate an accelerometer as greater information can be used as input to the control surface. When using a deflecting flap with an accelerometer, Buhl *et al.* [51] showed a force reduction of 85% can be achieved. In order to achieve faster responses, efforts towards smaller flap sizes have been made [52]. With a stepped deployment, a flap size of 0.01c has been shown to attain 90% of steady state lift within a convective time of τ = 9. As one may expect, faster deployment rates cause shorter rise times for the flap to obtain half the lift magnitude of steady state. However, preceding this point, the rate at which steady state lift value is approached remains the same regardless of the deployment rate, as shown in Fig. 2.8b. This suggests the modification in Kutta condition is not dependent on the actuator. Despite rise times appearing to be fast for flap deployment, transient measurements from Bak *et al.*, [48] indicate that force responds at a slower rate when actuation is terminated as opposed to deployment of the actuator. The non-dimensional time for lift to respond from the baseline to steady state for a stepped flap deflection is τ = 6.5. The response for a terminated flap takes a non-dimensional time of τ = 10.

2.2.2 Other Flow Control Concepts

2.2.2.1 Aerodynamic Bleed

One form of aerodynamic flow control is bleed where fluid is advected from a region of high pressure to a region of low pressure through internal channels. Such a transfer of fluid would occur from the lower surface to the upper surface, to produce variations in lift and drag forces for separation control [53] or modification of tip vortices [54]. An apparent advantage with bleed is that it does not require an external source of air, as it is ambient fluid which travels through the conduits of the airfoil. However, the strength of the air ejected from the outlet becomes reliant on the pressure differential, as Filippone [55] notes. In addition, the jet is further weakened by viscous forces as flow traverses through the channels. Regardless, a large change in lift force has been shown [56] to be

feasible. Piezoelectric actuators were used to move louvres, thereby allowing a control over the response and volume of air, see Fig. 2.9a. At high angles of attack, bleeding near the leading edge, along the upper surface in the range $0.03 < x/c < 0.07$, incited greater lift reduction with greater blowing strengths. An estimated momentum coefficient of C_μ = 0.000547 was capable of reducing lift by ΔC_L = - 0.7 through inducing a larger separated region, Fig. 2.9b.

With large changes in force observed by Kearney & Leonard [56], successful efforts towards enhancing control over volume flow rate in bleed have been investigated through varying porosity [57]. Efforts to control the strength of the bleeding air have also been carried out by Ho *et al.* [58], where valves determined the flow rates between regions to produce lift enhancement by 31%. Tinetti *et al.* [59] also explored, through simulations, the use of varying porosity to mitigate force undulations induced by the wake of a gas turbine rotor on stator performance. An alleviation of 18% of these force undulations could be achieved.

2.2.2.2 Gurney Flaps

One form of moving surfaces used for load control is the Gurney flap, which essentially is a small flat plate oriented perpendicular to the chord line, see Fig. 2.10a. The Gurney flap was introduced by Dan Gurney to improve downforce on the 1975 Indianapolis race car [60]. In 1978, Liebeck [60] consequently presented its ability to augment lift when placed on the lower surface, at the trailing edge. Hypothesised flow visualisation, shown in Fig. 2.10b, indicate a small separated region extending to the flap height upstream of the flap. This separated region causes a large pressure reduction near the flap location [61]. Aft of the Gurney flap, a pair of contra rotating vortices forms as shown in the experimental measurements of Tang & Dowell [61]. The flap deflects flow downwards, producing a greater downwash effect that contributes to the increased lift. The change in circulation of the perpendicular plate causes greater suction along the upper surface, particularly near the leading edge [61]. Unlike large moving control surfaces, the Gurney flap innately offers smaller inertia due to its small height of around 1-2% of the chord length.

Efforts were made to produce numerical solutions for the effect on lift by the Gurney flap. Modelling the effect of the protruding flap was performed by Liu & Montefort [62] by using the thin airfoil theory. As seen in Fig. 2.10c, the theory was used on a combination of a main and deflected segment, with the shorter segment representing the Gurney flap. The effect of the Gurney flap height on lift is represented with a square root relationship, Eq. [2.9].

$$\Delta C_L = q\sqrt{h/c} \qquad [2.9]$$

Where, the parameter q is a function of Reynolds number, however, when the model was compared to experimental data, the function q appears to be approximately equal to one, $q \approx 1$ [62],

see Fig. 2.10d. Steady state measurements of a Gurney flap located at x/c = 0.9 on the lower surface were taken by Tang and Dowell [61]. They show at low angles of attack, α = 3-5°, the gain in lift is $\Delta C_L \approx 0.3$. However, its effectiveness enhances as the airfoil incidence increases to near stall angle, α = 13°, with lift increasing by a further $\Delta C_L \approx 0.2$. This is a feature which has been noted by Heathcote *et al.* [63] for near trailing edge Gurney flaps on the lower surface.

The Gurney flap has been explored for mitigating aerodynamic loading for wind turbine [52] and aircraft application [63]. Heathcote *et al.* [63] showed when placing the flap on the upper surface, a large change reduction in lift is created. Placing the tab near the trailing edge was preferred for low angles of attack, but became submerged within the separated region at high angles of attack, diminishing its effect. As such, locations closer to the leading edge were far more effective for greater angles.

Due to the small forces associated with displacing the Gurney flap, they have been investigated for their frequency response [61, 64, 65]. A study by Tang & Dowell [61] showed increase in maximum lift coefficient during oscillations is proportional to the reduced frequency, as well as the phase lag. On the contrary, Heathcote *et al.* [66] notes the peak-to-peak change in lift, $C_{Lmin} - C_{Lmax}$, to reduce with reduced frequency, which is corroborated by the findings of Kinzel *et al.* [67]. Increasing the angle of attack further increases the decay with reduced frequency [66].

Smaller Gurney flaps, in the form of mini-tabs, have been tested with rapid deployment [52]. Despite the small height associated with mini-tabs, an adverse lift response occurs upon the transient activation which is seen to develop greater with faster deployment rates.

2.2.2.3 Jet Flaps

The jet flap consists of a narrow slot extending across the entire span of the wing, which expels high momentum air [68], see Fig. 2.11. The jet flap was originally developed for flow separation control. If blown tangentially on a rounded surface, the airflow will closely follow the profile of the surface. This behaviour is defined as the 'Coanda' phenomenon [69]. Tangential blowing accelerates the fluid above the shear layer [70]. The additional momentum provided by the jet invigorates the boundary layer to ultimately prevent it from separating. As such, the wing experiences 'supercirculation' [68]. A large suction peak near the jet illustrates supercirculation [70]. Preventing boundary layer separation provides the added benefit of reducing profile drag.

If blown perpendicularly from the lower surface, the emergence of the jet disrupts the flow causing the jet exit to be a fixed separation point [71], so that a separation bubble emerges to encompass the surface up to the trailing edge. An alteration in the Kutta condition is then realised as the separation bubble encourages flow to be entrained from the suction surface, thereby augmenting the circulation created by the aerofoil [72]. Consequently, this can be considered as an increase in

the effective camber which contributes to a greater lift coefficient [71, 73]. A commonly used indicator for the strength of the jet flap is the coefficient of momentum, in Eq. [2.10]. This parameter signifies the amount of mass flow rate utilised in comparison to the dynamic pressure acting on the wing [68]:

$$C_\mu = \frac{\rho_J A_J U_J^2}{\frac{1}{2}\rho_\infty U_\infty^2 S} \quad [2.10]$$

Where A_J is the area of the jet, and U_J denotes the jet velocity. The above equation is the three-dimensional definition. For infinite wing / airfoil experiments, the jet area can be reduced to jet width h_J and the following adaption is used [68]:

$$C_\mu = \frac{\rho_J h_J U_J^2}{\frac{1}{2}\rho_\infty U_\infty^2 c} \quad [2.11]$$

The jet flap has also been considered for manoeuvre load control. Yaw moment changes can be induced with the use of a normal blowing jet spoiler on the upper surface with a momentum coefficient as small as C_μ = 0.5% [74]. This device is ideally placed around the location of maximum thickness in order to realise a change in drag, with minimal change in lift. This creates a yawing force with minimal rolling moment. It is therefore preferable to a spoiler which would create lift change and has greater dependency on angle of attack.

The jet flap has also been shown to be a fast acting actuator, when it is located near the trailing edge, x/c = 0.95, on the lower surface [72]. With a short activation time of τ_{act} = 0.25, the lift response reached approximately 85% the steady state lift within 0.8 convective time units. However, a drag reduction is caused when initially deployed before increasing drag and reaching a steady state value.

2.2.3 Flow Control Summary

Section 2.2 has shown current flow control technologies, such as trailing edge flaps and spoilers, to be effective at load control. However, a large inertia is associated with them due to their large mass, thus producing a longer deployment time and inhibiting their frequency response. Alternative flow control techniques show potential with mitigating loads. However, Gurney flaps on upper surface reduce effectiveness with angle of attack, when placed near the trailing edge. While bleeding has shown to work effectively when using ambient air as a source, it remains a challenge to control the strength of air. The jet flap has a fast lift response which would be beneficial during gust encounters. Table 2.1 summarises the characteristics of the flow control technologies discussed in

section 2.2. Section 2.3 will present the alternative solution, the jet flap, and will discuss how the jet flap could be further modified to counter these issues.

Table 2.1 – Summary of flow control technologies.

Name	Max. Steady State ΔC_L	Frequencies	Energy Requirement	Feasibility
Spoilers	-1 (x/c = 0.733, flap length x/c = 0.1554, δ = 60°)	Low < 10 Hz	High – Large inertia	Currently in use Adds significant drag
Trailing Edge Flap	-0.7 (x/c = 0.90, flap length x/c = 0.10, δ = 50°)	High > 10 Hz	High – Large inertia	Currently in use Adds significant drag
Bleeding	-0.7 (0.03 ≤ x/c ≤ 0.07, C_μ = 0.000547)	Very High > 50 Hz	Very Low – Can use ambient air	Difficult to keep constant momentum coefficient
Gurney Flap	-0.3 (x/c = 0.6, h/c = 0.02)	High > 10 Hz	Low – Dependent on GF size	Could add significant drag
Jet Flap	0.16 (x/c = 0.98, C_μ = 0.029, δ = 90°)	Very High > 50 Hz	Very Low – If kept below C_μ = 0.05	Requires small space Plumbing

2.3 Steady Jet Flap

This section includes a comprehensive review of the steady jet flap, its benefits and the parameters associated with it. The steady jet refers to continuous blowing from the wing with air sourced externally, as was illustrated in section 2.2.2.3. This section is divided to illustrate the history of the jet flap, as well as the parameters with which the jet flap performance is dependent on. The illustration in Fig. 2.12 presents some of the parameters that will be reviewed. The jet deflection angle, δ, is the angle from the chordline at which the jet is directed at. The distance between points B and D is defined as the jet width. Other crucial parameters to be discussed include the jet flap

chordwise location and the momentum coefficient effect. Finally, the steady blowing jet flap will be reviewed for mitigating lift.

2.3.1 History of Jet Flap

Originally conceived in 1917, Hermann Föttinger proposed the idea of utilising a tangential jet to inject additional momentum into the upper surface boundary layer, thereby ensuring flow remains attached [68]. Despite the early origins of the jet flap, the idea didn't physically materialise until 1931 where Bamber's findings [75], not only justified the jet flap as a pertinent actuator for boundary layer control, but also proved to be the foundation stone for future experiments with the jet flap. It was shown when employing the active flow control method just aft of the mid-chord, a 96% gain in maximum lift coefficient could be obtained with a slot width of 0.667% of chord.

Employing the jet flap over a mechanical flap is known as the 'externally blown flap'. In 1958 the blown jet concept was applied to a real aircraft. Due to the small wing structure and therefore the innately large wing loading on the Lockheed F-104 Starfighter, the aircraft suffered from problematic issues such as extremely high stall speeds and landing speeds [76]. This justified the use of boundary layer control in the form of blown jets, which were blown tangentially along the upper surface of the wing at supersonic speed in order to augment the circulation on the wing at lower speeds and allow it to have short take-offs [77].

Further research was performed into the jet flap in 1963, when the Hunting H.126 was fitted with blown jet flaps to explore the benefits of the jet flap positioned near the trailing edge, whilst in flight, shown in Fig. 2.13. With hot gases emanating over the trailing edge control surfaces, it is able to augment the lift generated by the wing. As such, this provides the aircraft with additional thrust [78]. However, in the case of the Hunting H.126, the exhaust of hot gases meant that insulation was required in order to avert any structural issues and retain a light aircraft structure.

Despite the vast interest for the application of the jet flap, it has only ever been implemented on military and heavy transport aircraft [77]. However, the externally blown flap has failed to emerge on commercial aircraft thus far [79].

2.3.2 Parameters

2.3.2.1 Momentum Coefficient Effect

Spence [80] postulated that the increase in lift is directly proportional to $C_{\mu}^{0.5}$ for jets located near the trailing edge on the lower surface, shown in Eq. [2.12]. This model closely agreed with the purported theory of Dimmock [81, 82] for C_{μ}< 2 and δ = 31.4°. Although when the jet flap is deflected at δ = 90°, Spence's theory is found to be invalid due to flow separation occurring

regardless of momentum coefficient value. However, Spence's theory has been corroborated by tests with relatively high deflection angles, carried out by Traub and Agarwal [83] which were seen to exhibit a strong relationship between $C_\mu^{0.5}$ and C_L at low momentum coefficient values, $C_\mu \leq 0.03$, when the jet was deflected at $\delta = 70°$ (Re = 160,000). Furthermore, steady blowing tests carried out with $\delta = 90°$ by Traub *et al.* [71] have validated the theory, demonstrating its applicability for larger deflection angles. Conversely, further analysis implies that this dependency reduces with increasing jet momentum [83].

$$\Delta C_L \propto \sqrt{C_\mu} \qquad [2.12]$$

The lift coefficient has therefore been demonstrated to increase with the square root of momentum coefficient [71, 83]. However, for lower surface jets there is a momentum coefficient where the lift coefficient peaks and further increase in momentum coefficient leads to lift reduction. Much of this behaviour has been ascribed to the influence of a separation bubble formed at the leading edge [84]. The strong entrainment effect created by the jet causes the separation bubble to enlarge. As such, an increase in unsteadiness is seen to be proportional to the momentum coefficient. This associated unsteadiness leaves the shear layer susceptible to not reattaching and forming the separation bubble. A theory supported by Tuck and Soria [85].

Figure 2.14 shows how lift varies with momentum coefficient for a range of angles of attack between $-4° \leq \alpha \leq 4°$. This figure suggests the effect of momentum coefficient on lift coefficient is independent of low angles of attack [86]. For an angled jet at $\delta = 45°$, blowing from near the leading edge has little effect on lift at lower angles of attack. Closer to the stall angle, differences in blowing strength becomes apparent, as momentum coefficients below $C_\mu < 0.0158$ inflicted a lift loss; $C_\mu = 0.0026$ led to $\Delta C_L \approx -0.21$ at $\alpha = 11°$. Lift became greater than the baseline case above this momentum coefficient, with $C_\mu = 0.0366$ creating a change in lift coefficient of $\Delta C_L \approx 0.19$ [87]. When considering boundary layer control, Korbacher and Sridhar [68] suggest low jet blowing strengths are best suited when coupled with mechanical flaps.

Increasing the momentum coefficient whilst maintaining the jet deflection produced a trend in which stall angle would reduce. This reduction in stall angle has also been observed with other studies [70, 88]. The cause of the reduced stall angle is appertained to the steady jet promoting a thicker boundary layer [70]. As Seifert *et al.* [70] notes, an associated displacement of the stagnation point downstream from its original location, is incited by the steady jet inducing concomitant circulation. Consequently, the boundary layer evolves into a thicker profile. The concluding effect leaves the boundary layer more susceptible to detaching from the surface at smaller angles of attack in comparison to non-blowing cases.

2.3.2.2 Jet Deflection

Deflection of the jet can alter the behaviour of the actuator between boundary layer control and manipulating the aerofoil camber. Dimmock [81, 82] demonstrated for trailing edge locations varying the jet deflection between δ = 31.4°, 58.2° and 90° yields contrasting results. The experiments for an elliptical aerofoil at Re = 425,000, showed that a δ = 90° deflection always caused flow to separate from the surface. Whereas, flow remained attached for δ = 31.4° and 58.2°.

This behaviour of flow separation has also been observed with a jet deflection at 90° experimentally [89] and computationally [88]. Boeije *et al.* [88] performed a computational simulation for a jet placed on the lower surface of a NACA 0018 aerofoil at x_j/c = 0.90. It was shown that with a momentum coefficient of approximately C_μ = 0.0288 and Re = 6.6x10^5 a rise in lift coefficient of approximately $\Delta C_L \approx 0.4$ is possible for pre-stall angles due to the increased circulation created by the jet. Consequently, due to the entrainment effects associated with the jet, the flow on upper surface is directed downwards with a greater angle, near the trailing edge. As such, it appears high deflection angles can still incite a lift increase despite the supplementary flow separation.

Altering the jet deflection angle with a jet positioned near the leading edge also appears to influence performance. Goodarzi *et al.* [90] performed numerical simulations for a steady jet placed at x_j/c = 0.10, that demonstrated the variation in lift to drag performance for δ = 0°, 30° and 45°, see Fig. 2.15a. Angles greater than the tangential angle disrupt the flow which naturally incurs a greater drag penalty. Therefore, lift-to-drag performance drops off as the angle is increased. However, computational results of Goodarzi *et al.* [90] suggest a jet deflected at an angle greater than δ = 0°, will require large jet velocity ratios, in the region of 6, in order to produce lift-to-drag performance similar to unforced cases.

Interestingly, Dimmock [81, 82] results showed that increasing the jet deflection whilst maintaining the momentum coefficient contributed to a reduced stall angle; for example, jet deflection of δ = 90° at C_μ = 0.466 stalled at α = 2°, whilst the δ = 31.4° model at C_μ = 0.5 experienced stall at α = 6°. Lowry and Vogler [91] noted similar behaviour, when jet flaps were activated at higher deflection angles. With the steady jet findings of Dimmock [81] and Bradbury & Riley [92], a comparison made by Simmons *et al.* [93] on the effect of deflection angle on velocity decay demonstrated larger deflection angles suffer faster velocity decay, see Fig. 2.15b. In addition, larger jet deflection angles produce stronger contrarotating vortices. Furthermore, the jet is capable of greater penetration into the crossflow with when the jet is aligned parallel to the freestream [94].

One method of measuring the effect of jet deflections is using the lift magnification factor. This involves the difference between the change in lift and jet reaction divided by the jet reaction [86]:

$$\text{Lift magnification factor} = \frac{\Delta C_L - C_\mu \sin\delta}{C_\mu \sin\delta} \quad [2.13]$$

2.3.2.3 Jet Width

One would intuitively assume a larger jet width would manipulate the boundary layer to a greater effect creating greater change in lift. This is proven to be the case in early investigations into the effect of varying the width of a tangentially blown jet flap, carried out by Bamber [75]. However, the findings suggest that there will be a point where further widening the jet will eventually cause lift to decrease.

A steady jet would initially produce a pair of contra-rotating vortices when subjected to a free-stream velocity [95], an observation also noted by Krothapalli and Leopold [96]. The interaction between the jet flow and the cross-flow will result in the formation of a pair of contrarotating vortices, thereby introducing three dimensional effects. Introduction of these vortices can reduce the maximum lift attained by the lower surface jet; however, the detrimental effect of these vortices can be mitigated when a larger jet aspect ratio is used, as shown in Fig. 2.16.

An important aspect of the jet is its orientation to oncoming flow. Weston & Thames [94] performed a comparison of two configurations of a finite normal blowing jet of AR = 4; one positioned with longer side perpendicular to oncoming flow and the other with the long side parallel. In comparison to the parallel jet, the spanwise placed jet has a greater effect on the pressure immediately downstream of the jet. An increase in negative pressure is stimulated with increasing blowing jet ratio. This evokes greater gradients in pressure behind the jet.

Perpendicular jets exhibit a jet width relationship contrary to tangential jets. Computational results suggest the jet width for a perpendicular jet is inversely proportional the lift coefficient [97]. This is due to larger jet widths inherently propagating the size of the vortices from the jet, evoking greater turbulence and therefore a loss in lift.

2.3.2.4 Jet Location

Different chordwise locations will affect the jet's influence on lift and drag. As such, it is crucial to identify the optimum location for a steady blowing jet flap. Lockwood and Vogler [86] drew comparisons between jets positioned at x_j/c = 0.726 and 0.937 on the lower surface, with jet deflections of δ = 50° and 56°, respectively. Their findings suggested that at similar momentum coefficients, positioning the jet towards the trailing edge would enhance lift circulation and

consequently total lift. Although these studies used different aspect ratios and thicknesses, making direct comparisons difficult. However, this is corroborated by Mikolowsky and McMahon [98]. Normal blowing from the lower surface has also been shown to vary in effect with location. Mikolowsky and McMahon [98] showed lift could be amplified when displacing the jet further downstream, provided the jet was performing with a velocity not substantially greater than freestream. Larger load changes were seen with the jet velocity twice that of freestream. Locations nearer to the trailing edge induce larger lift changes due to a greater region of influence ahead of the jet for pressure to appreciate.

Two-dimensional CFD simulations carried out on a NACA0012 aerofoil for upper surface jets, by Huang *et al.* [99] showed variation in jet locations and momentum coefficients varied the efficacy, shown in Fig. 2.17. With a jet deflection of δ = 90°, results from Huang *et al.* [99] indicate regardless of the momentum coefficient utilised, a loss in lift is observed for any jet position up to and including $x_j/c \leq 0.2$. Increasing momentum coefficient only further reduced lift and increased skin friction drag. However, it was seen that a momentum coefficient value as low as C_μ = 2.5x10^{-6} was able to evoke significant changes in force. Interestingly, simulations for a post-stall incidence angle of α = 18° suggest for trailing edge locations smaller values of C_μ produce the largest increase in lift coefficient, regardless of deflection angle.

2.3.3 Steady Jets for Lift Reduction

Very scant research has been carried out to deduce the effects of using jets to reduce lift or to deal with gust load alleviation. However, this topic has received interest for wind turbine applications in order to mitigate extreme blade loading [72, 88]. It has been shown placing a jet on the lower surface of the aerofoil will increase circulation [72]. Inversely one would expect placing a jet near the trailing edge on the upper surface would reduce lift loads.

Numerical investigations carried out by Boeije *et al.* [88] showed placing a jet at x_j/c = 0.90 on the suction surface whilst blowing perpendicular to the surface can reduce lift. For a NACA0018 aerofoil the reduction was C_L = 0.275 for C_μ = 0.0175, when tested at an incidence angle of α = 8°.

Computational studies were also performed by Blaylock *et al.* [72] who showed that the jet can control lift effectively, when placed on the upper surface, see Fig. 2.18. However, when placing the jet on the lower surface, the jet had a more pronounced impact on the lift magnitude in comparison to the upper surface jet. The reason for this is because of the development of the boundary layer. The boundary layer on the suction surface becomes thicker towards the trailing edge, effectively submerging the jet in the boundary layer. As the boundary layer thickens with angle of attack, the jets' impact is consequently diminished. In order to create greater effect, one would expect that the

jet would require a greater momentum coefficient so as to overcome the shear layer. The reduction in lift did see a concurrent reduction in drag due to the associated reduction in induced drag.

2.3.4 Steady Jet Flap Summary

After reviewing the literature, it has been shown that the steady jet flap is an effective actuator for steady state conditions. Experimental studies have illustrated that the purpose of the jet is dependent on the jet deflection angle; low angles can be used to prevent flow separation through momentum injection, and high angles can be used to incite separation. The blowing strength of the jet, is defined with the momentum coefficient, and has been shown to be an important factor with the efficacy of the jet flap, as lift is dependent on the square root of the momentum coefficient. However, as it will be shown, the jet flap can be modified for periodic or transient deployment. As such, two forms of unsteady jet flaps will be considered in the following sections; pulsed jets and synthetic jets.

2.4 Unsteady Jets

Three unsteady state forms of the jet flap are the pulsed jet flap, synthetic jet and the oscillating jet. The pulsed jet is often deployed with square or sinusoidal wave profiles, whereas the synthetic jet cycles between a blowing and suction phase; hence, leads to zero net mass flux. Oscillating jets eject air with an undulating deflection angle. This section will discuss the efficacy of the pulsed jet first, as compared to the steady jet flap, as well as the parameters which influence this efficacy. Following this, the synthetic and oscillating jets will be reviewed separately, with their parameters being discussed.

2.4.1 Pulsed Jet Flap

Jet flaps which eject air from their exits intermittently are referred to as pulsed jets. Unlike synthetic jets, the pulsed jet does not have a suction phase, and is at rest in between ejection strokes. As such, the pulsed jet uses a square or sinusoidal wave profile. The notion of the pulsed jet is to inherently reduce the consumption of power, through reduced mass flow rates, whilst retaining the beneficial outcomes generated by continuous blowing. The pulsed jet is shown to be a fast-acting actuator, as Boeije *et al.* [88] showed half of steady state force can be attained within one convective time unit following activation. Furthermore, the effect of pulsed blowing on wind turbine blades has been shown to increase power production over steady blowing [100]. In addition, separation can be inhibited with pulsing jets located fore of the separation point in order to delay the stall angle, as the work of Scholz *et al.* [101] noted.

Pulsed jets have also been researched for wind turbine applications. A 2D URANS simulation by Bobonea [102] showed that at an angle of $\alpha = 5°$, the drag coefficient was reduced by

approximately 2.27% whilst lift coefficient increased by approximately 4.97%, when C_μ = 0.001. However, further amplification of the momentum coefficient sees it becoming detrimental to the drag coefficient and provides little benefit to increasing the lift coefficient. Performance of the blown flap could be improved with pulsation over the trailing edge flap [103, 104]. Although, this too depends on the Strouhal number of the flap, as Zhou *et al.* [103] shows lift change increases with excitation before reaching a maximum around *Str* = 0.206. Augmenting momentum coefficient for the pulsed blown flap concurrently increases lift coefficient, with the incremental load changes between momentum coefficients decreasing.

Lockwood [105] sought for improved propulsive systems performance with the use of a pulsed injection system, and thereafter purported the impact of which vortices emerging from the jet had on flow entrainment. Bremhorst & Hollis [106] later showed that the pulsed jet is far superior in entraining ambient flow than continuously blowing. The inherently distinct puffs produced by pulsed jets, are significantly more capable of mixing with surrounding fluid quicker than steady jets are [107]. However, the core within the vortex rings produced by the pulsed jets would require more time to mix [107, 108]. This is demonstrated by the findings of Johari *et al.* [108] which show the trailing jet velocity depreciates quicker than the vortex ring velocity. This signifies that the trailing jet possesses a superior entrainment rate.

2.4.1.1 Duty Cycle Effect

The significant advantage of pulsed jets utilising less mass flow rate has motivated the extensive study of pulsed jet behaviour. Effectively modulated jets will produce strong compact vortex rings which are capable of penetrating cross flow much further than steady jets [109]. This is evident in the findings of Johari *et al.* [110] who investigated the effect of varying frequency, injection time and duty cycles of a turbulent transverse jet. Inherently, the injection time is dependent on the pulsed frequency. With the jet set at a velocity ratio of five, a duty cycle of 0.2 and a pulsing frequency of 1 Hz, it was able to penetrate an additional 480% to its steady jet counterpart at x/d = 50, see Fig. 2.19a. This deeper penetration is attributed to the compactness of the vortices induced by pulsed jets [109], which have been captured by Hermanson [111] in Fig. 2.19b.

The ability for pulsed flow to produce deep penetrating vortex rings into the cross flow is heavily dependent on the injection time and duty cycle. Injection times strongly dictate the structure of the emanating jet flow; faster injection times will yield concentrated vortex rings [111]. On the contrary, larger injection times incite incoherent structures which are far less capable of penetrating cross flow effectively [111]. Duty cycles also retain a prominent role in effective penetration since it influences the distance between each pulse. Shorter duty cycles (≈ 0.2 - 0.3) ensure the vortex rings are not susceptible to interacting with one another in the near field, thus contributing to further penetration [111]. Consequently, this is translated into greater lift produced as has been corroborated

by Scholz *et al.* [101] , where comparisons between different duty cycles at a fixed frequency of k = 0.6 for a pulsed jet indicated 12% and 25% duty cycles attained the greatest lift coefficients as well as delaying stall. On the contrary, further increasing the duty cycle beyond 25% resulted in a trend of decreasing maximum lift coefficient. However, increasing the excitation to larger frequencies, the pulsed jet will perform analogous to continuous blowing jets [112].

Much of this behaviour described was substantiated with the observations made by M'Closky *et al.* [113], which suggest that injection times should be limited within 2.7 to 3.0 ms to attain effective penetration. It should be noted that within the same findings of M'Closky *et al.* [113], the pulsed formation penetrated more cross flow than the sine wave formation, despite similar frequencies. Experimental studies of Hermanson *et al.* [111] suggest that regardless of the duty cycle utilised, the pulsed jet attains superior penetration in comparison to the steady jet, albeit with identical time averaged velocities.

Influence of duty cycle on lift production becomes significant once the vortex is deprived of time to fully form [103]. As such, lower duty cycles generate more lift due to the vortex being more developed. This behaviour is also noted for airfoils with no flaps. Placing the pulsed jet nearer to the leading edge may coincide with the separation point of a fixed airfoil, thus extending the lift curve beyond the stall angle [114]. In the post stall region (α = 20°), Hipp *et al.* [115] found for a normal pulsed jet at a non-dimensional frequency of F+ = 1, a duty cycle of 5% provides an increase of lift two-fold to that of a duty cycle of 50%. Duty cycle ostensibly appears to take precedent over frequency, which is supported by Scholz *et al.* [101]. Further reduction in duty cycle could attain greater change in lift, than blowing for a longer duration with a greater frequency, provided the jet is not off long enough for the airfoil to return to the baseline case. As Hipp *et al.* [115] found shorter blowing durations provide the vortex sufficient time to reform a reattachment point nearer to the trailing edge, before the successive pulsed vortex is generated. Thus, an area of low pressure is retained for the succeeding vortex to have greater effect over the upper surface.

2.4.1.2 Frequency Effect

As it was mentioned previously, excessively increasing the frequency of the pulsed jet risks returning the jet behaviour to that of steady blowing jets. As such, it is necessary to explore the effect of frequency has on pulsed jets. As observed by Scholz *et al.* [101], despite providing an insignificant change in lift coefficient at pre-stall angles, varying reduced frequencies between k = 0.4 – 0.8 provided lift to increase beyond the stall angle for a given duty cycle, see Fig. 2.20. Closer inspection of Fig. 2.20 indicates that beyond the stall angle, blowing at k = 0.6 provides greater lift improvement than k = 0.4 & 0.8.

In spite of the fact that the frequency parameter is not as influential as the duty cycle effect, consecutive pulsed blowing is necessary to retain flow attachment on the upper surface. This is highlighted by an experimental investigation performed by Woo *et al.* [116]. When pulsing with one cycle, the jet at x/c = 0.15 creates a vortex which rolls up towards the trailing edge. Once the vortex is aft of the trailing edge, the upstream boundary layer is brought closer towards the surface. Thereby, extending the attached region to x/c = 0.60. The reattachment process lasts for over τ = 2. However, a force reversal is initially observed as the jet is initiated, due to negative vorticity produced by the clockwise vortex emanating from the jet. When increasing the number of pulses for the jet, the attached boundary layer is reinforced with every pulse. The ensuing pulse generates a vortex which disrupts the attached flow established from the first pulse. However, the latter pulse improves flow attachment by mitigating the separated region on the upper surface. Sudden deactivation of the pulsed jet sees the flow field returning to the baseline case at eight convective time units later than it takes reattachment process to complete.

2.4.1.3 Pulsed Jets for Lift Reduction

Very little research has been performed to investigate the use of pulsed jets in mitigating lift force. Regardless of this, Wong & Kontis [117] utilised a pulsed jet positioned above the suction surface at quarter chord. A reduced frequency of k = 0.316 incited a momentum coefficient of C_μ = 0.116. This produced a change in lift of C_L = - 0.05, and was accompanied by an increase in drag too. However, increasing the frequency of upper surface pulsed blowing will eventually lead to attaining results similar to the steady jet [118] .This trivial change in lift coefficient renders this technique ineffective.

Pulsed blowing from the surface of the wing has been investigated for gust load alleviation purposes. Kerstens *et al.* [118] showed pulsed blowing was effective for low reduced frequencies k < 0.09, subduing gust loads within +/-5% of reference lift. However, actuation becomes restricted by the natural response of the flowfield to be influenced by the jet, as lift is not altered until four convective time units after the jet is initially activated. As such, it is suggested that faster actuators will not make a difference as it is the time needed to force a change in in the flowfield being the dominant factor. Transient response of jet deployment was also performed by Williams *et al.* [119], shown in Fig. 2.21, who observed similar changes in lift force as the jet mitigated the gust induced force reduction.

2.4.2 Synthetic Jets

Synthetic jets generally consist of a membrane wall which periodically displaces to intake and force air out of a cavity [120], see Fig. 2.22a. The oscillation of the membrane forces the jet to perform ejection and suction in one period, as such, they do not require an additional air source other

than ambient air. Therefore, synthetic jets are otherwise known as zero-net-mass-flux (ZNMF) jets. This is an advantage many other actuators do not possess. The membrane can be driven by a piezoelectric driver [121] to reach high frequencies; however, synthetic jets have been produced using acoustically driven mechanisms, which use sound waves to displace a volume of air to produce vortices [122, 123]. As the jet relies on the oscillating diaphragm movement, maximum jet velocity can be obtained around resonance but these occur at extremely high frequencies [124]. Regardless, changes in the flowfield can be achieved by the jet as this stroking movement consequently produces a pair of vortices that are shed from the walls of the jet [125]. As the jet enters the suction phase during its downstroke, the vortices from the ejection phase are far enough away from the jet to be influenced [121]. The actuator is often used to delay stall and increase lift coefficient [124].

2.4.2.1 Momentum Coefficient Effect

Similar to steady jets, the blowing amplitude is also defined by the momentum coefficient, which only considers the phase averaged velocity during the ejection phase [120], see Eq. [2.14] for the two-dimensional definition. Goodfellow *et al.* [126] illustrate that provided the momentum coefficient is large enough, a reduction in wake size is obtained, shown in Fig. 2.21b. This is corroborated by Whitehead and Gursul [127]. This is due to the additional momentum from the jet delaying the separation point along the upper surface. Interestingly, as the synthetic jet relies upon the driving frequency of the actuator to obtain large momentum coefficients, this leads to a greater shedding frequency aft of the jet, despite the wake size reduction. Such wake reduction is accompanied with drag reduction, shown for Re = 1 x 10^5, drag is reduced to 34% of the baseline value for C_μ = 0.012.

$$C_\mu = \frac{\bar{I}_j}{\frac{1}{2}\rho_\infty U_\infty^2 c} \qquad [2.14]$$

Where $\bar{I}_j = \frac{2}{T}\rho_j h_j \int_0^{T/2} U_j^2(t)dt$

One use of the synthetic jet is to incite flow reattachment; Tuck and Soria [85] showed that actuating at a non-dimensional frequency of F+ = 1.3 lift increases by 50% for a momentum coefficient of C_μ = 0.0014 at α = 18°. At this angle, complete flow reattachment is not attained, but separation is suppressed well enough. Amitay *et al.* [120] show similar effects for a similar symmetrical airfoil. The range of angles that exhibit no flow separation is extended from 5° to α = 17.5°. Although lift is greater than the uncontrolled case for higher angles, the findings indicate flow isn't entirely attached.

The synthetic jet can entrain more flow than steady blowing, because its mean velocity decaying faster [121]. When directly compared to a normal blowing jet, the vortices ejected from the

synthetic jet cover a greater area to incite mixing [128]. Under freestream velocity, the synthetic jet slows down velocity near the jet location, but the added momentum from blowing accelerates flow in the far field, downstream of the jet [129].

2.4.2.2 Frequency Effect

The effectiveness of the synthetic jet is dependent on the driving frequency. Amitay & Glezer [130] show when non-dimensional frequency is greater than $F+ \geq 10$, there is no further benefit in terms of drag reduction or lift increase. However, below $F+ \leq 10$, the maximum lift coefficient reduces from the value attained near unity ($F+ = 1$). However, often the synthetic jet requires large voltages to drive the voice coils at high excitation frequencies even for low values of momentum coefficient; Goodfellow *et al.* [126] show a momentum coefficient of $C_\mu = 0.012$ at reduced frequency of $k \approx 12.7$ is obtained when applying a voltage of 275V to force piezoelectric actuators. Plasma synthetic jets have been explored by Wang *et al.* [131], in order to overcome the need for high voltages and were shown to produce fast exit velocities up to above 300 ms^{-1}, but this was only tested for small jet exit diameters. Despite the high voltage requirements, greater frequency excitation attains greater vorticity which assists the ejected flow to further penetrate into the freestream [129]. The size of the vortex pair enlarges as frequency excitation increases [126].

When tested on a flat plate, the generated vortices fail to amalgamate regardless of the level of excitation [121]. However, experimental investigations by Tuck and Soria [85] suggest this behaviour may be different when the synthetic jet is on an airfoil under freestream conditions. It was shown when testing above a non-dimensional frequency of $F+ = 1$, the vortices from the synthetic jet force flow reattachment aft of the leading edge, as continuously pulsing results in an amalgamation of these vortices, thereby augmenting vorticity. This ultimately increases lift until a stable value is attained [132]. Greater change in circulation could be achieved with a single ejection of a transient synthetic jet [133].

Gordon & Soria [129] noted the pair of counter rotating vortices emanate from the jet exit. However, a latency in their formation is observed. When the synthetic jet is operating within a freestream, the pair of vortices are carried away with external flow, therefore dissipating vorticity quickly as the jet is within the downstroke phase. During the downstroke phase, the synthetic jet extracts majority of its flow from near the jet exit, while ejected flow has more influence on flow further away from the jet. Gordon & Soria [129] note that at three diameter lengths away from the jet, the volume of flow influenced by the jet during the suction phase amounts to only 5% that of flow during the ejection phase.

2.4.2.3 Jet Location Effect

In order to obtain maximum lift increase, the optimal location has been suggested to be near the leading edge [134]. This is validated by Amitay *et al.* [120], who show the preferred location for maximum efficiency is near the separation point, as this allows using a smaller momentum coefficient. However, Widjanarko *et al.* [135] placed a normal blowing synthetic jet on the pressure surface near the trailing edge. It was observed that alteration in circulation becomes dependent on the recirculation region engendered by the jet flow. The separated region must extend towards the trailing edge in order to enhance downwash and therefore a negative change in circulation, otherwise a loss in lift is experienced.

2.4.2.4 Synthetic Jets for Lift Reduction

The synthetic jet has been explored for gust load alleviation. Stolk *et al.* [136] showed through computational methods that lift is decreases by 14.6% at F+ = 1, when the jet is located at the point of maximum thickness. When using frequencies around F+ = 0.5, locations closer to the trailing edge incites a superior sensitivity to changes in lift due to the influence on the Kutta condition. However, combining frequencies above unity with placing the synthetic jet close to location of maximum thickness are required to produce similar effect on lift to placing the jet close to the trailing edge. Further change in lift could be achieved with widening the jet width [137], therefore adding momentum.

The synthetic jet at the 'spoiler' position of x/c = 0.60 was investigated with RANS simulations by Xu *et al.* [125] for the purpose of gust load alleviation. The jet was capable of mitigating a sudden 1 – cos gust by approximately 4%. However, continuous normal blowing was capable of mitigating the load to a greater extent, as this deflects the shear layer away from the surface, hence enlarging the wake aft of the jet. Although the synthetic jet causes flow to reattach on to the surface during a gust response, it can be said that effective gust load mitigation is brought upon by creating a larger separated region above the airfoil. As such, the synthetic jet does not suit this requirement for lift reduction.

2.4.3 Oscillating Jet Flap

One form of the unsteady jet flap can be achieved by deflecting the jet angle in a sinusoidal fashion about an axis, see Fig. 2.22a. This is known as the oscillating jet flap, and the deflection is often achieved with the use of a fast acting servo-motor [138], in order to inject high momentum air in to slow moving air. Therefore, augmenting circulation by maintaining attached flow. Originally, the oscillating jet was hypothesised by Sears, as a potential actuator to counter gust loads due to its unsteady motion [139], therefore producing changes in lift. However, Viets also showed that the

oscillating jet could be used to enhance the mixing of air [140]. This is corroborated with the findings of Platzer *et al.* [141], who showed an enhancement of over 50% in volumetric flow rate exiting a steady blowing jet could be attained with an oscillating jet. Such behaviour is suitable for encouraging high momentum to mix with low velocity regions. Therefore, leading to suppression of a separated region. The strength of the jet is defined with the momentum coefficient parameter, but the velocity term is defined by the jet amplitude [70].

2.4.3.1 Momentum Coefficient Effect

Following the suggestion of Sears, Spence [139] carried out early theoretical work in order to attempt to depict oscillatory jet behaviour on a fixed airfoil through mathematical models. Such models were conceived by the dependency of oscillatory lift coefficients trends on the parameter $C_\mu k$, and supposed flow remained inviscid. The numerical solutions show lift remains close to the baseline case until reduced frequency reaches unity. After which, lift augmentation becomes proportional to excitation. In addition, lift response leads the phase angle of the jet. However, this is incongruent with experimental findings which show lift decreases with frequency [138]. Simmons & Platzer [138] investigated the use of an oscillating jet flap achieved by a rotating cylinder with a row of holes located at the trailing edge; oscillating with a momentum coefficient of $<C_\mu>$ = 0.14 at a reduced frequency of k = 0.5 retains approximately 70% of the lift achieved at k = 0. The effectiveness of the jet further reduces at higher frequencies, as Simmons [142] shows this magnitude falls to 42% at k = 1.03. The effect of momentum coefficients for trailing edge oscillating jet flaps was also highlighted [138]. It was observed that a larger momentum coefficient retains less force, as blowing with $<C_\mu>$ = 0.58 reaches almost 60% of baseline case for the same frequency. Further contradiction to Spence's findings was indicated with phase angle reaching some maximum before reducing with frequency. This maximum is expedited with a greater momentum coefficient, but with less lag response accompanied. However, a later investigation by Simmons & Platzer [143] showed larger momentum coefficients yield greater lag in lift response. Furthermore, the velocity decay is dependent on the jet strength, with greater blowing amplitudes expediting the decay [93]. Several experimental studies have indicated that Spence's theory work does not apply for realistic reduced frequencies below 2π [142, 144].

Prevention of flow separation is a highly coveted feature with oscillating jets. Trailing edge flaps are susceptible to flow separation, as the large deflection angles cause large adverse pressure gradients, reducing the effectiveness of the trailing edge flap. As such, Seifert *et al.* [70] experimentally investigated the oscillating jet at the hinge line of a trailing edge flap deflected at δ = 20°. It was shown the lift curve gradient remains constant despite blowing, although the curve is translated up, indicating an increase in lift. Although it was shown that steady blowing at C_μ = 0.008 increases lift by ΔC_L = 0.2, efficiency was greatly improved with the addition of an oscillating jet to

the steady jet. Steady blowing at eight times less the mass flow rate, with oscillating jet simultaneously at $<C_\mu>$ = 0 .01 at F+ = 2 obtains a further change in lift ΔC_L = 0.3. Pressure measurements illustrate a positive pressure gradient near the trailing edge with steady blowing, representing partial separation over the flap. The improved lift from the oscillating jet is due to the flow on the upper surface becoming fully attached. As the angle of attack increases beyond α = 6°, it was found that excitation needed to be augmented to produce analogous lift changes [70].

The added momentum from the jet reduces the separated region until fully attached, but stall angle is brought about earlier with steady blowing, as the change in circulation leads to the stagnation point displacing further along the lower surface. This leads to a greater boundary layer height which leaves the airfoil vulnerable to separating early [70]. Conversely, oscillation produces vortices which encourage mixing between flows within and above the separated region. This is seen with Seifert *et al.* [145] as steady blowing at the hinge line precipitated an earlier stall by $\Delta\alpha$ = -2° compare to the basic airfoil. In contrast, stall was delayed by $\Delta\alpha$ = 2° with oscillating jet, despite lower power.

The entrainment mechanism induced by the oscillating jet mitigates drag [70], consequently Seifert *et al.* [145] observed for a given lift to drag ratio, oscillating uses over six times less mass flow rate than steady blowing, as steady blowing relies on momentum to overcome viscous forces [146]. When seeking for the optimum location for a given combination of steady and oscillating momentum coefficients, lift can be increased by a further $\Delta C_L \approx 0.5$ when displacing the jet from the leading edge to the hinge line of the deflection flap. As such, the optimum location for the jet must be located near the separation point for maximum efficiency.

In order to ensure the benefits of oscillatory blowing extend to higher Reynolds numbers, Seifert & Pack [146] tested a zero-net mass flux edition of the oscillatory jet at the hinge line of a downwards deflected flap. At Re = 28.2x10^6, lift was increased by 2.3 times at F+ = 0.7 for a momentum coefficient of $<C_\mu>$ = 0.0005. Concomitantly, wake sizes reduce approximately in half which translate to a drag reduction, shown in Fig. 2.22b. Such findings highlight the effect of oscillatory blowing is independent of Reynolds number. Wake size and drag reductions were also noted by Hites *et al.* [147], as drag was reduced to 69% of the baseline case when blowing with $<C_\mu>$ = 0.0001 and F+ = 0.73. Steady blowing did not provide any benefit in drag savings until freestream was at M = 0.3. Interestingly, lift magnitude diminished due to steady blowing which is dissimilar to findings from Seifert *et al.* [70]. At lower freestream velocities, the steady jet increased drag by 34% as the minimum velocity in the wake was reduced by approximately 3%. It becomes apparent the oscillating jet is more suitable for flow reattachment purposes.

2.4.4 Unsteady Jet Flap Summary

The review of the jet flap in section 2.4 has shown the technology has the potential to be a fast-acting actuator for various purposes. Manipulation in lift is shown to be possible with the jet flap, however, it has been observed that each form of the jet is capable of achieving this to varying degrees. Their characteristics are summarised in Table [2.2]. Pulsed and synthetic jets are possible to use with high actuation frequencies; however, synthetic jets rely upon the ambient air which may inhibit its blowing strength. Oscillating jets are effective at mixing air to reduce flow separation on the wing, but this may not be a good technique to mitigate gust loads.

Table 2.2 - Summary of jet flap strategies.

Jet Flap	Advantages	Disadvantages
Steady	Attains large changes in lift	Not suitable for dynamic situations
		Requires external supply of air
Pulsed	Can be used in a loop control system	Requires external supply of air
	Ejected flow profile can be manipulated	
	Fast response	
Synthetic	Does not require external air supply	Cannot attain high momentum coefficients
	Can achieve high frequencies	
Oscillating	Reduces separation on airfoil effectively with low energy	Requires external supply of air
	Can achieve high frequencies	

2.5 NACA 0012

As mentioned in the summary, the airfoil under consideration for this project is the NACA 0012. Numerous experimental studies have been performed for this airfoil, which makes it ideal to test with. From these studies itt appears that the type of stall behaviour for the NACA 0012 has been disputed; Sunneechurra and Greenblatt [148, 149] have both suggested that the NACA 0012

experiences a leading edge stall, see Fig. 2.24. However, it has been seen that stall behaviour with the NACA 0012 is heavily dependent on the Reynolds number. Subjecting the NACA 0012 profile to low Reynolds numbers in the order of 10^3, the separated boundary layer will be incapable of reattaching to the surface [150]. This is a characteristic of trailing edge stall.

Further increasing the Reynolds number provides the boundary layer with enough momentum to reattach. It was observed that the NACA 0012, in a Reynolds number region of the order of 10^5, is subjected to a short bubble formation at pre-stall angles [151-153]. The laminar boundary layer detaches near the leading edge. However, the boundary layer is able to reattach to the surface because of its transition from laminar to turbulence, ultimately the incipient formation of separation bubble is observed [151]. Increasing incidence causes the bubble to continue to extend in size [151], as the reattachment point extends downstream to the trailing edge. Contiguously, the short bubble evolves to become a long bubble, which indicates the onset of stall [152]. Stall is then brought about once the flow completely separates from the end of the trailing edge. This type of stall is denoted as thin aerofoil stall [23]. The separation bubble which appears on the suction surface decreases in size and moves upstream towards the leading edge with Reynolds number.

A computational study carried out by Mittal and Saxena [154] exhibited dissimilarity in stall angles for a NACA 0012 profile, when ascending and descending angles. The dissonance in stall angles is pertained to the greater unsteadiness involved with decreasing angles; separation point remains constant until suddenly appearing at the leading edge. With increasing incidence, the separation point displaces in a steady manner towards the leading edge, subsequently containing the unsteadiness and yielding a greater stall angle.

2.6 Gap in the Literature

Gust alleviation is of huge importance to fixed-wing, rotorcraft and wind turbine design. There has therefore been detailed research into different candidate technologies including active flow control. Active flow control has been extensively researched and has shown the potential of various actuators for inhibiting flow separation or augmenting lift. Pertinent to the current project, the jet flap has received particular interest. Various studies have exhibited the impact a steady jet flap has on increasing lift, whilst unsteady jets have been used to improve separation control. However, limited research has been performed for steady and unsteady variations of normal and upstream blowing jets. Preliminary work indicates their ability to disrupt flow and instigate lift reduction but many gaps remain in the understanding of this potentially significant flow control approach.

In particular the jet flap actuator has not been experimentally studied to investigate its potential for alleviating unsteady gust loads. A computational study [125] has indicated their ability to mitigate lift with fast frequency response effectively alleviating gust loads. Such characteristics of an actuator are important, as the onset of gusts requires a fast-responsive actuator to effectively

mitigate sudden changes in lift loads. In addition, the effectiveness of the jet flap with increasing frequency has yet to be observed, which would ultimately determine the efficacy of the jet flap when acting against high frequency gusts. It is therefore necessary to experimentally investigate the jet flap in this context.

2.7 Aim and Objectives

The aim is to investigate the jet flap as a load control approach in steady and unsteady states, and understand the mechanisms by which it effects a change in force. This aim will be met through several individual objectives:

- Investigate the efficacy of the jet flap for mitigating lift loads in steady state conditions. This should include both normal and upstream blowing; plus, the effect of varying chordwise location, momentum coefficient and angle of attack.
- Investigate the effect of periodic deployment of the jet flap. Consider reduced frequencies up to $k \leq 0.471$, with various chordwise locations, momentum coefficient values and angles of attack.
- Investigate the efficacy of the jet flap with transient response. Consider the time delay for the jet flap at various chordwise locations and angles of attack.

2.7 Figures

Figure 2.1 – Illustration of a typical continuous gust profile [11].

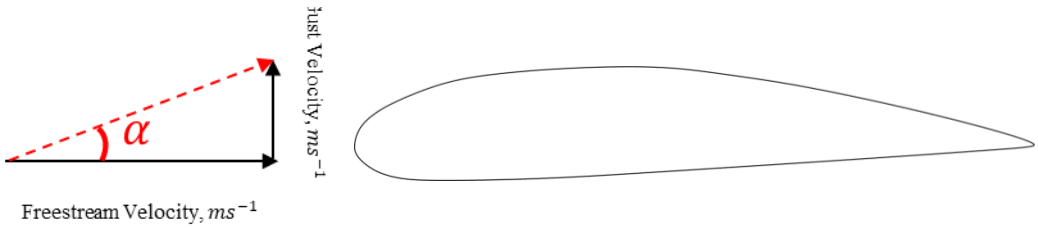

Figure 2.2 – Illustration of effective change in angle of attack caused by vertical gust.

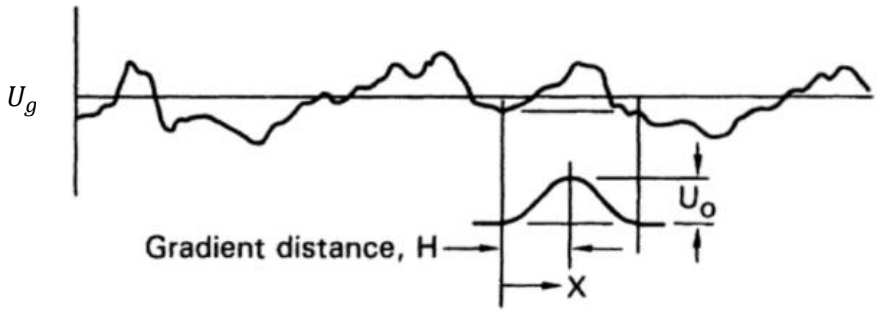

Figure 2.3 – Illustration defining a discrete gust profile [11].

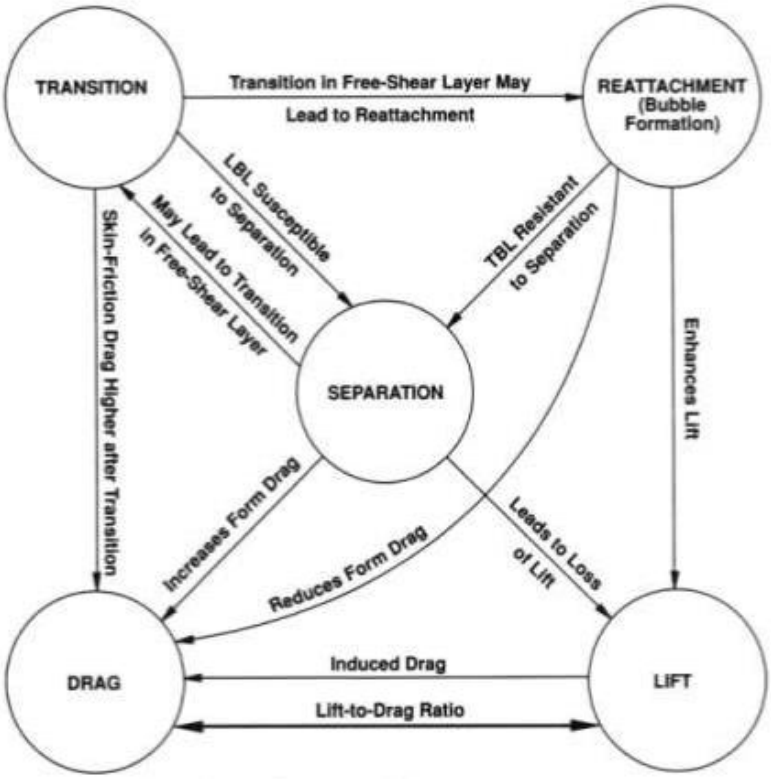

Figure 2.4 – Correlation of flow control objectives [22].

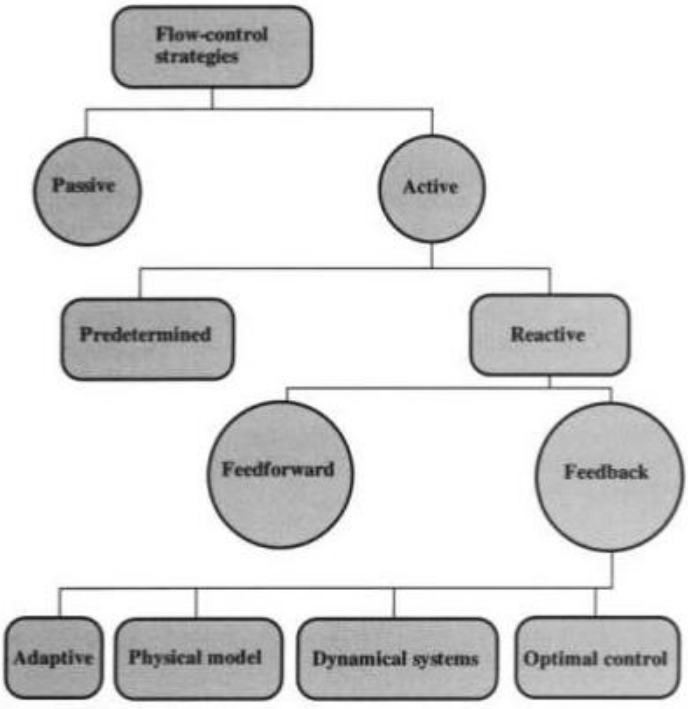

Figure 2.5 – Approaches to flow control [22].

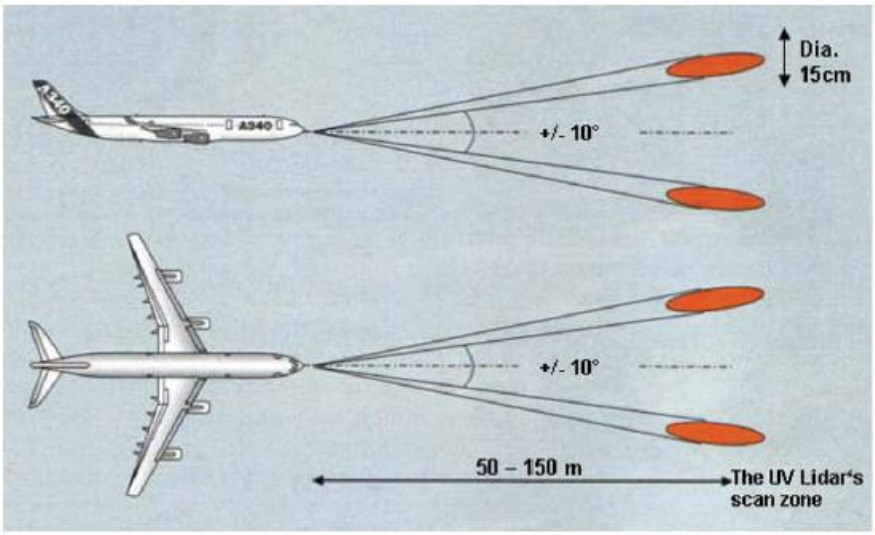

Figure 2.6 – Range of gust detection for Lidar system [33].

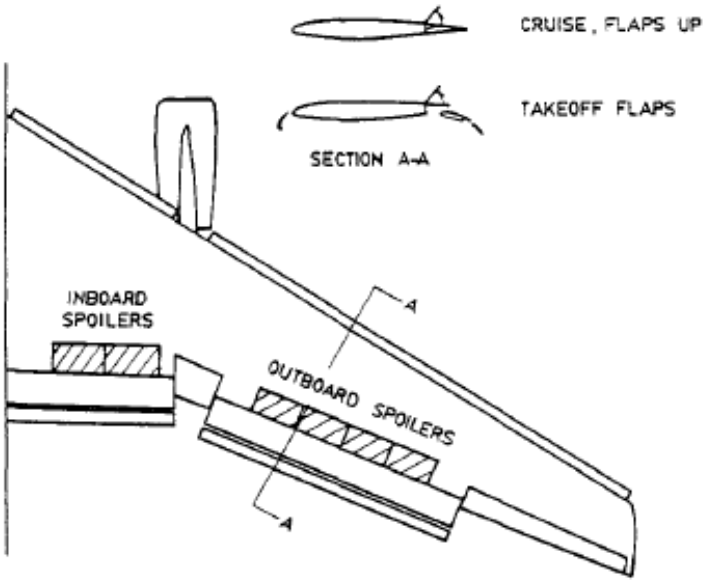

a)

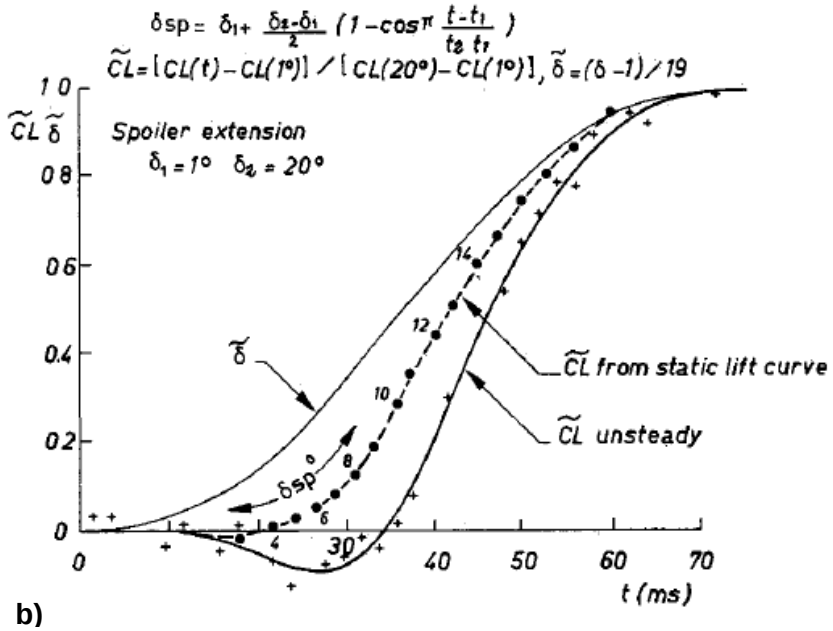

b)

Figure 2.7 – a) Illustration of spoiler location on wing [38]; b) Transient deployment of spoiler by Consigny *et al.* [35].

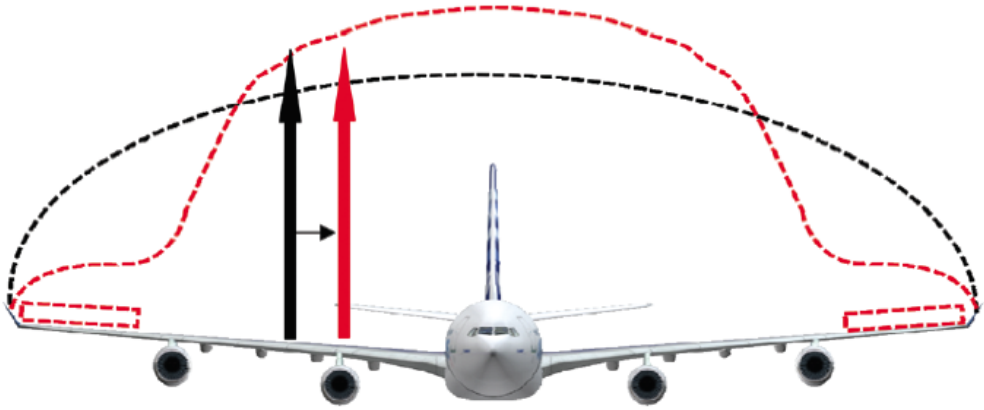

a)

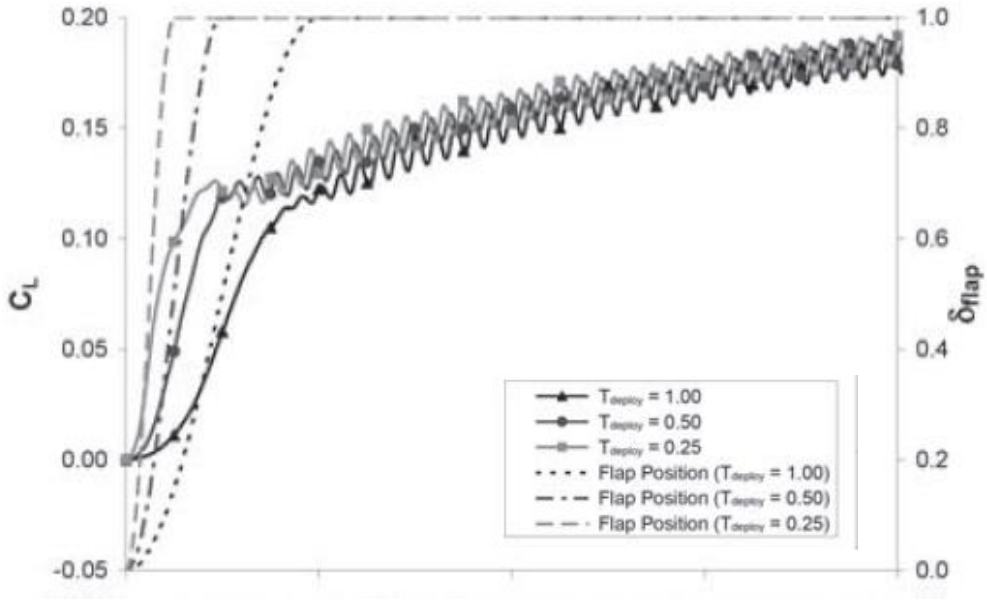

b)

Figure 2.8 – a) Load alleviation induced by outboard ailerons [33]; b) The effect of deployment rate with transient response of aileron [52].

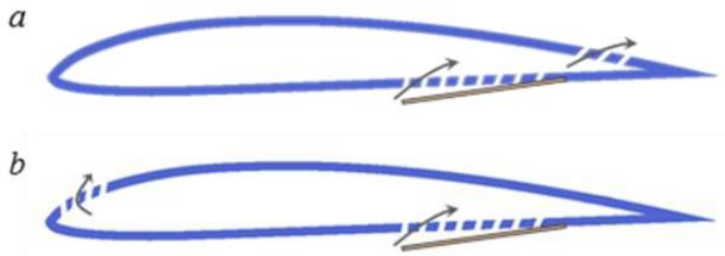

a)

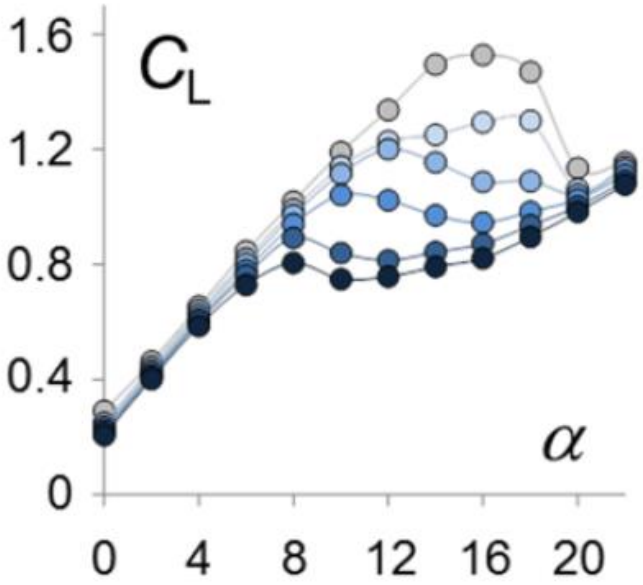

b)

Figure 2.9 – a) Louvers actuate to control bleed [56]; b) The effect of bleed strength on lift coefficient [56].

a)

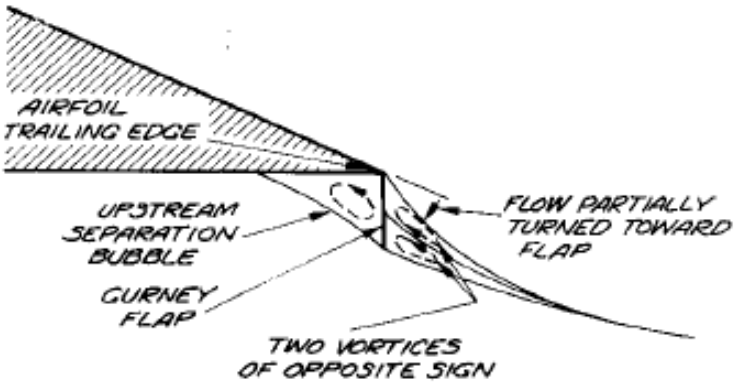

b)

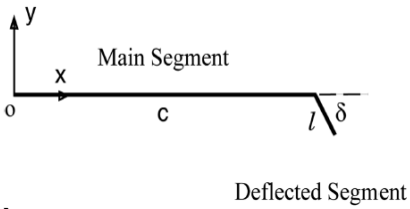

c)

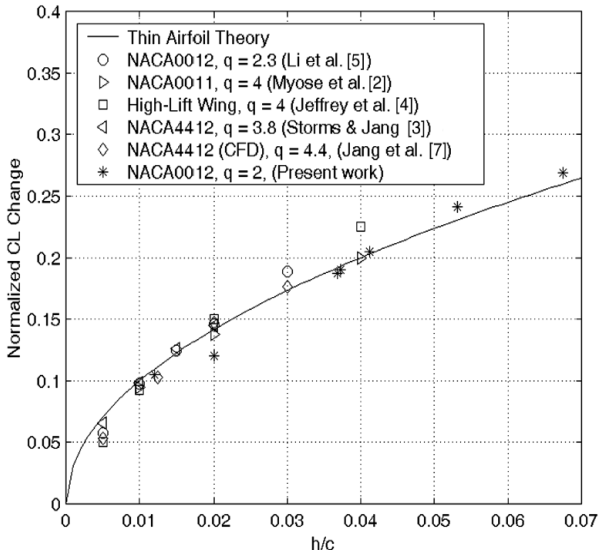

d)

Figure 2.10 – a) Illustration of a Gurney flap [60]; b) Suggested flow visualisation around Gurney flap by Liebeck [60]; c) Model of protruding flap used by Liu & Montefort [62]; d) Lift as a function of Gurney flap height [62].

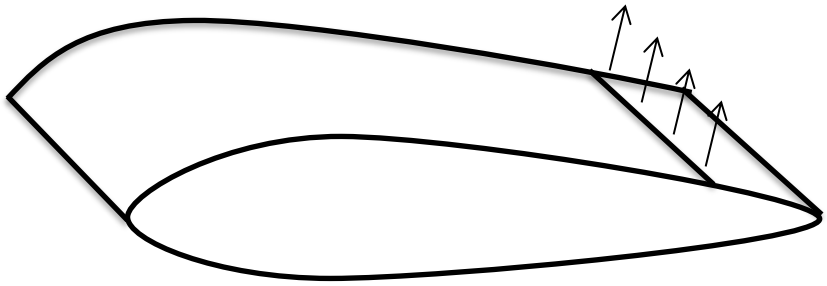

Figure 2.11 - Air ejected normally to the aerofoil surface [72].

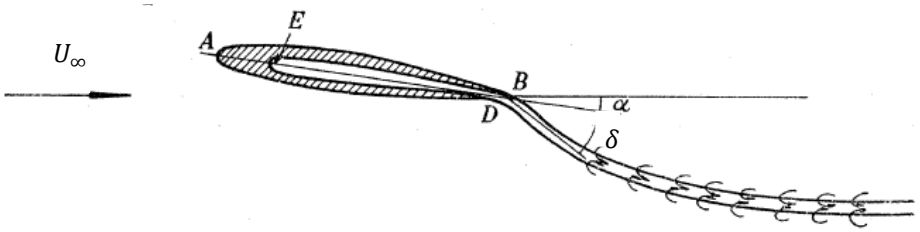

Figure 2.12 - Schematic of the parameters involved with the jet flap [80].

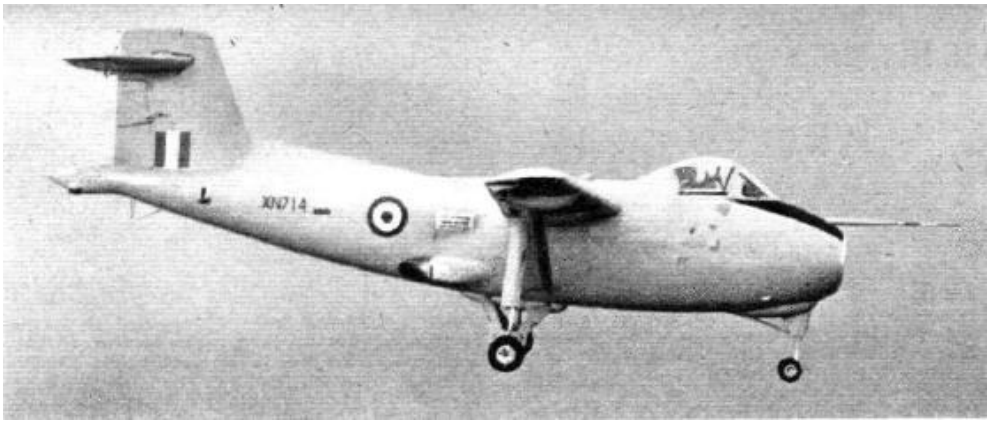

Figure 2.13 - Hunting H.126 [78].

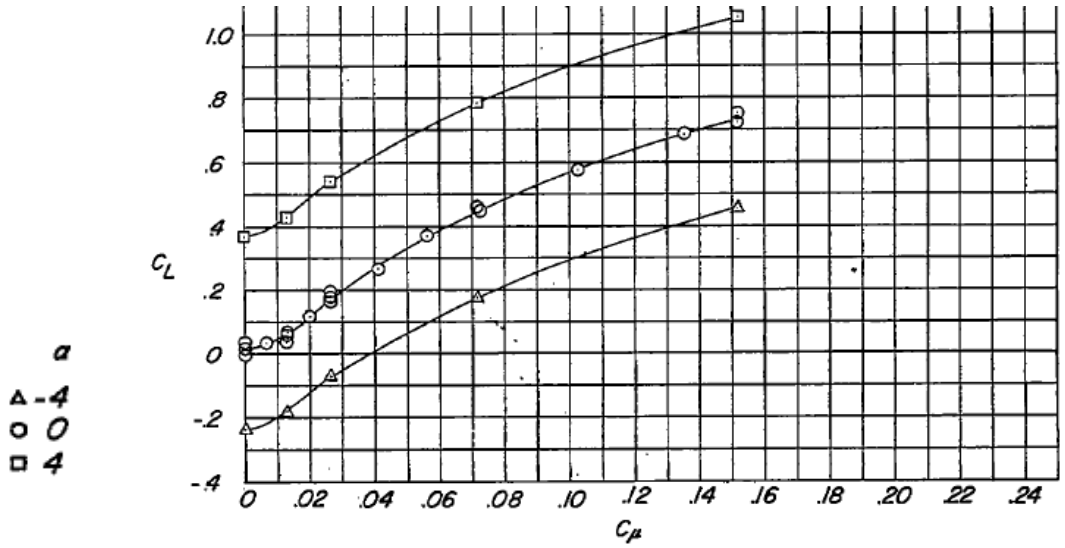

Figure 2.14 - Graph indicating the increase in lift associated with larger momentum coefficients [86].

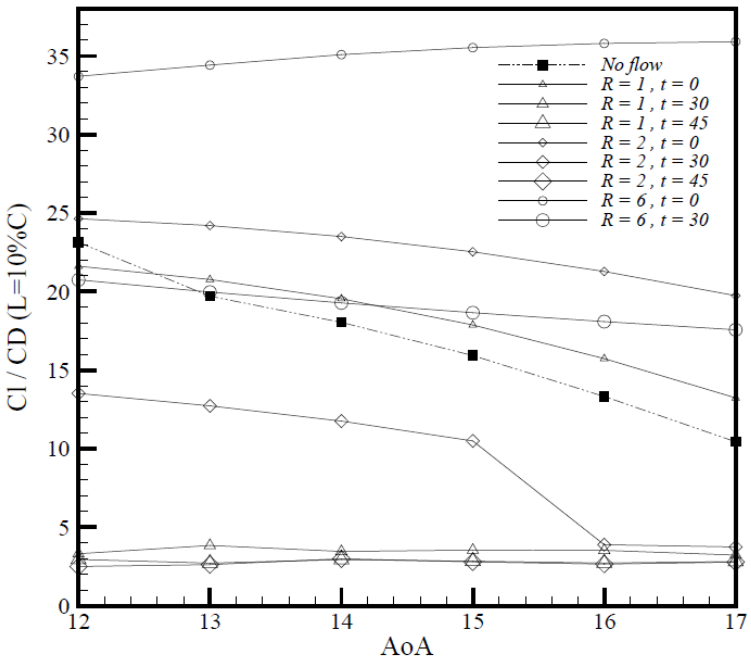

a)

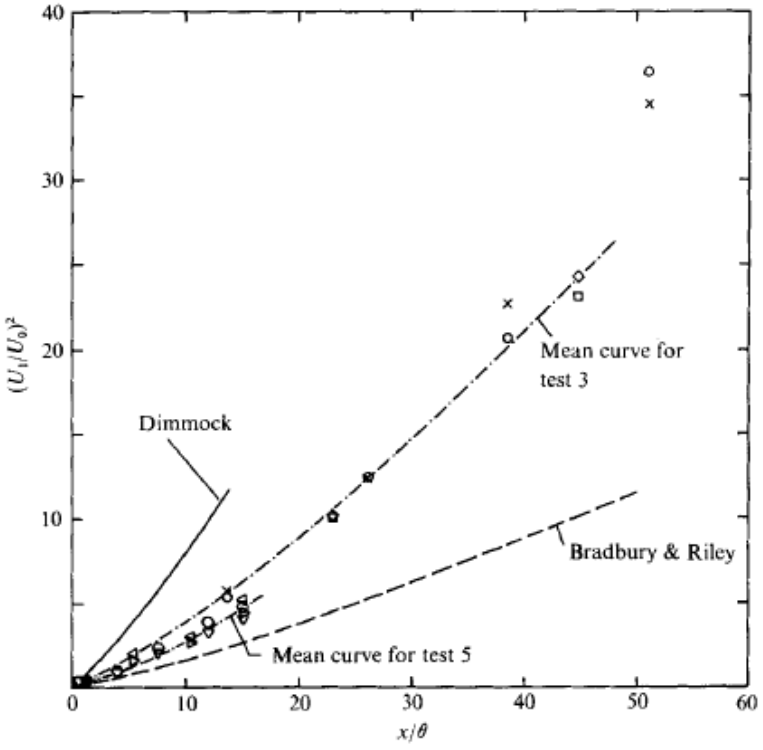

b)

Figure 2.15 – a) Effect on lift to drag ratio with jet deflection angle [91]; b) Study by Simmons *et al.* [93] on the effect if deflection angle on velocity decay.

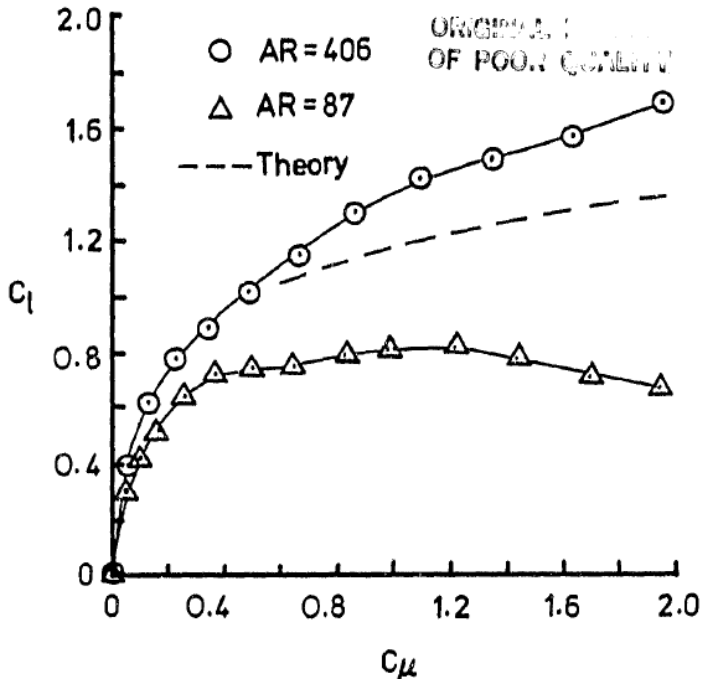

Figure 2.16 – Effect of jet aspect ratio [96].

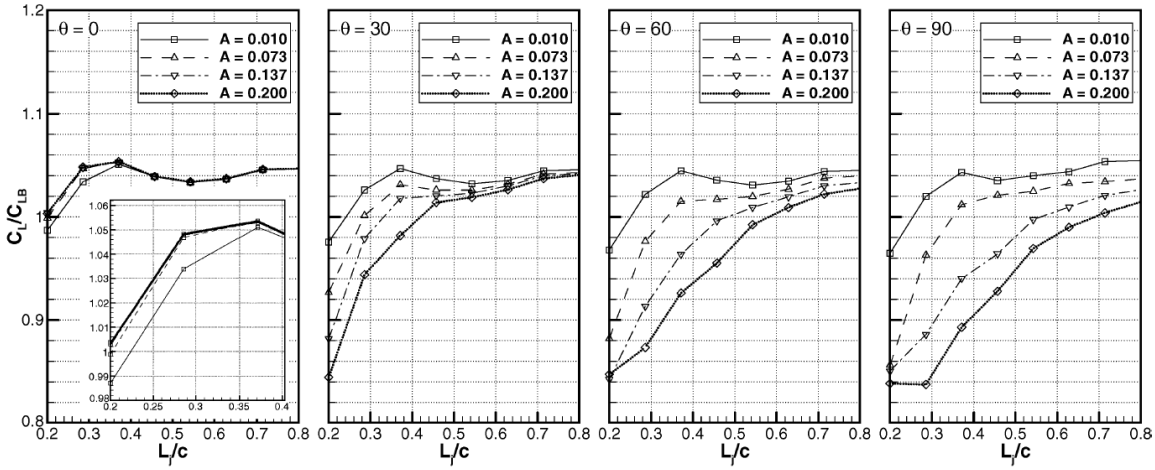

Figure 2.17 – Effect of vary jet location [99].

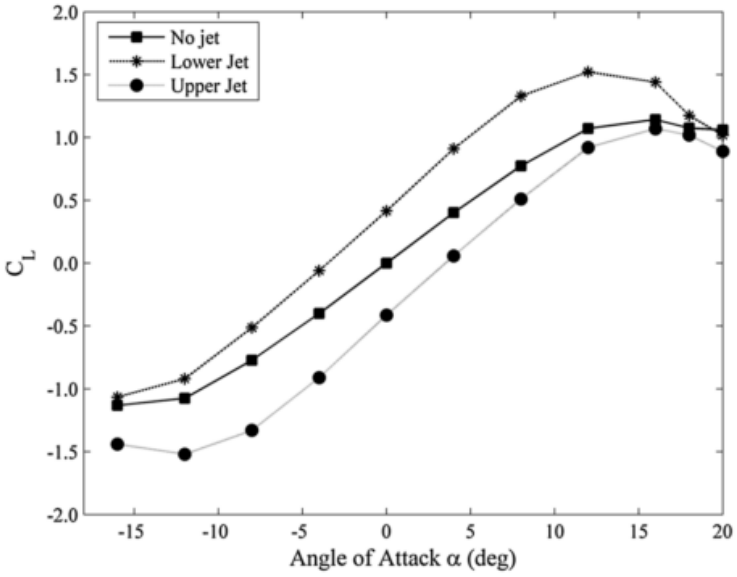

Figure 2.18 – Variation in lift coefficient when jet placed on lower or upper surface [72].

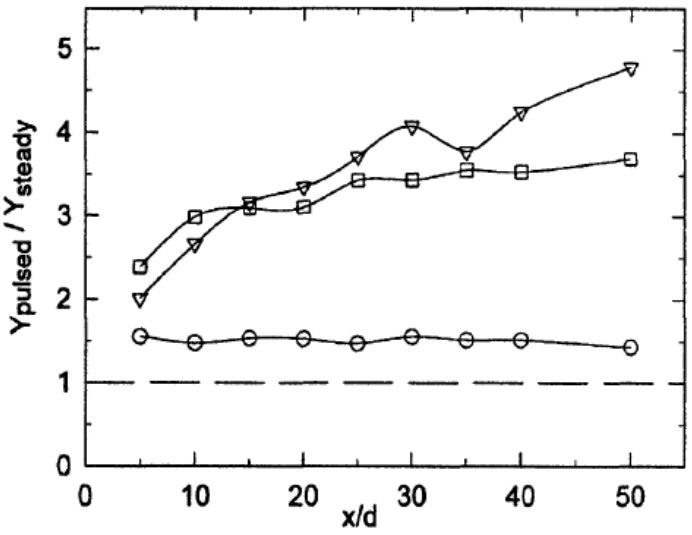

a)

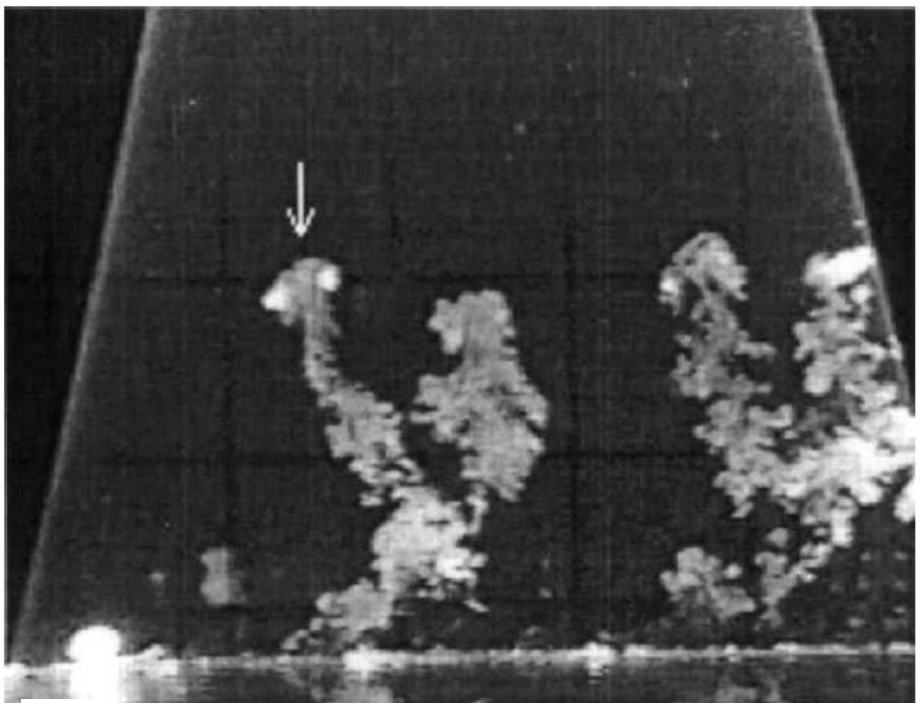

b)

Figure 2.19 – a) Penetration of vortices from pulsed blowing at a DC = 0.2 [110]; b) Vortices produced by pulsed blowing convecting downstream [111].

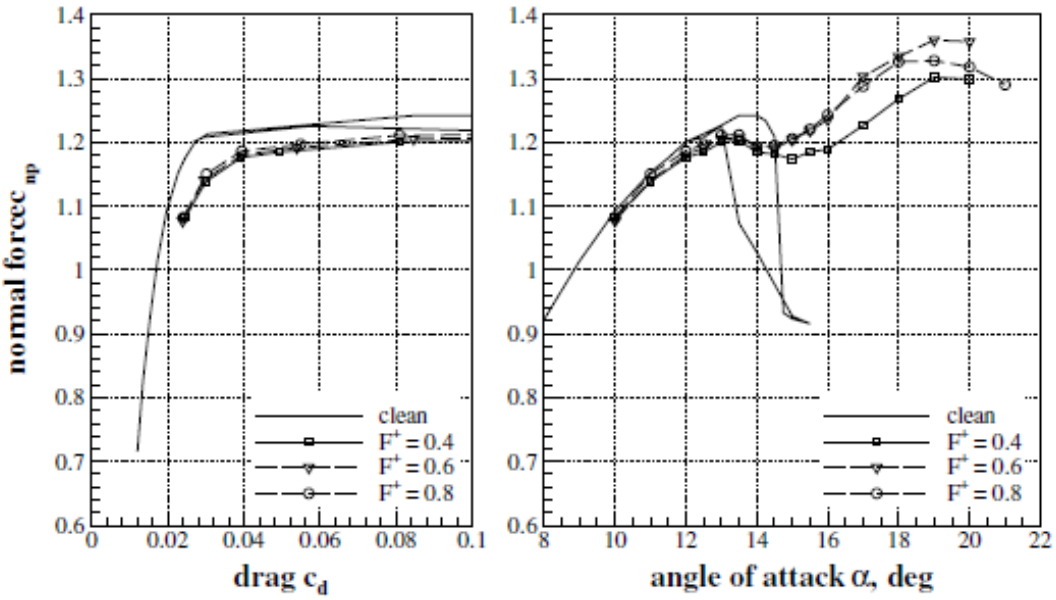

Figure 2.20 –The effect of frequency with leading edge pulsed blowing is shown in the work of Scholz *et al.* [101].

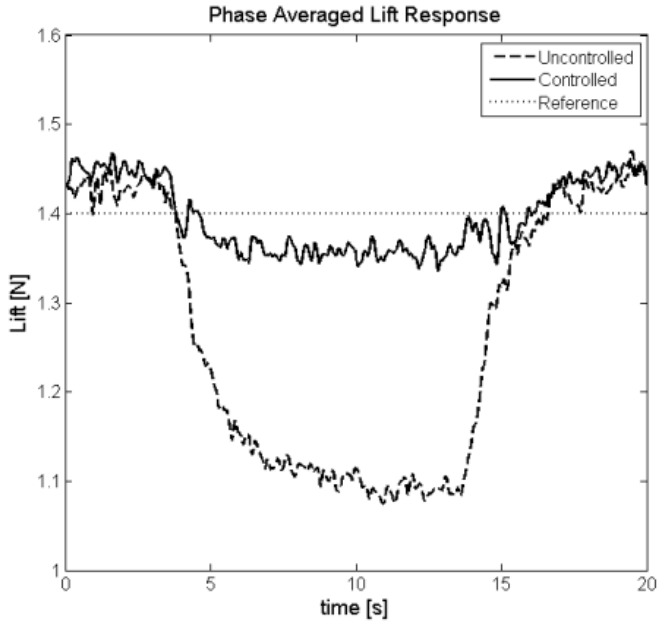

Figure 2.21 - Transient response of jet by Williams *et al.* [119].

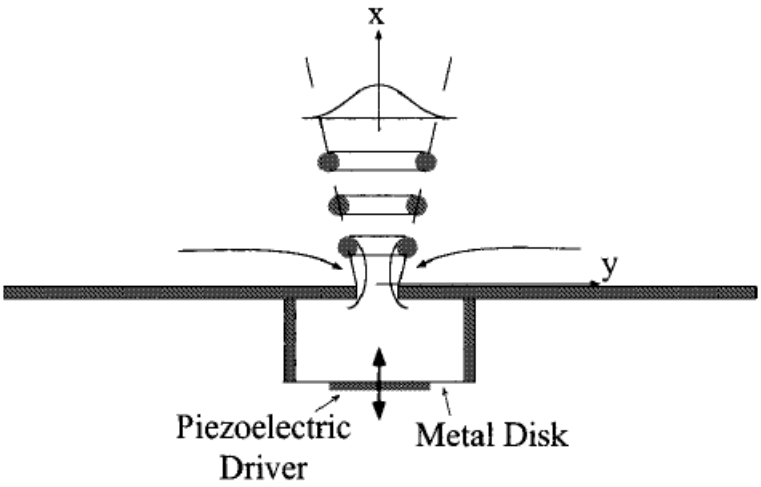

a)

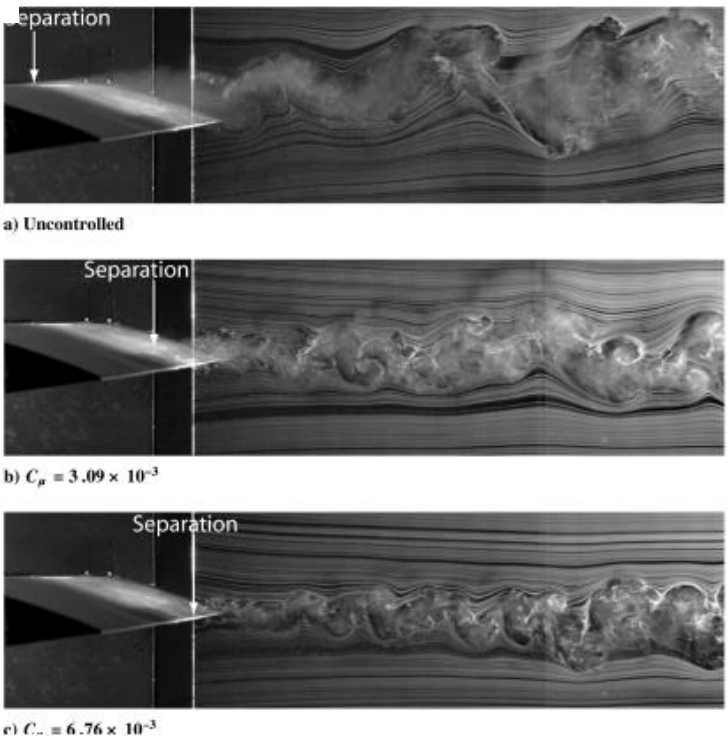

b)

Figure 2.22 – a) Synthetic jet actuated by piezoelectric driver [121]; b) Wake size reduces with momentum coefficient [126].

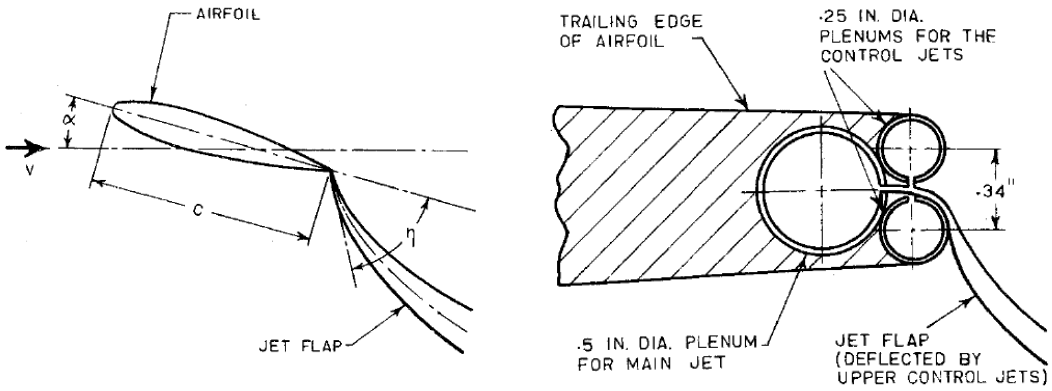

a)

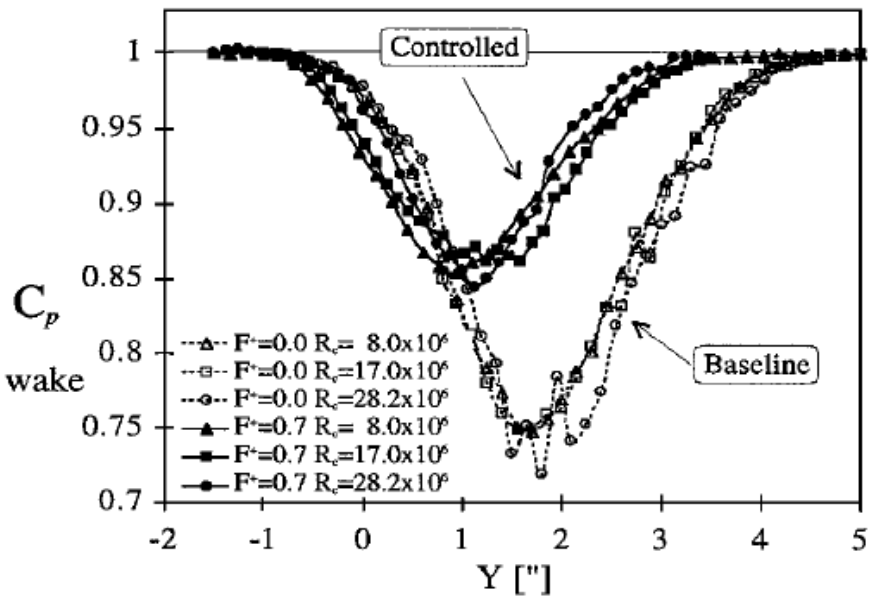

b)

Figure 2.23 – a) Flap is oscillated about an axis [138]; b) Wake size is shown to reduce with oscillating jet flap [146].

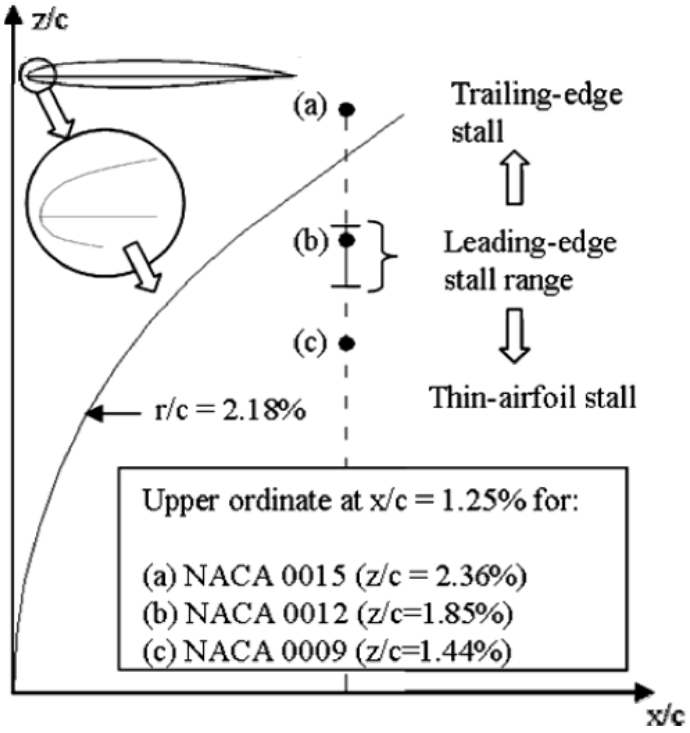

Figure 2.24 - Stall definition for NACA airfoils [148].

Chapter 3 : Experimental Methods

3.1 Apparatus

3.1.1 Wind Tunnel

Experiments were carried out in the large closed-circuit wind tunnel, at the University of Bath. The test section had dimensions of 2.13 x 1.51 x 2.70 m. A pitot-static tube was located at the entrance of the test section, but not in-line with the airfoil, to measure the freestream velocity, U_∞. The pitot tube was connected to a Digitron 2020P differential manometer that gave a digital reading of the dynamic pressure, q. The freestream velocity for all experiments was fixed at 20 ms^{-1}, with an uncertainty of 0.25 ms^{-1}.

3.1.1.1 Blockage Effects

The presence of the wind tunnel walls will interfere with the flow pattern observed around the model. The limited area within the cross section of the wind tunnel can alter the flow pattern to produce one that is different to free air. Therefore, it was crucial to ensure that the blockage effects did not diminish the reliability of the results. The model spanned the entire cross section of the wind tunnel so that the walls acted as end plates. This meant that the root and tip of the wing would not be able to produce tip vortices. Since the model is under quasi two-dimensional conditions, the following blockage effects are relevant to the tests carried out [155, 156]:

Solid blockage

Due to conservation of mass, the presence of the airfoil in the cross section of the tunnel would have incited air velocity around the model to increase beyond the velocity upstream. For all the angles considered here, the solid blockage was kept acceptably under 0.32%.

Wake blockage

The formation of the wake would cause blockage effects of its own. The wake compels air velocity outside the wake to increase in order to ensure the same volume of fluid is being transported across the wind tunnel. As such, a pressure gradient is created between inside the wake and outside. For all angles considered, the wake blockage was kept acceptably under 2.8%.

Wall boundary layer interference

Wind tunnel walls form boundary layers which could ultimately manipulate the transition point on a two-dimensional model. The laminar region on the aerofoil can be influenced by the wall boundary layer if this is turbulent. This is significant if the transition point occurs towards the rear of the model [156]. As such, the boundary layer of the wind tunnel walls could severely affect the

force measurements on aerofoils. However, studies have shown that the wall interference does not a detrimental effect to the force measurements [157]. As such, the wall boundary layer effects were considered to be insignificant.

3.1.1.2 Turbulence Intensity

The turbulence intensity of the wind tunnel was determined to ensure that there was no unsteadiness present to render any doubt with the results. The turbulence intensity is defined below in Eq. [3.1] [155]:

$$TI = \frac{\sqrt{u'}}{U_\infty} \qquad [3.1]$$

Where u' is the root mean square of velocity fluctuations, and U_∞ denotes the freestream velocity. In order to obtain the turbulence intensity for the wind tunnel used, a TSI 1210-T1.5 hot wire anemometer was placed exactly mid-span across the test section. The hot wire, connected to a DISA 56C16 General Purpose Bridge and a bridge card, recorded readings at a sampling frequency of 2 kHz for 10 seconds, for a range of freestream velocities between 5 - 24 ms^{-1}.

As shown in Fig. 3.1, the turbulence intensity for a free-stream velocity of U_∞ = 20 ms^{-1} was no larger than 0.4%. It is seen with free-stream velocity, the turbulence intensity decreases, which may be because the wind tunnel is designed for higher velocities of up to 60 ms^{-1}. Confidence in the turbulence intensity value, was validated with the criteria suggested by Barlow *et al.* [155]. Barlow *et al.* [155] suggests that a turbulence factor for a wind tunnel must remain below 1.4, for it to be considered as low; the turbulence factor for a turbulence intensity of 0.4% is approximately 1.3.

3.1.2 Airfoil

The NACA 0012 airfoil was selected for experiments due to its representative behaviour and the wide availability of experimental data for comparison. Dimensions of the airfoil were selected to fit the length of the wind tunnel cross-section, see Fig. 3.2. As such, the chord length was c = 0.5 m and the span b = 1.5 m. With the airfoil span at 1.5 m, this meant spacing between wind tunnel walls and airfoil was kept to 5 mm. This gives enough clearance to prevent the airfoil from touching the wind tunnel walls. As such, the walls act as end plates for the airfoil, effectively producing two-dimensional conditions. Characterised by the values of the chord length and freestream velocity mentioned, the Reynolds number was determined as *Re* = 660, 000. Aerodynamic data collected at this Reynolds number is considered to be reliable and consistent [158].

Although the NACA 0012 is a profile which has been applied for rotorcraft blades, the availability of a large database of aerodynamic data for the profile makes it a relevant and useful airfoil to experiment with. As such, it is the airfoil that has been selected for this project. The airfoil possesses a leading edge radius curvature of 0.0158c, whilst the maximum thickness of 0.06c is situated at around x/c = 0.30 [45].

3.1.2.1 Tripping

The boundary layer on the aerofoil was manipulated by placing a trip wire to give a fixed transition point. This effectively simulates conditions with higher Reynolds numbers. Tripping the boundary layer near the leading edge would modify the separation bubble and the stall behaviour [149]. If the entire separation bubble is inhibited, the airfoil will experience a trailing edge stall [148]. If the wire is placed too close to the leading edge, the wire would ultimately act as a 'stall strip'. Thus, consideration of the trip wire location was imperative.

It has been suggested that locating the tripping wire at x/c = 0.10 is most effective for NACA four-digit aerofoils [149, 155]. Coincidently, the NACA 0012 experiences its peak velocity at this location. However, testing was still required to determine the most efficient location for a trip wire. Another relevant issue that had to be considered was the thickness of the trip wire. If the thickness of the wire is greater than the boundary layer thickness, a precipitous drop in maximum lift will occur [155]. Boundary layer thickness was determined as 0.67 mm, based on a flat plate profile. A roughness height definition proposed by Tani [159] projected a diameter of 0.26 mm may need to be employed. Consequently, two wire diameters of 0.5 mm and 0.3 mm were tested.

From Fig. 3.3, the thicker wire corroborated the theory by acting as a 'stall strip'. It is suspected the 0.5 mm wire is protruding above the boundary layer at 0.05c. However, 0.3 mm wire did not bring about an early stall, shown in Fig. 3.3a & b, thus, all experiments were carried out with this roughness height. Subsequent tests investigated which location is optimal for the respective roughness height. Following observations from the tests carried out, it appeared that locating the trip wire at x/c = 0.10 produced the most consistent results, see Fig. 3.3c & d. It was also seen to be the least detrimental to both lift and drag magnitudes. It is evident that x/c = 0.15 produced similar results to x/c = 0.10, which is due to this location sharing a similar peak velocity to x/c = 0.10. However, since the majority of theory favoured locating the wire at x/c = 0.10, it was logical to select this location. The trip strip was placed at the same location for both surfaces, as this has been suggested for lifting surfaces [155].

3.1.2.3 Airfoil Validation

Two-dimensional experimental data for a symmetrical airfoil, NACA 0012, was collected for angles of attack between $0° \leq \alpha \leq 20°$, shown in Fig. 3.4. Normal blowing was achieved by cutting slots perpendicular to the surface. The presence of the slots on the upper surface, particularly at x_j/c = 0.08, would cause an imperfection in the symmetrical profile. In order to prevent the slots from behaving as cavities producing vortices, tape of 0.13 mm thickness was used to cover them across the entire span. Force measurements for positive angles reveal zero lift force being generated at α = 0°, confirming that the presence of the slots had negligible influence. Increasing the angle of attack leads to a stall angle of α = 13°, with a maximum lift coefficient of C_{LMax} = 1.10. Data collected from literature, for a NACA 0012 airfoil at similar Reynolds numbers to the data collected at University of Bath is included for experimental validation. Comparative data from Sheldahl & Kilmas [160] and Jacobs & Sherman [161] were performed with Reynolds numbers of Re = 7 x 10^5 and 6.6 x 10^5, respectively. Jacobs & Sherman [161] observed analogous stall behaviour; C_{LMax} = 1.11 at α = 13°. However, there is less agreement between datasets within the post-stall region. Data from Sheldahl & Kilmas [160] appears to suffer from leading-edge stall, indicated by the extreme loss in post-stall lift, i.e., a loss in lift of ΔC_L = -0.6 from α = 11° to 16°. However, it begins to recover some of this lift beyond α = 16°.

In order to achieve upstream blowing, airflow emanating from the jet has to be diverted upstream across the upper surface. An additional carbon fibre piece was attached downstream of the jet, as shown in Fig. 3.2. The piece extends 5 mm (1% c) upstream of the jet, and protrudes above the jet by 0.5 mm (0.1% c). As such, the auxiliary piece attached to deflect the jet produces an alteration in the airfoil profile. It was important to ensure the protrusion from the carbon fibre piece does not produce a variation in lift force from the 'clean' baseline airfoil, by acting as a mini-tab device. As such, additional force measurements for no blowing cases with the piece attached for individual jet locations at x_j/c = 0.08, 0.60 and 0.95. As shown in Fig. 3.4, force measurements confirmed in all cases produced similar results to the 'clean' case, i.e., with trip device. The stall angle remained at α = 13°, despite having the stepped protrusion installed. The piece at x_j/c = 0.08 was not thick enough to bring about an early stall. Since the piece attains a thickness of t_j = 0.5 mm, it would have behaved as a tripping device, particularly near the leading edge where the original trip wire is located, x/c = 0.10 As such, the baseline case throughout this report is in reference to the NACA 0012 airfoil without the addition of the upstream blowing piece.

3.1.3 Jet Flap

Five locations have been selected to investigate the effect of chordwise location on the behaviour of the jet flap: x_j/c = 0.08, 0.60, 0.75, 0.85 & 0.95. Locating the jet flap between x/c = 0.75 – 0.95 is intended to observe the effect of a jet flap near the trailing edge. At x/c = 0.60, the jet

flap is projected to behave as a 'spoiler' on the wing, as this is in the vicinity of current mechanical spoilers [162], while the jet at x/c = 0.08 is intended to identify the benefit of a jet flap near the leading edge. To maintain two-dimensional conditions, the jet flap covered the entire span of the wing.

The airfoil was composed of two parts; the first 0.725c of the airfoil was composed of a carbon fibre composite, reinforced with an internal aluminium alloy structure and Rohacell® XT foam for stiffness and retaining low weight, also shown in Fig. 3.2. Two aluminium tubes at x/c = 0.08 and 0.60 were installed as plenum chambers, as these locations coincide with the two jet slots located on the first part of the airfoil. These tubes had a length, width and height of 1.5 m, 0.022 m and 0.019 m, respectively. The remaining 0.275c was rapid prototyped using DuraForm® PA plastic due to its complex internal design. This trailing edge section was manufactured as five interchangeable parts, in order to prevent warping effects associated with rapid prototyping larger dimensions. The trailing edge section was designed to act as a plenum chamber for jet flaps located downstream of x/c = 0.725. As such, three slots of jet width h_j = 1 mm (0.2%c), are located on this former part at x_j/c = 0.75, 0.85 & 0.95. The DuraForm® PA plastic material which forms the trailing edge section had a high tensile strength of approximately 4000 MPa, therefore, allowing it to withstand the accrual of pressure within the plenum chamber and avoiding any deformation.

3.1.4 Hot Wire

In order to determine the velocity of air ejected from the jet slots, a hot wire anemometer was used. The hot wire anemometer model used was the TSI 1210-T1.5. It measured the velocity at the jet exit to provide the average momentum coefficient for respective flow rates. The hot wire was connected to DISA 56C16 General Purpose Bridge, where a CTA Bridge card was programmed specifically to the hot wire. The General Purpose Bridge was connected to a data acquisition box where a Wheatstone bridge circuit was applied to amplify the signals received by the hot wire.

Calibration of the hot wire had to be performed before applying it for use at the jet exit. This procedure involved placing the hot wire device 15 mm ahead of a 3 mm diameter Pitot tube, within a 2 m length pipe that has a 52 mm internal diameter. The pipe was connected to the air supply. Measures were taken to ensure the stem of the Pitot tube was not obtrusive to the uniform flow within the pipe. Gould [163] posited that the ratio of the cross-sectional area of the Pitot tube to the cross-sectional area of the pipe must not exceed 0.05. It follows that the Pitot tube was not detrimental to the uniformity of the flow and the hot wire was placed upstream of its location to minimise its effect even further.

The relatively small pipe diameter allowed the air supply to provide high dynamic pressure. As such, the hot wire was calibrated for speeds up to 42 ms^{-1}, as this is in the region of the same

velocity required to achieve C_μ = 0.02. Data was collected at 1 ms^{-1} intervals, at a 2 kHz sampling rate for 10 seconds at each point. The calibration yields a relationship between voltage and velocity in the form of Eq. [3.2]; otherwise, known as 'King's Law', where 'A', 'B' and 'n' are constants which determined after calibration:

$$V^2 = A + B(U_e)^n \quad [3.2]$$

As seen in the calibration curve in Fig. 3.5, deviation from the best curve fit is more pronounced towards the lower velocities. This is due to the hot wire not being entirely accurate at extremely low velocities, partly because of its sensitivity to natural convection [164]. The solid line in Fig. 3.5 represents the fit of data to King's Law equation, and shows a very good fit.

3.1.4.1 Unsteady Blowing System

Steady state blowing consisted of sourcing compressed air from the University of Bath compressors, through a pipe leading to the wing root. However, for unsteady blowing, this approach is not possible and required additional alterations to achieve. As such, a bespoke valve system, shown in Fig. 3.6 was used to create unsteady jet profiles for periodic and transient measurements. High frequency actuation of the jet flap required a fast response control valve, Enfield LS-V25s Proportional Pneumatic Control Valves. One control valve has a flow capacity of 1300 LPM, which meant four control valves were used to maximise flow capacity for unsteady blowing. As these control valves were controlled externally, each control valve was supplemented with an Enfield D1 Proportional Linear Motor Valve Driver. Pressure is stabilised and filtered with an Ingersoll Rand ARO filter/regulators combination. The system was controlled through a LabView programme on a desktop. The desktop communicated to the drivers via a National Instruments compactRIO.

The in-line pipe leading to the wing had a 25.3 mm diameter, whereas the ports for the control valves were a quarter of this diameter. As such, a setup had to be configured to accommodate for the large flow capacity requirement. As shown in Fig. 3.7, the block diagram illustrates the setup used. The system comprised of compressed air at 6.5 bar from the University compressors, which is split to two Ingersoll Rand ARO filter/regulators. The two streams are then separated into two pairs of Enfield LS-V25s Proportional Pneumatic Control Valves to give four streams that are recombined at the wing inlet. Hot wire measurements at the exit of each of the four valves were taken to ensure there was no lag between them.

3.1.4.2 Static Hot Wire Measurements

In order to avoid three-dimensional effects, it was necessary to ensure the flow emanating along the jet span was limited to a deviation from mean velocity below 10 %. With air supplied only at the root of the airfoil, it was inevitable the jet profile along the jet span would not be uniform. A

method to produce a uniform jet profile was sought. The airfoil was adapted to house 2 mm thick porous polyethylene sheets beneath the airfoil surface. As shown in Fig. 3.8, the modification of internal design of the trailing edge possesses a fixed vicinity for the porous plastic sheets to be fitted within. For the jets at x_j/c = 0.08 & 0.60, the airfoil was laser cut to place the porous sheets above the plenum chamber exit, then held within place with two aluminium blocks which span the airfoil. A gap of 1 mm separated the two aluminium blocks.

The hot wire anemometer was held in place with a traverse system and situated approximately 2 mm above the jet exit, where it was traversed across the entire span. It was essential to measure the accurate jet velocity as near as possible to the exit, as jet strength dissipates with distance. At each location, the hot wire was traversed across the jet width to determine the peak velocity before recording measurements. In order to obtain a high spatial resolution map of the velocity profile, measurements were taken every 2.5 cm along the span, resulting in 59 locations. Data was collected at a sampling frequency of 2 kHz for 10 seconds. Furthermore, in order to mitigate experimental error, the hot wire anemometer was traversed along the span three times. The measurements were then averaged using a MATLAB code. This procedure was repeated for every jet slot, x_j/c = 0.08, 0.60, 0.75, 0.85 & 0.95. To prevent any leakage of air when blowing from the slots downstream of *x/c* = 0.725, it was found most effective to seal the inactive slots with silicone gel.

Figure 3.9 shows a typical profile of the trailing edge jet before and after the porous sheets were installed. It is evident that the porous plastic sheets created a pressure drop to encourage a uniform distribution. Consequently, a maximum deviation of the mean jet velocity of approximately σ_{vel}/U_j = 5% was achieved.

Volumetric flow rate of air supplied to the airfoil was quantified using a SMC PF2A703H-10-68 digital flow switch for air, connected to a 30V power supply. The flow meter has an accuracy of ±1%, at room temperature (20°C). Consequently, the flow meter was calibrated to determine the flow rates for coefficient of momentums. The determination of the coefficient of momentums was attained by placing the hot wire at three different locations along the span to ultimately obtain an average C_μ value. Measurements were taken without freestream velocity. Data points were collected for 20 various flow rates, a general equation to relate momentum coefficient to the flow rate was obtained.

3.1.4.3 Dynamic Hot Wire Measurements

Similar to steady blowing measurements, calibration of jet velocity profile was required for periodic and transient deployment. Hot wire measurements were performed to identify peak jet velocities and determine a relationship to voltages. However, in order to avoid buffering effects

associated with high frequency sampling rates, an alternative bridge in combination to a signal conditioning system was necessary. The bridge used was a TSI® 1750 Constant Temperature Anemometer bridge with a control resistor tailored to the hot wire. The hot wire remained as the TSI 1210-T1.5® hot wire anemometer used for steady blowing measurements. Signal was conditioned using a National Instruments compactRIO with 16-bit analogue to digital converter module, NI-9205.

As the control valves preceded the jet exit, the lag between the input signal, used to activate the valves, and the output signal, measured by the hot wire at the jet exit, was determined. The input and output measurements were recorded and then post-processed in MATLAB to identify the phase delay of the jet. This phase delay was found to increase with jet frequency. Measurements were determined for three jet locations; x_j/c = 0.08, 0.60 & 0.95.

Periodic measurements taken at five equally spaced stations along the jet span were taken initially to confirm a negligible lag between jet output near the airfoil root and tip. As such, for calibration of periodic blowing, measurements were taken at the mid-span location for a range of reduced frequencies, $0 \leq k \leq 0.471$, using a 1 – cos waveform. A total of 100 blowing cycles for a single reduced frequency was performed at a sampling frequency of 5 kHz and subsequently phase-averaged. Figure 3.10a shows an example of the jet profile at k = 0.079. The lag between is taken in to account for phase calculations for unsteady force measurements. Due to the amplitude of the jet velocity reducing with frequency, the power to the valves had to be adjusted and calibrated to maintain a peak momentum coefficient. As a result, the maximum momentum coefficient attainable throughout the range of frequencies was C_μ = 0.016.

Transient measurements were taken with the control valves configured to deploy a square wave profile. This forces the jet to react immediately. Calibration was performed with a total of 400 cycles consisting of 2 seconds on and 2 seconds off, at a sampling frequency of 5 kHz. The measurements were then phase-averaged. An example of transient deployment can be seen in Fig. 3.10b, where a delay is observed until the maximum velocity is obtained. This delay is taken forward into consideration for force measurements.

3.2 Force Measurements

3.2.1 Apparatus

3.2.1.1 Static Force Balance

As shown in Fig. 3.11, a dual-axis binocular strain gauge force balance was manufactured using 2014T6 Aluminium alloy for the static force measurements. A Wheatstone bridge configuration was used for the four strain gauges for each force axis. Such configuration meant the force balance could measure both lift and drag forces. The locations of these strain gauges were

contained in close proximity to the thinnest sections of the binocular design, as this is where maximum surface strain would be subjected by the force balance. A spigot within the force balance provided a hole for the shaft attached to the airfoil to be inserted and secured using grub screws.

In order to avoid unwanted resonance with the force balance, the second moment of area had to be as large as possible. However, a compromise on rigidity had to be made. As such, the second moment of area at the thinnest section was calculated based on the dimensions of the binocular design:

$$I_{xx} = \frac{bh^3}{12} - \frac{b(2R)^3}{12} \quad [3.3]$$

Due to lift force magnitude exceeding that of the drag force, the section dedicated to lift measurements was sized larger than the drag section. As such, the target surface strain for the lift section was taken as nine times the local surface strain, $\varepsilon \approx 5\text{x}10^{-5}$, whilst the target surface strain for the drag section was taken as the local surface strain. With this in consideration, the second moment of area was determined from the equation below:

$$\varepsilon = \frac{FLh}{2EI_{xx}} \quad [3.4]$$

The forces used were based on lift and drag coefficients obtained at stall angles from literature [161]. The length, L, used was based on the distance from the root of the force balance to the mid-span of the wing.

3.2.1.2 Unsteady Force Balance

The binocular force balance had a low resonant frequency. However, in order to explore a wider range of frequencies, it was necessary to increase the resonant frequency so as to mitigate uncertainty within this range. To increase the resonant frequency the following alterations were made:

1. The wind tunnel frame was reinforced by applying steel girders as corner blocks to the frame.
2. The stiffness of the wing was increased through installation of internal steel rods.
3. The binocular strain gauge force balance was replaced with an air bearing system, as exhibited in Fig. 3.12.

The force balance frame consisted of aluminium alloy struts, and two rods positioned perpendicular to the airfoil. Air was supplied to the system from the University of Bath's shop air supply, and was provided constantly to minimise wearing of these rods, from friction caused from

any motion incurred by the airfoil. With the rods aligned in one axis only, this meant the force balance would only measure the normal force, i.e. lift, acting on the airfoil, therefore, neglecting the drag force. In addition, the airfoil remained fixed in position and required to be rotated manually to change the angle of attack. The angle was monitored with a SICK incremental encoder which had a measurement precision of ± 0.02°. Force measurements were taken with a FUTEK Miniature S Beam Load Cell LSB200, which has a loading capacity of ± 445 N, and has an uncertainty of ± 0.05% of rated output.

3.2.2 Calibration

3.2.2.1 Static Force Calibration

A translation between forces acting on the airfoil and voltage was needed for the strain gauge configuration. Such a calibration of the force balance would produce a linear relationship between the two parameters. A pulley system was utilised in the test section, and aligned in the direction of the force axis to be calibrated. The symmetrical airfoil was set at angle of attack of α = 0°. For calibration of the normal force, or lift, the pulley system was aligned perpendicularly to the airfoil direction, see Fig. 3.13. The drag force was calibrated with the pulley system aft of the trailing edge.

With the pulley system in place, a series of known masses were applied to act at the mid-chord of the airfoil. Increments of 1 kg masses were used to accrue up to 10 kg of force acting on the airfoil, for the normal force calibration. For the drag force, increments of 100 g up to 500 g were applieed. Voltages were recorded using a 2-channel LabView programme connected to a data acquisition DAQ system, at a sampling rate of 2 kHz for 10 seconds, totalling 20,000 samples. This was repeated three times for each weight. A MATLAB code was used to produce an average value and a linear curve fit applied to give a gradient of force per voltage. These linear fits had R squared values around $R^2 = 0.998$.

3.2.2.2 Unsteady Force Calibration

With the new unsteady force balance installed in the wind tunnel, a dynamic calibration was necessary before proceeding with unsteady force measurements. Kumme [165] outlined a procedure for accounting the frequency response of the force measurement system to known frequencies and force. This technique was subsequently incorporated with the force balance calibration procedure, by producing a transfer function to correlate input and output forces together. The force calibration provided information on the amplitude ratio and phase delay of the system to input forces acting on the FUTEK load cell in the force balance. The procedure, as shown in Fig. 3.14, involved an external source of force acting on the airfoil at the centre of gravity of the airfoil-force balance system. A carbon fibre shaft with a rose joint at one end was secured to the airfoil with a bolt and clevis. The

rose joint would account for any discrepancies in alignment between the airfoil and force axis. The opposing side of the shaft was connected to another FUTEK S load cell, which determined the input force acting on the airfoil. This input force was provided by an electromechanical shaker, which was capable of applying large forces in a sinusoidal manner at extremely high frequencies. Due to the large input forces, it was essential to ensure the shaker was securely mounted as to avoid any interfering resonance.

The electromechanical shaker was forced by varying the frequency and voltage amplitude through LabView. The airfoil was forced at a range of frequencies between 1 Hz $\leq$ f $\leq$ 20 Hz, with 1 Hz intervals. Input force for each frequency was taken for a magnitude of ± 10 N, 25 N & 50 N. The amplitude ratio and phase angles were determined through averaging 100 cycles. To ensure measurements from the two load cells were collected simultaneously and to avoid any buffering, the data was obtained using a National Instruments CompactRIO (cRIO) NI9205 module with controller, at a sampling rate of 5 kHz. Similar to the steady force measurement calibration, a linear force-to-voltage relationship was determined through a static calibration with the new force measurement system. A set of ten known weights were applied on to the airfoil and remained over a period of ten seconds in order to achieve a mean voltage value. The relationship value is then applied to the unsteady calibration measurements.

A fitted curve was determined using the measurements collected for the three force magnitudes, as illustrated in Fig. 3.15. A peak amplitude ratio of 20.08 is observed at f = 7 Hz, or k = 0.569, indicating that the resonance of the system had improved over the binocular force balance design. A large increase in phase angle coincides at this frequency, shown in Fig. 3.15b. However, prior to the resonant frequency, a small increase in amplitude ratio indicates an initial natural frequency at f = 5.4 Hz. A third natural frequency is noticed at f = 12.95 Hz. Due to the large uncertainties attributed to force measurements at resonance, measurements above the 6 Hz are removed from consideration.

3.2.3 Uncertainty Analysis

When observing experimental results, errors will inherently manifest. However, it was pertinent to determine the significance of uncertainties involved and ensure they were kept to a minimum when possible. By ensuring measurement procedures were exercised with minimal uncertainty, this inhibited the possibility of errors propagating through to force coefficient values. In order to determine the uncertainties involved, the methods posited by Moffat [166, 167] have been employed. These methods utilise the root sum square combination to account for each variable involved to produce an approximate uncertainty value:

$$\delta R = \sqrt{\left\{\sum_{i=1}^{N}\left(\frac{\partial R}{\partial X_i}\partial X_i\right)^2\right\}} \quad [3.9]$$

3.2.3.1 Steady Blowing Setup Uncertainty

The uncertainty of the steady blowing setup heavily depends on the precision of the hot wire anemometer used for jet velocity measurements. As mentioned earlier, the hot wire was calibrated to speeds up to 43 ms^{-1}, which ultimately produced a best fit curve to relate velocity to voltage readings obtained during tests. As such, the uncertainty for the hot wire was characterised by the deviation of the jet velocity measured by the hot wire, to the value obtained by an equation obtained for the best fit curve. For this case, a maximum value of 2% was experienced. Other variables that heavily dictate the uncertainty with the steady blowing setup include the dynamic pressure and surface area uncertainties, which values were both stated earlier. Furthermore, the area of the jet slot must also be taken in to consideration, which was calculated to be 0.15%. Subsequently, the final uncertainty for momentum coefficient is calculated to be 2.6%.

3.2.3.2 Static Force Measurements Uncertainty

The level of uncertainty for the force measurements was determined with the combination of particular variables. The uncertainties involved with the dynamic pressure depend on fluctuations with manometer readings as well as the accuracy of the pitot-static tube. The pitot tube uncertainty was stated by the manufacturer as ± 1%. For this case, the uncertainty in the dynamic pressure readings was determined as ± 1.58%. In addition, the uncertainty involved with the surface area of the wing was calculated as ± 0.158%.

Steady force measurements required a force-to-voltage ratio to be acquired, in order to determine the force acting on the airfoil. As such, the uncertainty involved is a combination of voltage readings and known masses applied to the airfoil via a pulley system. The measuring scales used retained an accuracy of ± 0.005 kg. However, this accumulates with a greater number of weights. The voltage is converted to force, with a constant, determined with known weights attached to the wing in a pulley system. Measurements were taken over a 10 second period with a sampling rate of 2 kHz. Therefore, uncertainty in the force balance calibration was calculated as ± 1.4%, based on the data collected during the calibration procedure. Consequently, the uncertainty in the static force measurements accounts to ± 2.1%.

3.2.3.3 Dynamic Force Measurements Uncertainty

Uncertainty for unsteady state force measurements stems on the calibration techniques and force balance involved. When performing dynamic calibration of the force balance, an uncertainty arises with the static calibration performed to determine a force-to-voltage ratio. An averaging uncertainty is associated, which tends towards an accurate value with increasing number of cycles captured. As such, it is dependent on the frequency. Such uncertainties contribute to calibration uncertainties of amplitude ratio and phase angle. An uncertainty in the position within the phase cycle arises, which is mitigated with a higher sampling frequency. However, the uncertainty with the amplitude ratios and phase angles used for the correction of force, depended on the curve fit tool used in MATLAB, for the three sets of data acquired for the three force magnitudes. As such, calibration uncertainty for amplitude ratio was determined to be ± 5%, with uncertainty coverage of 95%, and phase angle uncertainty was ± 2°.

Uncertainty in phase-averaged lift coefficient is dependent on the uncertainties from the static and dynamic force calibrations. As such, a combination of the two gives the uncertainty for the normal force. Whilst the conversion to lift coefficient compounds these uncertainties with that of the area and dynamic pressure. Consequently, the uncertainty in mean lift coefficient is determined with the accruement of all uncertainties from the total number of cycles, N, and the addition of the baseline lift coefficient uncertainty, $\delta C_{L,off}$. A maximum uncertainty for mean lift coefficient was found to be $\delta \Delta C_{L,mean}$ = ± 2%. Amplitude lift coefficient uncertainty is derived with the combination of uncertainties for minimum and maximum lift coefficients, to produce a maximum uncertainty of $\delta(C_{L,min} - C_{L,max})$ = ± 4% for the range of frequencies investigated. Phase angle uncertainty arose from the dynamic calibration and hot wire measurements, to give a maximum uncertainty of $\delta\varphi$ = ± 1.5°. Transient force measurements are also time dependent, but are normalised by the lift coefficient when blowing is off, which compounds the total uncertainty. Maximum uncertainty is determined as approximately $\delta\left(\frac{\Delta C_L(t)}{\Delta C_{L,off}}\right)$ = ± 3%.

3.3 Particle Image Velocimetry (PIV)

3.3.1 Apparatus

Particle Image Velocimetry (PIV) is a non-intrusive quantitative technique for measuring flow fields. In this application the freestream flow is seeded with small particles of oil, a plane of interest along the upper surface of the airfoil was illuminated with a laser to capture the particle motions. Despite the jet flap air supply not being seeded, the emanating flow is rapidly entrained into the seeded mainstream. High resolution cameras capture a sequence of image pairs with a small temporal separation. The two-dimensional images are cross-correlated and averaged in a global image acquisition software to extract the particle motion and therefore flow velocity.

An EverGreen 200mJ 15 Hz Nd:YAG double-pulse dual laser was used to illuminate a plane of interest. One side of the test section was fitted with a transparent window, which allows the laser to be situated outside of the test section, and clamped on a raised platform, as shown in Fig. 3.16. Due to the presence of the pressure taps at the mid-span of the airfoil, the laser was illuminated perpendicularly to the airfoil at a spanwise location of z/b = 0.6. The primary plane of interest for the investigation was the upper surface of the airfoil, where the jet flaps are located. In order to achieve the required laser sheet for the plane of interest, the laser is fitted with a collimator lens and two lenses of 25 mm and 50 mm. As the laser is aimed from one side of the test section, this administers the lower surface to be concealed from illumination. The airfoil was painted in matte black to prevent reflection of the laser affecting the illumination of particles.

The freestream air was seeded with olive oil droplets, produced with the use of a TSI 9037-6 Generator; a six-jet atomiser. Measures were taken to ensure the oil particles would not be detrimental to the illumination of the laser. An extremely small particle diameter would not be an effective medium in illuminating laser light. On the contrary, a large particle diameter would result in surplus drag. One method of validating the eligibility of the particle diameter was by determining the settling velocity with the Stokes drag equation [168]:

$$u_\infty = \frac{g d_p^2 (\rho_p - \rho_f)}{18\mu} \qquad [3.8]$$

For the particle diameter to be acceptable, the settling velocity is required to be insignificant. With the oil droplet diameter induced by the atomiser equal to d_p = 1 µm, the density of the olive oil particle ρ_p = 860 kg/m^3, the air fluid density ρ_f = 1.225 kg/m^3, and air dynamic viscosity μ = 1.8 x 10^{-5} kg/ms, the settling velocity was calculated as 0.00013% of the freestream velocity. This is deemed to be an insignificant settling velocity and therefore, the oil droplet diameter is appropriate for flow visualisation purposes.

The glass paneled wind tunnel floor meant two TSI® PowerView™ CCD cameras were placed in a tandem configuration, 1200 mm below the plane of interest. The dual camera configuration allows covering the entire airfoil while maintaining a high-resolution image, with an overlap region. The cameras were fitted with two Nikon AF 50 mm NIKKOR f/1.8D lenses, at a f-stop value of *f/5.6*. This f-stop value is low enough to capture sharp images while permitting enough light into the cameras sensor. The pair of cameras were fixed to a turntable which is capable of being rotated with an angular precision of ± 0.25°. It follows that the cameras were rotated with respect to the airfoil angle of attack, in order to align parallel to the airfoil plane.

3.3.2 Calibration

Spatial calibration was performed by placing a ruler which extends into the plane of view for both cameras. This is performed to identify the overlap region and to calculate the spatial resolution required to determine the velocity data in the captured images. The ruler is aligned to be parallel to the airfoil chord. A TSI® LaserPulse 610034 synchroniser was used to synchronise the camera and laser, as well as altering the exposure and temporal separation between pulses from the laser. To complete phase-averaged PIV measurements for periodic and transient deployment, an external trigger from the synchroniser was connected to the National Instruments CompactRIO. The external trigger meant the cameras were capturing images at specific moments in the phase cycle, determined by the LabView software.

Processing of PIV images was carried out with the TSI® Insight 4G software, which made use of a recursive Fast Fourier Transform cross correlator. Following image processing in Insight 4G, the images were post-processed in MATLAB. A custom code was created to merge the time or phase-averaged velocity field data and utilised a weighted average to account for the overlapped region between the two cameras. Velocity field data was rotated depending on the angle of attack of the airfoil.

3.3.3 Uncertainty Analysis

Uncertainty associated with calibration methods arises with human error and the equipment utilised. The error involved with laser alignment was estimated to be ± 1 mm, as it was ensured the laser was aimed at the plane of interest. Focus on the camera lenses was adjusted to be subjected on to the plane, while the high aperture accordingly rectified any small discrepancy in laser alignment. Through methods detailed by Prasad [168], the aperture used was sufficiently high to avoid any error associated with focusing. Another error due to calibration was the error associated with the spatial calibration scale and was estimated to be 0.2% of the chord length. The uncertainty with PIV measurements is dependent on image quality, and a high-resolution camera inevitably reduces the size of each pixel. This effect is compounded with the use of a 50 mm focal length which produces a low magnification factor. As Prasad [168] suggests a computing error, known as ‘bias error’, with the determination of particle displacement may occur if the seeded particle diameter is too small in comparison to the pixel size.

One source of error that was inevitable was the ‘acceleration error’, which occurs with the estimation of local velocity during the processing phase [168]. This error is proportional to the length of time between pulse separation, Δt of the laser [168], but must not be small enough to provoke complications in discerning the displacement of the particle. As such, a pulse separation of Δt = 10 μs was deemed appropriate through tentative methods. As follows, uncertainty with instantaneous velocity measurements were found to be typically below ± 7% of freestream velocity, as determined by Insight 4G. The software employs a ‘primary to secondary peak ratio’

approach proposed by Charonko & Vlachos [169], which evaluates a displacement error when cross-correlating the two images taken between Δt. However, this uncertainty was minimised with the collection of large image sets. Suggestions for a minimum number of images required to produce satisfactory averaged velocity data could be as low as 10 [170]. However, a preliminary PIV test was conducted to understand at which number of images the mean flow velocity begins to converge. Consequently, the number of images taken for phase and time-averaged experiments was in excess of this quantity to guarantee accurate estimates in velocity. Therefore, the uncertainty in PIV measurements is estimated at approximately ± 1% of the freestream velocity.

3.4 Static Pressure Measurements

Steady state pressure measurements along the airfoil surface were acquired to enhance understanding of upstream blowing behaviour and its effect on lift. Pressure measurements were performed with 40 pressure taps located at the mid-span of the airfoil. Taps of 2 mm diameter are located on both the upper and lower surfaces. The jet slots interfere with positioning on the upper surface giving 19 pressure taps located on the upper surface and 21 taps on the lower surface. Pressure tap hubs were implemented within the trailing edge in order to collect pressure measurements from taps. These hubs held hypodermic tubes which would transition into plastic tubing of 3.175 mm diameter. Pressure measurements were performed using a Scanivalve Corp PDCR23 differential pressure transducer with a range of ± 6900 Pa. The pressure transducer was calibrated using a Druck DPI portable transducer calibrator. To minimize uncertainty, each use consists of three repeats sampled at 1 kHz. Measurements were conducted for three jet locations; x_j/c = 0.08, 0.60 & 0.95, for a range of angles of attack α = 0°, 5°, 8°, 10° & 13°.

3.4.1 Pressure Measurements Uncertainty

Calibration of pressure required a conversion from voltage to pressure, which has an associated uncertainty. The total uncertainty for static pressure measurements is further accrued with dynamic pressure and a reference measurement taken with $U_\infty = 0\ ms^{-1}$. Consequently, typical uncertainty with the time averaged pressure measurements is estimated to be δC_p = ± 2.1%.

3.5 Experimental Parameters

3.5.1 Steady Measurements

3.5.1.1 Static Force Measurements

Force measurements were performed for two deflection angles of the jet flap. Normal blowing is achieved with the jet flap ejecting a sheet of air perpendicular to the airfoil surface. This angle has

been seen to disrupt and separate flow effectively [81], which is suspected to create a loss of lift. Upstream blowing refers to the jet blowing tangentially along the airfoil, in the opposing direction to freestream velocity. It is expected the interaction of the high momentum flows would thereafter create a stagnation point, and turn flow away from the upper surface.

For steady blowing experiments, the jet flap was investigated at all five chordwise locations, x_j/c = 0.08, 0.60, 0.75, 0.85 & 0.95. A stepper motor with an angle precision of ± 0.25° was used to rotate the airfoil and force balance. For every momentum coefficient, the airfoil was investigated at angles between $0° \leq \alpha \leq 20°$ for every 1° interval. Momentum coefficient for normal blowing was kept below C_μ = 0.02, and tested at five various values; C_μ = 0.004, 0.008, 0.012, 0.016 & 0.02. However, as upstream blowing was achieved with the addition of a small carbon fibre piece above the jet exit, a reduction in jet area by 50% is realised. This effectively doubled the momentum coefficients tested for normal blowing, for the same volumetric flow rate. A conversion between coefficient of volumetric flow rates and momentum coefficients between the two deflection angles can be found in Table 3.1.

Table 3.1 - Conversion of values between coefficient volumetric flow rate and coefficient of momentum.

Coefficient of Volumetric Flow Rate, C_Q	**Coefficient of Momentum, C_μ**	
	Normal Blowing	**Upstream Blowing**
0.002	0.004	0.008
0.0028	0.008	0.016
0.0035	0.012	0.024
0.004	0.016	0.032
0.0044	0.02	0.04

A data acquisition DAQ system was used in combination to a LabView programme to collect voltage readings during experimentation. The sampling frequency for data was 2 kHz for 10 seconds, which was repeated three times for each angle of attack. This was then repeated again when declining the airfoil from α = 20° to 0°. Prior to recording data for every new angle, steady blowing was allowed some time to reach a steady state. Jet thrust was also considered by recording force measurements with steady blowing activated at zero-freestream velocity. The lift force generated by the jet thrust was subsequently removed from the force measurements at freestream velocity, U_∞ = 20 ms^{-1}. Conversion of the normal and parallel forces acting on the airfoil and force balance to their

respective lift and drag coefficients was achieved with simple trigonometry, as shown in Eqs. [3.5] & [3.6].

$$L = F_y \cos\alpha - F_x \sin\alpha \quad [3.5]$$

$$D = F_x \cos\alpha + F_y \sin\alpha \quad [3.6]$$

Despite the parallel forces being utilised for determination of lift, it is assumed that the jet flap would only be activated during short periods of time. As such, the effect on drag is not as considerable as the overall fuel saving benefits expected with effective gust load alleviation techniques. Therefore, only lift coefficient will be presented for assessment of the jet flap.

3.5.1.2 Static PIV Measurements

In order to elucidate the differing mechanisms involved with normal blowing and upstream blowing, PIV measurements were performed for both deflection angles. Camera sensors differed between the two blowing methods. For normal blowing, two TSI® PowerView™ CCD 4 MP cameras (2048 x 2048 pixels) with an overlap region of 100 mm were used. The entire airfoil chord is covered within a field of view equivalent to 550 mm x 350 mm. Baseline measurements were performed for angles of attack α = 0°, 5°, 8°, 10° & 13°, which extends to the post-stall region. For the same angles of attack, PIV for normal blowing was completed for the three locations near the trailing edge; x_j/c = 0.75, 0.85 & 0.95. Close-up images were taken with one TSI® PowerView™ CCD 2 MP camera fitted with a Nikon 200mm f/4 AF-D Macro lens, but this was limited to the jet at x_j/c = 0.95 at α = 0°.

An upgraded camera sensor was utilised for PIV measurements of upstream blowing, with two TSI® PowerView™ CCD 8 MP cameras (3,312 x 2488 pixels). The dual camera arrangement was configured to have an overlap region of 35 mm. However, the field of view was revised in MATLAB to be analogous to the field of view for normal blowing. Measurements were performed for three jet locations at x_j/c = 0.08, 0.60 & 0.95, for the same angles of attack stated for normal blowing. A common jet location of x_j/c = 0.95 allows the two jet deflection angles to be compared. Interrogation window sizes for the entire airfoil surface and close-up images were of 32 x 32 pixels and 40 x 40 pixels, respectively. This produced a spatial resolution of 4 mm (0.8%c) for images of the entire airfoil surface and 1.3 mm (0.26%c) for the close-up images. For all cases performed, the time-averaged velocity field data was generated from 450 image pairs.

3.5.2 Periodic Measurements

3.5.2.1 Periodic Force Measurements

Periodic force measurements were performed with upstream blowing, only. The jet was deployed with a sinusoidal signal, in the form of Eq. [3.7], for a range of reduced frequencies between $0 \leq k \leq 0.471$, or $0 \leq f \leq 6$ Hz. This frequency range falls below the resonant frequency of the system. The peak momentum coefficient was maintained with increasing frequency. The number of chordwise jet locations was reduced to three; x_j/c = 0.08, 0.60 & 0.95. Due to less pressure resistance within the trailing edge plenum chamber, the maximum momentum coefficient possible to investigate for the jet at x_j/c = 0.95 was C_μ = 0.032. Therefore, three momentum coefficients are investigated at this location; C_μ = 0.016, 0.024 & 0.032. However, large momentum coefficients were not attainable for jets at x_j/c = 0.08 & 0.60. The jet momentum coefficient for these locations was set at C_μ = 0.016.

$$U_j(t) = U_{jmax} \times [1 - \cos(\pi f t)] \quad [3.7]$$

A National Instruments compactRIO system was used for data acquisition, at a sampling rate of 5 kHz for output signal acquisition. A total of 350 cycles were performed and phase-averaged, for angles of attack α = 0°, 5°, 8°, 10°, 13° & 16°. Post-processing in MATLAB was performed to determine the amplitude and phase angles from the signal. This process required the output signal to be assessed in the frequency domain, through a Fast Fourier Transform, where the phase and amplitude information were extracted. This information is revised using the dynamic force balance calibration data and reverted to the time domain, where the lift coefficient values are obtained. The compactRIO module acquired the input signal and the output force signal channelled through the FUTEK load cell. Knowledge of the phase difference between the input and output signals could be used in conjunction to the phase difference between input signal and jet response obtained through hot wire measurements. Only the aerodynamic phase difference is considered for force measurements; the angle between the jet response and lift response.

3.5.2.2 Periodic PIV Measurements

Periodic PIV measurements were performed for upstream blowing only, with the dual 8 MP camera configuration. However, the field of view was extended to 675 mm x 350 mm in order to observe more of the wake region. For a reduced frequency of k = 0.393, PIV measurements were completed for three jet locations; x_j/c = 0.08, 0.60 & 0.95. However, angles of attack were nominated based on the jet flap performance exhibited in force measurements. Table 3.2 indicates the angles selected for assessment at each jet location.

Table 3.2 - Experimental values for periodic PIV measurements.

Jet Location, x_j/c	Angle of Attack, α
0.08	10° & 13°
0.60	5°, 8°, 10° & 13°
0.95	0°, 5°, 8°, 10° & 13°

Data for the jet was captured at four phases in the blowing cycle for periodic cases; φ = 0°, 90°, 180° & 270°. A total of 450 image pairs were captured to be phase-averaged, and post-processed with the method outlined in section 3.4.

3.5.3 Transient Measurements

3.5.3.1 Transient Force Measurements

Transient measurements have been performed to evaluate the lift response of the jet flap with immediate deployment. The rapid deployment was achieved by activating the jet with a square wave profile. Transient measurements were taken for three jet locations; x_j/c = 0.08, 0.60 & 0.95, for a momentum coefficient of C_μ = 0.016. The angles of attack considered varied for each jet location. A summary of which angles were tested for every location is found in Table 3.3.

Table 3.3 - Experimental values for transient force measurements.

Jet Location, x_j/c	Angle of Attack, α
0.08	10° & 13°
0.60	5°, 8°, 10°, 13° & 16°
0.95	0°, 5°, 8°, 10°, 13° & 16°

Activation/deactivation of the transient jet remained constant for five seconds, which is equivalent to 200 chord lengths of travel, to let the force stabilise to steady-state. Transient measurements were repeated over 20 cycles, to produce a phase-averaged signal. Signal processing was performed in MATLAB, in a similar procedure to periodic force measurements. Lift force was obtained through converting the signal to the frequency domain and revised using the dynamic force balance calibration. Time delay of the lift response is determined for each case considered.

3.5.3.2 Transient PIV Measurements

Setup for transient PIV measurements is identical to periodic tests. Velocity field data was captured for activation and deactivation phases of the jet. However, only certain cases were selected from force measurements for PIV. Table 3.4 displays the selected cases performed for transient PIV.

Table 3.4- Experimental values for transient PIV measurements.

Jet Location, x_j/c	**Angle of Attack, α**
0.08	10°
0.60	10°
0.95	0°, 10° & 13°

As seen in Table 3.4, a common angle of attack among the jet locations was chosen at α = 10° for the purpose of comparison. Seven convective time units are chosen to complete PIV measurements, to fully demonstrate the jet flap behaviour between steady states. Four of these measurements lie within the rise/fall stage. The number of images captured was 450, to produce phase-averaged velocity data.

3.6 Figures

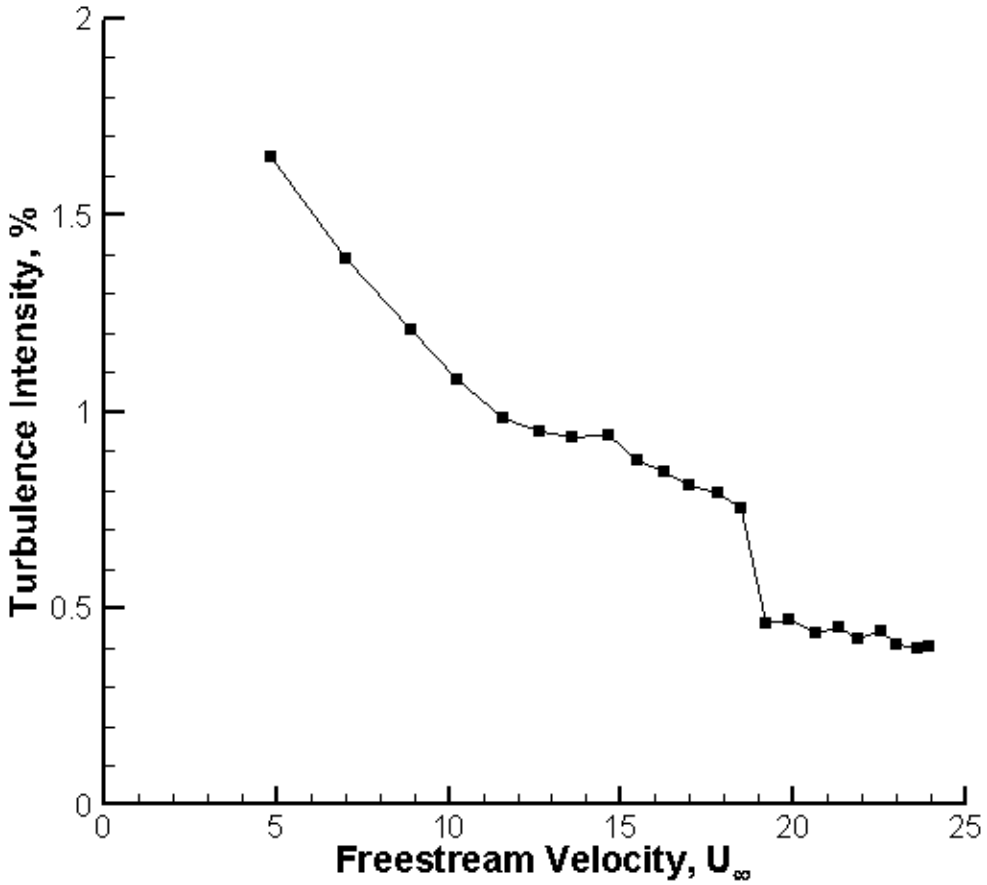

Figure 3.1 - Turbulence intensity vs. Freestream velocity for closed-loop wind tunnel.

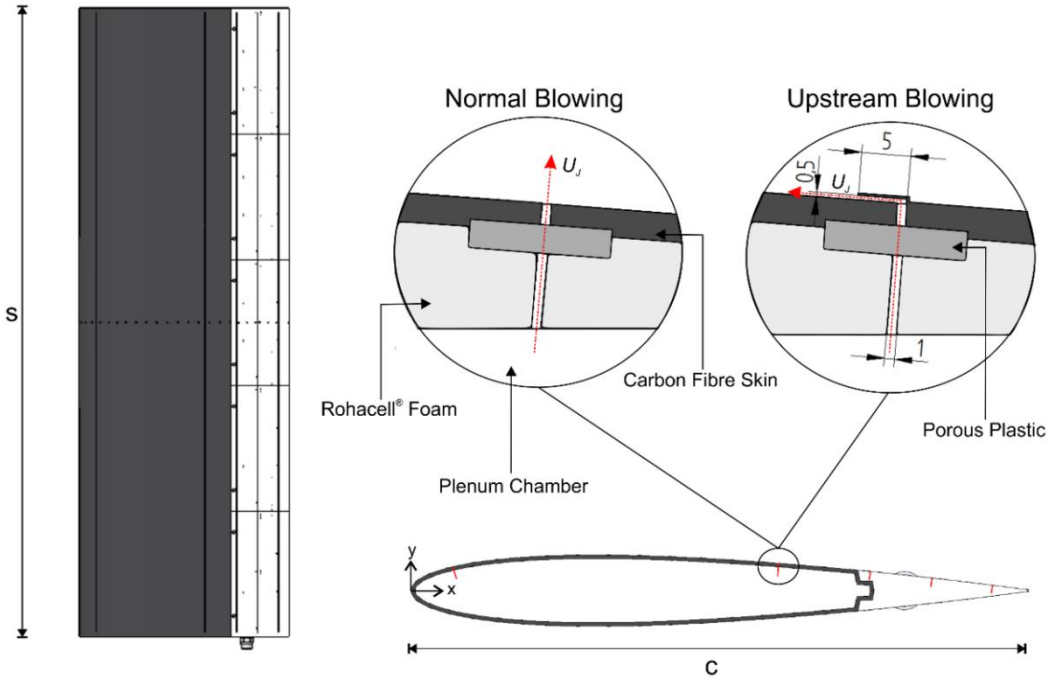

Figure 3.2 - Wing setup and chordwise locations of jets, dimensions in millimetres.

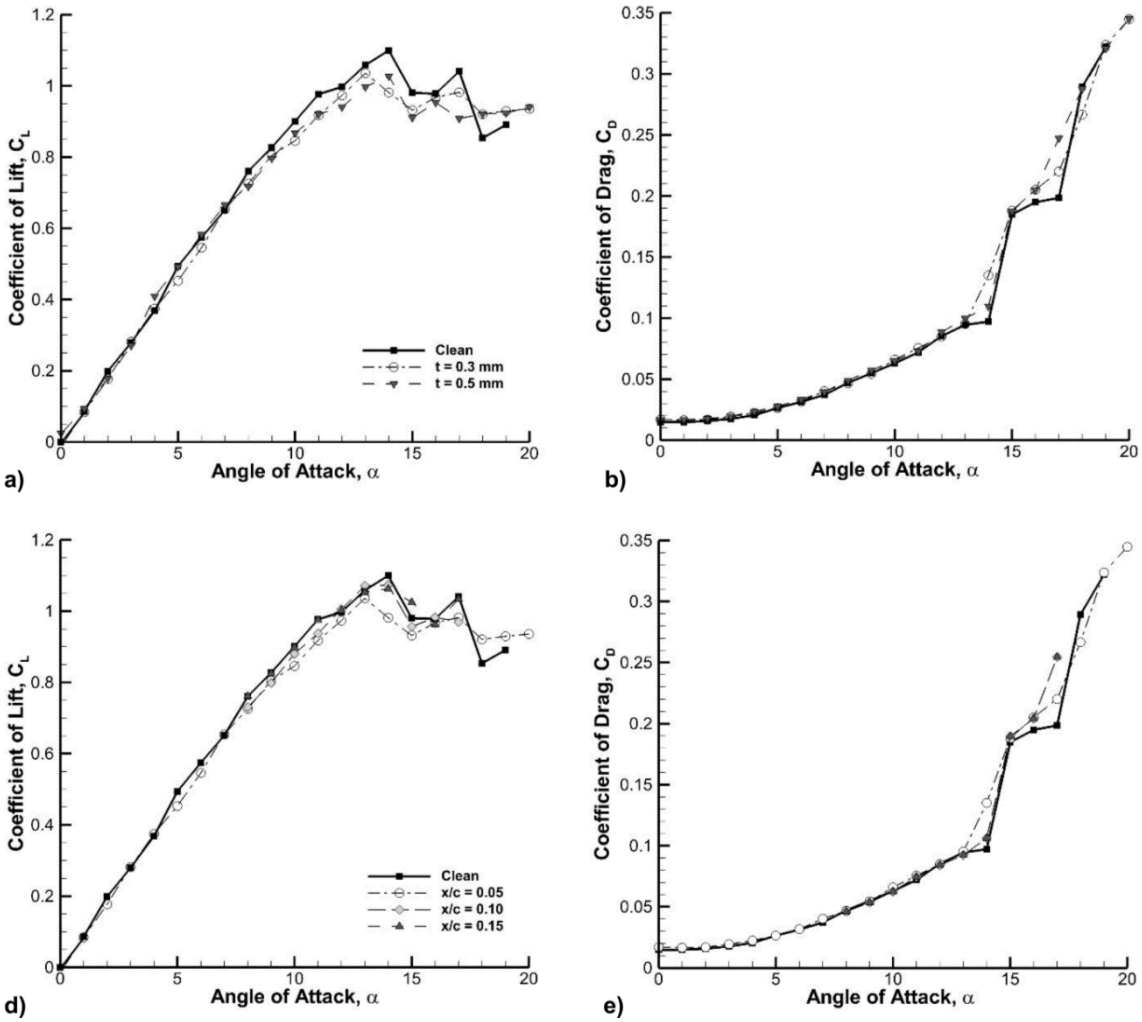

Figure 3.3 - Force measurements conducted to determine trip wire and thickness; a) & b) show effect of trip wire thickness, d) & e) show effect of trip wire location on lift and drag, respectively.

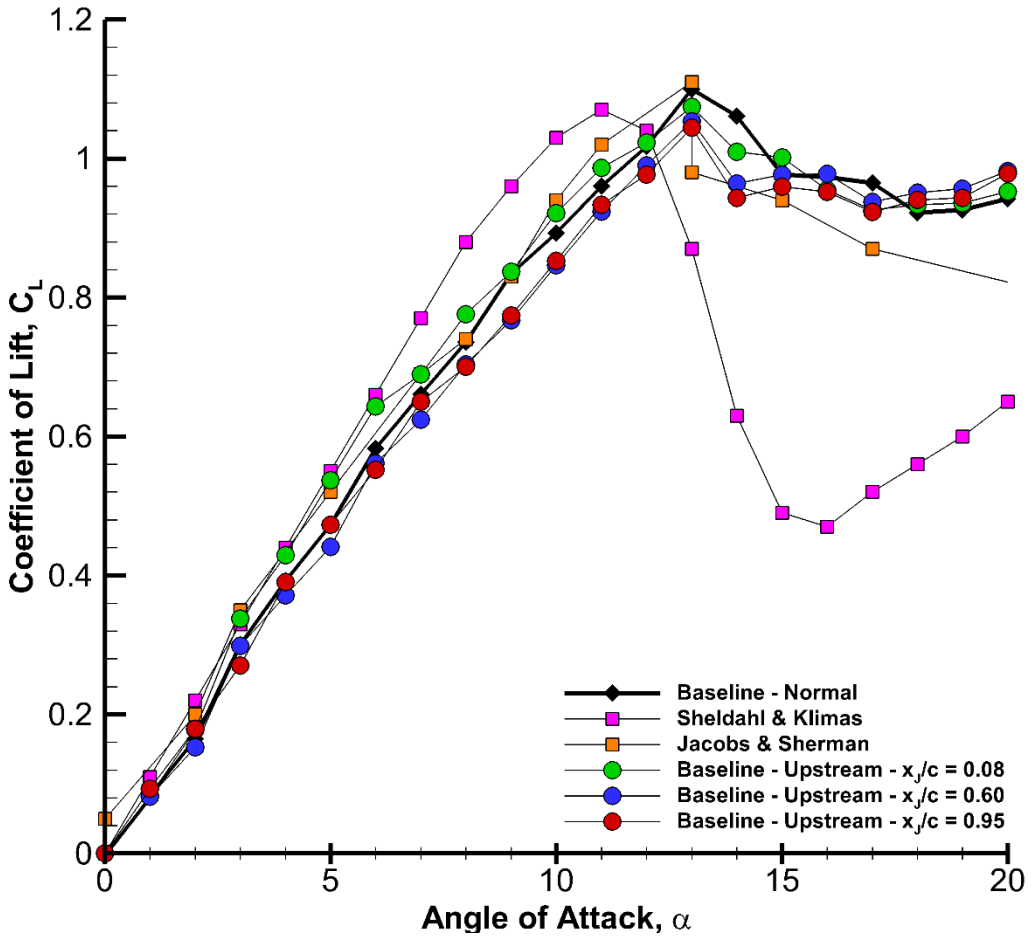

Figure 3.4 - Literature validation for NACA 0012 airfoil, with unforced upstream and normal blowing cases.

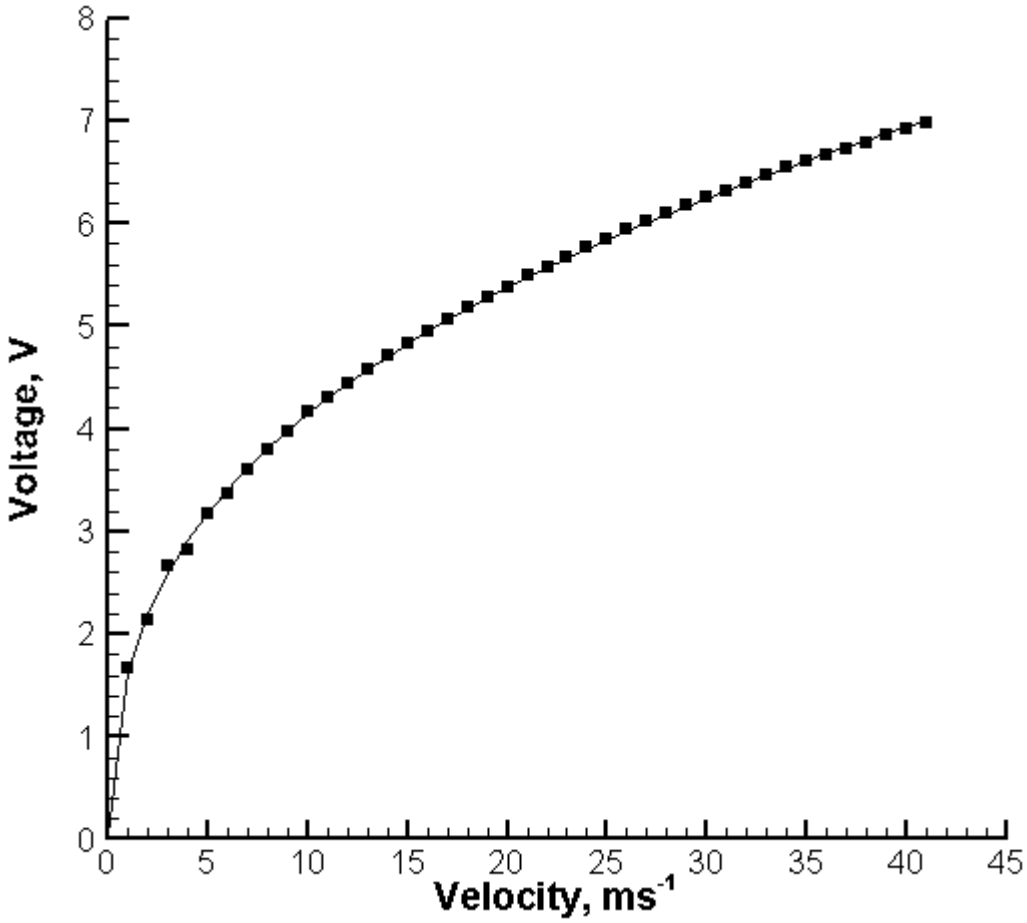

Figure 3.5 - Voltage vs. jet velocity for hot wire calibration.

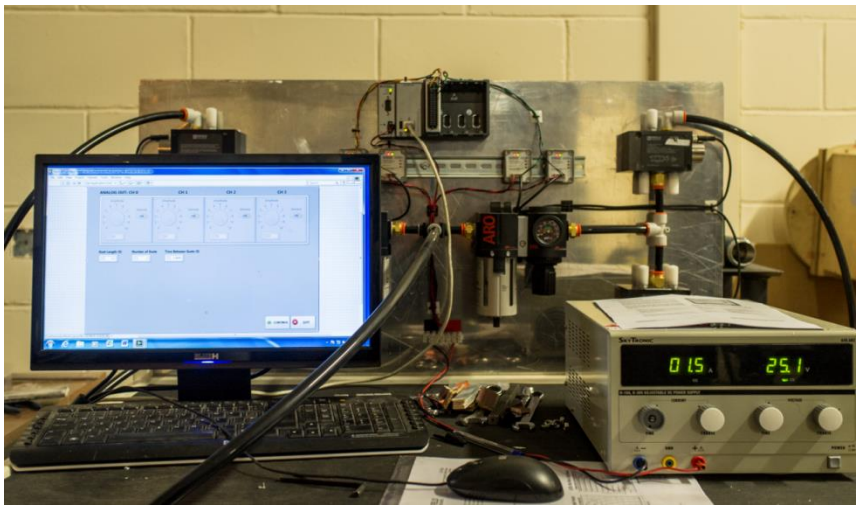

Figure 3.6 - Photograph of bespoke unsteady valve system.

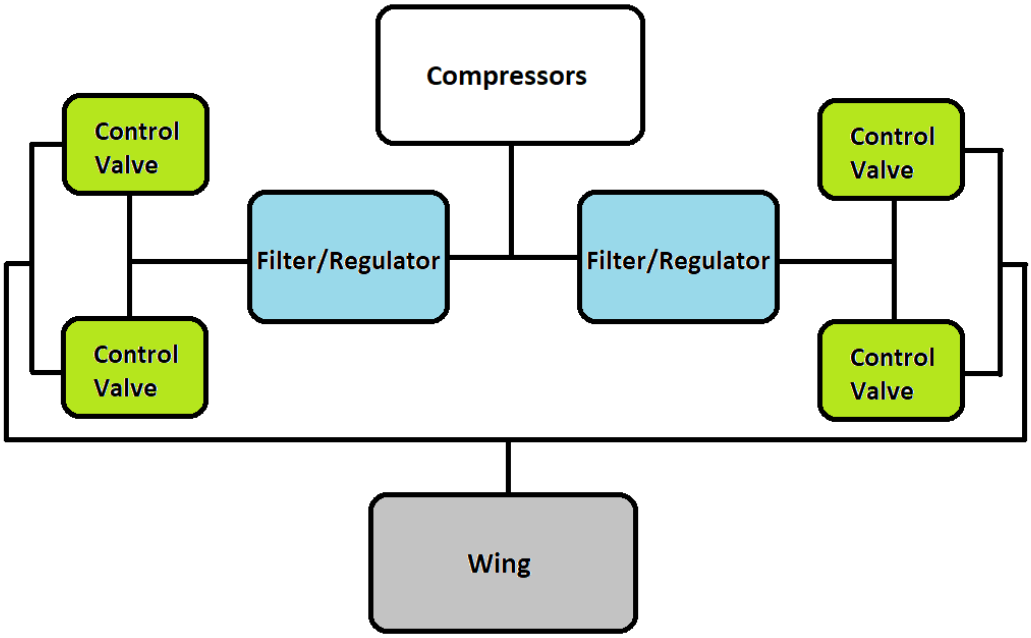

Figure 3.7 - Block diagram of the unsteady blowing setup.

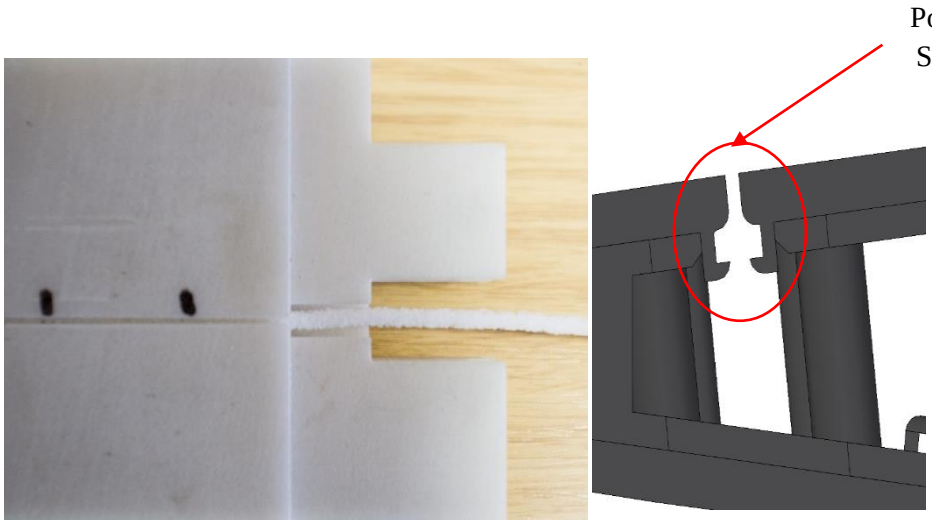

Figure 3.8 - Illustration of porous plastic in position.

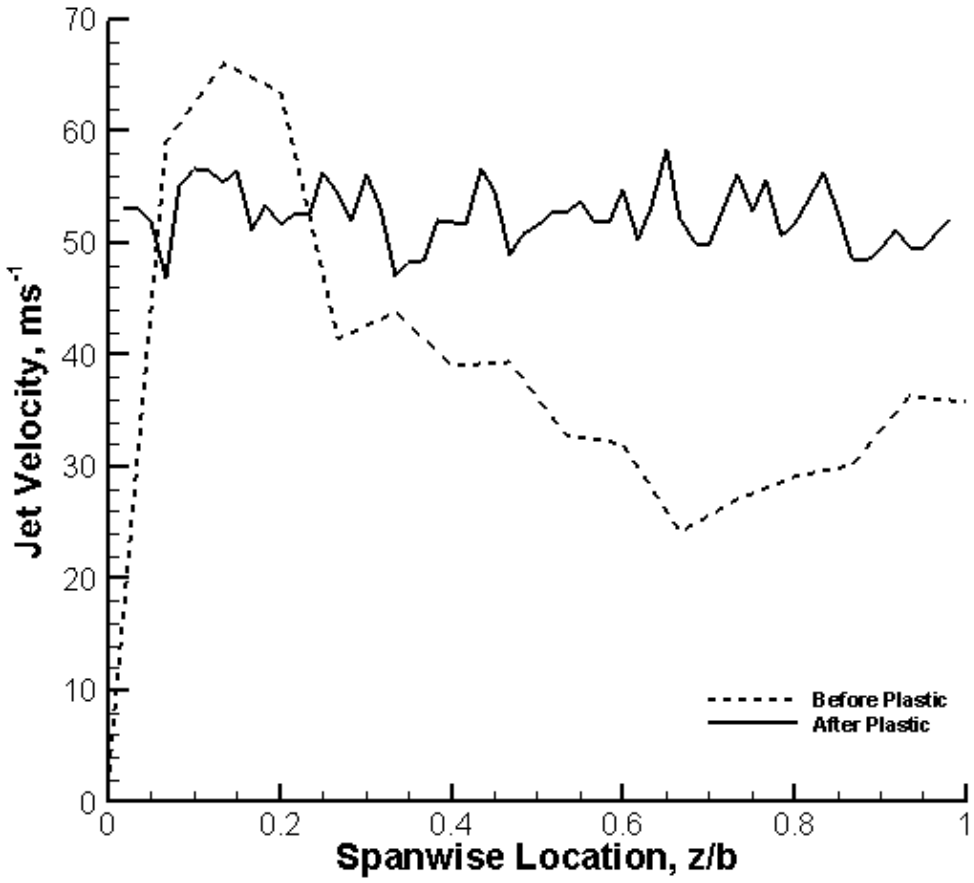

Figure 3.9 - Comparison of jet velocity measurements before and after porous plastic installation.

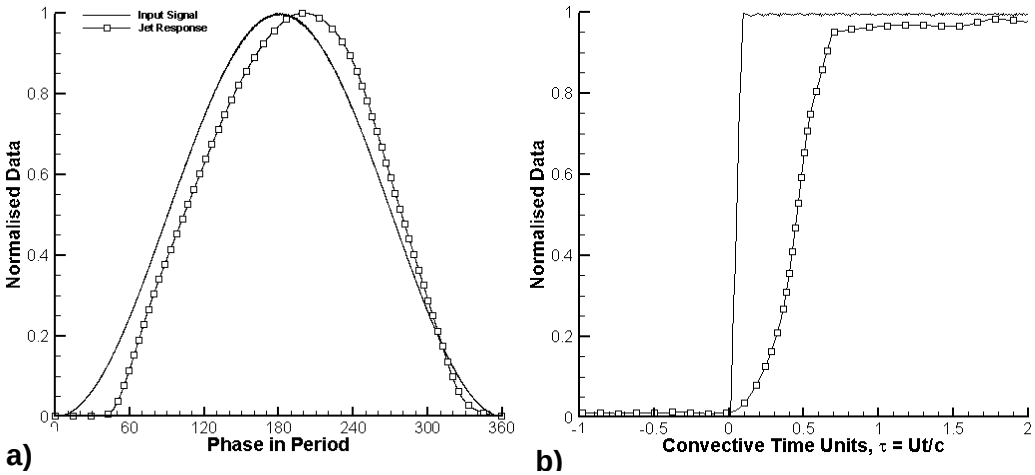

Figure 3.10 - Example of jet velocity response to input signal for a) Periodic deployment and b) Transient deployment.

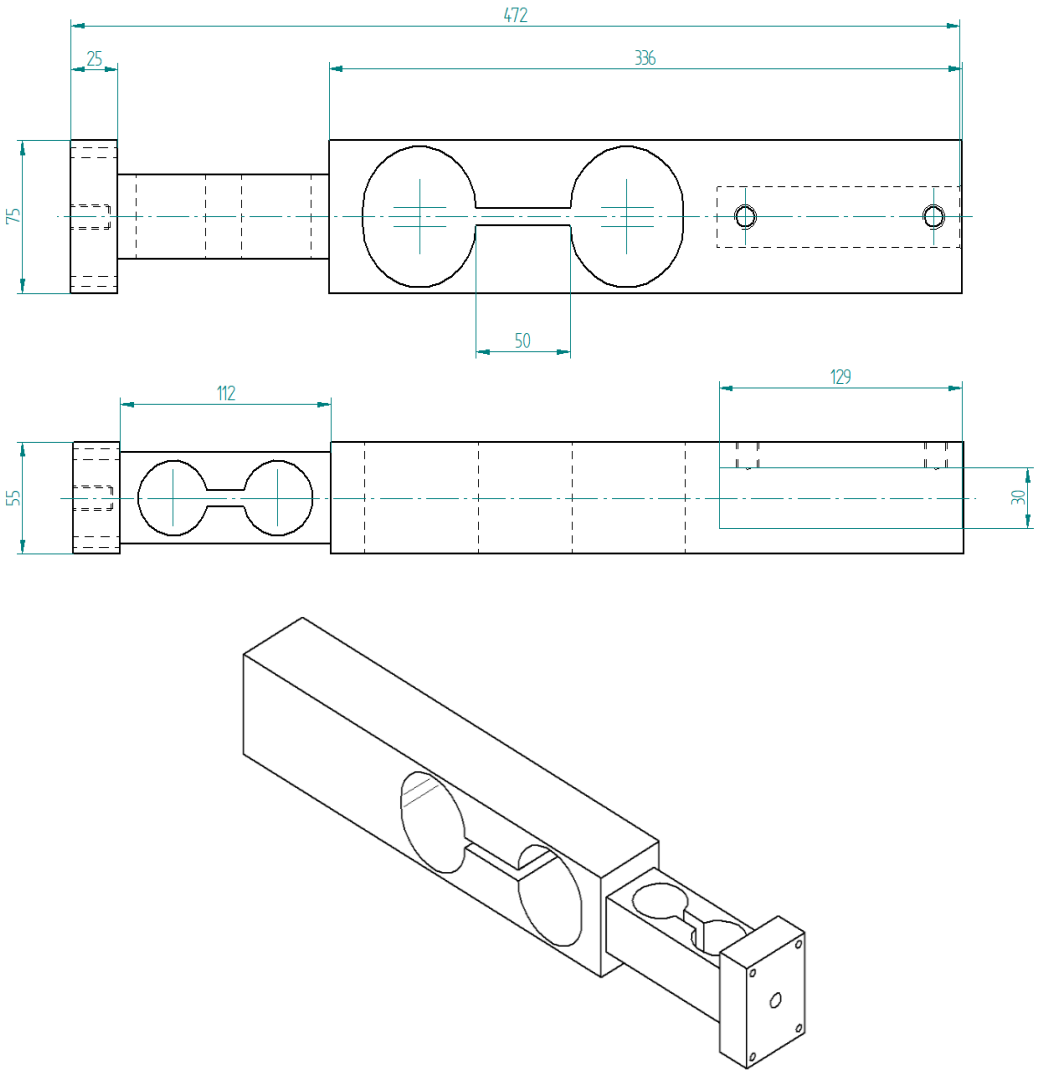

Figure 3.11 - Dimensions of two-axis force balance used for steady-state measurements; Dimensions are in millimetres.

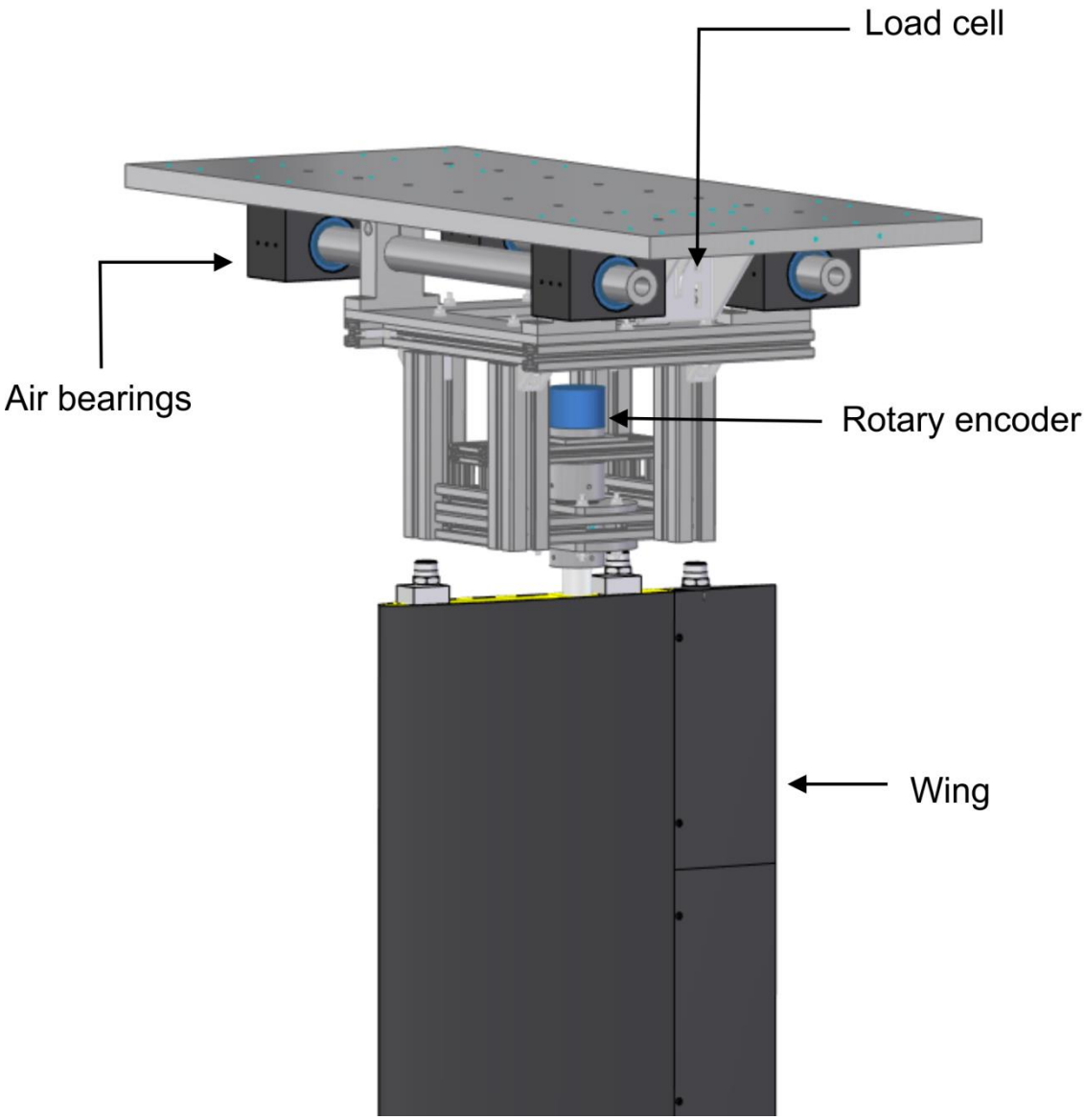

Figure 3.12 - Force balance used for dynamic measurements.

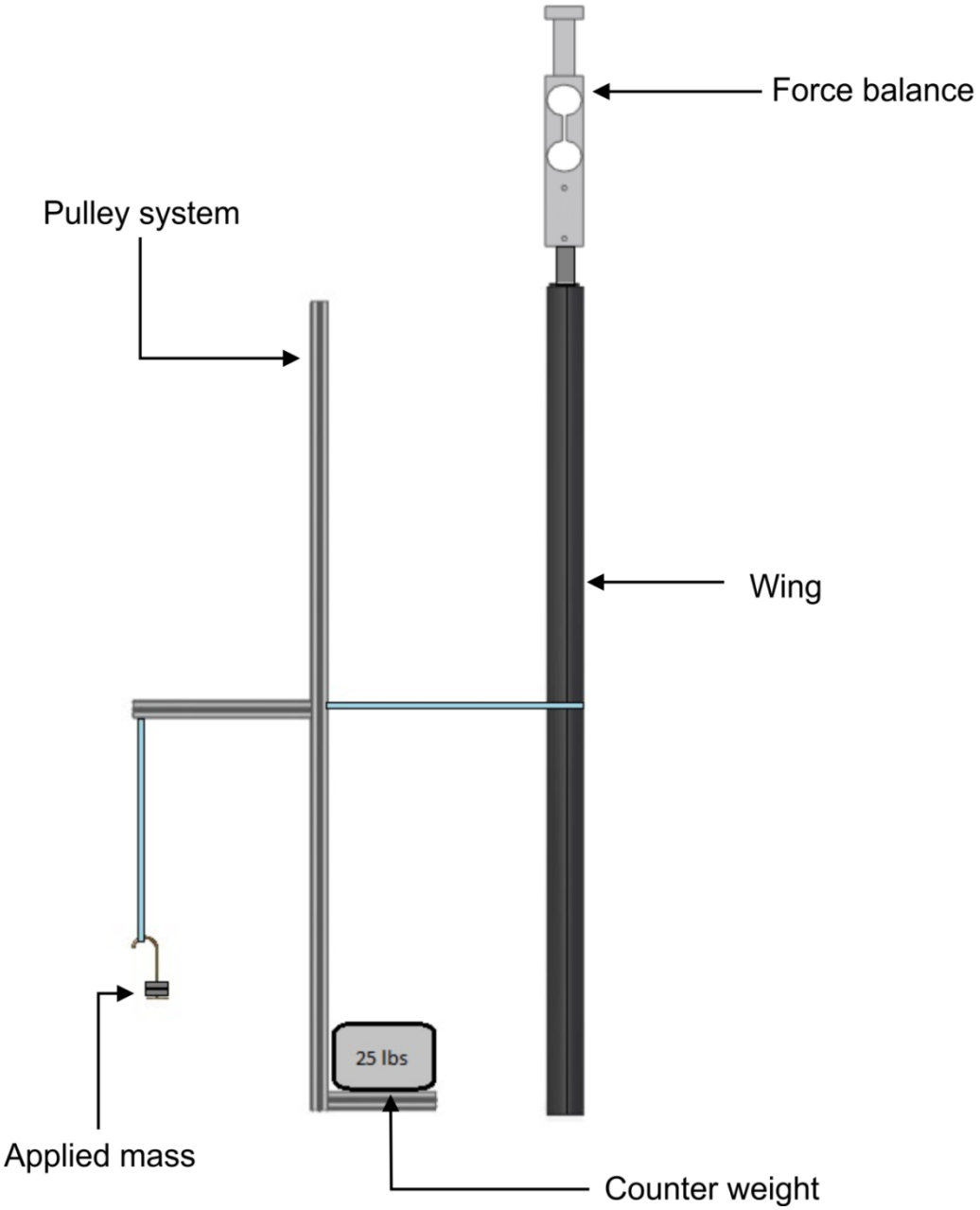

Figure 3.13 - Calibration method used for steady-state measurements.

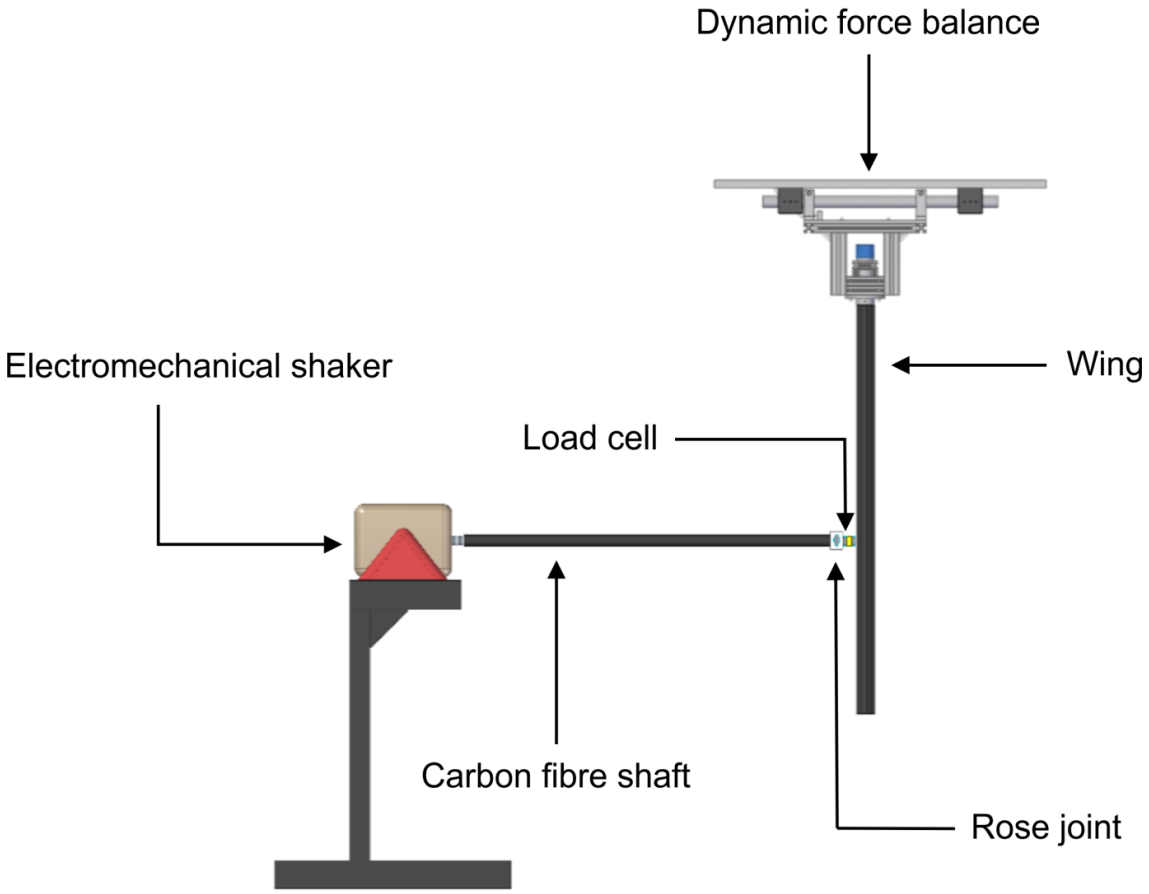

Figure 3.14 - Calibration method used for dynamic force measurements.

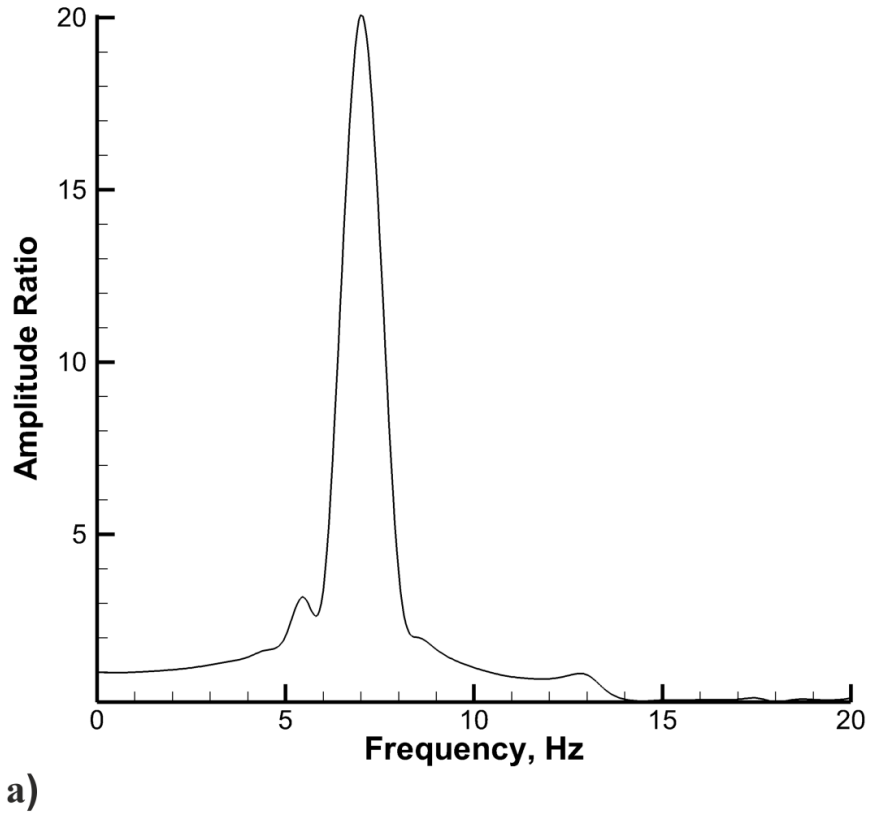

a)

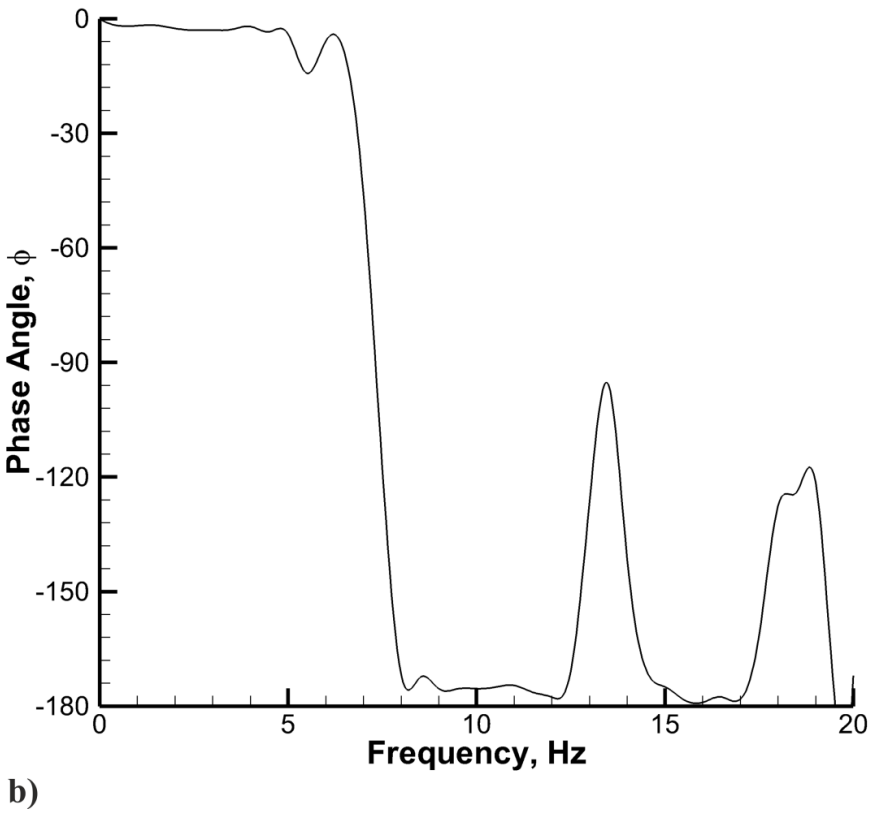

b)

Figure 3.15 - Dynamic force balance calibration measurements, a) Amplitude ratio vs. Frequency, b) Phase angle vs. Frequency.

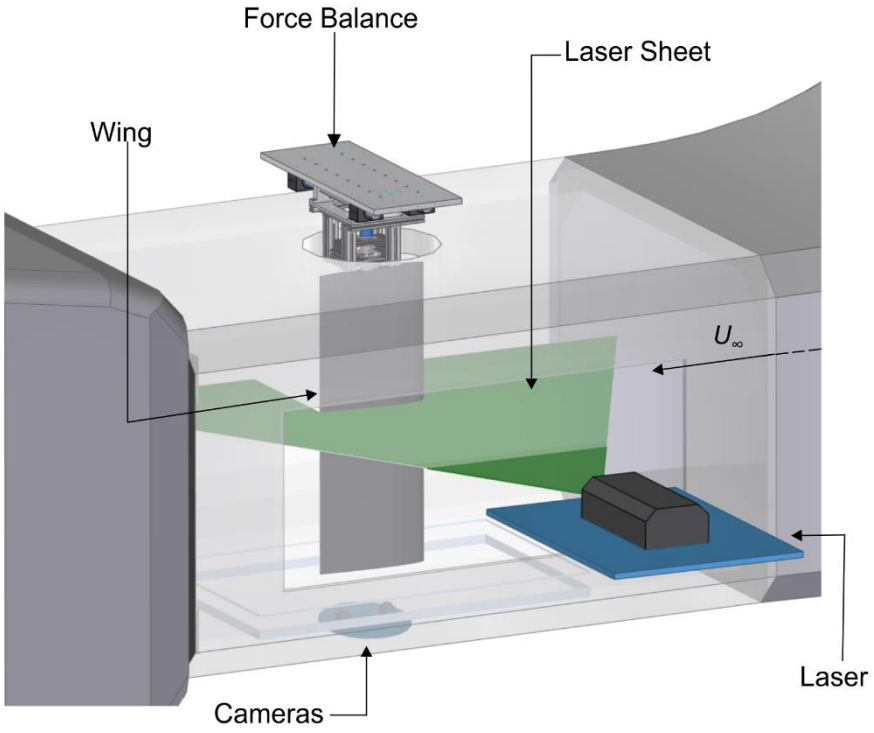

Figure 3.16 - Experimental setup of particle image velocimetry in wind tunnel.

Chapter 4 : Steady State Measurements

Two blowing methods are investigated in this chapter; normal blowing and upstream blowing. Due to the differences in jet exit areas, the volumetric flow rate coefficient is used throughout this chapter. Please refer to Table 3.1 for conversion to momentum coefficient. Both methods are examined separately, before drawing a comparison between the two deflection angles.

4.1 Force Measurements

4.1.1 Normal Blowing Force Measurements

4.1.1.1 Effect of Varying Volumetric Flow Rate Coefficient

Time averaged force measurements were conducted for a range of angles, $0° \leq \alpha \leq 20°$, with normal blowing at five chordwise locations; x_j/c = 0.08, 0.60, 0.75, 0.85, 0.95. For the latter three jet locations, flow rate coefficient is varied between C_Q = 0.20 – 0.44%, while the former two locations are tested with a maximum flow rate coefficient, C_Q = 0.44%. The effect of varying volumetric flow rate on lift coefficient is presented in Fig. 4.1. The 'baseline' case refers to the case with no blowing activated. For a symmetrical airfoil, the baseline starts with C_L = 0 at α = 0°, and culminates at the stall angle, α = 13°, with C_L = 1.10. The change in lift coefficient from the baseline case is presented in parallel to the lift curves.

For x_j/c = 0.95, in Fig. 4.1a, the dependency of flow rate on lift is evident with angles below the stall angle. The smallest flow rate C_Q = 0.20% induces the smallest change; for example, at α = 0°, the change in lift coefficient is ΔC_L = -0.034. The change in lift increases as the flow rate rises. This is seen until α = 13°, where the lift coefficient returns to the baseline case. Regardless of the flow rate, the change in lift remains relatively constant for pre-stall angles.

At x_j/c = 0.85, normal blowing is more effective at higher angles of attack. This is illustrated in Fig. 4.1b where a negative gradient is observed for change in lift. Once the stall angle is reached, normal blowing becomes ineffective for all flow rates considered. The change in lift increases with flow rate coefficient. However, it appears to reach a maximum at C_Q = 0.40%, as further enhancement beyond this flow rate produces a negligible change.

When tested at x_j/c = 0.75, blowing appears to have an insignificant effect on lift force, as shown in Fig. 4.1c. Difference with blowing strength only appears once nearer to stall angle. Although blowing at C_Q = 0.20% brought about an earlier stall angle, it did little to alleviate lift force at all angles preceding stall. The largest lift reduction was observed at the stall angle when blowing

with C_Q = 0.28% & 0.35%. Maximum lift coefficient for both flow rate coefficients was recorded at C_L = 0.99 at α = 13°. Therefore, producing a change in lift coefficient of ΔC_L = -0.11. Further increase in blowing strength to above $C_Q \geq$ 0.40% shows negligible changes from the baseline curve at all angles. When considering the normal blowing jet flap for employment on commercial aircraft, it would not seem appropriate to locate it at this location due to its inefficiency at low angles.

4.1.1.2 Effect of Varying Normal Blowing Location

Figure 4.2 shows the effect of varying normal blowing jet location for a fixed volumetric flow rate coefficient, C_Q = 0.44%. As demonstrated in the lift curve, normal blowing is most effective when located nearest to the trailing edge. The clearest illustration of this can be seen at α = 0°, where lift reduction enhances as the jet displaces downstream along the chord. When examining the performance for angles below the stall angle, the x_j/c = 0.95 jet demonstrates the largest lift reduction at every angle. Lift reduction attained for the x_j/c = 0.85 jet becomes comparable to the trailing edge jet beyond $\alpha \geq$ 11°. The jet is ineffective when placed at x_j/c = 0.75, but delays stall angle to α = 14°. The x_j/c = 0.60 jet shows an identical trend in lift, while the leading edge jet appears to create lift enhancement, particularly at higher angles of attack. Hence, this indicates normal blowing is only effective for lift reduction purposes when closest to the trailing edge. In the post-stall region, normal blowing does not have an effect for all jet locations investigated.

4.1.2 Upstream Blowing Force Measurements

4.1.2.1 Effect of Varying Volumetric Flow Rate Coefficient

Figure 4.3 shows time-averaged force measurements for upstream blowing for three chordwise locations at all flow rate coefficients considered. Presented in the left column are lift coefficient figures for each jet location; the right column presents the change in lift relative to the baseline. Figure 4.3a shows the time-averaged force measurements for the upstream jet configuration at x_J/c = 0.95. Increasing flow rate at this location is most beneficial for when operating at lower angles of attack. Upstream blowing with C_Q = 0.20% at α = 5°, causes a drop in lift of ΔC_L = - 0.11. In comparison, the lift reduction is increased to ΔC_L = - 0.18 for C_Q = 0.44%. The effect of increasing the flow rate coefficient is to increase the gradient of the lift curve, as the curves converge at α = 13°. The case of blowing at C_Q = 0.40% provides the most consistent lift reduction in the range of ΔC_L = 0.17 – 0.20 up to α = 13°.

In Fig. 4.3b, a distinct relationship between change in lift and flow rate coefficient develops at x_J/c = 0.60, indicating there is a significant benefit to increasing the flow rate up to α = 14°. Lift reduction caused by the C_Q = 0.20% jet is relatively insignificant until $\alpha \geq$ 9°. The largest lift

reduction for this flow rate is noticed at α = 14°, where the peak lift coefficient is diminished to C_L = 0.93 with C_Q = 0.20%. In comparison, the lift coefficient for this angle of attack is C_L = 0.82 for C_Q = 0.44%. Similar to the jet at x_J/c = 0.08, the stall angle is delayed with the maximum flow rate to α = 19°. However, the change between each lift curve appears to reduce with increasing flow rate coefficient, which implies an asymptote at higher flow rates.

When placing the upstream jet at x_J/c = 0.08, the effect of increasing flow rate is not apparent until α = 9°, where a difference in lift coefficient between C_Q = 0.20% and C_Q = 0.44% is ΔC_L = - 0.08. With increasing flow rate coefficient, the gradient of the lift curve decreases as the point of stall becomes less distinct. Interestingly, stall is brought forward to α = 11° with C_Q = 0.20%, but is delayed to α = 19° with C_Q = 0.44%. Beyond α = 11°, the curves converge to α = 13°, where negligible difference between flow rate coefficients is observed. Utilising the lowest flow rate coefficient is sufficient to induce a lift reduction at large angles of attack; ΔC_L = - 0.28 at α = 13°.

4.1.2.2 Effect of Varying Upstream Blowing Location

Time-averaged force measurements are compared for all five chordwise locations for the maximum flow rate coefficient, see Fig. 4.4. As noted earlier, trailing edge locations are preferable for low angles of attack. For angles of attack below α = 5°, as the upstream blowing jet location progresses from trailing edge to leading edge, the lift coefficient gradually depreciates. For example, for α = 0°, the change in lift coefficient reduces from ΔC_L = - 0.20 for x_J/c = 0.95 to ΔC_L = - 0.01 for x_J/c = 0.08.

As the angle of attack increases, the gradient of each of the lift curves becomes apparent, with locations near the trailing edge maintaining a larger gradient and more linear trend. As a result, a point of intersection is observed between α = 9° and 11°, where all chordwise locations provide similar lift force. The smaller gradient attributed with leading edge jets, means the ability to mitigate lift is enhanced at higher angles. Consequently, the jet at x_J/c = 0.95 creates the least change in lift at α = 13°. Furthermore, upstream blowing, at all chordwise locations, extends its influence to beyond the stall angle to maintain the lift reduction.

4.1.3 Literature Validation

Spence [80] postulated the square root of the momentum coefficient to be proportional to the change in lift, for jet flaps located near or at the trailing edge with low deflection angles. In order to validate this theory, the change in lift with momentum coefficient for all normal and upstream blowing cases at an angle of attack of 0°, are presented in Fig. 4.5a. Spence corroborated his theory with the use of jets blown tangentially from the trailing edge [81]. As such, the literature data, shown

in Fig. 4.5a is representative of lift augmentation/drag reduction with the use of lower surface jet flaps [71, 81, 86, 171].

Since the NACA 0012 has a symmetrical profile, it is possible to make the comparison of pressure surface jets to suction surface jet flaps at α = 0°. Coloured circle and square symbols depict results for upstream blowing and normal blowing cases, respectively. Upstream blowing force measurements at jet locations x_J/c = 0.75 and 0.85 was performed with the maximum momentum coefficient, for the sake of comparison. However, for other locations, all five momentum coefficients are performed for both upstream and normal blowing. Only literature data was collected and curve fitted using MATLAB. As evident in Fig. 4.5a, there is a square root dependency between momentum coefficient and change in lift coefficient. The fitted curve follows a similar path to that of the data collected at University of Bath, in particular with trailing edge locations, regardless of the blowing direction used.

The most analogous case to normal and upstream blowing force measurements at x_J/c = 0.95, was that of Traub *et al.* [71]. This is expected due to similar parameters as the jet investigated by Traub *et al.* [71] was a normal blowing jet at x_J/c = 0.98, on a symmetrical airfoil. For other jet locations, the effectiveness is clearly reduced. There is a monotonic reduction as the jet flap approaches the leading edge for both normal and upstream blowing. At this angle, α = 0°, there is therefore no advantage/disadvantage to upstream blowing.

For higher angles of attack (e.g. α = 13° in Fig. 4.5b) upstream blowing is preferable for alleviating lift, irrespective of jet location. Contrary to the measurements at α = 0°, leading edge locations are now preferable. For x_J/c = 0.08 it is extremely effective for even small blowing coefficients, C_μ = 0.008. For normal blowing no obvious trend is discernible as the magnitude is comparatively small.

The two parameters are related as $C_\mu = 2C_Q^2/(h_j/c)$, however, C_Q is more meaningful for comparison between the two blowing methods, as stated by Al-Battal *et al.* [172]. First of all, the theoretical modelling of the counter flowing wall jets [173] suggests that the main parameter is U_j/U_∞. Secondly, unlike the applications in which the momentum addition is important (such as the delay of flow separation), forced separation of an attached boundary layer can be considered due to a source whose strength is proportional to C_Q. A similar situation occurs for the cases where the suction acts as a sink [174,175] and the volumetric flow rate coefficient becomes the main parameter. In addition, this parameter is representative of the power input into the system.

If Figs. 4.5a and b were plotted as a function of C_Q rather than C_μ, both normal and upstream blowing flow rate coefficient values would span the same range. However, the lift reduction data do

not collapse with neither C_μ nor C_Q. The purpose of blowing, in this project, is not to inject momentum to the flow, but to stagnate the local flow in order to modify the effective camber of the airfoil. Allowing the jet to act as a source suggests a source coefficient in the form of volumetric flow rate coefficient. Therefore, corroborating the requirement to compare on the basis of C_Q with C_μ reported for reference.

A form of the lift augmentation ratio can be determined by dividing the change in lift coefficient by the momentum coefficient (i.e. $\Delta C_L/C_\mu$). Figure 4.6 shows how this aerodynamic gain varies with momentum coefficient for α = 0°. For jet flaps near the trailing edge, upstream and normal blowing both exhibit greater magnitude of $\Delta C_L/C_\mu$ compared to upstream locations. A loss in magnitude with increasing momentum coefficient occurs. This behaviour is corroborated by Traub *et al.* [71] whose data shows an analogous trend to that of upstream blowing at x_j/c = 0.95. When comparing the magnitude of $\Delta C_L/C_\mu$ between upstream blowing and normal blowing at x_j/c = 0.95, it can be shown that magnitude values produced are similar for a given momentum coefficient. This is evident at C_μ = 0.008, where both methods produce a magnitude around $\Delta C_L/C_\mu \approx$ 9 - 10. However, given that C_μ = 0.04 for upstream blowing and C_μ = 0.02 for normal blowing share the same work rate, it can be shown that normal blowing is more efficient in this particular case. Demonstrably, the magnitude of $\Delta C_L/C_\mu$, and therefore the effectiveness, of upstream blowing jet reduces as the jet is located nearer to the leading edge.

4.2 Particle Image Velocimetry Measurements

4.2.1 Normal Blowing Particle Image Velocimetry

Time-averaged Particle Image Velocimetry measurements were completed to visualise local behaviour in order to fully comprehend the flow physics surrounding the normal blowing jet flap. Normal blowing PIV was examined for a range of angles between $0° \leq \alpha \leq 13°$, for three jet locations; x_j/c = 0.75, 0.85 & 0.95.

Figure 4.7 demonstrates the effect of increasing blowing strength at x_j/c = 0.95. The flow rate coefficients considered with the PIV setup were C_Q = 0.20%, 0.35% & 0.44%. Streamlines indicate complete flow attachment for the baseline case at α = 0°. However, even when blowing with the smallest strength, C_Q = 0.20%, a slight perturbation in the flow over the upper surface near the jet is observed. As mentioned in section 4.1.1.1, despite the flow field change, this blowing strength could only generate a modest lift change at this angle. When blowing with a larger flow rate coefficient, the flow perturbation becomes more pronounced. Such perturbation increases the camber of the aerofoil near the trailing edge, which can cause a change in the Kutta condition.

At α = 5° the inclined airfoil experiences greater velocity magnitude near the leading edge, as the baseline airfoil generates positive lift above α = 0°. Normal blowing does little to disturb flow from the upper surface with C_Q = 0.20%. Significant change is observed with C_Q = 0.44%, as the increased blowing strength incites an increased wake size aft of the jet. This behaviour is also noted at α = 8°. Flow separation along upper surface is noted with the baseline case at α = 10°. Once again, the weakest blowing strength is insufficient to change the flow field, which agrees with the force measurements. The jet appears to be injecting momentum into the separated region, which is also observed for α = 13°. Hence, indicating the jet still has an effect within a large separated region.

PIV measurements were taken at the maximum flow rate coefficient, C_Q = 0.44%, for three jet locations; x_j/c = 0.75, 0.85 & 0.95. From Fig. 4.8, it can be seen that locating the jet flap furthest downstream at x_j/c = 0.95 appears to have attenuated the separation bubble size observed in the baseline case at α = 13°. This is expected as placing the jet close to the trailing edge benefits from using the high momentum ejected in near proximity to the lower surface. The upwash effect is much stronger in this location and is more apparent at lower angles.

When at x_j/c = 0.85, deflections in the streamlines are still present; however, there is an apparent change in the size of the separation bubble seen at α = 13° due to the increased space between the jet and the trailing edge. This recirculation region is able to effectively entrain flow from the lower surface, thereby inducing an upwash effect. This flow behaviour is associated with a 7.5% lift reduction. The streamline deflection effect strengthens with angle of attack for this location. Much of the behaviour observed at x_j/c = 0.85 is present with the jet located at x_j/c = 0.75. Force measurements taken with the jet flap at the x_j/c = 0.75 location indicated that it was not an ideal location to alleviate lift loads. Analysis of PIV flow fields show at lower angles, the jet flap has little to no effect with perturbing freestream streamlines. When activating at stall angle (α = 13°), the jet flap successfully disrupts flow within a separated region. In comparison to the no blowing case, the separated region has divided into two separate regions, consequently forming a recirculation region which exists between the jet slot and the trailing edge. This behaviour is corroborated by the 2.5% reduction in lift observed during the force measurements.

4.2.2 Upstream Blowing Particle Image Velocimetry

4.2.2.1 Effect of Varying Volumetric Flow Rate Coefficient

Presented in Figs. 4.9 to 4.11 are time-averaged velocity magnitude fields of baseline cases and upstream blowing with three different flow rate coefficients at x_J/c = 0.08, 0.60 & 0.95. For x_J/c = 0.95, Fig. 4.9, a slight perturbing of streamlines above the jet occurs at α = 0°. The increase in flow rate only serves to deflect flow away from the upper surface at a greater angle. This suggests there is

separation occurring within the local region, hence, the smallest flow rate C_Q = 0.20% induces a change of ΔC_L = -0.08.

Although not visible at the smallest flow rate, velocity magnitude reduces significantly downstream of the jet at α = 5° when blowing with a flow rate greater than $C_Q \geq 0.35\%$. At C_Q = 0.44%, this reduction can also be seen occurring at around $x/c \approx 0.85$. This behaviour is observed at α = 8°. However, the smallest blowing strength appears to incite flow separation starting from $x/c \approx$ 0.80. Increasing the blowing strength to C_Q = 0.35%, sees separation starting from similarly the same location, but a discontinuity in the separated region is noticed at $x/c \approx 0.88$ to 0.97. When at C_Q = 0.44%, this discontinuity stops just upstream of the jet. It is unclear whether flow reattaches within this region, but increasing the flow rate strength from C_Q = 0.20% to 0.44% produces a further lift reduction of ΔC_L = -0.032. For α = 10°, separation appears to enhance in size at a greater rate when increasing from C_Q = 0.35% to 0.44%, when compared to the change from C_Q = 0.20% to 0.35%. The dependency on flow rate coefficient becomes vastly clearer for the trailing edge jet at α = 13°. With increasing blowing strength, the angle at which the shear layer deflects from the airfoil surface increases.

The x_J/c = 0.60 jet at α = 0° is capable of producing a noticeable change in the flow field even at the smallest flow rate coefficient, C_Q = 0.20%, as shown in Fig. 4.10. The velocity of the flow above the jet intensifies as the flow rate coefficient is increased. Furthermore, the high velocity region close to the leading edge diminishes with flow rate coefficient. However, the velocity in the far field increases, with a larger region being influenced by the increased flow rate coefficient. Immediately aft of the jet, a reduction in velocity magnitude is created, alluding to the initiation of separated flow. The subsequent result on the lift curve, shown in Fig. 4.3b, is minimal, with the C_Q = 0.20% & 0.44% jets producing a change of ΔC_L = -0.02 and ΔC_L = -0.06, respectively.

Increasing the angle of attack to α = 5° and an increase in flow rate coefficient continues to reduce velocity magnitude to a greater extent near the leading edge region. The separated shear layer downstream of the jet becomes distinct when blowing with C_Q = 0.20% & 0.35%, with the size of the wake augmenting with increased flow rate coefficient. However, a flow rate coefficient of C_Q = 0.44% initiates the separation upstream of the jet, subsequently enlarging the separated region. Upstream of the accelerated flow caused by the jet, a confined region of significantly reduced velocity magnitude is observed. The reducing effect becomes stronger with flow rate coefficient. Despite the formation of separation, the C_Q = 0.20% jet maintains a negligible effect in lift reduction to the jet at α = 0°, ΔC_L = -0.02. Lift is mitigated by 19.2% with a flow rate coefficient of C_Q = 0.44%.

Similar behaviour to the cases of α = 5° is observed for α = 8°. All three flow rate coefficients are strong enough to induce a separated shear layer on the upper surface. Ostensibly, C_Q = 0.35% is able to provoke separation upstream of the jet. Extent of separated region is enhanced as the flow rate coefficient increases. As separated region increases in size, freestream flow is deflected further from the suction surface. Hence, increasing the effective camber of the airfoil to enhance lift mitigation; lift produced by blowing at C_Q = 0.20%, 0.35% & 0.44% is 3.5%, 12.2% & 16.6% lower than baseline case, respectively. The weakest blowing strength at α = 10° is sufficient enough to provoke a separation region comparable in size to C_Q = 0.44% at α = 8°. An increase in blowing strength displaces the separation point forward.

The baseline case for α = 13° ostensibly exhibits a strong separated region. However, this separated region is enlarged once momentum in the opposing direction is introduced, as the flow is deflected away from the surface of the airfoil. This is surprising given that the jet is submerged completely in the separated region but the effect is clear. Variation in flow rate coefficient produces small change in the flow field. Velocity magnitude in the near field of the jet is seen to augment with flow rate coefficient, suggesting momentum is being transferred within the separated shear layer. However, the region of high velocity near the leading edge is suppressed in comparison to the baseline configuration. It is the behaviour that creates the largest change in lift coefficient, as lift is reduced by 26.7% with a flow rate coefficient of C_Q = 0.44%.

At x_J/c = 0.08, presented in Fig. 4.11, it is interesting to note the difference in flow field with blowing strength observed at α = 0°. Although blowing from this location had no effect on lift at this angle, blowing with a larger flow rate coefficient saw a small separation bubble emerge, which reattaches downstream of the jet. Velocity magnitude reduces in strength ahead of the jet, but intensifies above the jet. A similar trend can be seen at α = 5°, where blowing at C_Q = 0.35% appears to force flow away from the surface. At C_Q = 0.44%, a separation bubble is produced that forms at the jet location and closes at $x/c \approx 0.45$. This leads to a lift reduction of ΔC_L = -0.065 being realised.

A flow rate of C_Q = 0.20% appears to invoke separation which becomes more obvious towards the trailing edge, for α = 8°. At C_Q = 0.35%, the streamlines deflect and return towards the surface, suggesting flow is not fully separated with this flow rate but is enough to incite a change in lift of ΔC_L = -0.082. However, flow is fully detached at the largest flow rate coefficient, as no reattachment point is observed. The jet manages to diminish the high velocity magnitude ahead of the exit, but only increases lift reduction to ΔC_L = -0.115. At α = 10°, the jet causes flow to separate downstream of the mid-chord for a flow rate of C_Q = 0.20%. Fully detached flow is realised from the jet location when increasing to C_Q = 0.35%. Further increasing the jet strength causes the shear layer to displace at a larger angle. All jet strengths manage to deflect the shear layer away at α = 13°.

4.2.2.2 Effect of Varying Upstream Blowing Location

Shown in Figs. 4.12 to 4.14 are time-averaged velocity magnitude data for the baseline case and jet locations x_J/c = 0.08, 0.60 & 0.95 at three flow rate coefficients, C_Q = 0.20%, 0.35% & 0.44%. Upstream blowing induces different behaviour when varying the chordwise position. When positioned at x_J/c = 0.08 & 0.60, the jet incites a significant increase in velocity magnitude near the jet location at α = 0°. Flow emanating from the jet impinges with the oncoming freestream flow. However, flow close to the surface is seen to decelerate aft of the jet. When corroborated with the force measurements in Fig. 4.3, the flow field differences caused by the jet at x_J/c = 0.08 are insufficient to produce a significant change in lift, in comparison to the baseline airfoil. In contrast, the jet at x_J/c = 0.95, no acceleration in flow near the jet is distinguished. As indicated by the streamline deflection, the airfoil experiences an effective increase in camber towards the trailing edge creating an upwash effect.

As the angle of attack increases to α = 5° for x_J/c = 0.08, a separation bubble that extends to $x/c \approx 0.30$ is produced. Streamlines indicate a slight deflection in flow path due to this short separation bubble. Ahead of the jet location, the region of high velocity magnitude reduces significantly. This behaviour is also observed ahead of the jet at x_J/c = 0.60, except the separation extends beyond the trailing edge. Nevertheless, the x_J/c = 0.95 case still creates greater lift reduction, ΔC_L = -0.18 versus ΔC_L = -0.09. This indicates that the lift mitigating effect created by entraining flow from the pressure surface supersedes the lift reduction caused by separation.

At α = 8°, the airfoil is approaching the region in which all three jet positions create similar lift mitigation. The increase in angle of attack at x_J/c = 0.08, causes the separation bubble to burst leaving a recirculation region. The jet continues to reduce velocity magnitude near the leading edge. At x_J/c = 0.60, the jet exhibits behaviour similar to α = 5°, with the separated region slightly enlarged. Although velocity flow fields indicate significant differences in performance for the jets at x_J/c = 0.08, 0.60 and 0.95, the three cases produce similar lift mitigation by $\Delta C_L \approx$ -0.11 to -0.17 with x_J/c = 0.95 still the most effective.

From Fig. 4.14 at α = 13°, for x_J/c = 0.08, the shear layer is displaced upwards at a greater angle which produces a larger wake region. The shear layer deflection which incites a larger separated region is seen to be fundamental in augmenting lift alleviation to ΔC_L = -0.33. The jet at x_J/c = 0.60 and x_J/c = 0.95 produces similar flow fields, which indicate the jet possesses enough momentum to permeate upstream, up to the point of separation, before impinging with the freestream flow. The interaction between the two opposing flows deflects the shear layer at a greater angle, to evoke a larger recirculation region compared to the baseline case. Despite the similarity in flow

fields, the jet at x_J/c = 0.60 produces mitigation in lift by ΔC_L = -0.29 as opposed to the ΔC_L = -0.20 produced by the jet at x_J/c = 0.95. Leading edge locations are now more effective. This figure demonstrates the two contrasting mechanisms for lift reduction. The traditional method of flow entrainment and effective camber, which is more effective at low angles and the trailing edge; and forced separation, which is more effective at high angles and the leading edge. Which mechanism to exploit will depend on the scenario.

4.3 Upstream Blowing Pressure Measurements

4.3.1 Effect of Varying Volumetric Flow Rate Coefficient

Figures 4.15 to 4.17 present coefficient of pressure plots for baseline and upstream blowing at all locations considered, with varying volumetric flow rate coefficient between C_Q = 0.20% to 0.44%. For x_J/c = 0.95, shown in Fig. 4.15, the behaviour is the same at every angle of attack. Increasing the jet strength compels pressure along the entire upper surface to increase, which translates to lift mitigation. This agrees with the force measurements which demonstrated a dependency on jet strength for effective lift reduction. Additionally, it was seen that upstream blowing from near the trailing edge was still effective at stall angle, even with the smallest flow rate coefficient. Pressure plots corroborate this as pressure experiences a small augmentation.

Figure 4.16 presents the respective coefficient of pressure plots for upstream blowing for x_J/c = 0.60. Increasing the flow rate coefficient incites the positive pressure gradient on the upper surface to become more adverse. Consequently, suction is reduced upstream of the jet, although aft of the jet, negative pressure is recovered. The pressure created downstream of the C_Q = 0.20% jet is indifferent to that of the baseline case. However, negative pressure in this region is augmented when utilising a greater flow rate coefficient. For example, at α = 8°, pressure measurements reveal jets of C_Q = 0.35% & 0.44% produce similar suction forces. Upstream blowing with C_Q = 0.35% creates a lift coefficient reduction of 12.2%, however this can be enhanced to 16.6% with a flow rate coefficient of C_Q = 0.44%.

Figure 4.17 illustrates the effect blowing from x_J/c = 0.08 has on surface pressure. It was shown that the jet did not reduce lift at α = 0°, however, examination of the corresponding pressure plot illustrates the jet has an effect on the lower surface pressure. Although increasing the flow rate coefficient sees a reduction in suction on the upper surface, it can be seen that the lower surface pressure also increases in parallel. This ends up being counter-productive as the differential in pressure from both surfaces remains relatively the same when compared to the baseline case. The effect on the lower surface is reversed for higher angles of attack, as increasing jet strength mitigates

lower surface pressure. Furthermore, pressure upstream of the jet also reduces, but pressure is analogous to the baseline case when examining the plots downstream of the jet.

4.3.2 Effect of Varying Jet Location

Coefficient of pressure plots for baseline and upstream blowing at three chordwise locations, with a flow rate coefficient of C_Q = 0.44%, are presented in Figs. 4.18 to 4.20. With the jet at x_J/c = 0.95, pressure along the entire upper surface is increased which ultimately causes reduction in lift. In comparison, the jet at x_J/c = 0.60 decelerates the flow ahead of the jet, where flow emanating from the jet impinges with the oncoming freestream flow. The effect is transposed ahead of the jet, where suction is lost from C_p = -0.16 to 0.34 at x/c = 0.52. Flow accelerates above the jet to subject the airfoil to greater suction, by engendering a peak suction $C_{(p,min)}$ = -0.53 at x/c = 0.67. Therefore, mitigating any lift losses, as this equates to a change in lift coefficient of ΔC_L = -0.06. The acceleration in velocity magnitude immediately downstream of the jet at α = 0°, presented in Fig. 4.14 at x_J/c = 0.08, is corroborated in Fig. 4.20a by the increase in suction when compared to the baseline case. Downstream of the jet, the pressure along the upper surface is increased, but is also increased on the lower surface. This indicates positioning the jet towards the leading edge influences the lower surface pressure.

As the angle is increased to α = 5°, an increase in local pressure coincides with the reduction in velocity magnitude ahead of the jet location, as seen in Figs. 18-20b This behaviour continues to be exhibited at larger angles. Upper surface pressure decreases ahead of the jet at x_J/c = 0.95. The ejected flow from x_J/c = 0.60 jet decelerates flow along the upper surface upstream of the jet, mitigating suction up to the separation point. Aft of the jet, suction is augmented along the surface towards the trailing edge. Interestingly, the jets at x_J/c = 0.60 & 0.95 present analogous pressure data between $0.01 \leq x/c \leq 0.32$. Acceleration of flow near x/c = 0.08 induces greater suction in the region $0.08 \leq x/c \leq 0.20$. An immediate low-pressure wake has been shown to be innate for spanwise jets [94]. The point of maximum suction has displaced from x/c = 0.01 for the baseline case to x/c = 0.10 for jet at x_J/c = 0.08, with peak suction increasing from $C_{(p,min)}$ = - 0.91 to $C_{(p,min)}$ = - 1.30. However, downstream of x/c = 0.20 suction loss is minimal explaining the marginal loss in lift, ΔC_L = -0.07.

Increasing to α = 8°, it is observed upstream of x/c = 0.52, the jet at x_J/c = 0.60 engenders the least suction until the point where flow accelerates ($\approx x/c$ = 0.67) to stimulate a reduction in pressure compared to the baseline case, see Fig. 4.20c. As was shown in Fig. 4.14, the separation bubble, seen in the x_J/c = 0.08 case, bursts when increasing the angle of attack to α = 8°. One would expect the large separated region created by the jet at x_J/c = 0.08 would incite a greater change in lift

in comparison to the jet at x_J/c = 0.95. However, while a suction loss ahead of the jet at x_J/c = 0.08 is presented in Fig. 4.20c, the pressure created beyond x/c = 0.10 by the baseline case is recovered. In contrast, the jet at x_J/c = 0.95 influences the pressure induced along the entire upper surface, thereby explaining the alleviation in lift of ΔC_L = -0.17. This confirms that as long as the jet has enough momentum, it is preferred to place the upstream jet closer to the trailing edge as the ability to influence pressure within a greater area on the suction surface is enhanced.

Inclination of the airfoil to α = 10°, the blowing from the x_J/c = 0.08 jet subjects the lower surface to a reduction in pressure. Due to its close proximity to the leading edge, this suggests upstream blowing is inciting an effect on the lower surface flow. On the contrary, the upper surface experiences an increase in pressure fore of the jet, but pressure recovers downstream of x/c = 0.30. This demonstrates the leading edge jet incites lift mitigation through manipulating flow upstream and on the lower surface, rather than downstream. However, although the x_J/c = 0.60 jet attenuates suction upstream of the jet, it does not have enough momentum to manipulate the lower surface pressure. While the pressure plot for the trailing edge jet maintains an offset from the baseline case. Hence, reducing suction along the entire upper surface.

Further increase in angle of attack to α = 13°, as shown in Fig. 4.20e, the baseline airfoil produces negligible pressure beyond $x/c \geq 0.80$. The constant pressure upstream of jet at x_J/c = 0.95 indicates separation of flow. The difference in lower surface pressure between jets at x_J/c = 0.60 & 0.95 is crucial for effective lift mitigation. Contrary to the trend observed at previous incidences, magnitude of C_p reduces ahead of x_J/c = 0.60 jet to recover an analogous wake to the x_J/c = 0.08 jet. At x_J/c = 0.08, the upper surface pressure reduces significantly in negative pressure due to the severe mitigation in velocity magnitude ahead of the jet. As such, the suction peak at x/c = 0.01 is diminished by the upstream jet. A near constant pressure region is noticed between $0.10 \leq x/c \leq 0.18$; which is indicative of flow separation [176]. In addition, the lower surface experiences a loss in pressure. It follows that, positioning the jet closer to the leading edge has a greater effect on lower surface.

4.4 Effect of Blowing Direction

Time-averaged force measurements shown in Fig. 4.21, compare upstream and normal blowing at maximum volumetric flow rate coefficient with the baseline. Normal blowing appears to work effectively when located near the trailing edge, as shown in Fig. 4.21a. At x_J/c = 0.95, it is able to attain an approximately constant change in lift coefficient of ΔC_L = -0.15 up to stall. This reduction in lift is augmented with upstream blowing by approximately 33%. In addition, upstream blowing continues to have an influence on the lift generated with high incidences. With both methods being

tested with the same volumetric flow coefficient, it can be established that upstream blowing provides greater efficiency and is the preferred method for the purpose of lift mitigation, considering the locations investigated.

As the jet location moves to x_J/c = 0.60, shown in Fig. 4.21b, the normal blowing jet is rendered ineffective at all angles of attack. However, upstream blowing exhibits similar behaviour at high angles of attack, to the jet at x_J/c = 0.08 but the effect is weakened. It is able to alleviate lift at all angles considered.

Normal blowing at x_J/c = 0.08, shown in Fig. 4.21c, has a negligible change on lift coefficient until α = 5°, where lift is appreciated by an average of ΔC_L = 0.06 to α = 11°. Hence, normal blowing provides no lift mitigation capabilities when located near the leading edge. In contrast, efficiency of lift mitigation with upstream blowing appears to be dependent on angle of attack. The peak lift coefficient observed at α = 13° is reduced by 30% with upstream blowing. Alleviation of lift is seen to extend into the post stall region, with the point of stall being delayed to α = 19°.

Time-averaged velocity flow fields are presented in Fig. 4.22 to compare baseline measurements with normal blowing and upstream blowing at x_J/c = 0.95, for the maximum flow coefficient of C_Q = 0.44%. These flow fields are comparable with the force measurements shown in Fig. 4.21. At α = 0°, blowing produces deflection in streamlines near the location of the jet. However, differences between blowing directions are not discernible in the global flow field. Hence, the regions of interest near the trailing edge are analysed with smaller grid sizes in the inset. The baseline airfoil exhibits attached flow along the entire upper surface. However, with normal blowing a separation point is observed at the location of blowing. This generates a separation bubble which extends from the jet location to the trailing edge. Due to this separated region, the streamlines external to the bubble are deflected upwards, causing an upwash effect. The normal jet is capable of entraining flow from the pressure surface, particularly when located near the trailing edge. Due to such close proximity to the lower surface, the normal jet is able to modify the Kutta condition, and hence the circulation of the airfoil [72]. Within the recirculation region, two counter-rotating vortices are produced. Similar flow field behaviour for a normal jet flap at x_J/c = 0.95 on the pressure surface has been observed by Blaylock *et al.* [72].

The point of separation for upstream blowing occurs outside the region of interest, indicating a larger separated region is formed in comparison to normal blowing. Therefore, the large region of influence produced by upstream blowing, is able to affect the upper surface pressure gradient and increase the camber to a greater extent. This effect contributes to understanding the difference

observed in force measurements; upstream blowing jet reduces lift greater than normal jet by $\Delta C_L \approx$ -0.06.

Increasing the angle of attack to α = 5°, increases velocity magnitude near the leading edge. When employing the either of the two blowing methods, a reduction in this velocity magnitude is observed, alluding to an alteration in the pressure gradient. Normal and upstream blowing maintain ability to increase the effective camber of the airfoil, as flow continues to be diverted away from the surface of the airfoil. The change in lift coefficient for normal blowing reduces in comparison to the α = 0° case, with a change in lift coefficient of ΔC_L = -0.11 realized. Regardless of deflection angle, the trailing edge region is seen to suffer a loss in velocity magnitude. The change in lift coefficient for upstream blowing jet is ΔC_L = - 0.18.

At α = 8°, high velocity magnitude regions near the leading edge for both deflection angles are not as intense as presented in the baseline. This suggests the jet flap consistently affects the adverse pressure gradient irrespective of angle of attack. The camber effect begins to diminishes for normal blowing as the change in lift coefficient reduces to ΔC_L = - 0.09. In comparison to the α = 5° case, flow separates earlier with upstream blowing correlating with the lift coefficient change of ΔC_L = - 0.17.

Flow separation initiates near the leading edge of the airfoil for all cases investigated at α = 13°. The increase in velocity magnitude local to the jet location indicates the normal blowing jet injects momentum into separated region. The inset figure shows that the normal jet continues to divert flow away from the surface of the airfoil. This behaviour is conducive to the change in lift of ΔC_L = - 0.12. The momentum injected tangentially along the surface with upstream blowing, impinges the freestream velocity to deflect flow upwards, thereby enlarging the separated region to create a large recirculation zone. This behaviour agrees with the force measurements observed in Fig. 4.21, as a change in lift of ΔC_L = - 0.20 confirms upstream blowing retains a relatively constant change in lift across the linear region of the lift curve. Due to the greater effectiveness of upstream blowing across the board, it shall be the subject of further investigation.

The force and PIV measurements in this chapter have clearly shown blowing perpendicular to the airfoil surface is not the most effective blowing direction, if the purpose is to deflect the flow near the trailing edge region. It is the significance in flow deflection which determines the lift reduction capability. For typical momentum coefficients used for flow control (on the order of 10^{-2}) and blowing slot width ratio h_J/c (on the order of 10^{-2}), the magnitude of the jet velocity is on the order of the freestream velocity. Hence, for the jet velocity ratio around unity, sufficient deflection of the flow may not be achievable. If the jets in crossflow [177] are considered to find a rough estimate, the jet trajectory (defined as the time-averaged streamline originating at the jet exit) reaches

an asymptotic distance of 2 to 4 jet exit width h_J from the wall for U_J/U_∞ = 1 to 2. In contrast, counter flowing wall jets can provide larger deflections. The time-averaged dividing streamline (originating from the stagnation point on the wall) can reach an asymptotic distance of 7 to 15 jet exit width h_J from the wall [178] for U_J/U_∞ = 1 to 2. Certainly, this behaviour is evident in the PIV data collected in this chapter, and is clearly interpreted in the sketch shown in Figs. 4.23 & 4.24. In Figs. 4.23 & 4.24, contour maps are presented to show the change in lift coefficient with varying chordwise location and angle of attack, for a maximum volumetric flow rate. Interpretative sketches are drawn for a varying angle of attack. For normal blowing, the greatest change in lift was observed for x_J/c = 0.95. This was the only location to see full separated flow. When the jet is placed upstream, it fails to induce a complete separation and flow reattaches. It is likely that the increased lift observed with normal blowing at x_J/c = 0.08 is due to a positive change in effective camber. At α = 10°, upstream blowing for all locations produces a similar change in lift coefficient. Separation occurs within all three sketches. Freestream flow collides with flow from upstream blowing to produce a stagnation point. Upstream blowing air forces the freestream flow to be diverted away from the surface of the airfoil.

4.5 Conclusions

Time averaged force, flowfield and pressure measurements were completed for the steady jet flap. The jet flap was configured to be tested for two deflection angles; normal blowing and upstream blowing. Normal blowing is found to diminish in effect as the jet is displaced away from the trailing edge. As it reaches the leading edge location, lift is seen to increase at higher angles of attack. Within the post-stall region, the influence normal blowing has on force becomes ineffective. However, for a given flow rate coefficient, the upstream blowing jet at x_J/c = 0.95 is capable of further reducing lift by 33% over normal blowing. Unlike normal blowing, upstream blowing maintains an effect on lift with upstream locations. When placing the jet at x_J/c = 0.08 or 0.60, lift reduces further with angle of attack. Lift is further reduced with blowing strength. This relationship is summarised by the theory of Spence, as force measurements show to corroborate this for both deflection angles. Comparison of both deflection angles with flowfield measurements at x_J/c = 0.95, show that each blowing method reduces lift using a different mechanism. For normal blowing, flow is entrained from the lower surface to realise a change in the Kutta condition, while upstream blowing achieves flow reduction by deflecting the shear layer further away from the surface. These measurements indicate that upstream blowing is far more effective for lift mitigation purposes, hence, will be the focus of dynamic measurements in the following chapters.

4.6 Figures

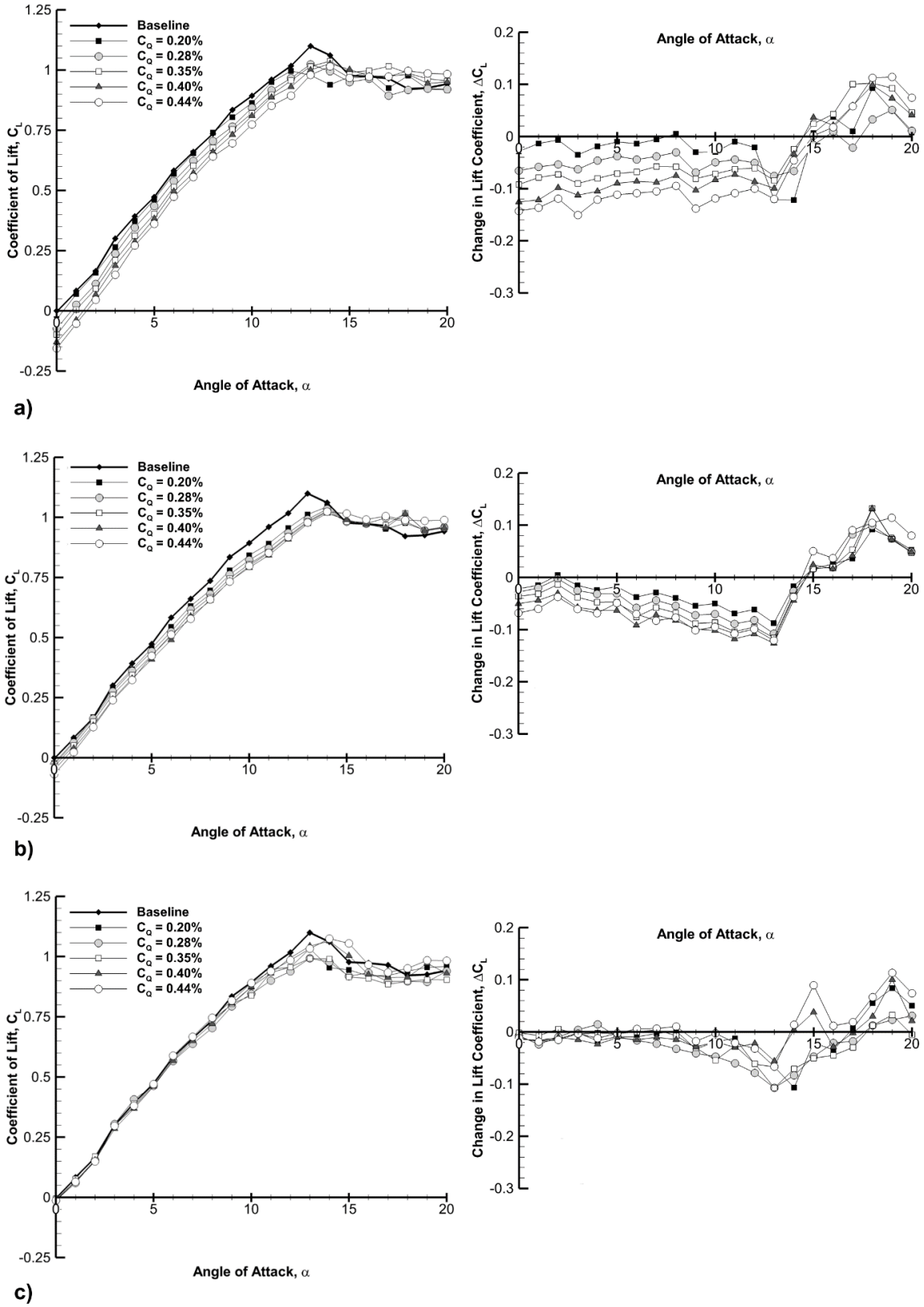

Figure 4.1 - Time-averaged lift coefficient, for normal blowing, showing the effect varying flow rate coefficient a) at x_J/c = 0.95; b) at x_J/c = 0.85; c) at x_J/c = 0.75.

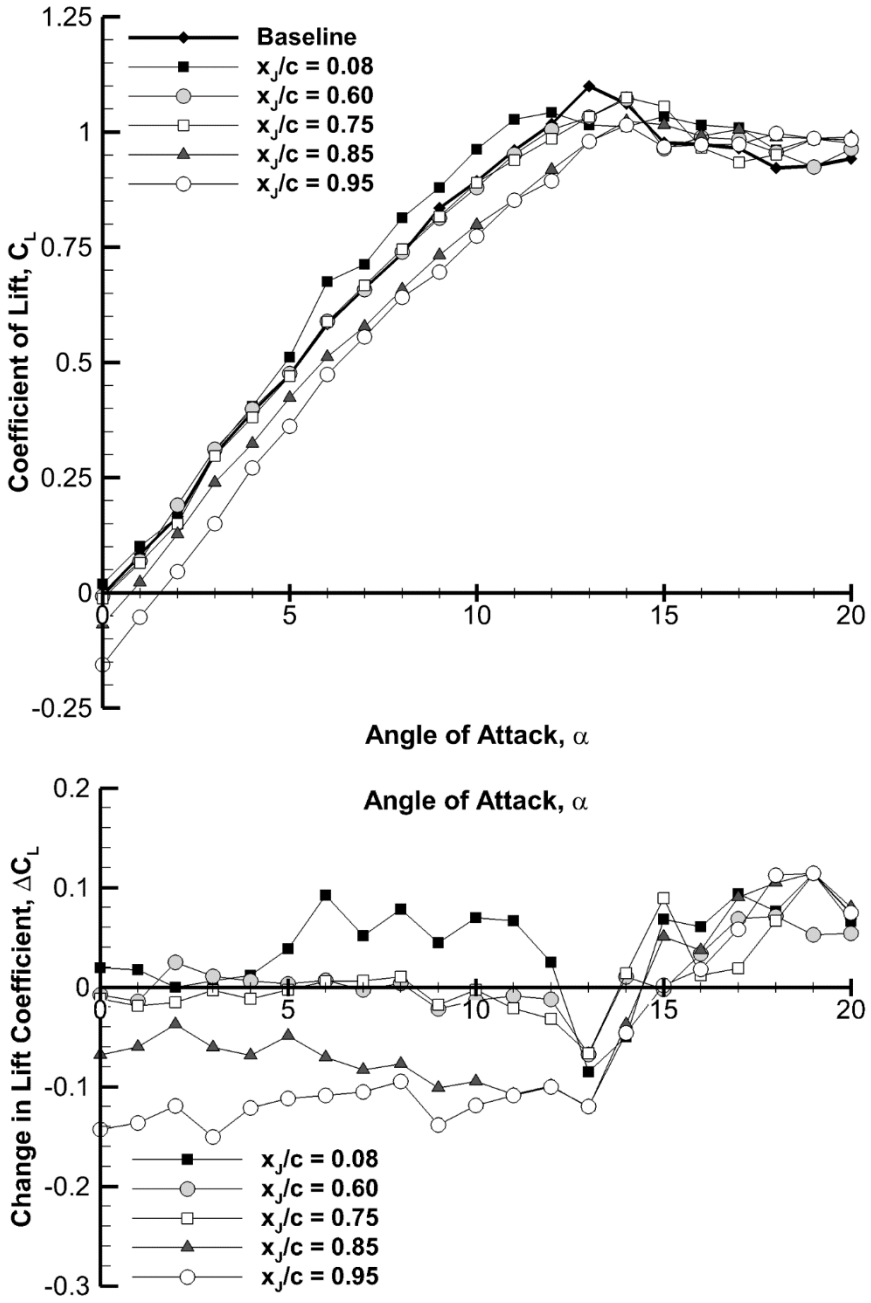

Figure 4.2 - Effect of varying chordwise location for normal blowing at C_Q = 0.44%.

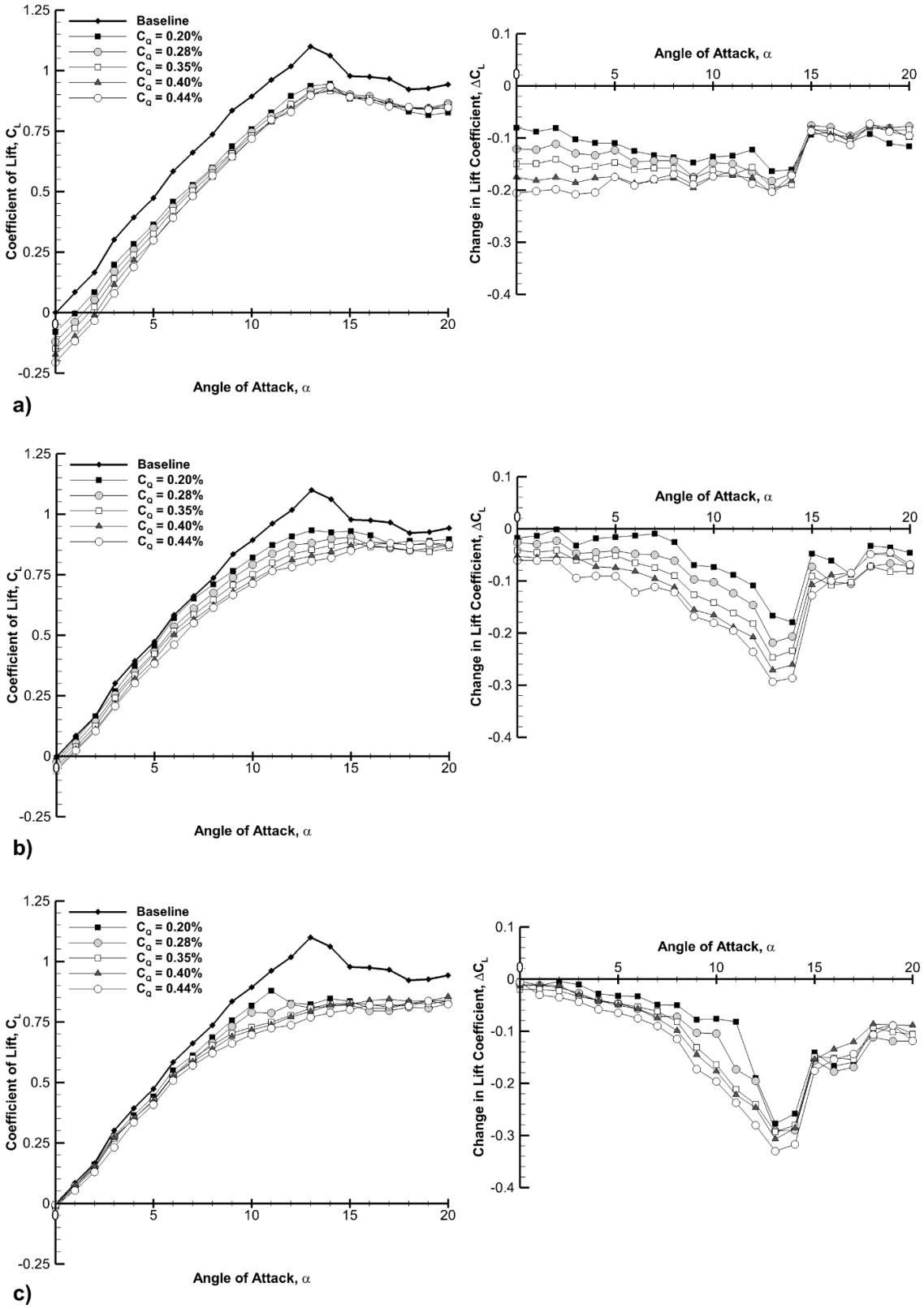

Figure 4.3 - Time-averaged lift coefficient, for upstream blowing, showing the effect varying flow rate coefficient a) at x_J/c = 0.95; b) at x_J/c = 0.60; c) at x_J/c = 0.08.

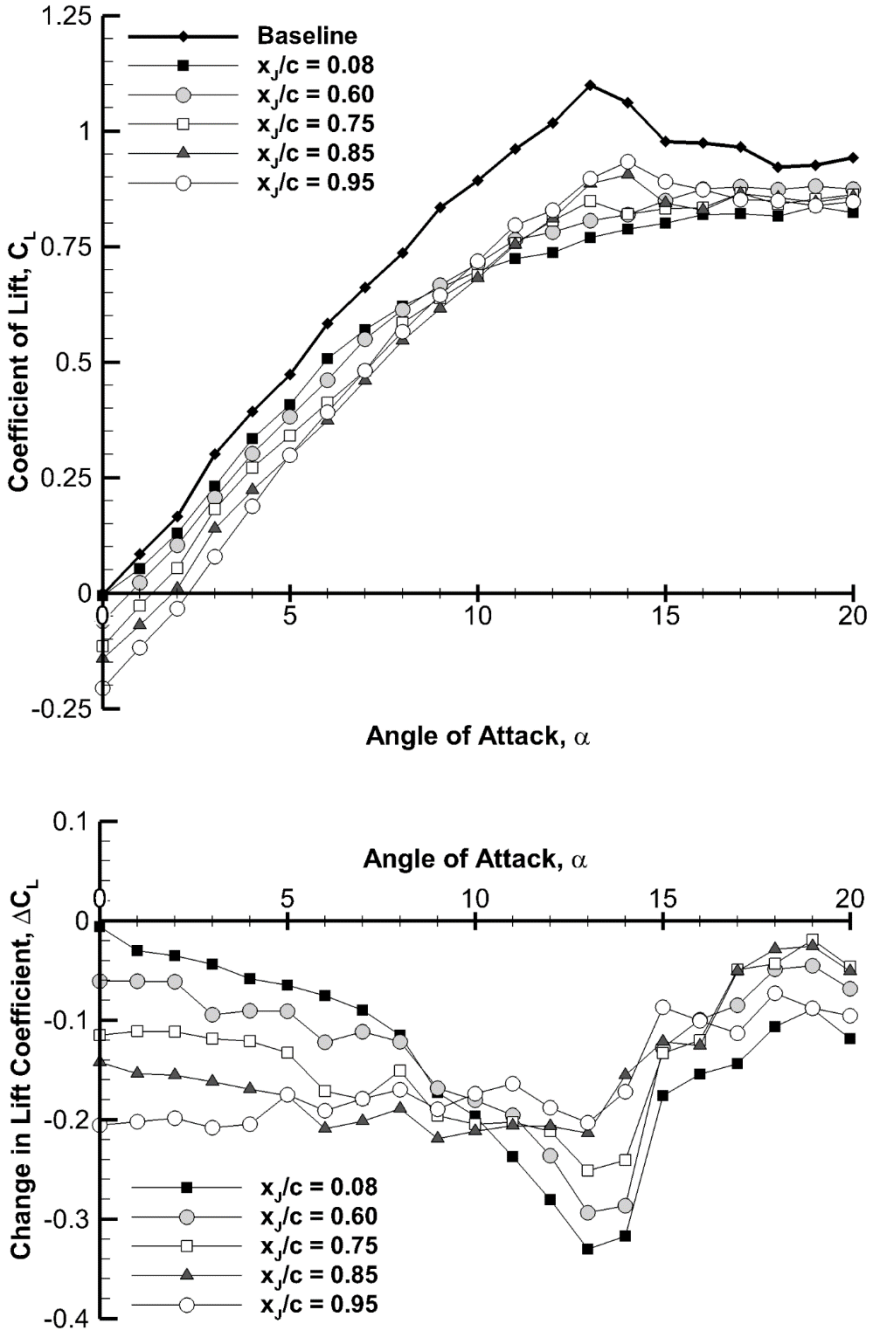

Figure 4.4 - Effect of varying chordwise location for upstream blowing at C_Q = 0.44%.

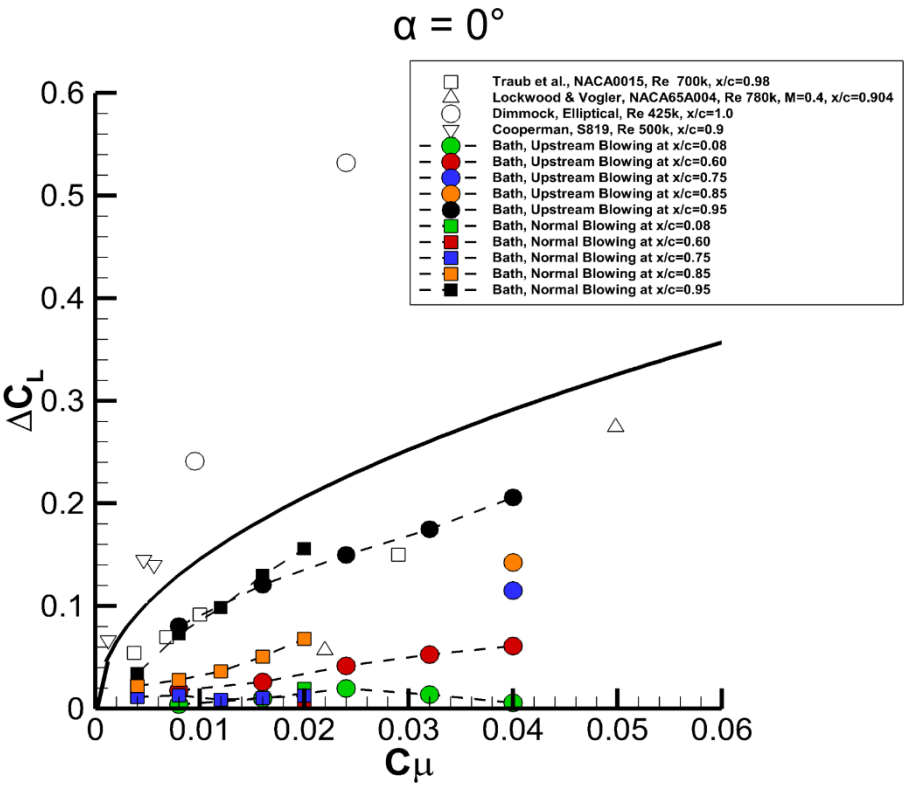

a)

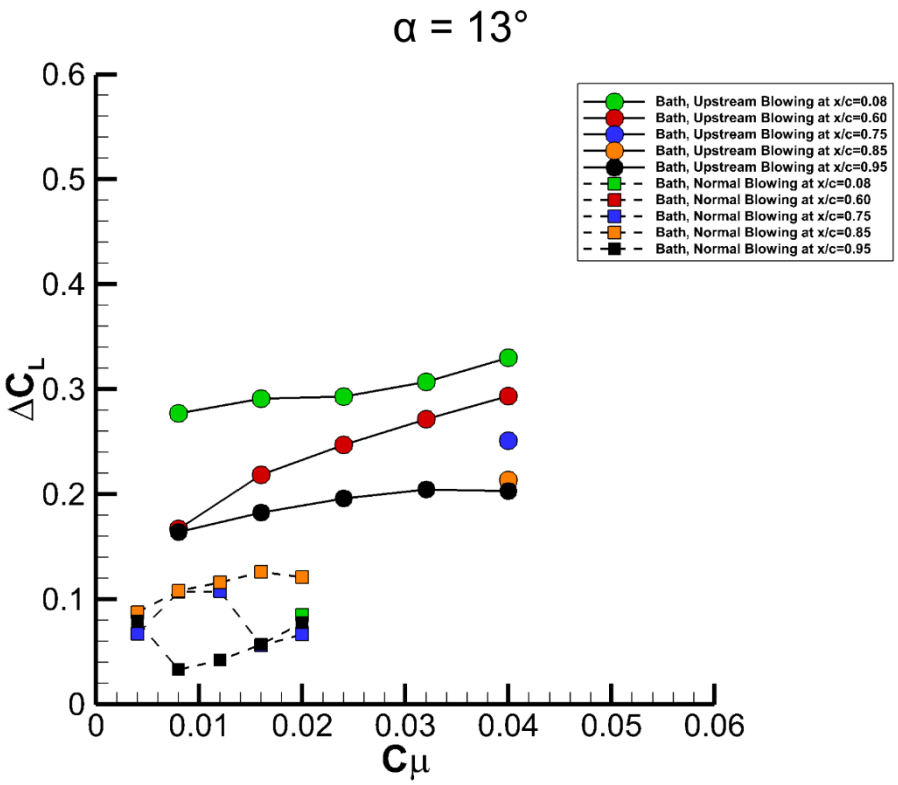

b)

Figure 4.5 - a) Experimental validation with data from the literature for α = 0° and b) α = 13°.

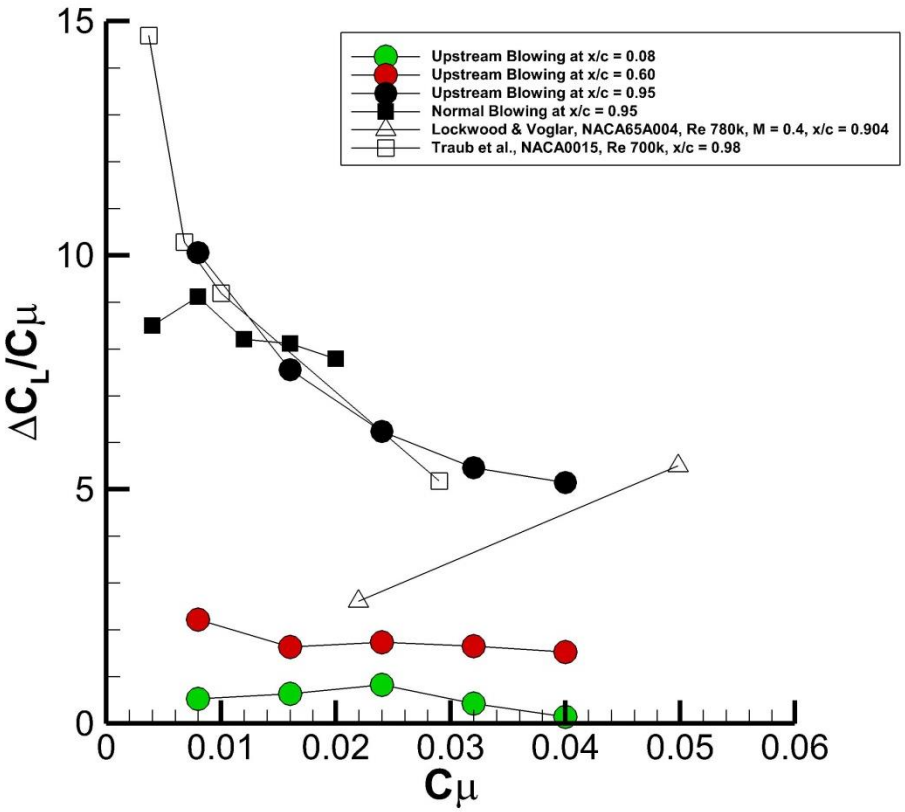

Figure 4.6 – Comparison of aerodynamic gain ($\Delta C_L/C_\mu$) with jet location and deflection angle for $\alpha = 0°$.

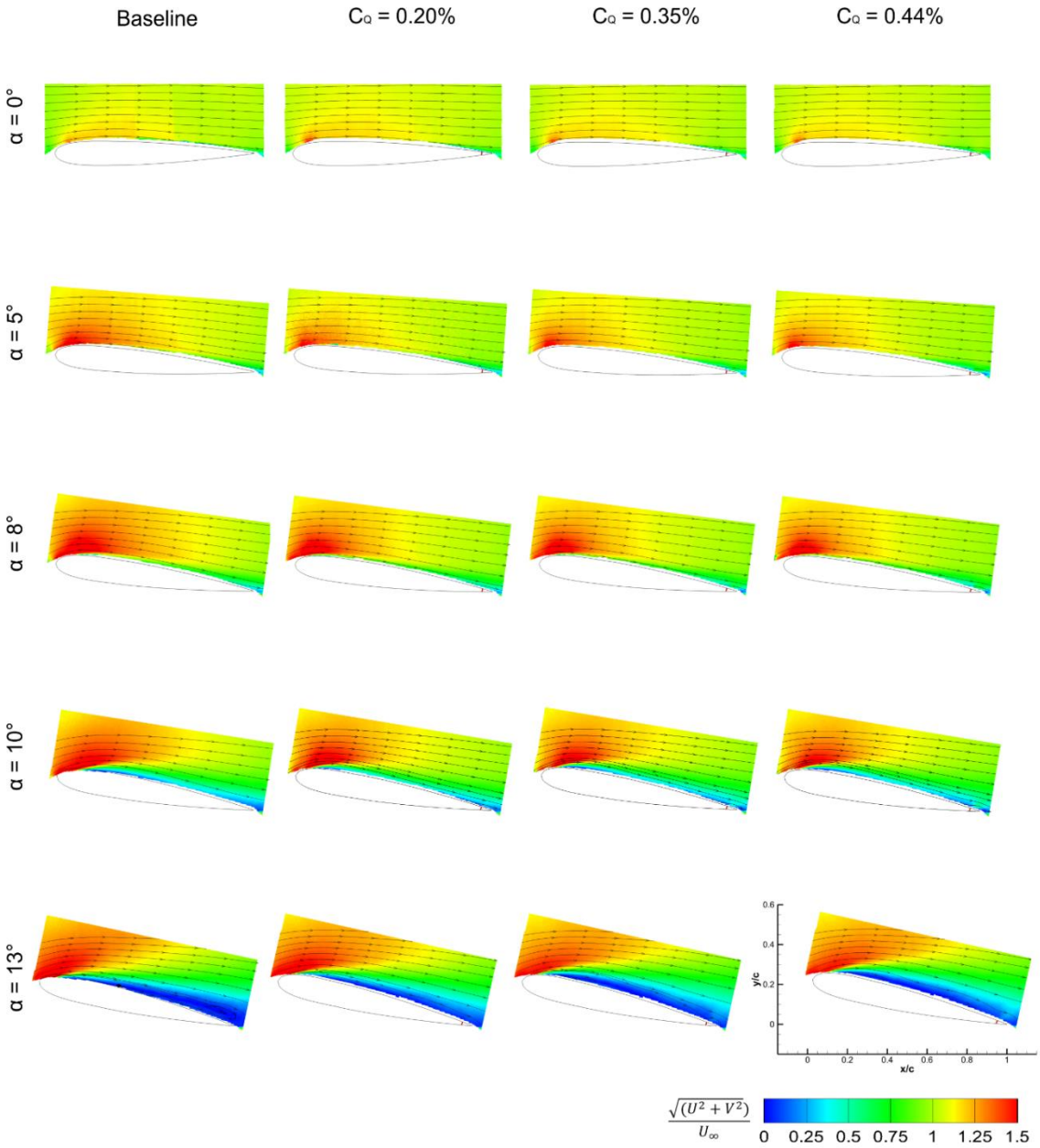

Figure 4.7 - Time-averaged velocity fields for normal blowing for x_J/c = 0.95, C_Q= 0.20%, 0.35% & 0.44% and α = 0°, 5°, 8°, 10° & 13°.

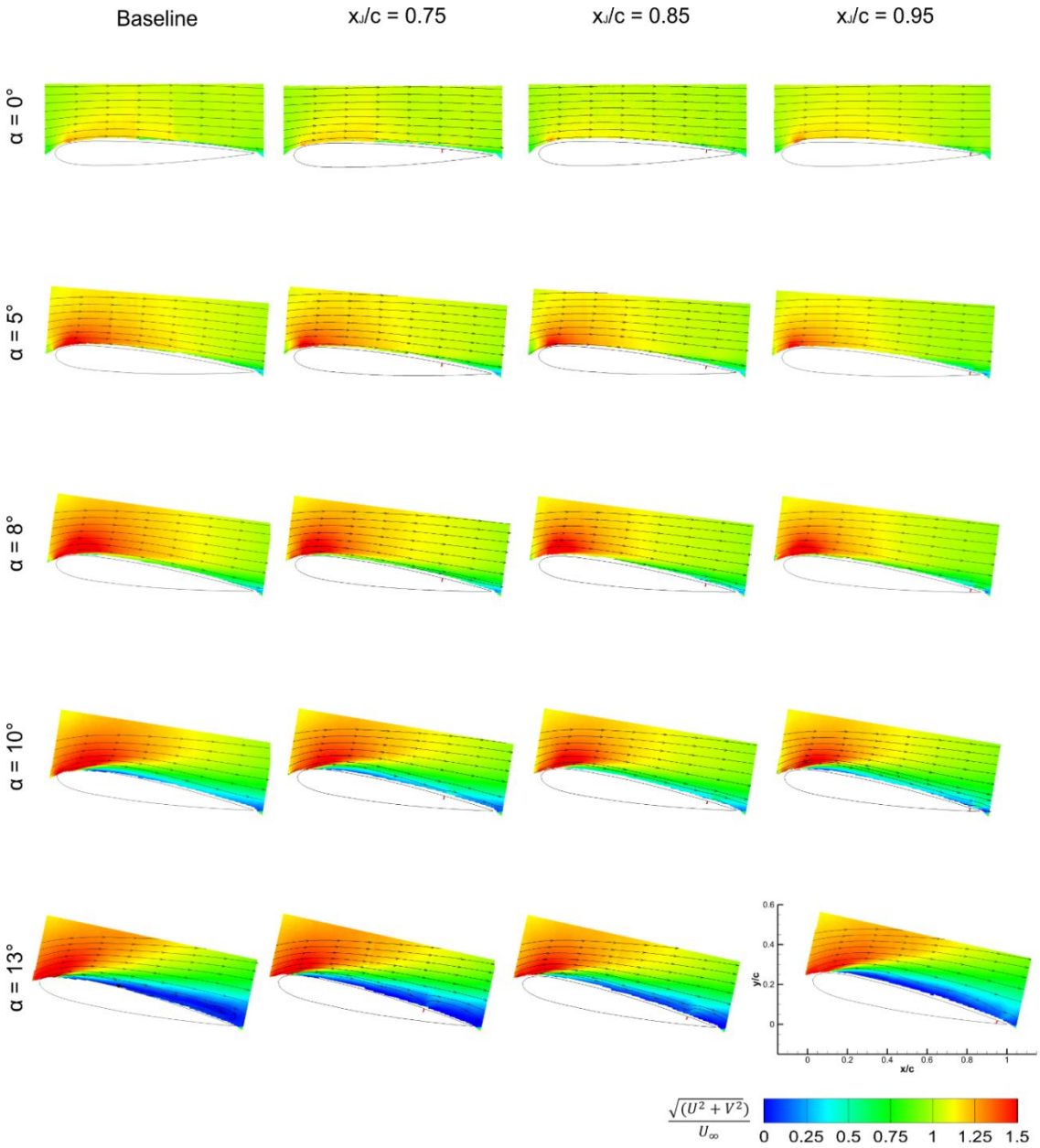

Figure 4.8 - Time-averaged velocity fields for normal blowing for x_J/c = 0.75, 0.85 & 0.95, C_Q = 0.44% and α = 0°, 5°, 8°, 10° & 13°.

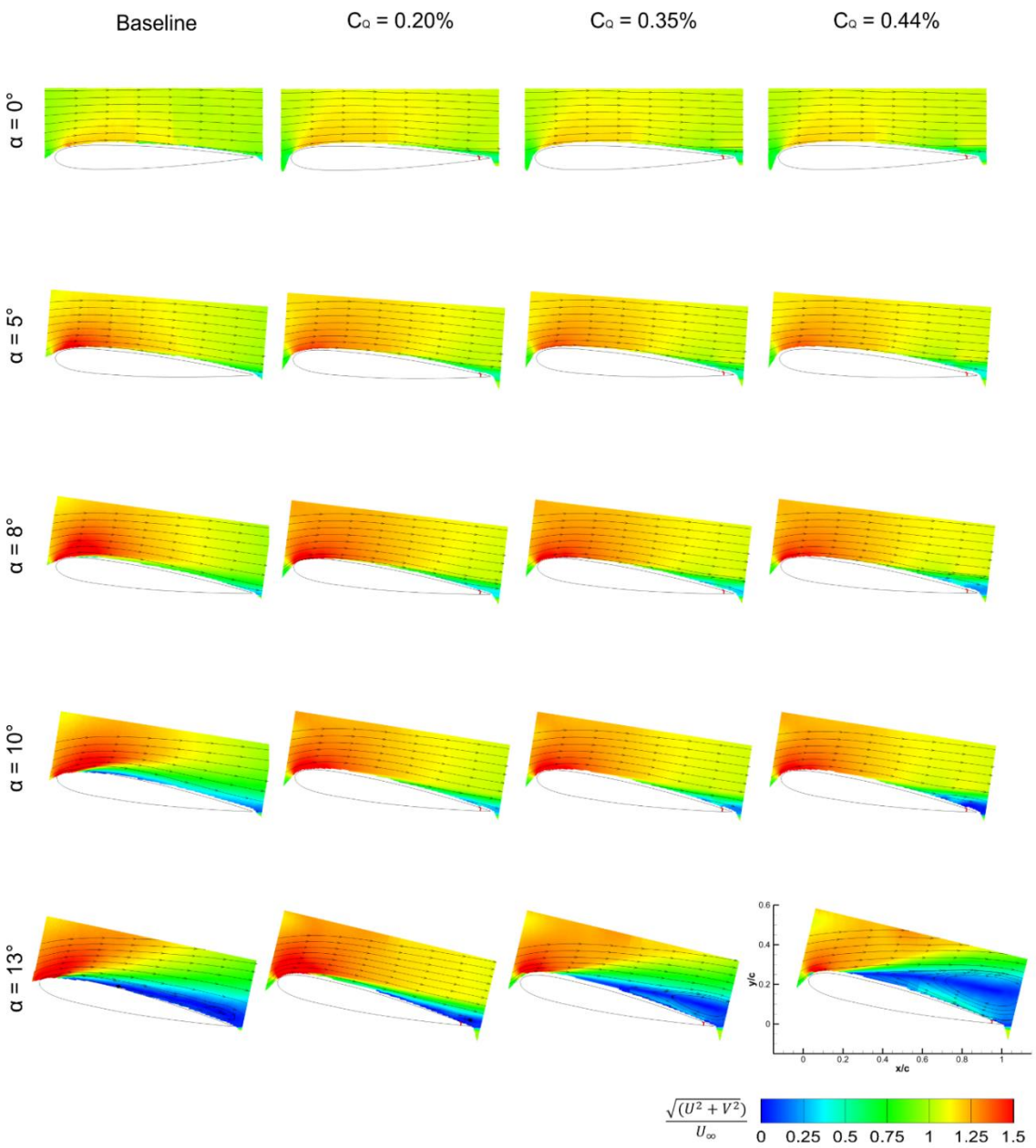

Figure 4.9 - Time-averaged velocity fields for upstream blowing for x_J/c = 0.95, C_Q= 0.20%, 0.35% & 0.44% and α = 0°, 5°, 8°, 10° & 13°.

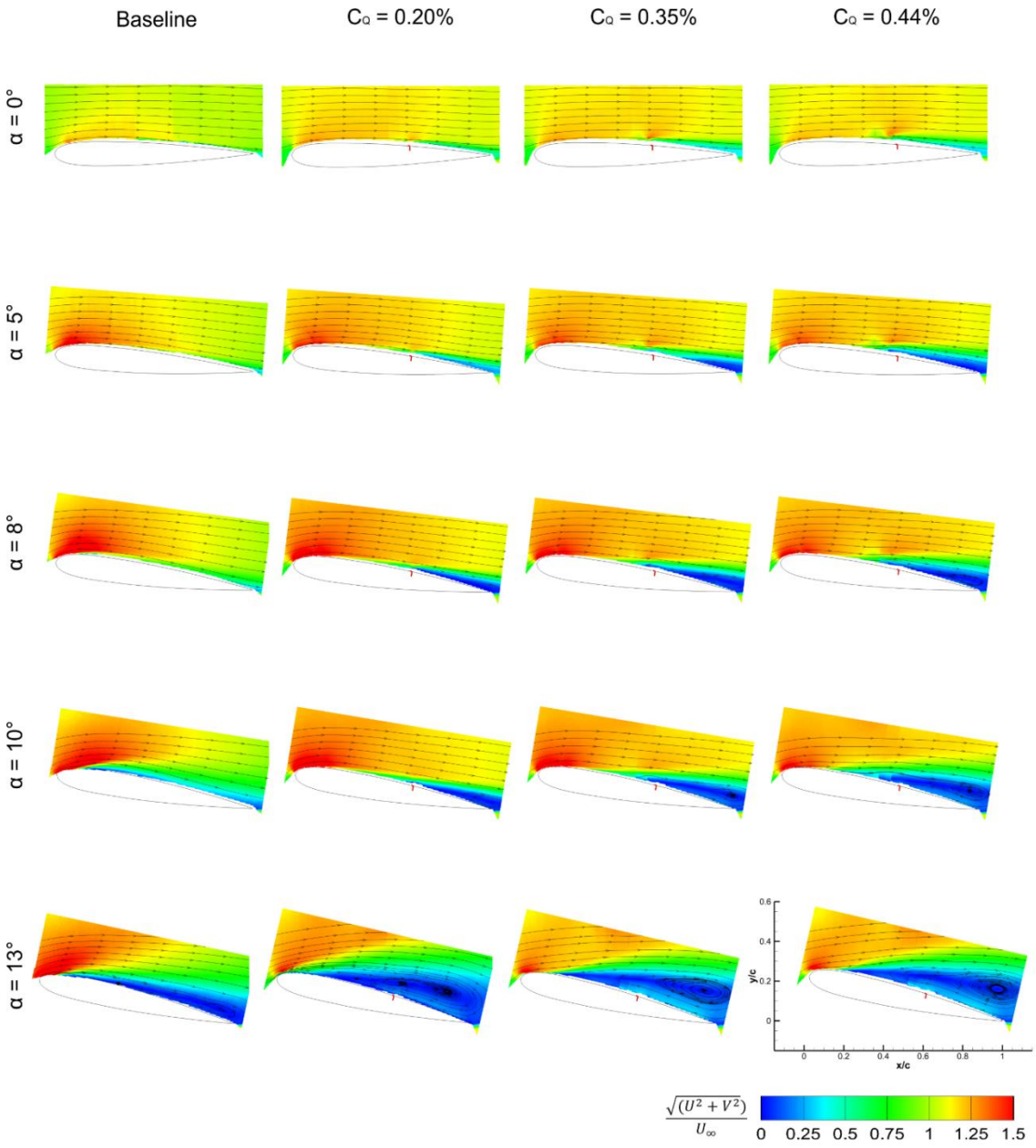

Figure 4.10- Time-averaged velocity fields for upstream blowing for x_J/c = 0.60, C_Q= 0.20%, 0.35% & 0.44% and α = 0°, 5°, 8°, 10° & 13°.

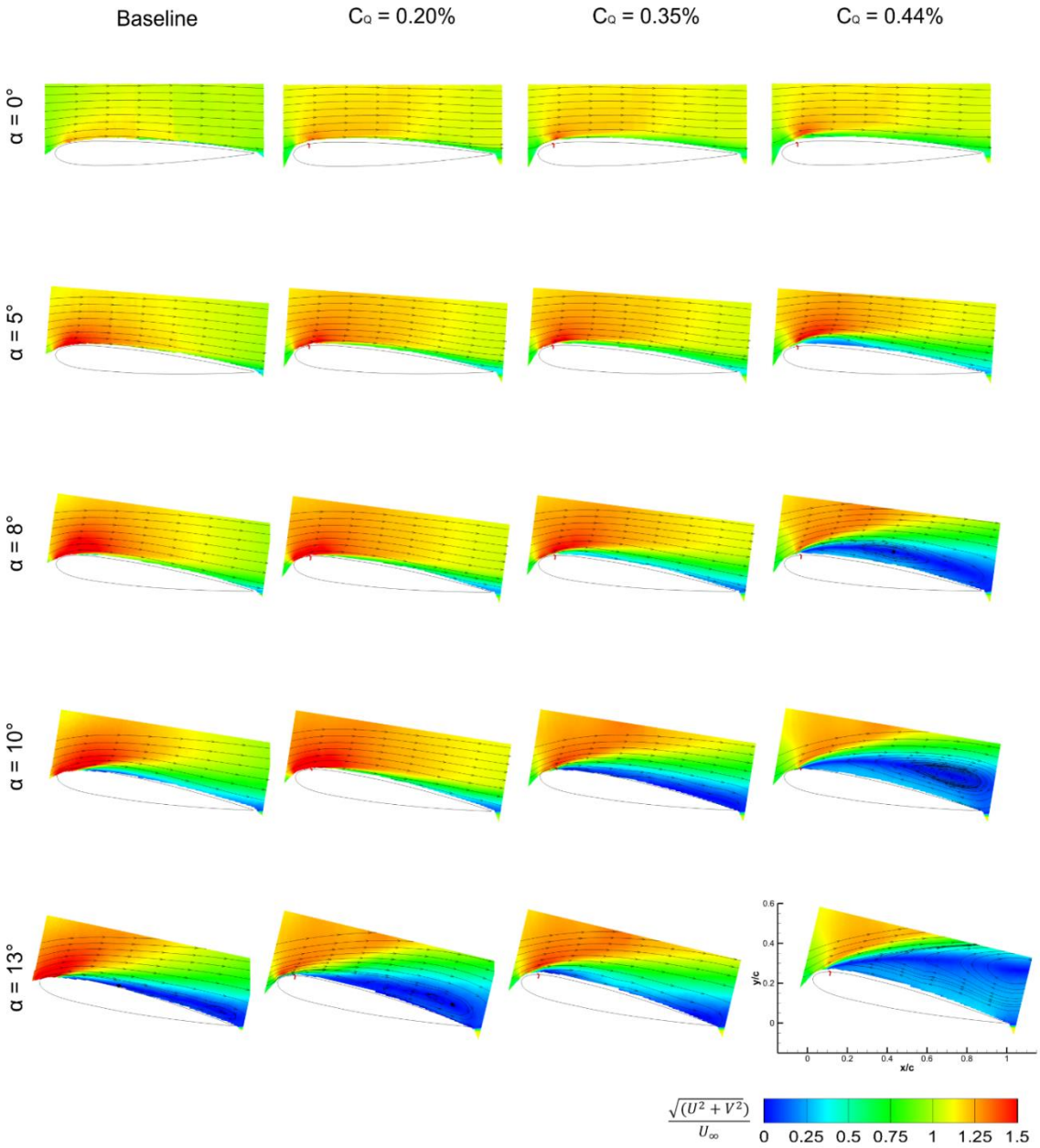

Figure 4.11- Time-averaged velocity fields for upstream blowing for x_J/c = 0.08, C_Q= 0.20%, 0.35% & 0.44% and α = 0°, 5°, 8°, 10° & 13°.

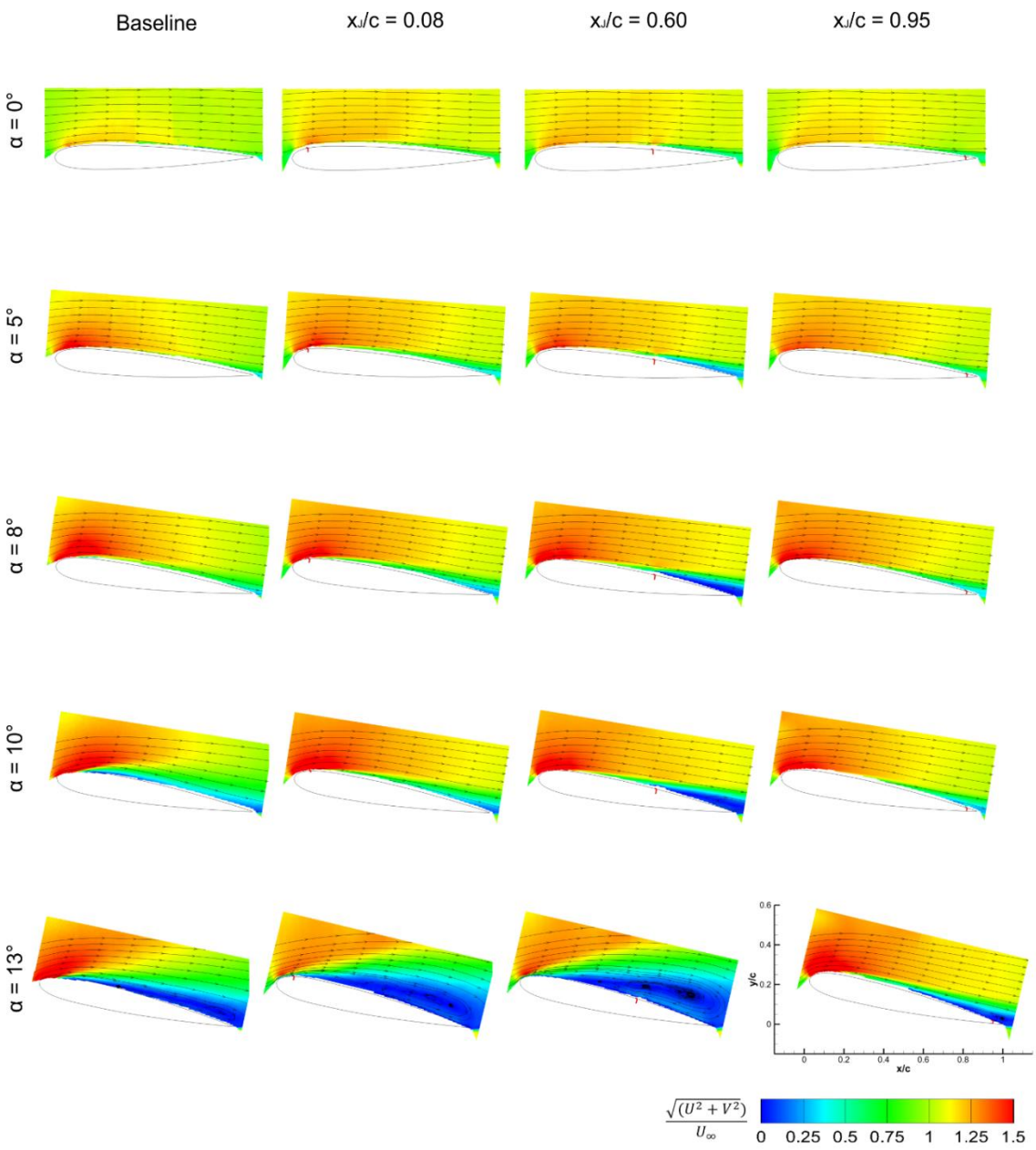

Figure 4.12- Time-averaged velocity fields for upstream blowing for x_J/c = 0.08, 0.60 & 0.95, C_Q = 0.20% and α = 0°, 5°, 8°, 10° & 13°.

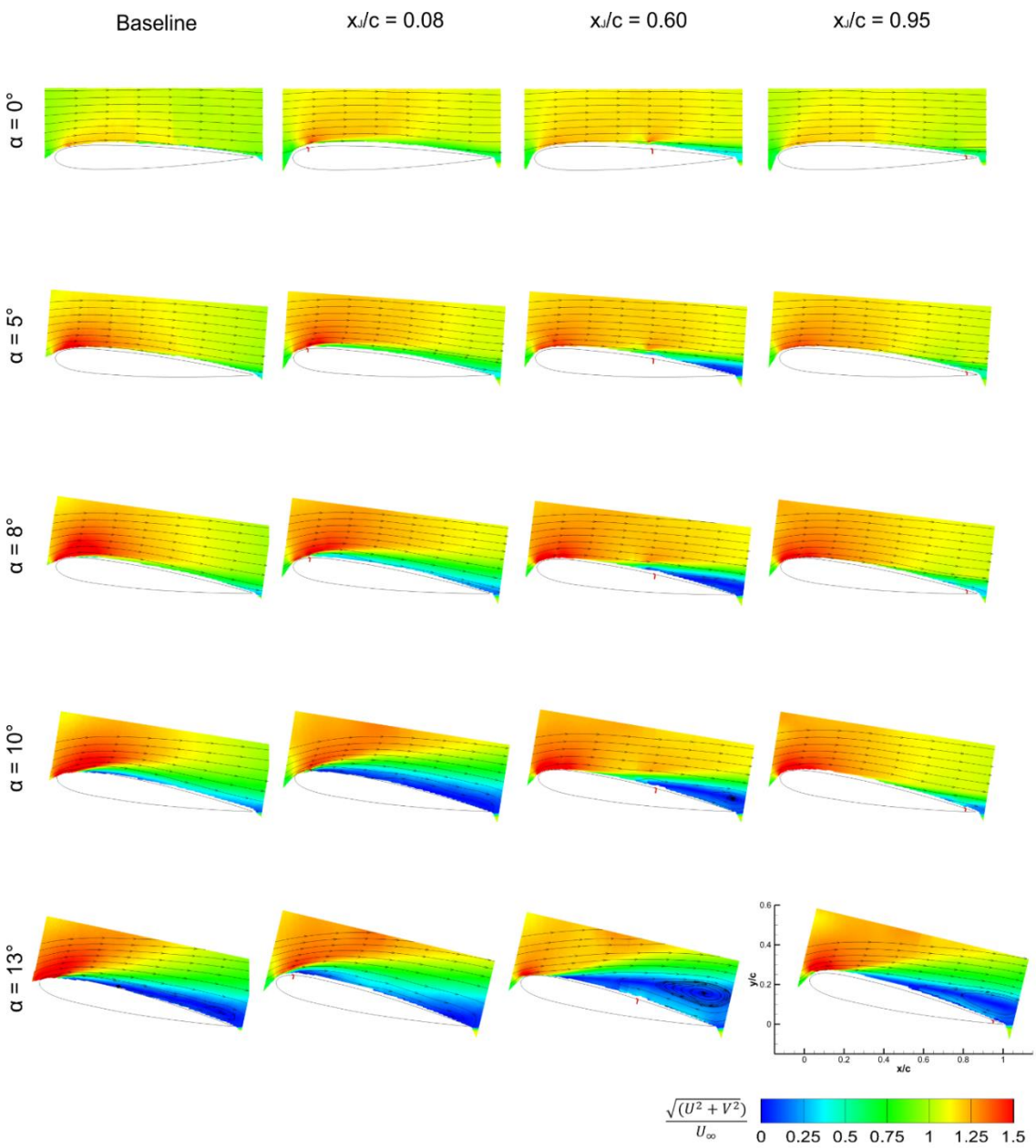

Figure 4.13 - Time-averaged velocity fields for upstream blowing for x_J/c = 0.08, 0.60 & 0.95, C_Q = 0.35% and α = 0°, 5°, 8°, 10° & 13°.

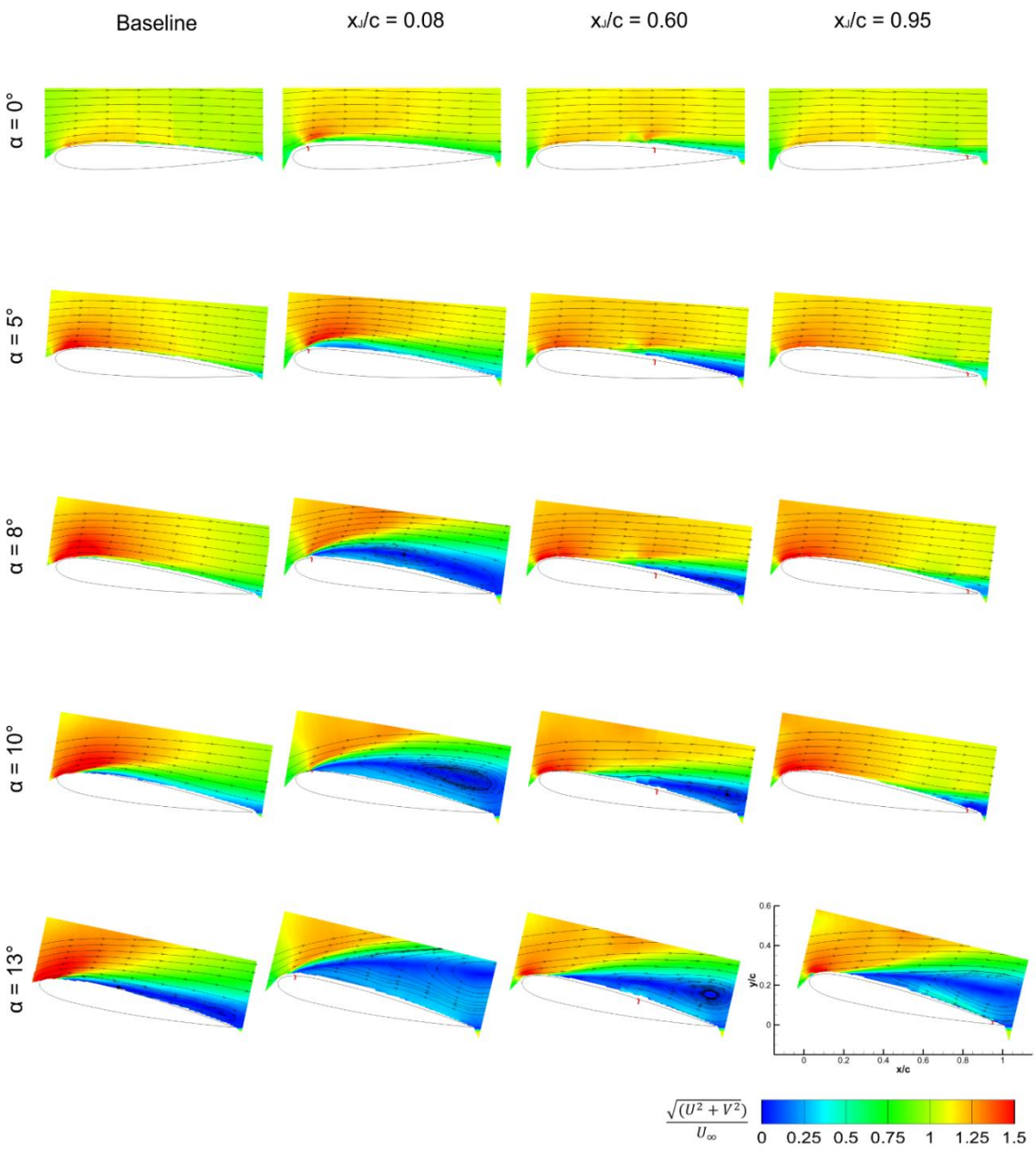

Figure 4.14 - Time-averaged velocity fields for upstream blowing for x_J/c = 0.08, 0.60 & 0.95, C_Q = 0.44% and α = 0°, 5°, 8°, 10° & 13°.

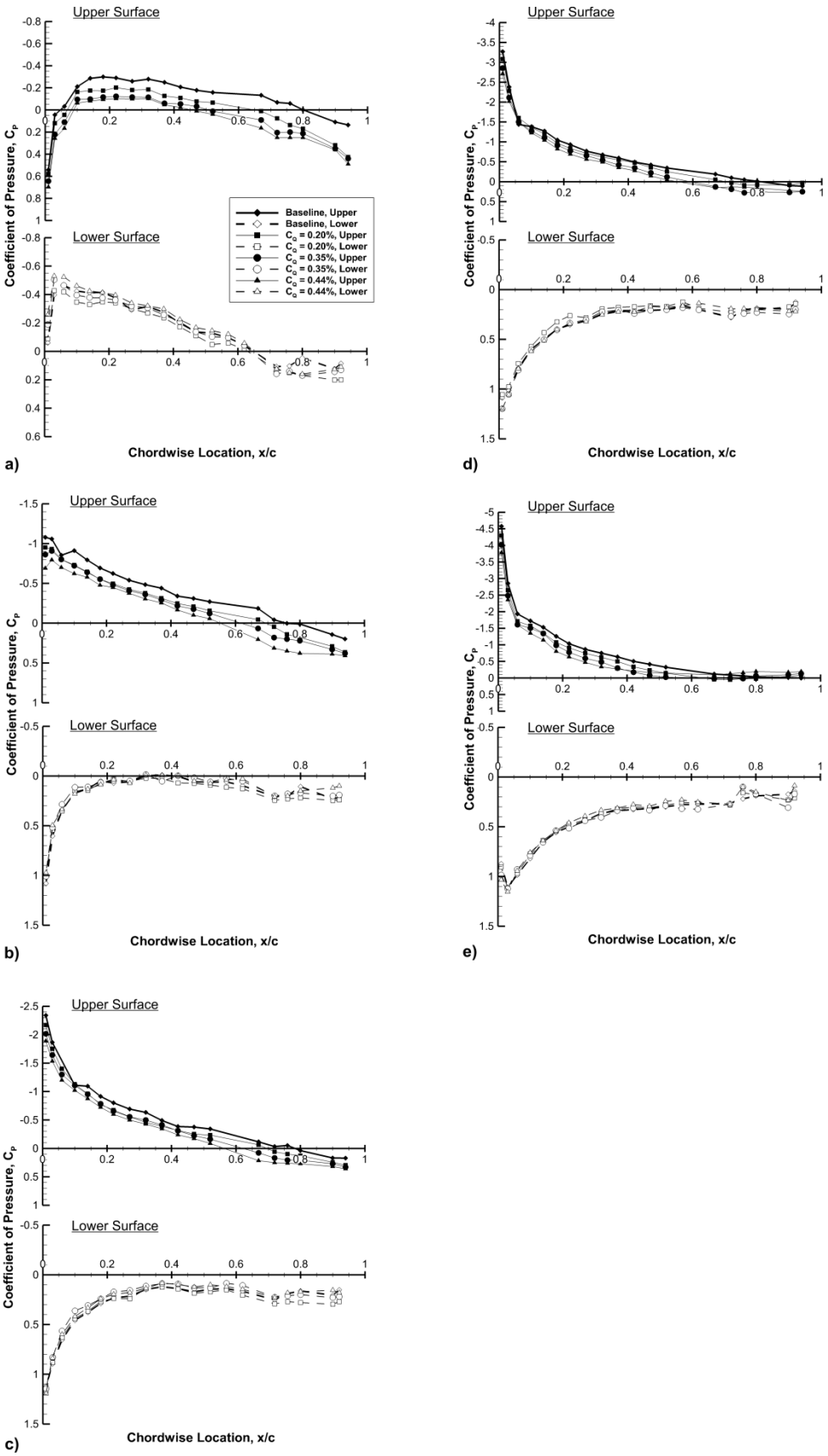

Figure 4.15 - Coefficient of pressure for upstream blowing for C_Q = 0.20%, 0.35% & 0.44%, x_J/c = 0.95 at: a) α = 0°; b) α = 5°; c) α = 8°; d) α = 10°; e) α = 13°.

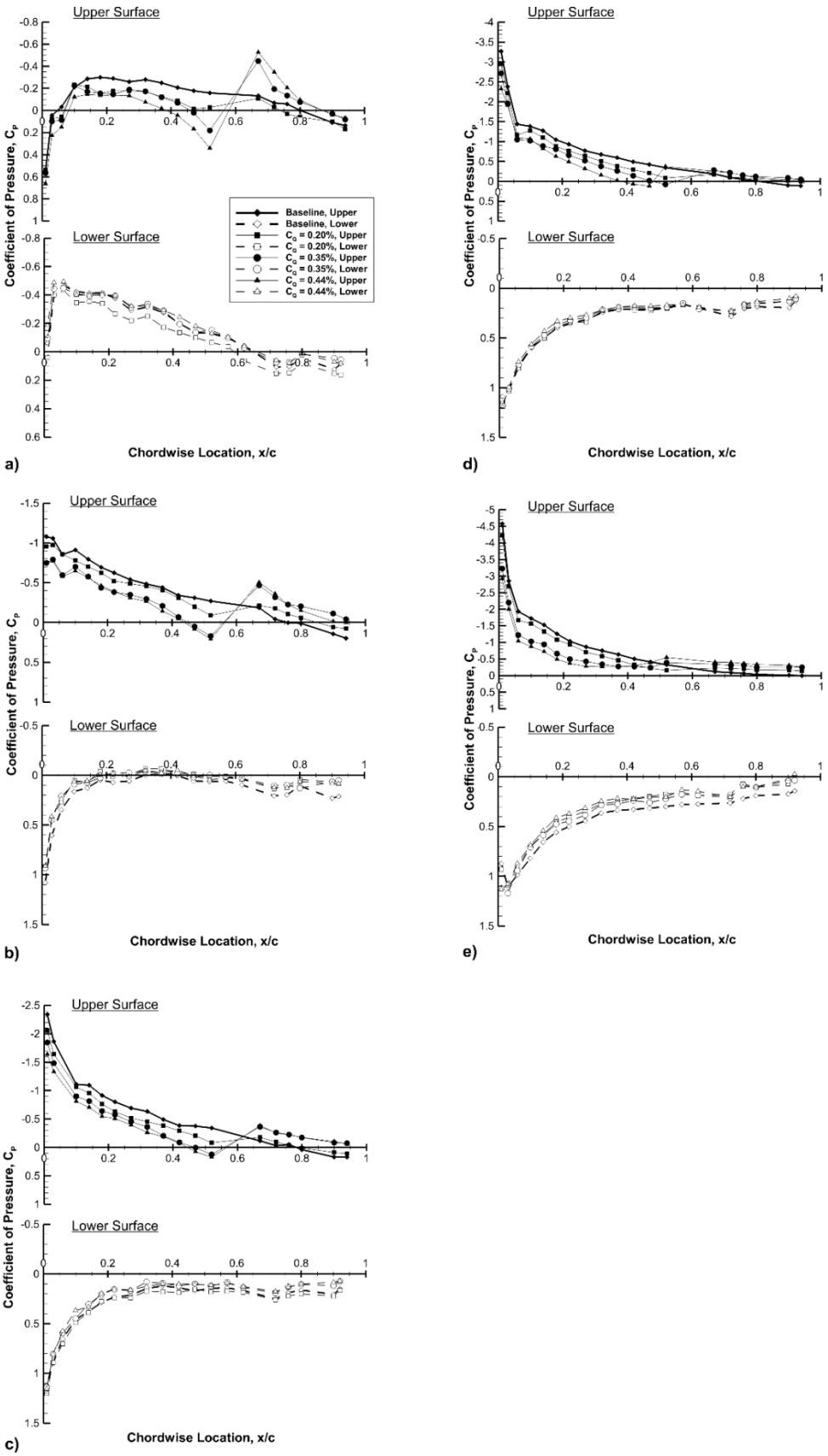

Figure 4.16 - Coefficient of pressure for upstream blowing for C_Q = 0.20%, 0.35% & 0.44%, x_J/c = 0.60 at: a) α = 0°; b) α = 5°; c) α = 8°; d) α = 10°; e) α = 13°.

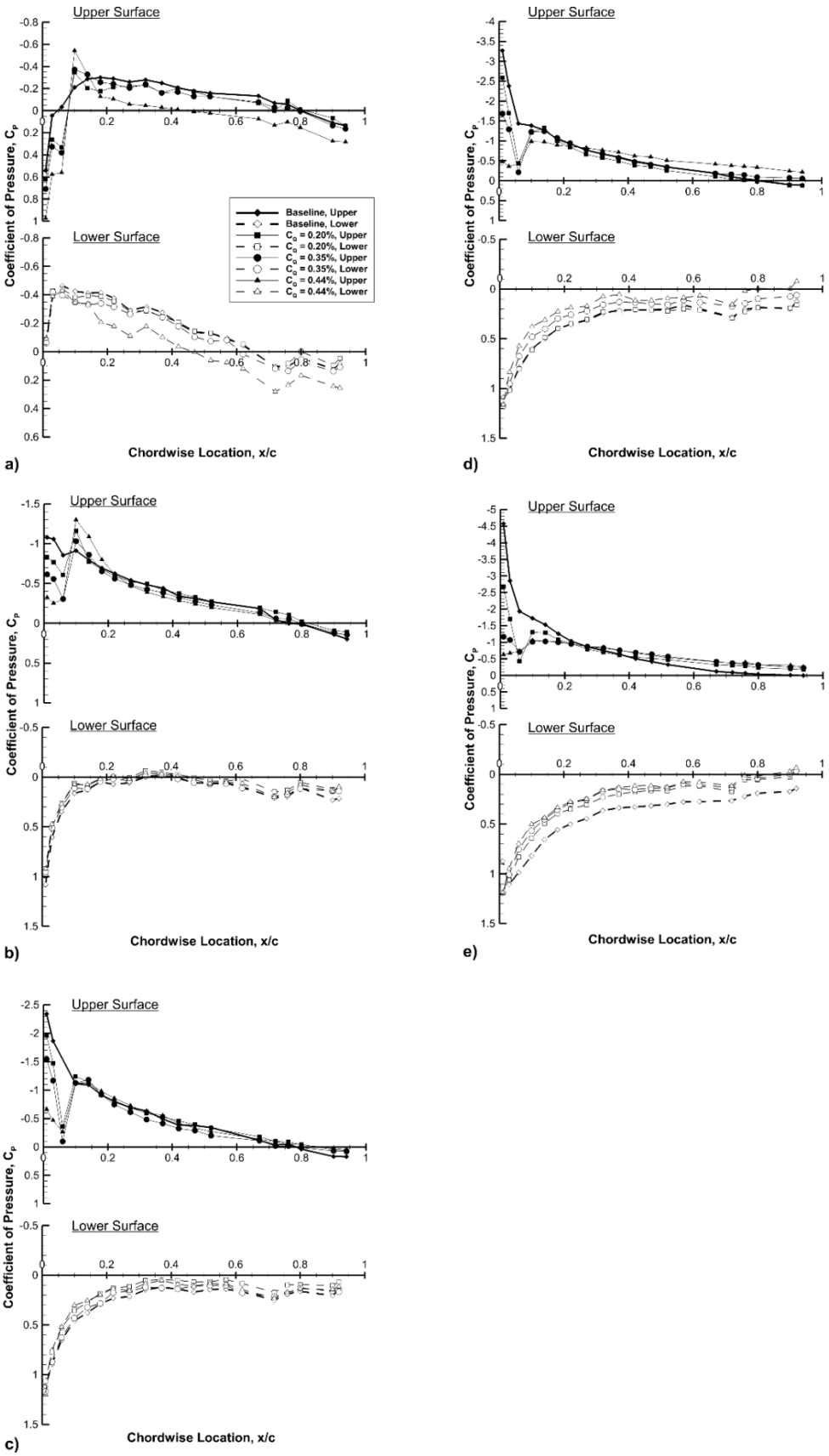

Figure 4.17 - Coefficient of pressure for upstream blowing for C_Q = 0.20%, 0.35% & 0.44%, x_J/c = 0.08 at: a) α = 0°; b) α = 5°; c) α = 8°; d) α = 10°; e) α = 13°.

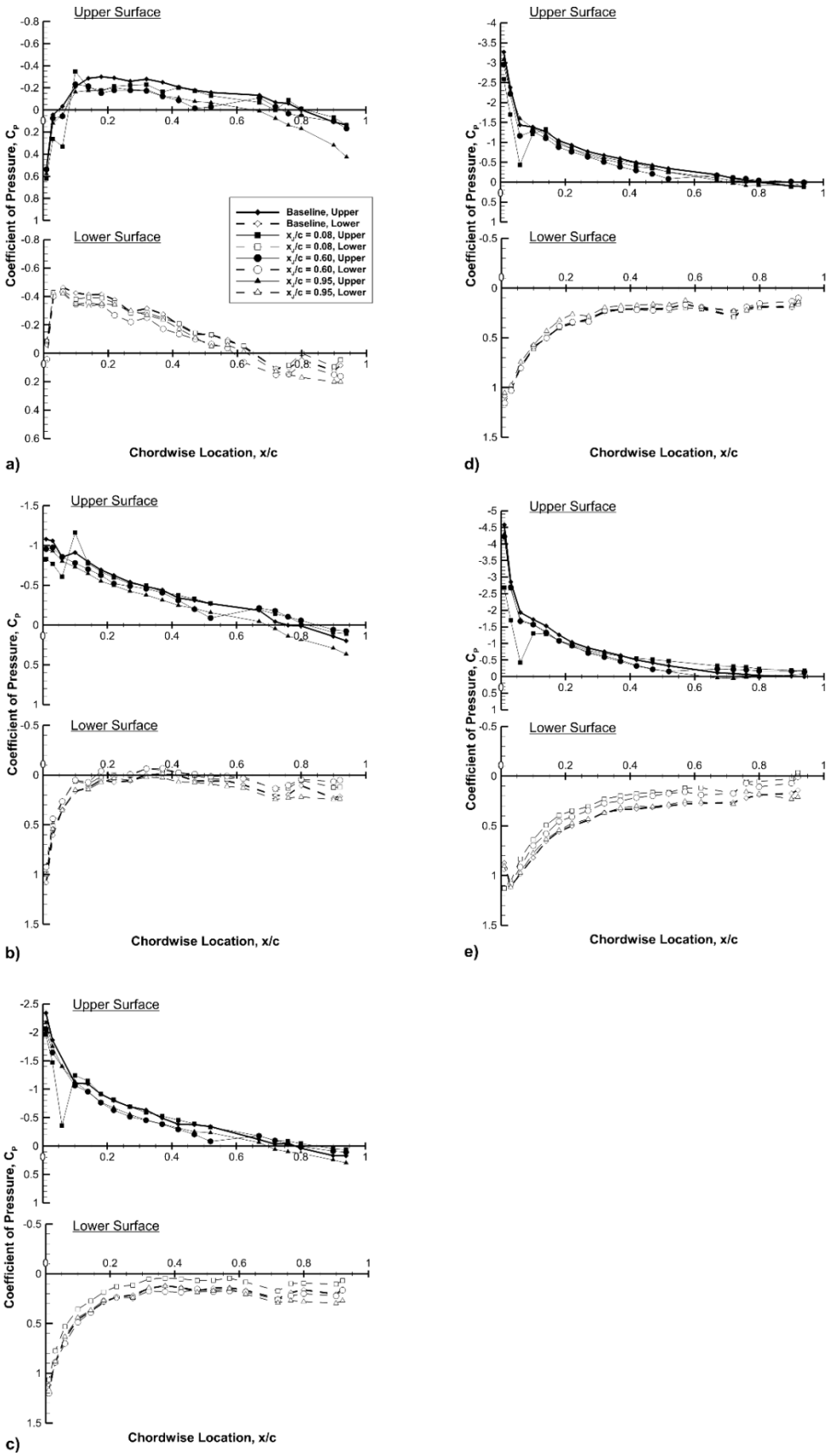

Figure 4.18 - Coefficient of pressure for upstream blowing for x_J/c = 0.08, 0.60 & 0.95, C_Q = 0.20% at: a) α = 0°; b) α = 5°; c) α = 8°; d) α = 10°; e) α = 13°.

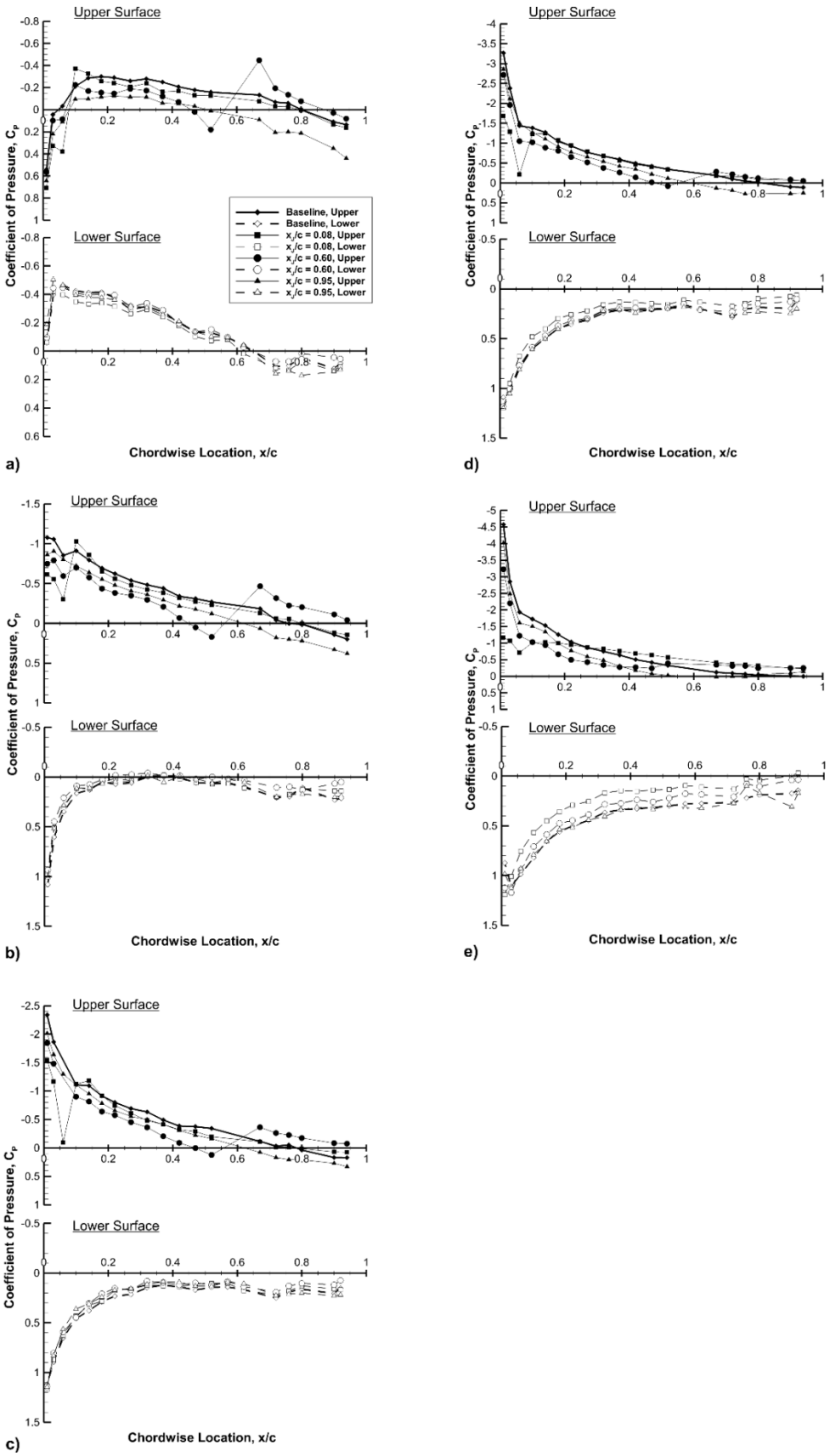

Figure 4.19- Coefficient of pressure for upstream blowing for x_J/c = 0.08, 0.60 & 0.95, C_Q = 0.35% at: a) α = 0°; b) α = 5°; c) α = 8°; d) α = 10°; e) α = 13°.

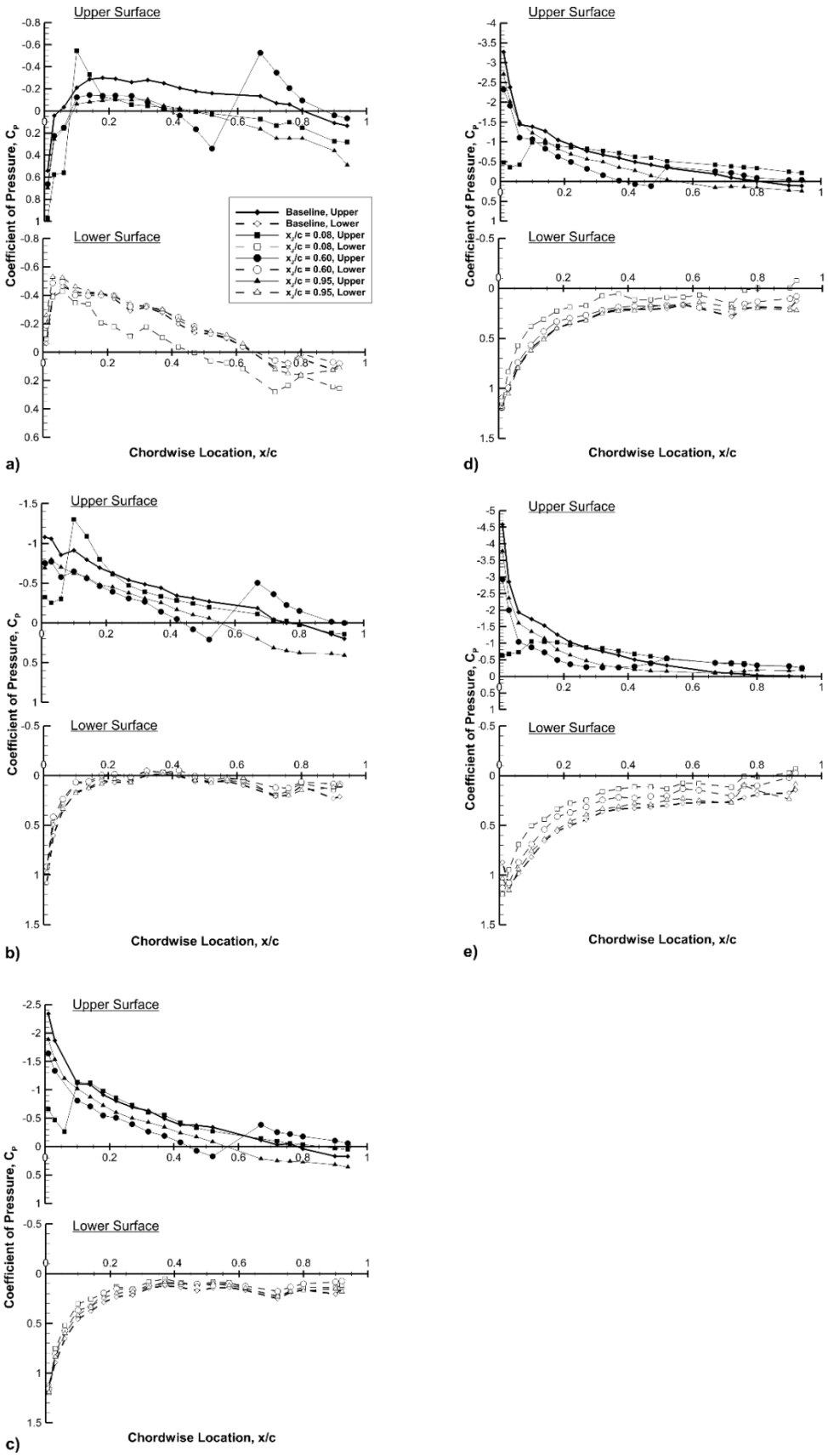

Figure 4.20 - Coefficient of pressure for upstream blowing for x_J/c = 0.08, 0.60 & 0.95, C_Q = 0.44% at: a) α = 0°; b) α = 5°; c) α = 8°; d) α = 10°; e) α = 13°.

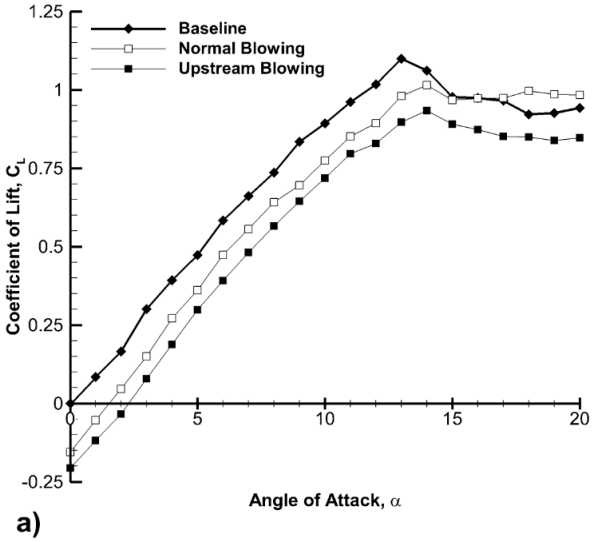

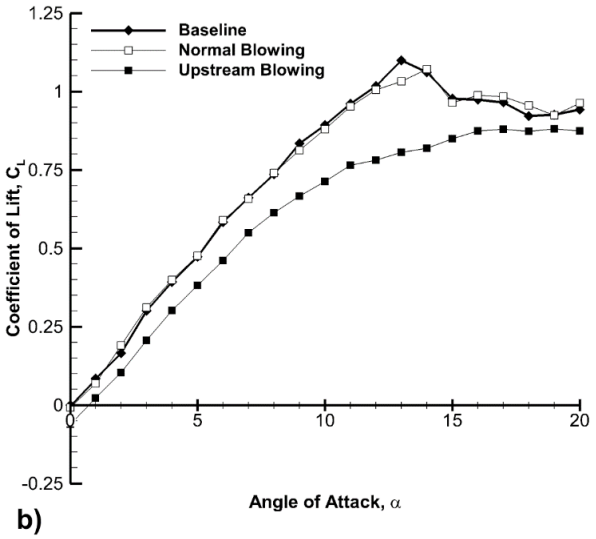

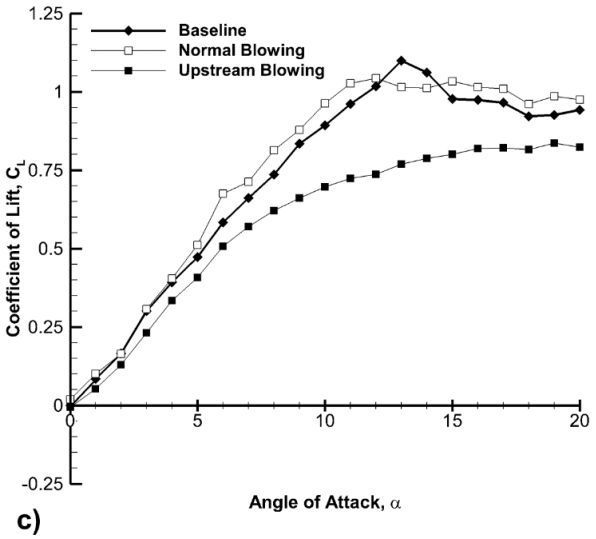

Figure 4.21 - Time-averaged lift coefficient comparing normal blowing (C_μ=2.0%) to upstream blowing (C_μ=4.0%) C_Q = 0.44% for: a) x_J/c = 0.95; b) x_J/c = 0.60; c) x_J/c = 0.08.

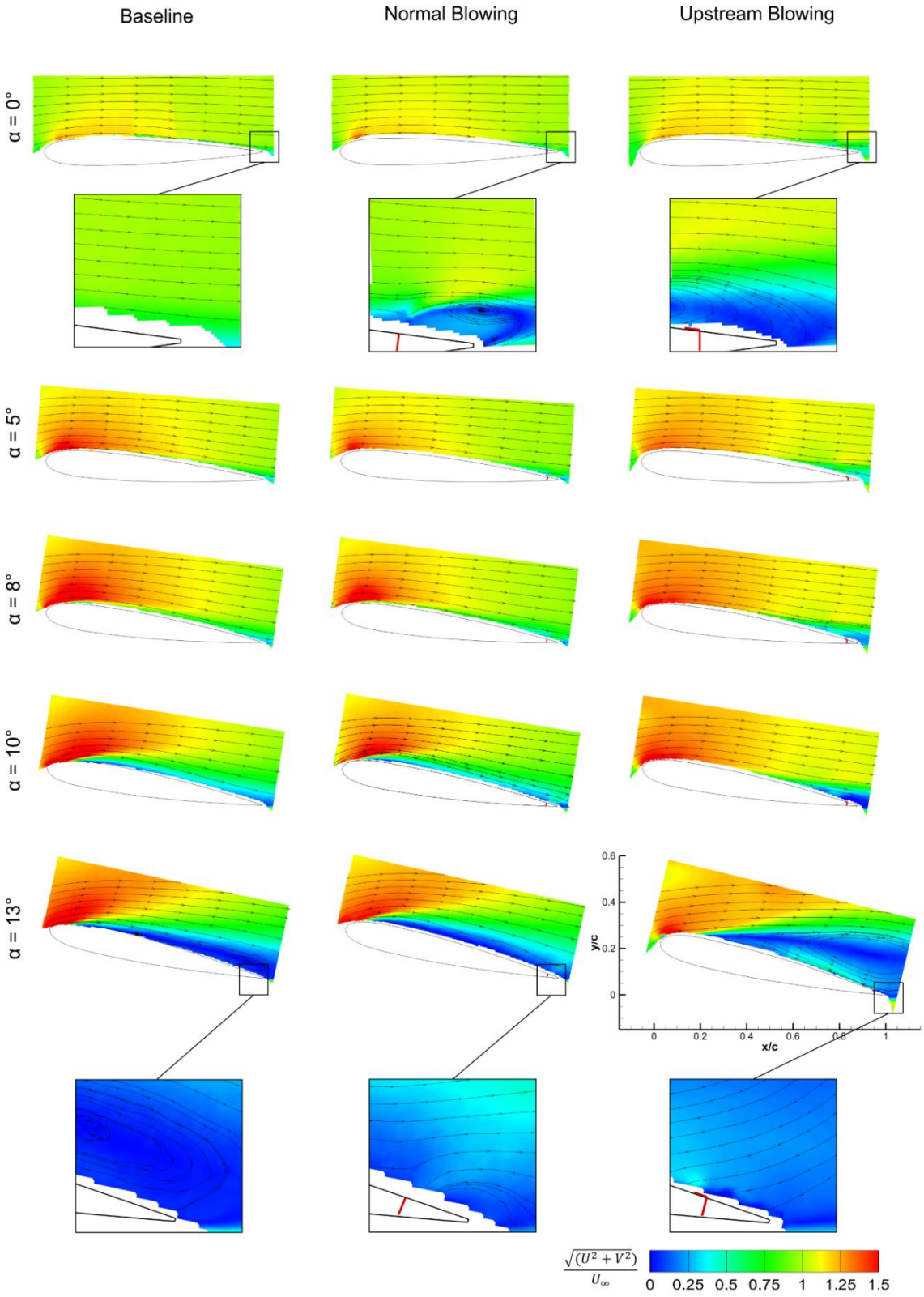

Figure 4.22 - Time-averaged velocity fields comparing at normal blowing (C_μ=2.0%) to upstream blowing (C_μ=4.0%) for x_J/c = 0.95, C_Q=0.44% and α = 0°, 5°, 8°, 10°.

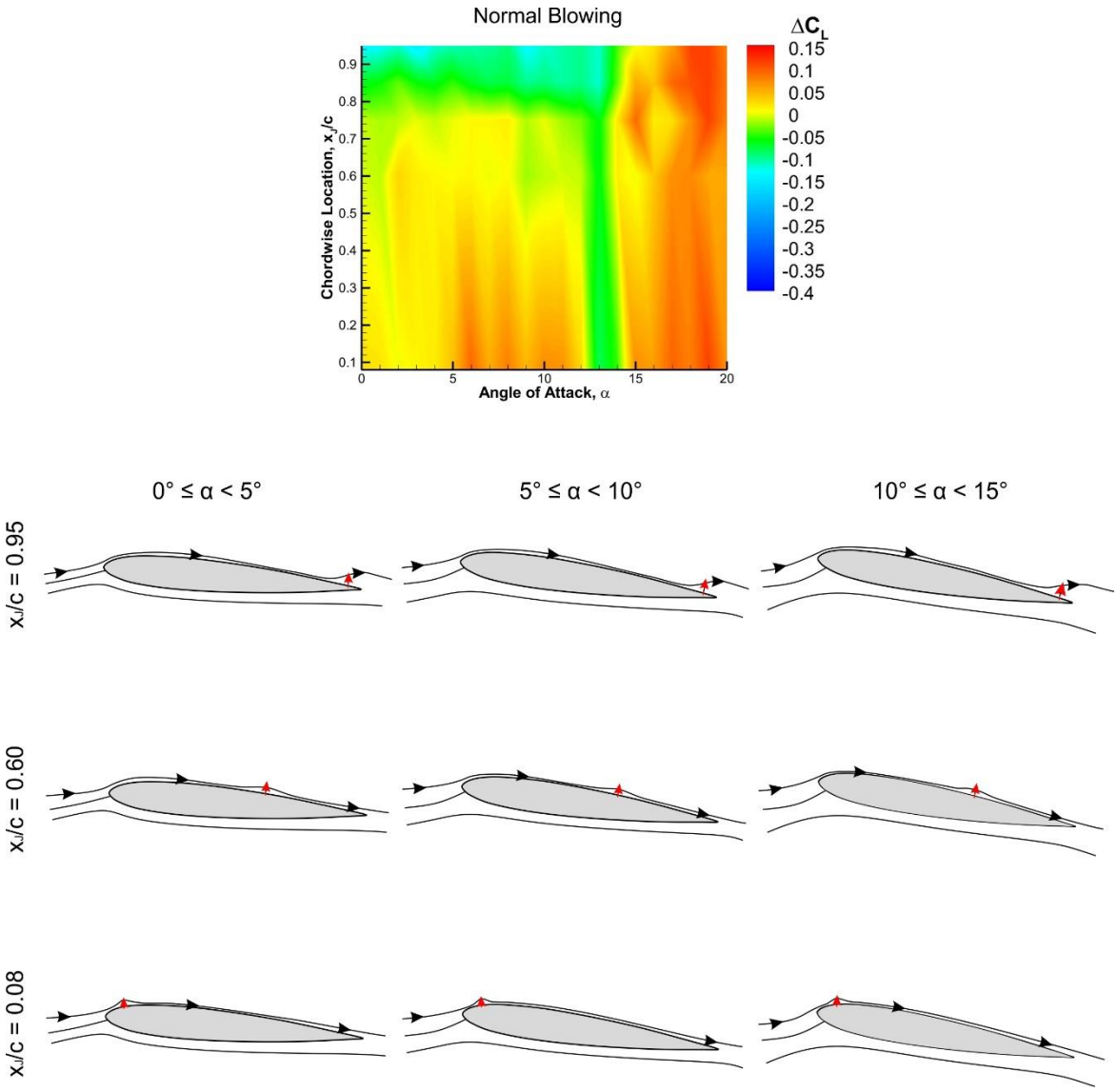

Figure 4.23 – Contour maps of change in lift coefficient with jet location and angle of attack for C_Q = 0.44%, with interpretive sketches of normal blowing.

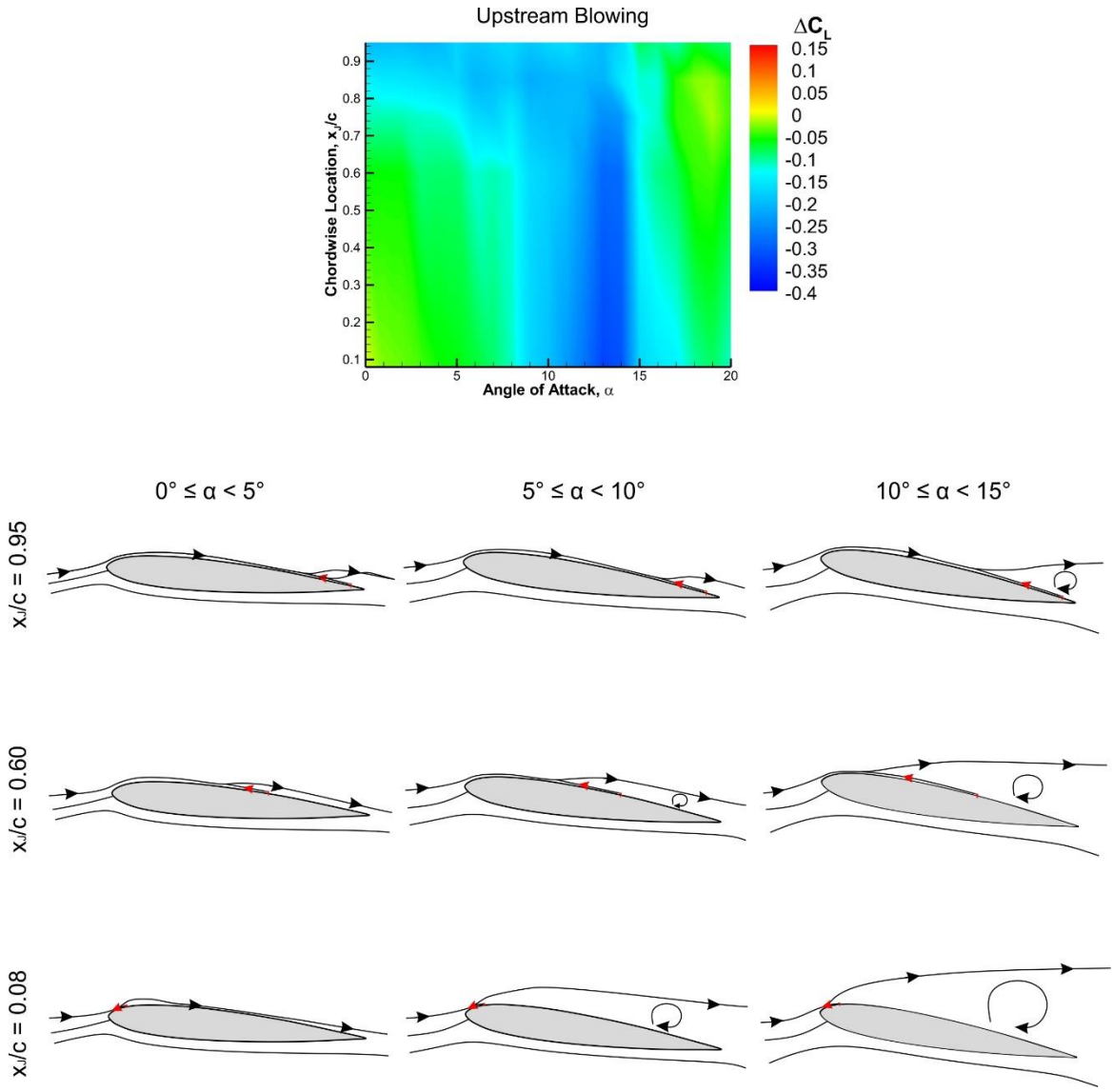

Figure 4.24 – Contour maps of change in lift coefficient with jet location and angle of attack for C_Q = 0.44%, with interpretive sketches of upstream blowing.

Chapter 5 Periodic Measurements

5.1 Definition of Terminology

Before proceeding with presenting the findings for a dynamically actuated upstream blowing jet, it is necessary to define the notations used throughout this chapter. Figure 5.1 illustrates an example of lift response to a sinusoidal jet velocity profile. The solid black line corresponds to the phase-averaged jet velocity determined by hot wire measurements, where its maximum is revised to occur at a phase in period of φ = 180°. Velocity signal is normalised for the minimum and maximum to be represented with 0 and 1, respectively. The resultant lift response is defined with the dashed black line, and should be read using the right-hand y-axis. The horizontal dashed red lines show the k = 0 steady state limits; baseline force measurements with blowing off at the top (C_{LOff}), and steady blowing on at the bottom (C_{LOn}). The difference ($\Delta C_L = C_{LOff} - C_{LOn}$) equates to the change in lift coefficient incited by steady blowing. The periodic lift response ultimately yields a maximum lift coefficient, C_{Lmax}, and a minimum C_{Lmin}, within the period. The difference between the two terms gives peak-to-peak change in lift, $C_{Lmin} - C_{Lmax}$. Mean value of the periodic lift is denoted with C_{Lmean}, and is shown in Fig. 5.1 as the dashed green line. Periodic lift coefficient varies with time, and the change between this value and the static baseline measurement is defined as $C_L - C_{LOff}$.

5.2 Steady State Validation

Steady state blowing for the experimental data presented in Chapter 4 was conducted with a direct pipe line from the Department's compressors, in order to minimise pressure losses allowing high momentum coefficients at all locations. To achieve unsteady jet profiles, a bespoke valve system was incorporated between the compressors and the airfoil. With this new unsteady system incorporated the hot wire measurements were repeated to confirm the jet exit velocities and spanwise uniformity. Due to the extra pressure loss it was not possible to perform high mass flow (C_μ > 0.016) measurements at x_j/c = 0.08 and 0.60. With this new source line, the steady state force measurements were repeated for all angles of attack investigated for unsteady force measurements, α = 0°, 5°, 8°, 10°, 13° & 16°. Figure 5.2 and 5.3 compare the data to data with the unsteady experimental arrangement. The solid symbols illustrate the measurements from chapter 4; and the open symbols the new measurements. Generally, there is reasonable agreement to within the bounds of experimental uncertainty. The only exception is the x_j/c = 0.08 location shown in Fig. 5.2c which is particularly sensitive around the stall angle. This is not surprising given the sensitivity of the flowfield to separation around this angle as exhibited in chapter 4. The agreement is best for the x_j/c = 0.95 and higher momentum coefficients as the mechanism for lift change is not as sensitive.

5.3 Force Measurements

5.3.1 Phase Averaged Force Measurements

The upstream blowing jet is investigated with varying reduced frequency between $0 \leq k \leq 0.473$. Three jet locations are considered for six angles of attack between $0° \leq \alpha \leq 16°$. Figures 5.4 to 5.8 demonstrate the effect of reduced frequency on C_{Lmin} and C_{Lmax} relative to the no blowing case. The difference between the lines is the amplitude of lift. Comparison of changes in lift coefficient at k = 0 is indicative of change in steady state blowing lift coefficient, as previously described.

Blowing with a momentum coefficient of $C_\mu = 0.016$ for $x_j/c = 0.95$ and $\alpha = 0°$, Fig. 5.4a shows little deviation from zero in the difference between maximum lift coefficient and no blowing, until 0.314. Beyond this reduced frequency, the maximum lift coefficient begins to reduce below the y = 0 line. Similarly, minimum lift coefficient progressively appreciates slightly with frequency. Therefore, the mean lift coefficient experiences minimal change; for $\alpha = 0°$, ΔC_{Lmean} = -0.058 at k = 0, and ΔC_{Lmean} = -0.059 at k = 0.471. When increasing the angle of attack to $\alpha = 5°$, shown in Fig. 5.4b, the steady state change in lift remains analogous to the previous case of $\alpha = 0°$. However, in comparison to the previous case, a steeper gradient towards smaller maximum lift coefficient is observed beyond k = 0.157. The change in minimum lift coefficient to no blowing remains unchanged from Fig. 5.4a. Consequently, the mean lift coefficient becomes lower with increased frequency. At $\alpha = 8°$, the change in lift at k = 0 is ΔC_L = -0.137, as observed in Fig. 5.4c. This is lower than what is observed in Fig. 5.4b. For the range of reduced frequencies, ensuing values for minimum lift coefficient are increased from $\alpha = 5°$; for k = 0.314, $C_{Lmin} - C_{Loff}$ = -0.122 at $\alpha = 5°$, and $C_{Lmin} - C_{Loff}$ = -0.106 at $\alpha = 8°$. Similarly, the maximum lift coefficient concomitantly reduces. Therefore, the two data lines converge with one another towards higher frequencies. This indicates a reduction in amplitude with frequency.

The change in steady state lift coefficient at k = 0 is reduced by 31% when increasing the angle of attack from $\alpha = 8°$ to 10°, as shown in Fig. 5.4d. However, the minimum lift coefficient value does not vary significantly, whilst the maximum decreases as frequency increases. Thus, the mean lift coefficient decreases across the frequency range. At k = 0.157, ΔC_{Lmean} = -0.057, which reduces to ΔC_{Lmean} = -0.071 at k = 0.471. Moreover, the amplitude is seen to reduce considerably at higher frequencies. At the stall angle, the differential between steady state forces at k = 0 remains similar to $\alpha = 10°$, as observed in Fig. 5.4e. Furthermore, the maximum lift coefficient reduces as soon as excitation is applied. Hence, a distinct difference in gradients is noticed between the two data lines. While the maximum lift coefficient lessens with frequency, the minimum maintains a relatively flat data line. This tends towards a minor amplitude of $C_{Lmin} - C_{Lmax}$ = - 0.012 at k = 0.471. Figure

5.4f shows behaviour of the trailing edge jet in the post-stall region, at α = 16°. At k = 0, the change in lift coefficient is significantly diminished to ΔC_L = -0.037. Subsequently, minimum lift coefficient with frequency retains a gradient of approximately zero. This demonstrates a significant reduction in amplitude in comparison to angles preceding stall, for the entire frequency range considered. Maximum lift coefficient migrates from y = 0 when the jet is excited with frequencies above k = 0.236.

Figure 5.5 shows the effect on minimum and maximum lift coefficients when increasing the momentum coefficient to C_μ = 0.024. When examining α = 0° in Fig. 5.5a, it is evident the increased blowing strength incites a greater change in lift coefficient at k = 0, with ΔC_L = -0.15. A similar amplitude is retained when excitation begins at k = 0.079. However, minimum lift coefficient amplifies with frequency, causing the amplitude to diminish beyond k = 0.079. At α = 5°, the differential between steady blowing lift and the baseline case is slightly greater at ΔC_L = -0.184, as seen in Fig. 5.5b. Despite the large steady state amplitude, the gradient of the minimum lift coefficient line is steeper to that observed in Fig. 5.5a, as this inclines towards $C_{Lmin} - C_{Loff}$ = -0.112. A decay initiates at k = 0.236 for the solid line, which remained constant for lower frequencies. Figure 5.5c indicates the change in lift at k = 0 for α = 8°, remains similar to earlier angles. Although, the gradient for the maximum lift coefficient declines at a faster rate in comparison to the case analysed in Fig. 5.5b. Additionally, the minimum lift coefficient experiences a similar trend to the α = 5° case. This leads to mitigation in amplitude with greater frequency. At k = 0.393, the peak-to-peak amplitude reduces to $C_{Lmin} - C_{Lmax}$ = -0.068. This behaviour is also observed at α = 10°, in Fig. 5.5d.

When at stall angle, the two data lines mirror one another to converge towards similar values at k = 0.471, as noticed in Fig. 5.5e. Due to the symmetry in data, the mean change in lift coefficient remains at approximately, $\Delta C_{Lmean} \approx$ -0.08 for all frequencies. Both lines follow a non-linear profile, with larger changes in amplitude occurring at lower frequencies. When exceeding beyond the stall angle, similar performance to when blowing with C_μ = 0.016 is noticed in Fig. 5.5f. At k = 0, steady state force becomes reduced when matched to smaller angles, while the minimum lift coefficient retains a similar value throughout the frequency range, to produce a flat line.

Aerodynamic performance of the jet with a momentum coefficient of C_μ = 0.032 is presented in Fig. 5.6. Overall, for Figs. 5.6a to e, much of the behaviour is identical in comparison to blowing with C_μ = 0.024. A particular difference between the blowing strengths is the magnitude observed at k = 0. As shown in Fig. 5.6a, the amplitude is increased to ΔC_L = -0.166. Furthermore, this increase in amplitude occurs at all angles of attack. Although the minimum lift coefficient slowly increases with frequency, the maximum lift coefficient doesn't depart from a constant value until later frequencies. This is most noticeable with lower angles. At α = 0°, an obvious change in maximum lift coefficient initiates at k = 0.236, but for angles between α = 5° to 10°, this change starts at k =

0.157. Beyond this reduced frequency, the maximum lift coefficient attenuates to a lower value at a greater rate. In Fig. 5.6c, a change of $C_{Lmax} - C_{Loff}$ = -0.048 at k = 0.393 is induced, however, at α = 10° for the equivalent frequency, this reduces further to $C_{Lmax} - C_{Loff}$ = -0.058. The stall angle sees a smaller magnitude at k = 0, with ΔC_L = -0.156, as seen in Fig. 5.6e. This change from the baseline force measurement with minimum lift coefficient augments to a value of $C_{Lmin} - C_{Loff}$ = -0.104, and remains at this value until k = 0.471. Also, the trend for both lines is equal to what was noticed in Fig. 5.5e, for C_μ = 0.024, indicating the blowing strength only attenuates lift magnitude but much of the behaviour remains the same. When at α = 16°, the data lines shift upwards immediately after k = 0, which signifies a change in mean lift coefficient. Although this mean value is above y = 0, it remains extremely small $\Delta C_{Lmean} \approx$ -0.005.

Figure 5.7 presents data for the jet at x_j/c = 0.60, with a momentum coefficient of C_μ = 0.016. When examining the behaviour at α = 0°, in Fig. 5.7a, the steady state lift change is ΔC_L = -0.055. Correspondingly, the minimum lift coefficient of the jet achieved at this angle is relatively consistent throughout the range of reduced frequencies, $C_{Lmin} - C_{Loff} \approx$ -0.05, to produce a flat line. Maximum lift coefficient doesn't depreciate below $C_{Lmax} - C_{Loff}$ = -0.015. With the two lines following similar trends, the amplitude barely alters with reduced frequency. For k = 0.236 and 0.471, the amplitude is equal to $C_{Lmin} - C_{Lmax}$ = -0.0381. As the angle increases to α = 5°, amplitude at k = 0 increases over lower angles to ΔC_L = -0.091, as seen in Fig. 5.7b. It can be seen that the minimum lift coefficient remains constant until k = 0.157, at which point it is subjected to a rise. The same can be said about the maximum lift coefficient, which sees a depreciation in value beyond the same reduced frequency. Therefore, a reduction in amplitude proceeds.

Figure 5.7c shows much of the same behaviour of α = 5° taking place at α = 8°. The trends of the gradients are very similar, with k = 0.157 inciting an analogous amplitude to k = 0. Thereafter, the amplitude continues on to decrease with frequency. A significant disparity between the two angles is that the magnitude of the peak-to-peak amplitude is larger at α = 8°. This magnitude amplification continues on to α = 10°, as seen in Fig. 5.7d. At k = 0.157, the minimum lift coefficient change lowers to $C_{Lmin} - C_{Loff}$ = -0.176. However, maximum lift coefficient begins to reduce at this frequency. Thus, it can be said that the gradient increases with angle of attack. This is further corroborated at α = 13°, seen in Fig. 5.7e, where the maximum lift coefficient reduces from $C_{Lmax} - C_{Loff}$ = 0 once the jet is excited in a sinusoidal manner. Furthermore, the effectiveness of the jet at x_j/c = 0.60 increases with angle of attack, as steady state lift reduction enlarges to ΔC_L = -0.228. On the contrary, due to the larger gradient seen with the data lines, the large amplitude change is not sustained with greater frequency, and reduces to a small amplitude of $C_{Lmin} - C_{Lmax}$ = -0.023 at k = 0.471. In the post-stall region, at α = 16° in Fig. 5.7f, the trend resembles the case analysed at α = 0° as minimum and maximum lift coefficients fashion horizontal profiles with increasing frequency.

As such, the jet preserves near constant amplitude throughout the frequency range. Albeit at a reduced magnitude in comparison to α = 13°. This suggests that the increasing lift reduction ceases at α = 13° for the x_j/c = 0.60 jet.

Figure 5.8 shows the change from baseline force measurement to minimum and maximum lift coefficient as the jet is displaced upstream at x_j/c = 0.08, with C_μ = 0.016. As shown in Fig. 5.8a, the smallest amplitude at k = 0 out of all angles is observed at α = 0°. Thus, the leading edge jet starts with a change in lift of ΔC_L = -0.033. Nevertheless, minimum lift coefficient rises immediately and remains constant at a negligible change in lift; $C_{Lmin} - C_{Loff} \approx$ -0.006. This consequently produces a positive mean change in lift coefficient value. Proceeding to α = 5°, Fig. 5.8b, the amplitude at k = 0 amplifies to ΔC_L = -0.056. Despite this increase, the data along the two lines traverse parallel to one another. It is not until α = 8°, shown in Fig. 5.8c, where an increasing gradient is observed with minimum lift coefficient. In addition, the amplitude continues to increase with angle of attack, to ΔC_L = -0.102. This becomes reduced to $C_{Lmin} - C_{Lmax}$ = -0.033 at k = 0.471.

Figure 5.8d showing data for α = 10°, can be said to resemble to performance at α = 8°, albeit with enlarged amplitudes. For k = 0, there is an amplitude of ΔC_L = -0.213. For frequencies between 0.079 ≤ k ≤ 0.157, the amplitude remains constant. This is further noticed at frequencies between 0.236 ≤ k ≤ 0.314, although decreased. At α = 13°, Fig. 5.8e, the leading edge jet confirms a similar characteristic to the jet at x_j/c = 0.60, in which the steady state lift reduction increases with angle of attack. This is contrary to what was seen with the trailing edge jet. Large amplitudes are noticed with all frequencies. However, difference in amplitude between each end of the frequency range is also large. At k = 0.079, the amplitude is $C_{Lmin} - C_{Lmax}$ = -0.473, which reduces to $C_{Lmin} - C_{Lmax}$ = -0.136 at k = 0.471. Minimum lift coefficient increases with each frequency but maximum lift coefficient does not decrease until k = 0.236. As seen in Fig. 5.8f, the leading edge jet at α = 16° exhibits a differing performance to downstream locations. Firstly, amplitude is much larger in comparison, with ΔC_L = 0.291 at k = 0. Large amplitudes are consistent throughout the frequency range, as shown at k = 0.314, where $C_{Lmin} - C_{Loff}$ = -0.244. Furthermore, the minimum and maximum values do not stay constant, as was analysed with other jet locations.

Shown in Fig. 5.9 is the differential between minimum and maximum lift coefficients, to better evaluate amplitude with reduced frequency for all locations and angles considered. Lower angles show greater steady state amplitudes for x_j/c = 0.95. As amplitude decays with frequency, the dependency on angle of attack becomes more evident. At k = 0.471, the largest amplitude is produced at α = 0°, and decreases with angle. Additionally, much of the performance at α = 0° is retained at α = 5° for frequencies below k < 0.314. Once α = 16° is reached, the amplitude decay rate is small in comparison to earlier angles. It is apparent in Fig. 5.9b, jet performance with angle

of attack is altered when at x_j/c = 0.60. Steady state lift reduction increases with angle of attack until stall. When exciting the jet, the lowest amplitudes are attained at α = 0°. Although lift reduction decreases with frequency despite angle of attack, it can be noted that angles with larger steady state amplitudes suffer with a greater gradient. This would explain the grouping of values occurring at k = 0.471. Beyond stall angle, at α = 16°, the amplitude experiences little change from k = 0 when increasing frequency. This corroborates what was observed in Fig. 5.7f. Like the jet at x_j/c = 0.60, the leading edge jet induces greater steady state lift reduction, as shown in Fig. 5.9c. Negligible changes in amplitude with frequency is observed at α = 0°. However, the rate of decay in amplitude once again increases with angle of attack. At α = 16°, the leading edge jet continues to be effective at mitigating lift with increasing frequency.

The influence of momentum coefficient on amplitudes for all angles investigated at x_j/c = 0.95, is presented in Figs. 5.10 & 5.11. Overall, much of the trend patterns analysed for C_μ = 0.016 persists despite increasing blowing strength. When comparing Figs. 5.10a & c, steady state lift reduction obviously augments with blowing strength. Regardless of jet velocity, the jet at α = 0° is most effective with higher frequencies, k ≥ 0.314. On the contrary, amplifying jet strength appears to improve lift reduction at lower frequencies, k ≤ 0.157, at α = 10°. Cross examining Figs. 5.11a to f, it is observed that blowing strength has a greater influence on peak-to-peak amplitude with lower frequencies. As excitation is amplified to higher frequencies, amplitudes become identical regardless of momentum coefficient.

Another approach to quantifying amplitude is to normalise the phase averaged amplitudes with the change in lift coefficient between blowing on and off, see Figs. 5.12 to 5.14. When operating the jet at x_j/c = 0.95, seen in Fig. 5.12a, 75% of steady state lift reduction is retained at k = 0.314 for α = 0°. At this location, amplitude decays faster with greater angle of attack. In contrast, amplitudes eventually reach similar values at k = 0.471 with the jet at x_j/c = 0.60, as seen in Fig. 5.12b. Furthermore, poor lift retention occurs for the jet at α = 13°, where amplitude at k = 0.471 is at 10% of the steady state value. It can be noted that this is consistent with other locations at the same angle. From Fig. 5.12c, it can be seen that for angles higher than α > 0°, the leading edge jet is capable of preserving greater than 80% of steady state force when actuating below k < 0.2.

Comparison of momentum coefficients effects on amplitude for the jet at x_j/c = 0.95 is presented in Figs. 5.13 & 5.14. It can be determined that amplitude ratios are independent of jet velocity, as amplitude ratios decay at similar rates. This is in contrast to what was observed by Simmons, who found amplitude ratio to decrease with blowing strength for an oscillating jet [142]. One particular difference in trend between the cases is observed at α = 16° where higher ratios are manifested with the lowest blowing strength, see Fig. 5.14f.

Presented in Fig. 5.15 is the phase difference between the lift response and the measured jet response, for all locations studied. By definition there is no lag delay between the lift response and the jet at steady state blowing. As such, the dashed lines stem from φ = -180° to the first data point because the velocity is represented by a '1 – cos' and the lift by a '–sin' giving a -180° phase difference. Thus, larger phase angles represent greater lag responses. When comparing the phase difference for all three jet locations, it is apparent jet locations towards the trailing edge have less lag in response. The least lag is experienced at α = 0°, regardless of location. With increasing angle the lag increases reaching a maximum around stall $\alpha \approx$ 13° and then decreasing. When evaluating the effect of momentum coefficient on phase angle, it is apparent from Fig. 5.16 there is no significant change between blowing strengths, therefore indicating phase delay is independent of momentum coefficient.

5.3.2 Lift Response

Phase averaged force measurements were performed to examine the effect of varying reduced frequency between $0.079 \leq k \leq 0.471$. All locations were considered for a range of angle of attacks between $0° \leq \alpha \leq 16°$. Due to the periodic deployment, the lift coefficient becomes time dependent. As such, Figs. 5.17 to 5.29 present time dependent lift coefficient with jet flap deployment for a normalised period, for selected cases at C_μ = 0.016. Jet velocity is normalised with the maximum value, U_{jmax}, and is achieved at a phase in period φ = 180°. The lift response is quantified using the lift coefficient axis, and dashed lines are inserted to illustrate the maximum and minimum bounds attained with blowing off and on, respectively. Lift response at each frequency is separated into individual figures due to the phase averaged jet velocity data indicating differing profiles with frequency.

The periodic jet deployment creates an alteration in lift force, as shown in Fig. 5.17 for x_j/c = 0.95 at α = 0°. From Fig. 5.17a it is seen that the onset of jet velocity induces a nearly immediate change in lift. This leads to a maximum change in lift corresponding very near the maximum jet velocity. Maximum lift coefficient occurs at C_L = 0 for frequencies less than $k \leq 0.157$. Beyond this, the maximum gradually decreases with frequency. This consequently supports a reduction in peak-to-peak amplitude with increasing frequency.

As angle of attack increases for the trailing edge jet, the phase lag becomes more evident. This is evident through the minimum lift coefficient falling at a later phase in the period. At α = 8°, C_{Lmin} is initially attained at φ = 219° for k = 0.079, but delays to φ = 247° when exciting the jet at k = 0.393, as seen in Fig. 5.19a & e. The cyclic jet velocity at α = 13° induces a significant reduction in amplitude despite using a low frequency of k = 0.079. As the jet reaches k = 0.471, this amplitude

reduces to an extremely small value of $C_{Lmin} - C_{Lmax}$ = -0.012. Excitation in the post-stall region sees a shift in minimum and maximum lift bounds, as noted in Fig. 5.22.

When examining the frequency effect on lift response for x_j/c = 0.60 in Figs. 5.23 to 5.27, it can be seen at α = 5°, the peak-to-peak amplitude initially increases over steady state lift change with k = 0.079 in Fig. 5.23a. However, an additional frequency appears to influence the lift response at this location, as a double peak with maximum lift coefficient emerges. This effect is predominantly observed for lower angles of attack, as it ostensibly appears at k = 0.157 for α = 5°, but ceases to manifest for the frequencies considered at α = 13°. Phase delay with force continues to increase with frequency. Taking the α = 10° case in Fig. 5.25f as an example, it can be seen minimum lift coefficient establishes at approximately half a period after the maximum jet velocity.

A large phase delay is realised with low frequencies when varying the jet location to x_j/c = 0.08. Although the jet profile is sinusoidal, the response suffers from a delay before lift mitigation is observed. This behaviour can be noticed in Fig. 5.28b at α = 10°, where the lift remains around C_L = 0.88 between φ = 95° to 240° at k = 0.157. The phase delay becomes large enough to subject the airfoil to a minimum force within the next period of jet deployment by k = 0.314. Figure 5.29 signifies that this behaviour persists at α = 13°.

An alternative method to analyse the aerodynamic response of the jet is through hysteresis loops. As such, the lift coefficient change from the baseline case, $C_L - C_{Loff}$ is examined with the normalised blowing cycle, $C_\mu/C_{\mu max}$ in Figs. 5.30 to 5.34. At $C_\mu/C_{\mu max}$ = 0, the upstream blowing jet is inactive. When the momentum coefficient ratio reaches $C_\mu/C_{\mu max}$ = 1, the jet velocity is at its maximum strength. As such, the hysteresis loop develops in a clockwise direction towards the right-hand side of the figure. A change in lift of $C_L - C_{Loff}$ = 0 indicates no change from blowing off measurement.

With the jet at x_j/c = 0.95 in Fig. 5.30a, it can be seen that lift initially starts at $C_L - C_{Loff}$ = 0 for a reduced frequency of k = 0.079. As the frequency increases, the loop pivots about a mean lift change. Thus, causing the change in lift $C_L - C_{Loff}$ at $C_\mu/C_{\mu max}$ = 1 to tend towards lesser amplitudes. The loop expands in size with frequency, signifying an increased phase lag. Therefore, the dependency on frequency is strong. This further illustrated at α = 5°, in Fig. 5.30b, where excitation at k = 0.079 sees negligible phase lag before the lift response begins and leads to a peak $C_L - C_{Loff}$ = -0.147. As excitation frequency increases, the hysteresis loops shifts to a horizontal position, due to the phase lag. In addition, the difference between minimum and maximum lift coefficient decreases; i.e. from $C_{Lmin} - C_{Lmax}$ = -0.141 to -0.062 at k = 0.471. Amplitude changes become smaller at α = 13°, particularly at higher frequencies, see Fig. 5.30e. For frequencies between $0.314 \leq k \leq 0.471$, phase between lift response and jet velocity remains between $-108° \leq \varphi \leq -103°$.

As such, for these reduced frequencies hysteresis loops produce analogous lift responses before the jet reaches peak velocities. Following the maximum jet velocity, these loops differ with minimum $C_L - C_{Loff}$ values, thus indicating the amplitude decreasing, despite phase remaining relatively constant.

As alluded to earlier, the aerodynamic response of the jet is independent of momentum coefficient magnitude. Comparison of Figs. 5.30 to 5.32, for C_μ = 0.016, 0.024 & 0.032, corroborate this trend. Despite the increasing lift reduction, the maximum amplitude remains at k = 0.079 for pre-stall angles. Loops continue to expand with frequency, indicating an increasing phase lag that is proportional to frequency.

Amplitude changes for the jet at x_j/c = 0.60 start small with α = 0°, as observed in Fig. 5.33a. This amplitude increases with angle of attack. With α = 5°, lift response begins at $C_L - C_{Loff}$ = 0 for k = 0.079 in Fig. 5.33b, as the phase difference is relatively low at φ = -139°. As reduced frequency rises to k = 0.471, lift reduction does not begin until the jet reaches maximum jet velocity, suggesting a greater lag. This is validated with reference to Fig. 5.15b where the phase for this case is φ = -6°. While phase lag for the jet at α = 13° is not as small as the trailing edge jet, it does still exceed φ = -90° at k = 0.157, which is characterised by horizontal loops. With reference to Fig. 5.7e, it is obvious that the difference between minimum and maximum lift coefficients reduces with frequency. This is reflected in the size of the hysteresis loops significantly reducing with higher k.

Figure 5.34a indicates an indistinguishable amplitude change is realised with frequency for the jet at x_j/c = 0.08 with α = 0°. This is consistent with low angles of attack, as shown at α = 5° in Fig. 5.34b. In contrast, at α = 13° the upstream blowing jet becomes more effective at reducing lift when closer to the leading edge. Consequently, the hysteresis loops in Fig. 5.34e are far superior in size in comparison to the other two locations for the same momentum coefficient, shown in Fig. 5.30e & 5.33e. Even for low excitation frequencies, lift response is characterised by very large phase lags. As can be seen with k = 0.079, the phase difference is φ = -98°, subsequently causing the hysteresis loop to transform into an astonishing box-like form. The profile remains around $C_L - C_{Loff} \approx$ -0.04 before significant lift reduction begins around $C_\mu/C_{\mu max} \approx 0.90$. This highlights there is a large delay in response before the upstream blowing jet is able to incite a change in the flow. Increasing frequency to k = 0.157 sees the point of peak lift reduction occurring towards the end of the blowing cycle. Beyond this reduced frequency, the loops incline to a horizontal position, as phase difference increases above φ = 0° and the amplitude decays.

5.3.3 Modelling of Aerodynamic Response

The normalised time constant, $\kappa = TU_\infty/c$, of the upstream blowing jet with sinusoidal deployment can be determined by modelling the relationship between the amplitude ratio,

$(C_{Lmin} - C_{Lmax})/(C_{Lon} - C_{Loff})$, and frequency. In order to obtain the time constant, the aerodynamic response is defined using a first order system. Utilising the data presented earlier, a curve fit tool was used with MATLAB to fit data to Eqs. [5.1 & 5.2]. Time constants are acquired for all jet locations, for angles of attack between $0° \leq \alpha \leq 13°$ when deploying the jet with a momentum coefficient of C_μ = 0.016.

$$\frac{C_{Lmin} - C_{Lmax}}{C_{Lon} - C_{Loff}} = \frac{1}{\sqrt{(\omega T)^2 + 1}} \quad [5.1]$$

$$\angle [\tan^{-1}(-\omega T)] \quad [5.2]$$

Angular frequency, ω is determined with a simple conversion of reduced frequency to frequency, *f*. Due to the high phase lags associated with jet locations upstream of x_j/c < 0.95, Eq. [5.1] is used to exact the time constant from amplitude ratio for the model. Equation [5.2] calculates the time constant using the phase angle. Additionally, a comparison between Eqs. [5.1 & 5.2] is possible for x_j/c = 0.95. Comparing time constants between jet locations in Fig. 5.35, it can be noted the jet flap realises larger time constants at high angles of attack, as it is displaced towards the trailing edge. Larger time constants signify a slower rate of change in aerodynamic force. The time constant increases with angle for the trailing edge jet, indicating slower response. On the other hand, the jet at x_j/c = 0.60 remains at a similar constant between $5° \leq \alpha \leq 10°$, and significantly rises at α = 13°. Time constants at α = 10° & 13° for x_j/c = 0.08 appear analogous with one another. However, this is slightly misleading as it was shown earlier that jet flaps closer to the trailing edge respond with less phase lag.

When estimating κ, differences between Eqs. [5.1 & 5.2] become distinct when at α = 10°. Prior to this angle, the methods give similar time constants. Figures 5.36 to 5.39 demonstrates which method is suitable for each angle of attack. Figure 5.36d suggests the time constant of κ = 1.46 obtained with Eq. [5.1] produces a reasonable fit with data, but utilisation of this exact constant yields an extremely poor fit for phase angle estimation in Fig. 5.37d. This trend becomes reversed when using the time constant acquired with Eq. [5.2].

5.3.4 Literature Comparison

The normalised amplitude ratio,$(C_{Lmin} - C_{Lmax})/(C_{Lon} - C_{Loff})$, and phase angle could be used for comparison with findings from literature. As such, Fig. 5.42 compares literature data to force measurements presented earlier. Included in the comparison is Theodorsen's function, $C(k)$ [179]. Theodorsen's function is built on the thin airfoil theory to approximate the change in wake vorticity, and therefore, circulation, for an oscillating airfoil. While amplitude and phase data from

studies [138, 142] are for oscillating trailing edge jet flaps. Oscillating jet flaps are used due to their sinusoidal deployment, making them similar to the jet flap profile utilised in this study. It is therefore logical to use measurements conducted with the jet at x_j/c = 0.95 and α = 0°, for all momentum coefficients considered in this chapter.

The measurement taken for k = 0 is referred to as 'quasi-steady' conditions. Thus, Theodorsen's function exhibits an amplitude reduction from the quasi-steady state in the frequency domain. However, for lower reduced frequencies, below k < 0.2, amplitude ratios from the present study closely match that of Simmons [142] for a momentum coefficient of C_μ = 0.099. As demonstrated earlier, the amplitude reduction slowly increases with momentum coefficients between $0.016 \leq C_\mu \leq 0.032$. As frequency increases to k > 0.35, the amplitude ratios become similar to Simmons [142] and Theodorsen [179]. The trends suggest a relationship between C_μ and the normalised amplitude ratio reduction. Larger momentum coefficients incite a further reduction in effectiveness.

When considering the range of reduced frequencies with phase angle, a large discrepancy in phase delay findings is illustrated in Fig. 5.42b. The phase delays with Theodorsen [179] and the extremely high blowing strength tested by Simmons & Platzer [138] appear to reach maxima at k = 0.3. While in contrast, the lower jet strengths continue to rise in phase lag. The upstream blowing jet retains a faster response to the oscillating jet of Simmons & Platzer [138] with C_μ = 0.14 with low frequencies. It is unclear as to why large differences in phase angles arose amongst the studies; possibly being Reynolds number related.

5.4 Flow Field Measurements

Phase averaged particle image velocimetry was performed to examine the effect of a periodic deploying upstream blowing jet on the flow field. Velocity flow fields are presented in Figs. 5.43 to 5.53 for a range of angles of attack between $0° \leq \alpha \leq 13°$ for all three jet locations. Measurements were conducted with a fixed momentum coefficient of C_μ = 0.016, and for a fixed reduced frequency of k = 0.393. The common momentum coefficient permits the effect of jet location to be evaluated. Four phases within the period are selected to capture velocity data at, φ = 0°, 90°, 180° & 270°, to study the development of the flow field within the deployment cycle. Time-averaged velocity flow fields for blowing on and off conditions are presented alongside the phase-averaged data to evaluate similarities between steady and unsteady cases. In addition, the associated time dependent lift response to jet velocity figures are shown in conjunction to correlate the flow field characteristics to force measurements.

The unforced symmetrical airfoil produces a lift coefficient of C_L = 0 at α = 0°. This is reflected in the flow field with no blowing, Fig. 5.43, where flow remains attached to the surface. When deploying the jet at x_j/c = 0.95, for a reduced frequency k = 0.393, lift coefficient does not recover to the baseline case. The lift change evoked at φ = 0° from the baseline measurement is very small, $C_L - C_{Loff}$ = -0.03. It becomes difficult to discern any difference from the no blowing case. Similarly, lift coefficient is approximately the same at φ = 90°. Significant lift reduction is not realised until φ = 180°, where C_L = -0.09. A slight deflection in flow from the airfoil surface indicates a separated region manifesting. However, the separated region is not as large as the one observed with continuous blowing. Cycling to φ = 270°, lift is extremely similar to the case at φ = 180°. This is corroborated in the flow field where the separated region for both phases points, comparable in size.

Inclining the airfoil to α = 5°, shown in Fig. 5.44, a higher velocity magnitude region appears near the leading edge for the baseline case, in comparison to the previous angle. Much like the earlier angle of attack, the separated region produced by upstream blowing at φ = 0° & 90° initiates at similar upper surface locations. Consequently, lift coefficient for both cases is approximately $C_L \approx$ 0.46. Interestingly, the separated region increases in size to resemble that of continuous blowing, when maximum jet velocity is attained. Additionally, the magnitude in lift reduction is not as large due to the lower velocity magnitude region being engendered by steady state jet. Advancing a quarter cycle to φ = 270°, the jet is returning from the maximum velocity to U_j/U_{jmax} = 0.5. Separation begins to subside, however, the delay in lift response renders the lift coefficient at a lower value than observed at φ = 180°.

With the baseline case for α = 8° in Fig. 5.45, flow sustains attachment across the upper surface. Activation of the jet induces flow to detach at $x/c \approx 0.80$ and inclination of streamlines aft of this point suggests a change in aerodynamic camber happening. Such a modification in flow field produces a change in lift of ΔC_L = -0.137. As clearly indicated in Fig. 5.12b, periodic deployment at k = 0.393 cannot hold this amplitude change as it is reduced to approximately half. At φ = 0°, a region of reduced velocity, which starts at $x/c \approx 0.90$, enlarges until the trailing edge. This small discrepancy in flow field to the no blowing case is sufficient to reduce lift by $C_L - C_{Loff}$ = -0.063, therefore, shows the sensitivity to lift mitigation caused by the jet. This region lessens in effect at φ = 90°, as it closely follows the maximum lift coefficient at φ = 67°. The separated region becomes more intense at φ = 180°, as lift is declining towards the minimum lift coefficient. Lift at this point decreases from the baseline case by $C_L - C_{Loff}$ = -0.086. The separated region almost attains the size exhibited with continuous blowing, when the jet progresses to φ = 270°. The similarity between the two flow fields, again, emphasises how small differences could incite significant lift mitigation.

The baseline case at α = 10° produces a lift coefficient of approximately $C_L \approx 0.90$, shown in Fig. 5.46. A fully separated region becomes obvious at this angle, as the shear layer fails to reattach. This wake region is augmented in size with blowing and a lift change of $C_L - C_{Loff}$ = -0.065 is evoked at φ = 0°. Furthermore, a reduction in velocity magnitude within the wake region is evident. As was shown earlier, the phase lag increases with angle of attack, hence, the jet at φ = 90° coincides within the vicinity of the maximum lift coefficient during the phase cycle. Further reduction in velocity magnitude near the jet location, indicates an increased effectiveness of the jet at φ = 180°. The jet promotes an enhanced separated region at φ = 270°. This is validated with force measurements, where the phase lag governs minimum lift coefficient to occur at φ = 270°.

For the no blowing case at α = 13° in Fig. 5.47, there is a small separated region starting at approximately $x/c \approx 0.80$. Once the jet is activated in the continuous blowing case the separation advances to $x/c \approx 0.70$, enlarging the separated region to give a change in lift coefficient of ΔC_L = -0.09. For periodic blowing, the lift response does not reach the extremes of the baseline case, hence the lift is reduced relative to the no blowing case, but not as much as the continuous blowing case, regardless of the phase in the blowing cycle. This is evident when comparing the no blowing case to blowing at any moment in the cycle. In all phases considered, the separated region is intensified by the jet. At φ = 0°, lift is increasing so one would expect to see the separated region diminishing. This is more evident at φ = 90° where the effect of the jet is reduced, despite the increasing jet velocity. At φ = 180°, the jet reaches its maximum velocity magnitude and lift is reducing but due to the phase lag in response, minimum lift coefficient has yet to be attained. The separated size does not reach the size obtained through continuous blowing, and this is also the case at φ = 270°. This is expected as continuous blowing generates a larger lift reduction. However, this demonstrates the ability of the jet

to remain effective with periodic deployment, despite operating within a separated region caused by the high angle of attack. Generally, the amplitude of lift variation is small but in broad agreement with the flow field measurements.

Steady state blowing at α = 5° for the x_j/c = 0.60 jet, appears to create a region of intense velocity magnitude just above the jet flap, seen in Fig. 5.48. The momentum coefficient is large enough to incite flow separation from the jet location. It would also appear that upstream blowing mitigates velocity magnitude at the leading edge. With these variations in flow field, an amplitude change of ΔC_L = -0.091 is realised. This separated region is not replicated with periodic blowing, nor is the amplitude change. However, the large phase delay attributed with the near mid-chord jet causes the jet at φ = 0° to produce the smallest lift coefficient from the four phases considered. Although the separated region is not as extreme as continuous blowing, it is larger than other phases. For both φ = 90° & 180°, change in lift coefficient for both phases is $C_L - C_{Loff}$ = -0.037. However, the jet appears to start creating the high velocity region above the jet at φ = 180°. By the time it reaches φ = 270°, this region is a lot more visible as the separated flow begins to become more pronounced.

At α = 8°, the steady state case in Fig. 5.49 indicates an increase of velocity magnitude at the leading edge region, as well as the large recirculation region. It clearly can be seen that periodic blowing fails to reproduce this recirculation region. However, a separated region initiated at the jet location is sustained throughout the cycle, with small changes occurring between each flow field. This suggests flow field behaviour develops differently at this angle. The intensity of the recirculation region is at its strongest at φ = 0°. Velocity magnitude near the leading edge reduces with high frequency blowing, in comparison to the baseline case. As the size of the separated region remains identical between phase locations, this suggests upstream blowing reduces lift through influencing leading edge velocity magnitude. Continuous blowing only strengthens its ability to further mitigate the size of the high velocity magnitude region.

Continuous blowing at α = 10° provokes flow to separate from the upper surface, and is unable to reattach ahead of the trailing edge, as seen in Fig. 5.50. From the phases selected for the PIV study, the largest lift reduction is shown at φ = 0°, with $C_L - C_{Loff}$ = -0.114. Flow field measurements confirm this as the shear layer deflects at a similar angle to continuous blowing. However, the periodic jet does not attain the wake size of continuous blowing, and is incapable of mitigating the high velocity region near the leading edge, as observed with the steady state jet. The separated region diminishes in size at φ = 90°, to become imperceptible at φ = 180° where the lift response is close to the maximum lift coefficient. By φ = 270°, the jet is responding to the maximum jet velocity, thus, the flow field is developing towards what is observed at the beginning of the phase cycle.

Continuous blowing α = 13° incites a large recirculation region, with flow appearing to separate upstream of the jet at $x/c \approx 0.25$. This is caused by the jet flow impinging with freestream flow to deflect it away from the airfoil surface, thus inducing a low velocity region. The high velocity region near the leading edge is reduced in size, therefore contributing to the lift reduction, with ΔC_L = -0.23 for the continuous blowing. At the beginning of the cycle, φ = 0°, lift coefficient is near its minimum value, but is greater than the continuous blowing case. The separated region is reduced relative to continuous blowing. Fore of the jet the flow separates at $x/c \approx 0.40$, and is accompanied with a reduced wake size. Subsequently, as lift returns to the maximum lift coefficient, wake size begins to reduce gradually up to φ = 180°. As the cycle progresses to φ = 270°, the separated region grows to return to the size shown at φ = 0°.

For x_j/c = 0.08 at α = 10°, Fig. 5.52, continuous blowing compels the high velocity magnitude region to diminish in size, with low velocity ensuing along the entire upper surface, aft of the jet. Distinct separation occurs at $x/c \approx 0.20$, with separation enhancing in size with chordwise location. Periodic deployment at this frequency evokes a small amplitude change, with a large phase lag. It follows that at φ = 0°, lift is reducing and creates a change in lift of $C_L - C_{Loff}$ = -0.067. Interestingly, flow field measurements indicate the jet deployment induces separation to start just fore of the trailing edge, with little modification nearer to the jet. Minimum lift coefficient is nearer to φ = 90°, hence at this phase, lift is increasing but below what is observed at the start of the cycle. The density of streamlines around $x/c \approx 0.20$ indicates the shear layer detaches aft of the jet. Lift at φ = 180° approaches the maximum lift coefficient for this frequency. Separation remains present at this stage of the cycle. By φ = 270°, streamlines return closer to upper surface illustrating flow reattachment.

For α = 13°, continuous blowing forces separation to occur immediately at this location, deflecting the shear layer away from the surface at a larger angle to that seen with α = 10°. The combination of the larger recirculation region and deflection shear layer incites the largest change in lift coefficient observed throughout the cases considered, ΔC_L = -0.48. Minimum lift coefficient occurs at φ = 55°, with lift reduction of $C_{Lmin} - C_{Loff}$ = -0.35, despite the jet velocity being nearly zero at this phase. This is due to the large lag associated with the leading edge jet. The flow fields show the separated region grows and moves upstream between φ = 0° and 90° in agreement with the lift measurements. Flow near the leading edge accelerates at φ = 180° reaching maximum lift of C_{Lmax} = 0.94 at φ = 234°. Lift coefficient at φ = 270° decreases slightly to C_L = 0.925. This is validated with the flow field measurements as the wake size is small in comparison to measurements at other phases.

5.5 Conclusions

Phase averaged measurements were taken to analyse the efficacy of upstream blowing jet with periodic deployment, for reduced frequencies $k \leq 0.471$. In general, lift amplitude reduces with increased frequency. However, the jet flap remains an effective actuator with retaining lift amplitude with frequency. For the $x_j/c = 0.95$ jet blowing periodically at $k = 0.314$, lift amplitude is at 75% of the steady state change in lift at $\alpha = 0°$. It is observed that the jet flap performance varies with angle of attack, as shown at $x_j/c = 0.60$; increasing the angle of attack increases the change in lift at $k = 0$ but the rate of amplitude decay also increases, as shown at $k = 0.471$ where all angles achieve similar changes in lift. Evaluation of the effect of chordwise location shows that the jet remains effective at all locations considered. However, phase lag is found to be dependent on chordwise location and angle of attack; phase lag increases as jet is displaced upstream or if angle is increased for a given jet location. The aerodynamic response was modelled using a first order system in order to obtain time constant. At $\alpha = 0°$ for $x_j/c = 0.95$, shows time constant could be approximated as low as $\kappa = 1.46$. However, the time constant is proportional to the angle of attack, hence, increases. Phase averaged flow field measurements for $k = 0.393$ show upstream blowing incites a separated region by displacing the shear layer. However, the size of the separated region does not reach that of continuous blowing, as expected.

5.6 Figures

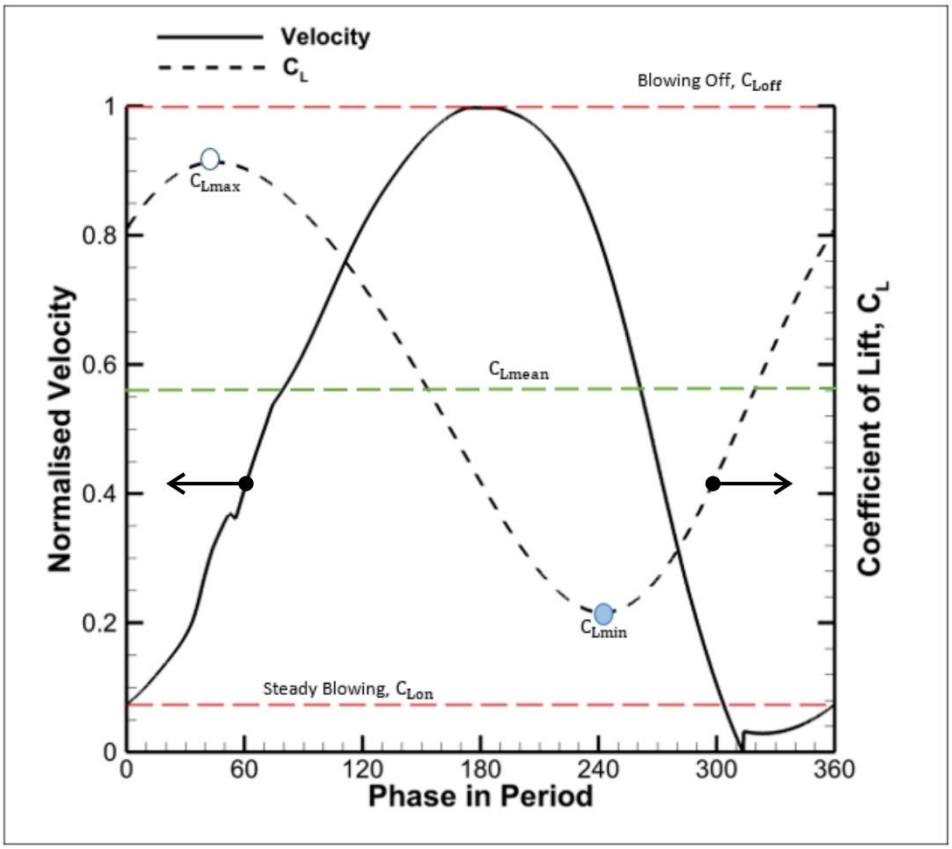

Figure 5.1 - Illustration of jet profile and lift response.

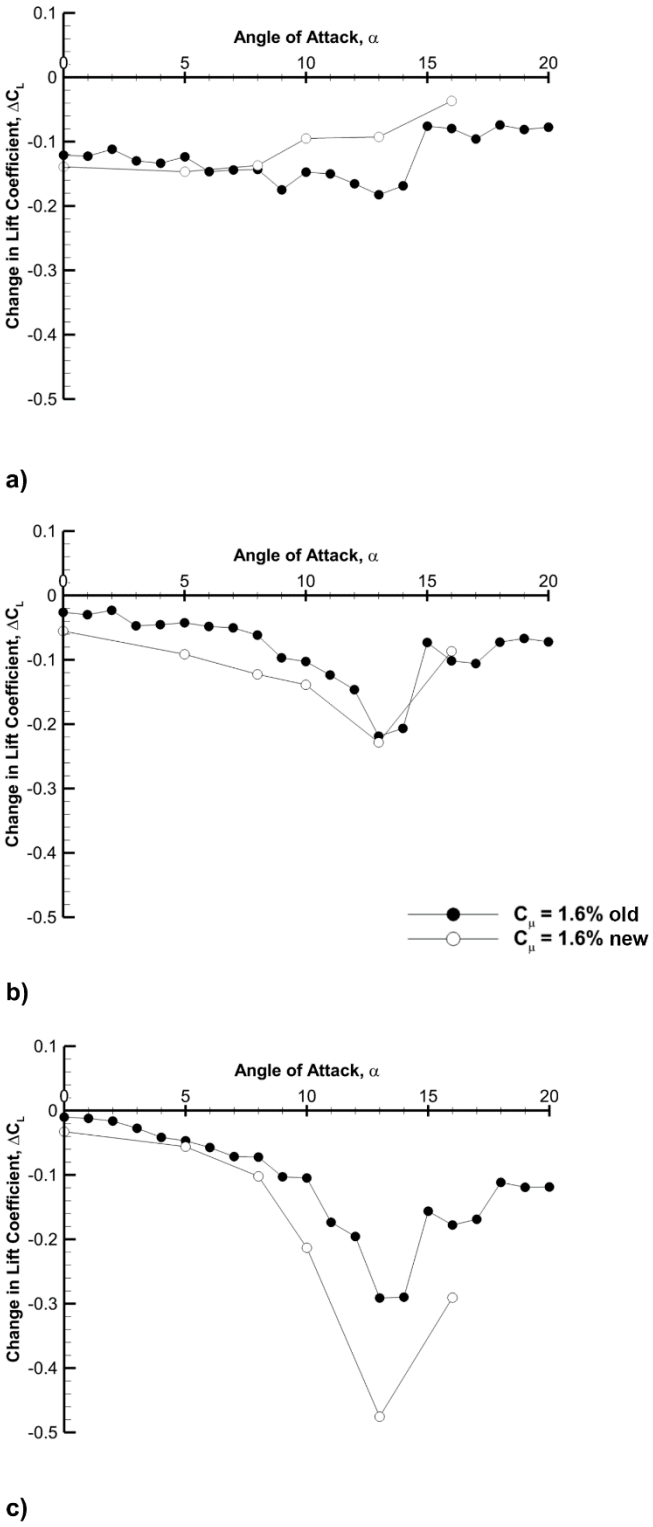

Figure 5.2 - Change in lift coefficient comparison between old data and new data at C_μ = 1.6%; a) x_j/c = 0.95, b) x_j/c = 0.60 & c) x_j/c = 0.08

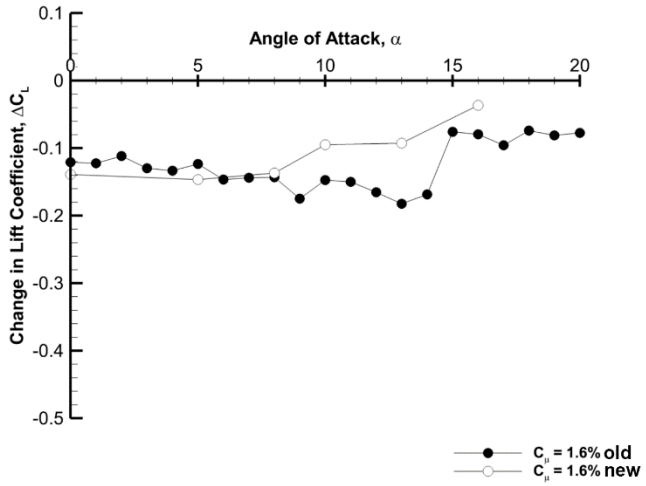

a)

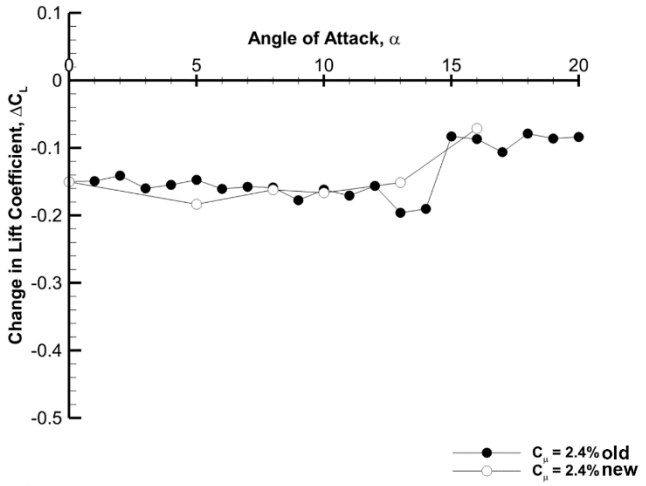

b)

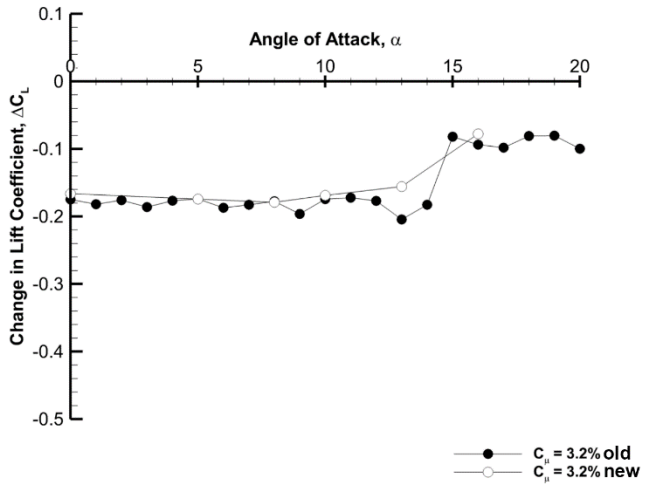

c)

Figure 5.3 - Change in lift coefficient comparison between old data and new data at x_j/c = 0.95; a) C_μ = 1.6%, b) C_μ = 2.4% & c) C_μ = 3.2%.

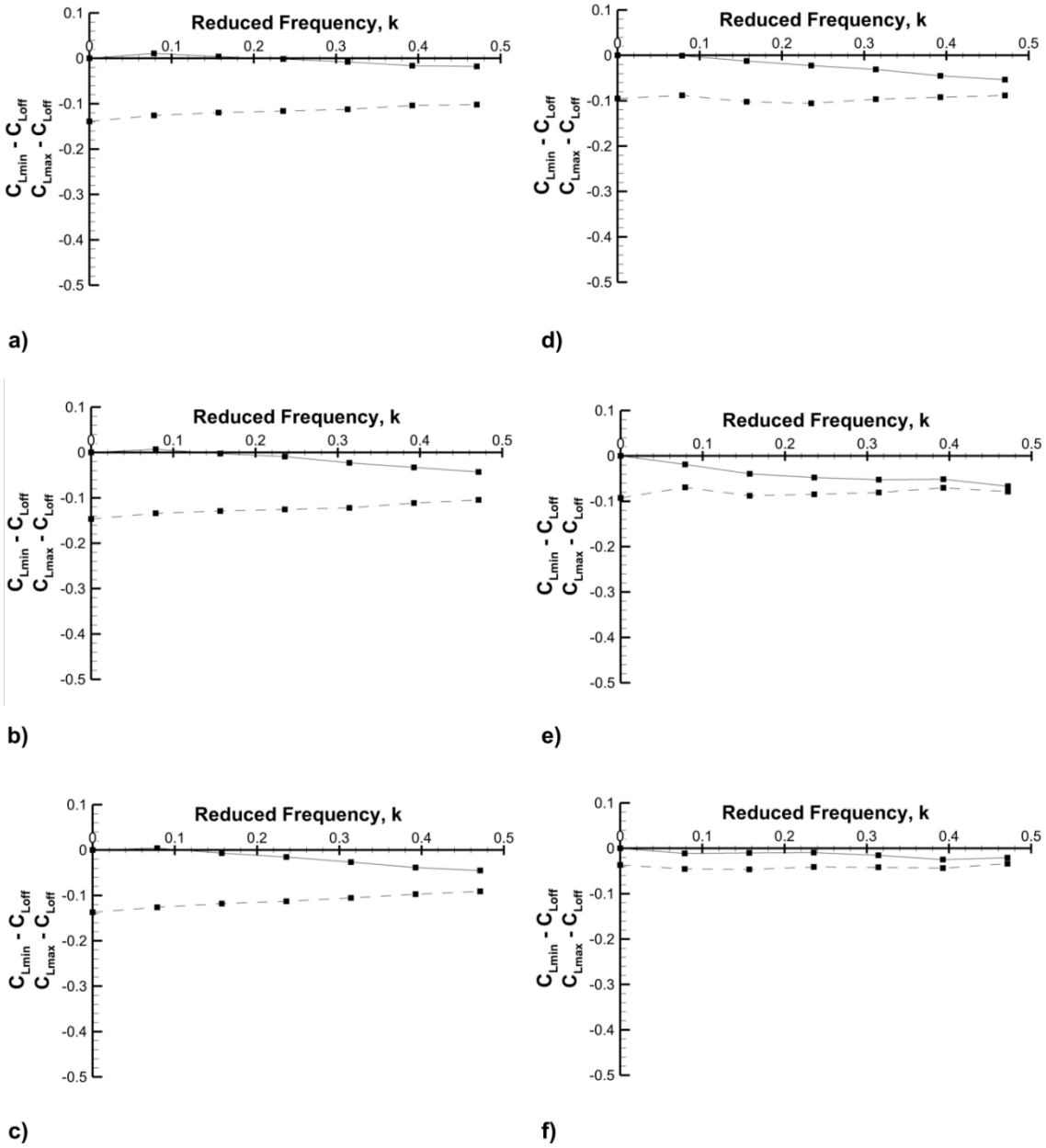

Figure 5.4 - $C_{L(min,max)}$) - C_{Loff}vs reduced frequency for x_j/c = 0.95 at C_μ = 1.6% for; a) α = 0°, b) α = 5°, c) α = 8°, d) α = 10°, e) α = 13° & f) α = 16°.

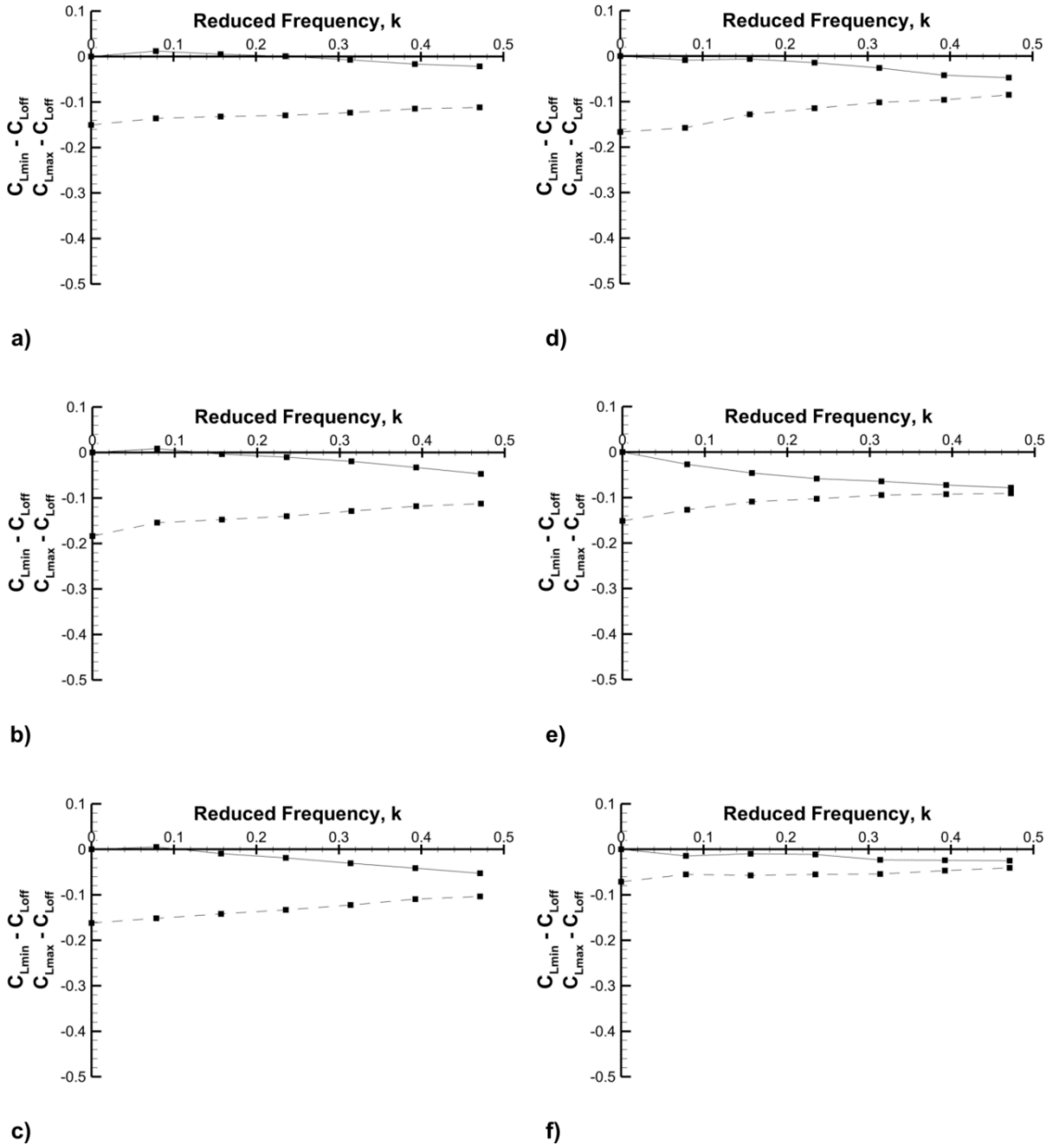

Figure 5.5 -$C_{L(min,max)}$) - C_{Loff}vs reduced frequency for x_j/c = 0.95 at C_μ = 2.4% for; a) α = 0°, b) α = 5°, c) α = 8°, d) α = 10°, e) α = 13° & f) α = 16°.

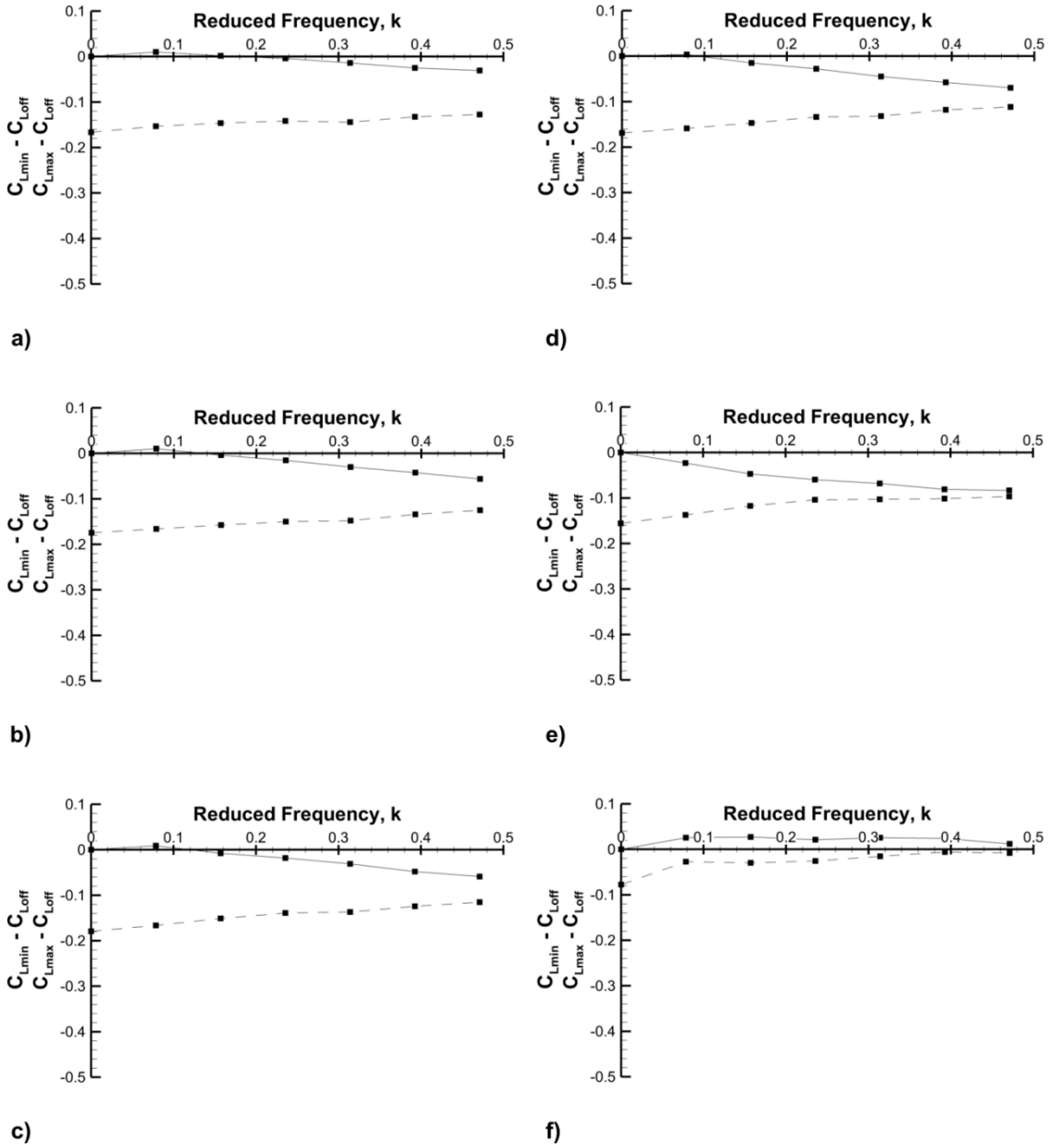

Figure 5.6 - $C_{L(min,max)} - C_{Loff}$ vs reduced frequency for x_j/c = 0.95 at C_μ = 3.2% for; a) α = 0°, b) α = 5°, c) α = 8°, d) α = 10°, e) α = 13° & f) α = 16°.

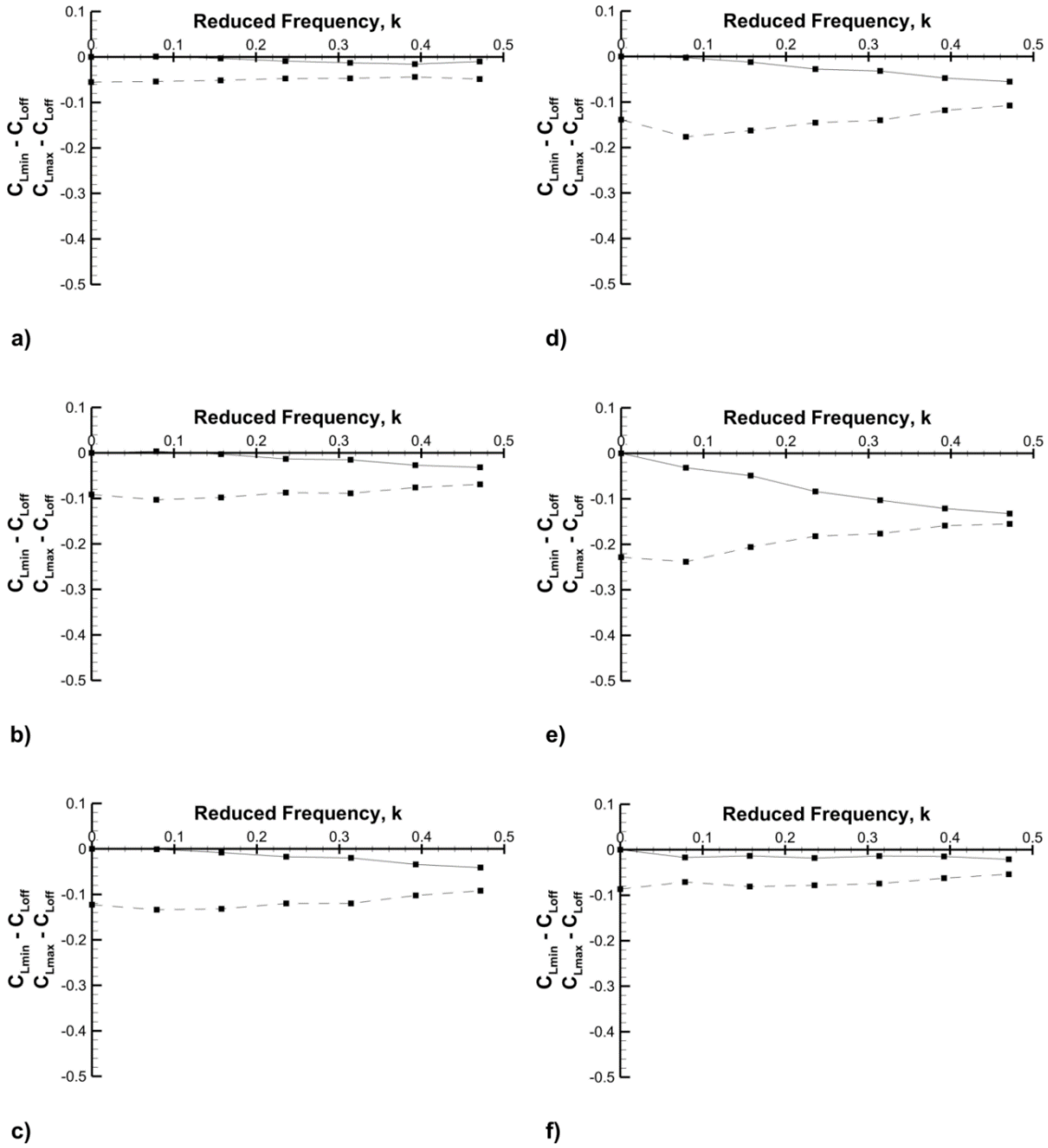

Figure 5.7- $C_{L(min,max)}$) - C_{Loff}vs reduced frequency for x_j/c = 0.60 at C_μ = 1.6% for; a) α = 0°, b) α = 5°, c) α = 8°, d) α = 10°, e) α = 13° & f) α = 16°.

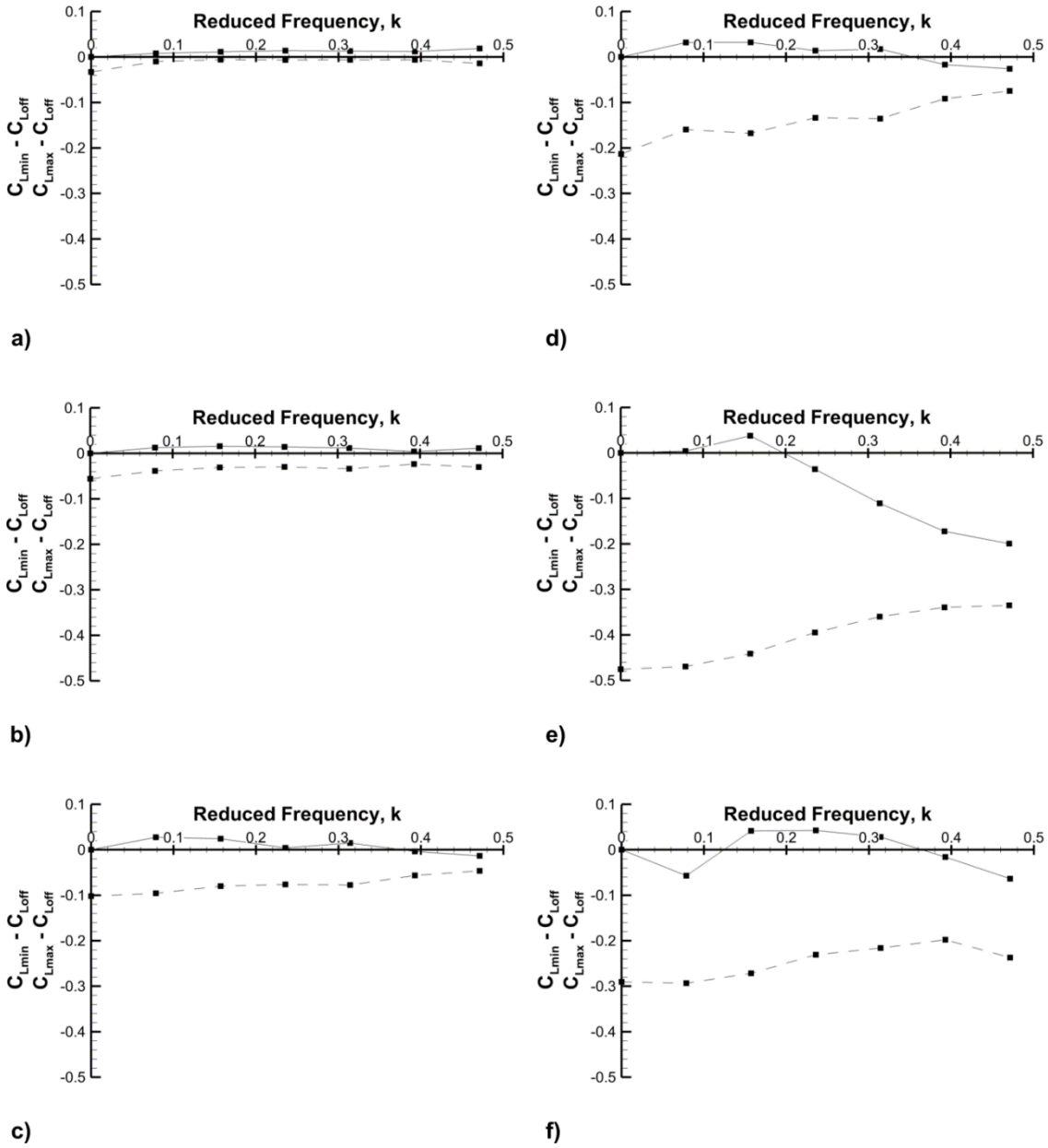

Figure 5.8 - $C_{L(min,max)} - C_{Loff}$ vs reduced frequency for x_j/c = 0.08 at C_μ = 1.6% for; a) α = 0°, b) α = 5°, c) α = 8°, d) α = 10°, e) α = 13° & f) α = 16°.

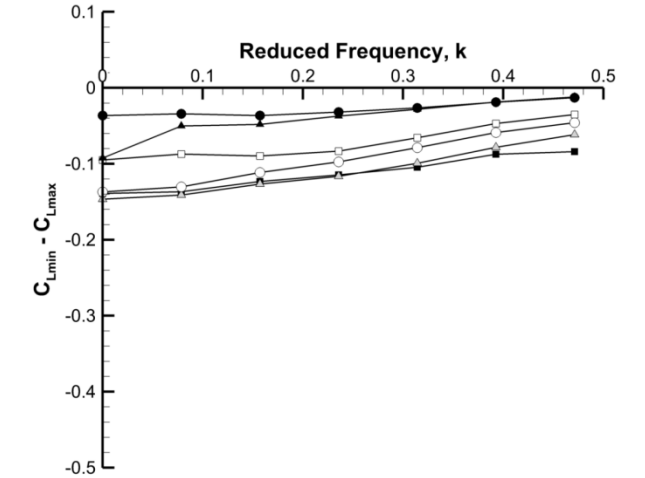

a)

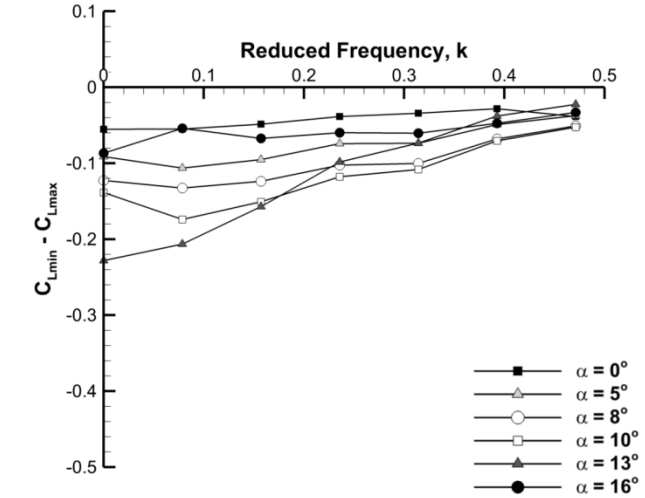

b)

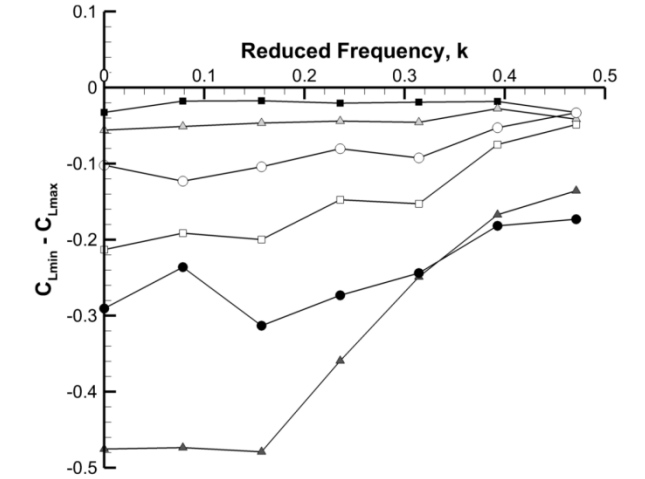

c)

Figure 5.9 - $C_{Lmin} - C_{Lmax}$ with reduced frequency, C_μ = 1.6%, for; a) x_j/c = 0.95, b) x_j/c = 0.60 & c) x_j/c = 0.08.

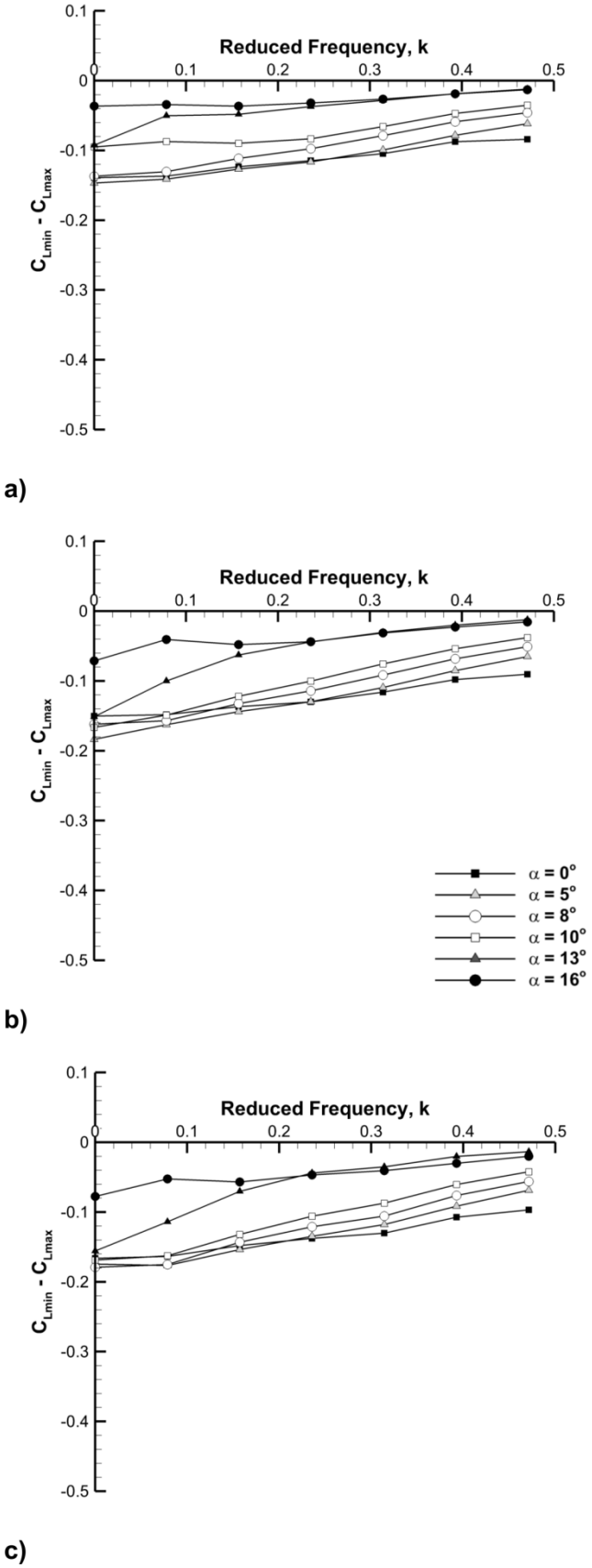

Figure 5.10 - $C_{Lmin} - C_{Lmax}$ vs reduced frequency for x_j/c = 0.95; a) C_μ = 1.6%, b) C_μ = 2.4% & c) C_μ = 3.2%.

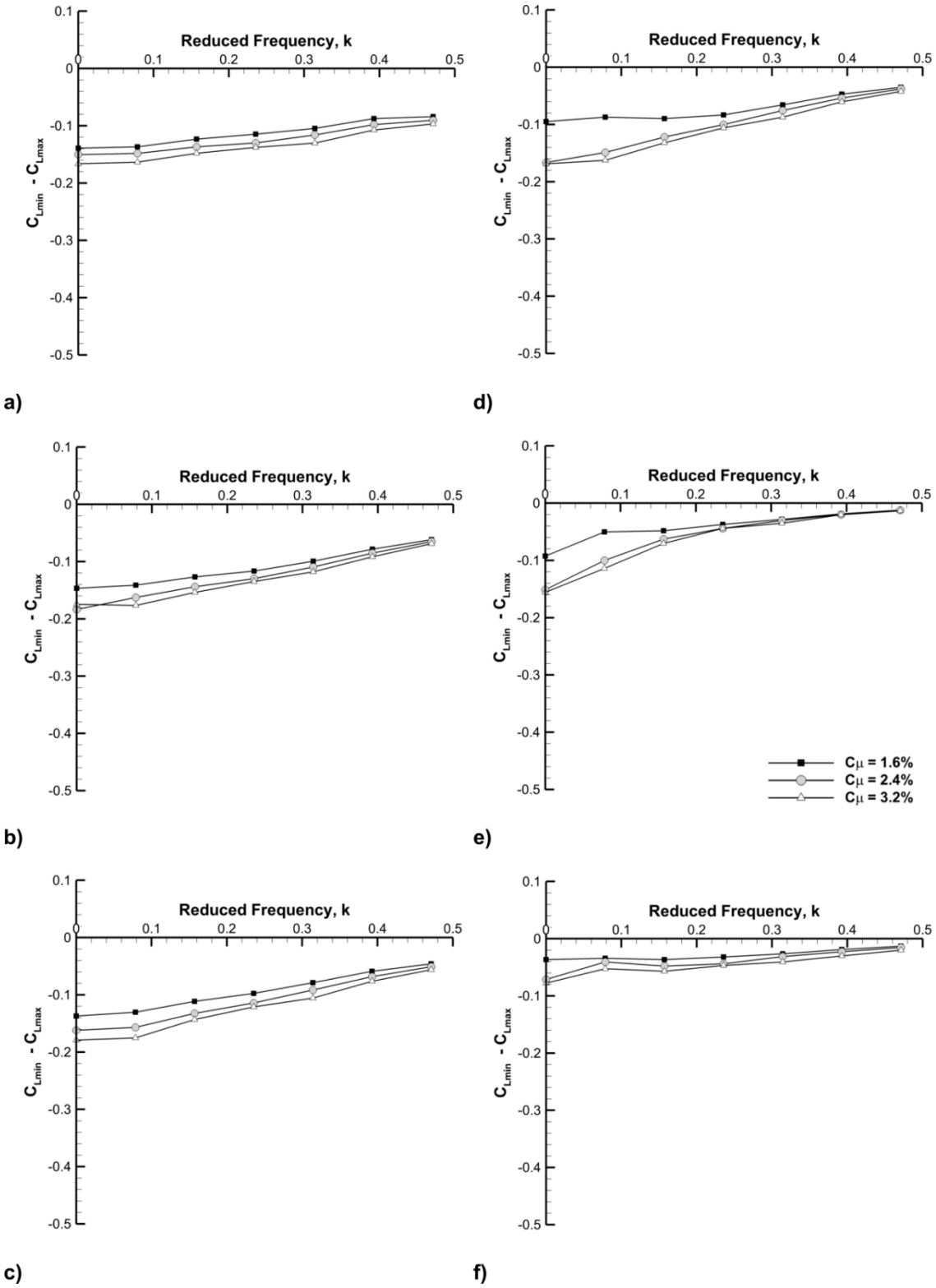

Figure 5.11 - $C_{Lmin} - C_{Lmax}$ comparison with momentum coefficient for x_j/c = 0.95; a) α = 0°, b) α = 5°, c) α = 8°, d) α = 10°, e) α = 13° & f) α = 16°.

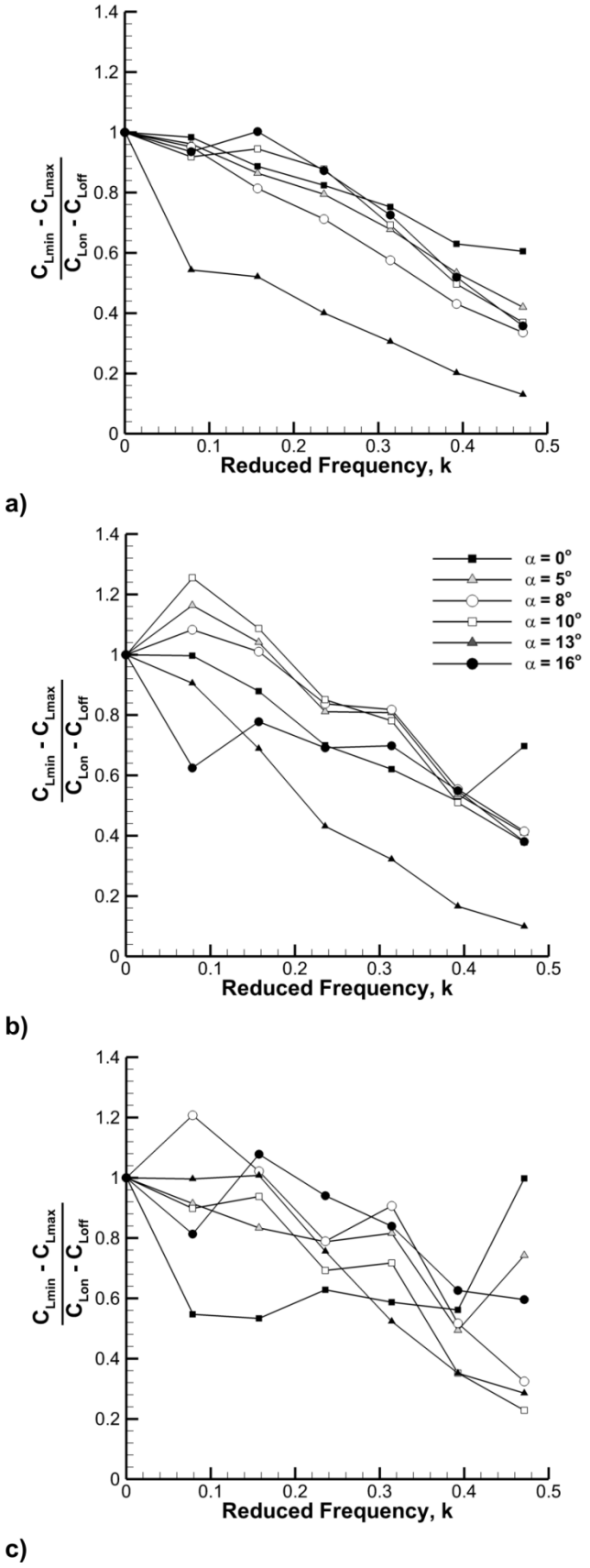

Figure 5.12 - Amplitude ratio with reduced frequency for C_μ = 1.6%; a) x_j/c = 0.95, b) x_j/c = 0.60 & c) x_j/c = 0.08.

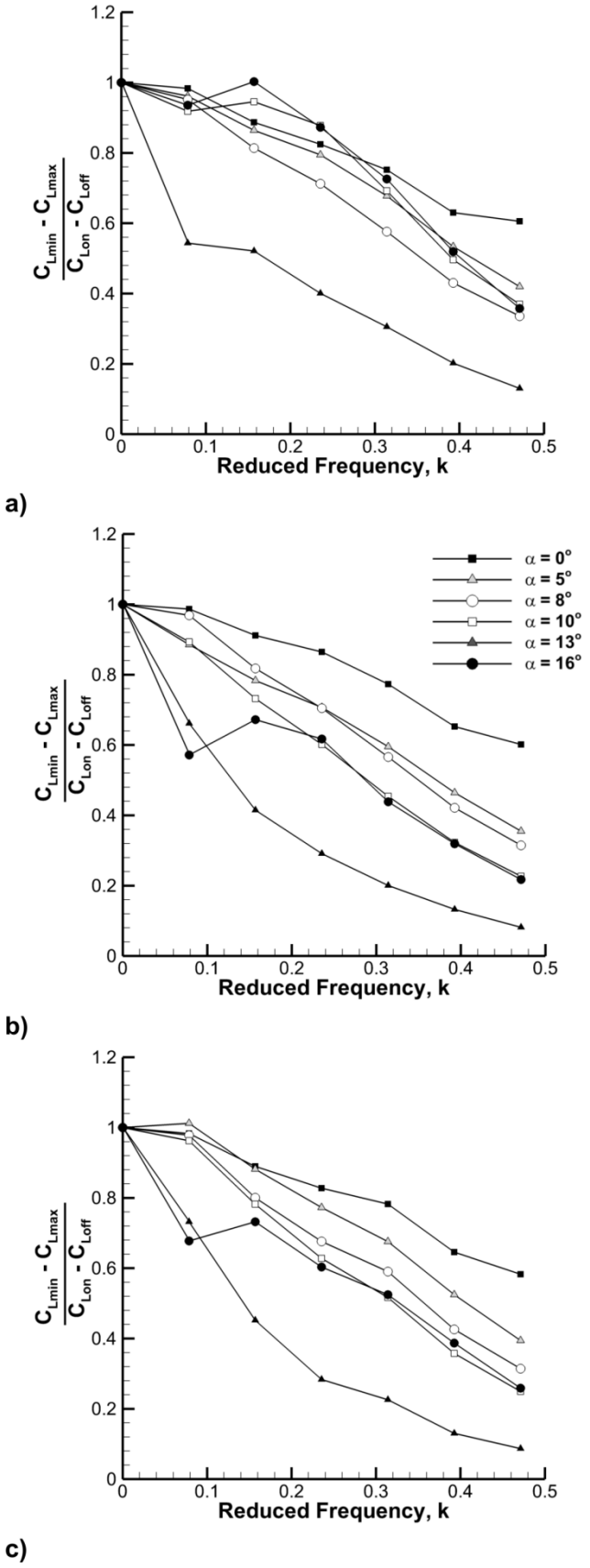

Figure 5.13 - Amplitude ratio with reduced frequency for x_j/c = 0.95; a) C_μ = 1.6%, b) C_μ = 2.4% & c) C_μ = 3.2%.

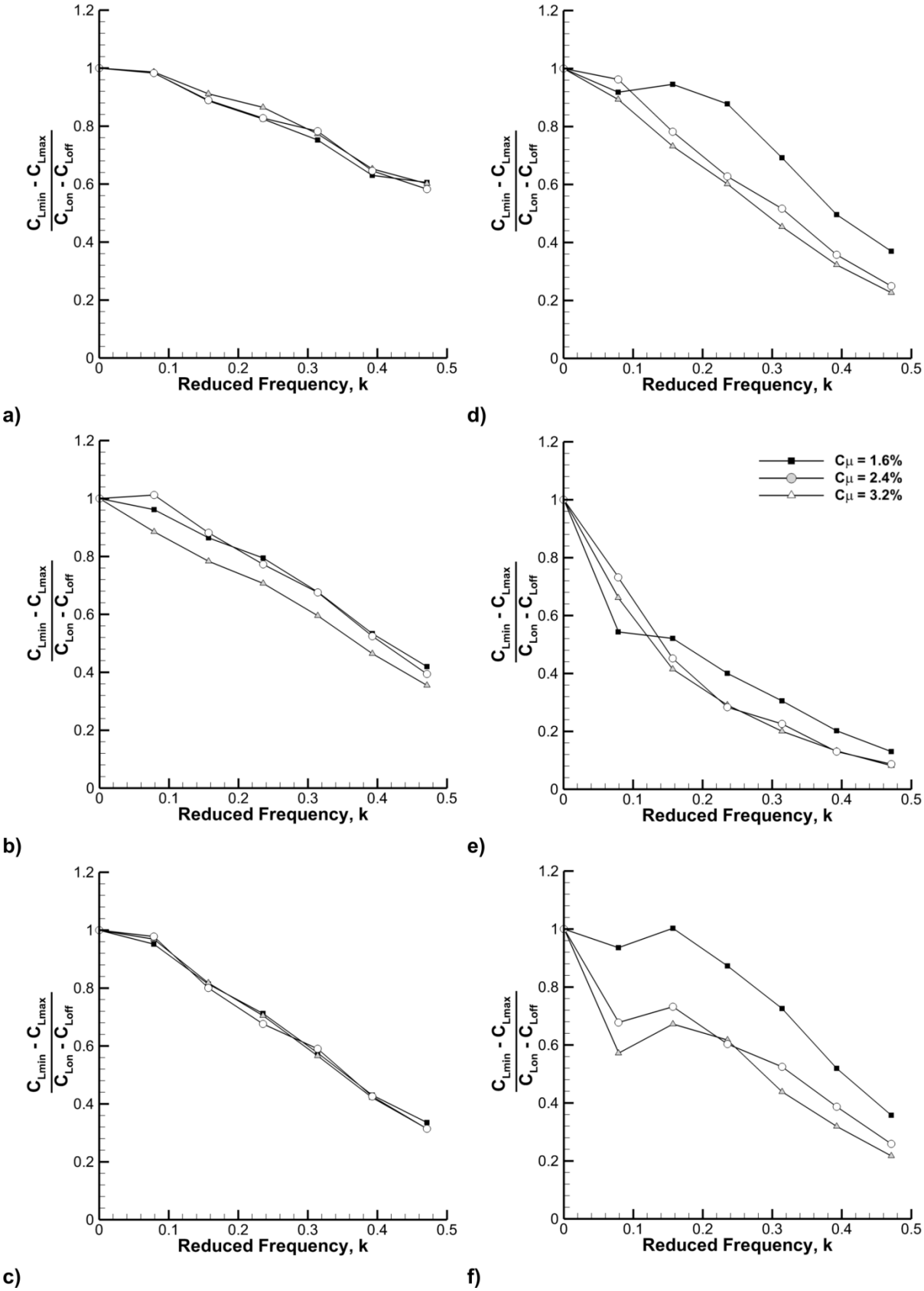

Figure 5.14 - Amplitude ratio with momentum coefficient for x_j/c = 0.95; a) α = 0°, b) α = 5°, c) α = 8°, d) α = 10°, e) α = 13° & f) α = 16°.

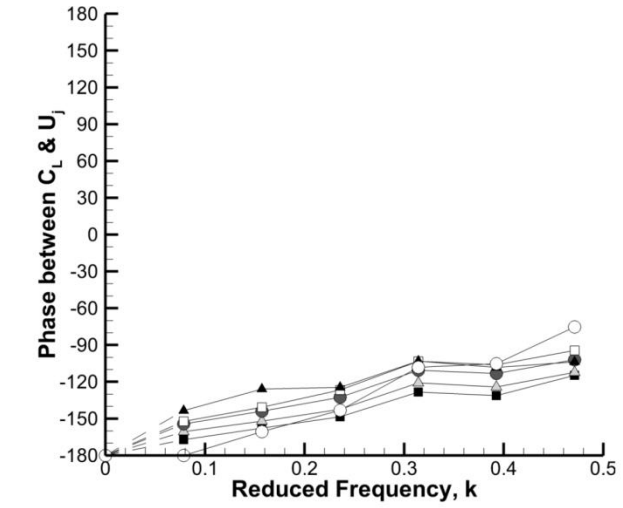

a)

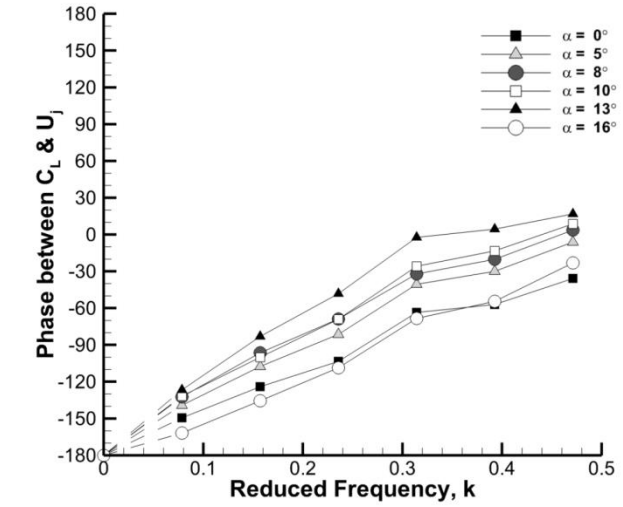

b)

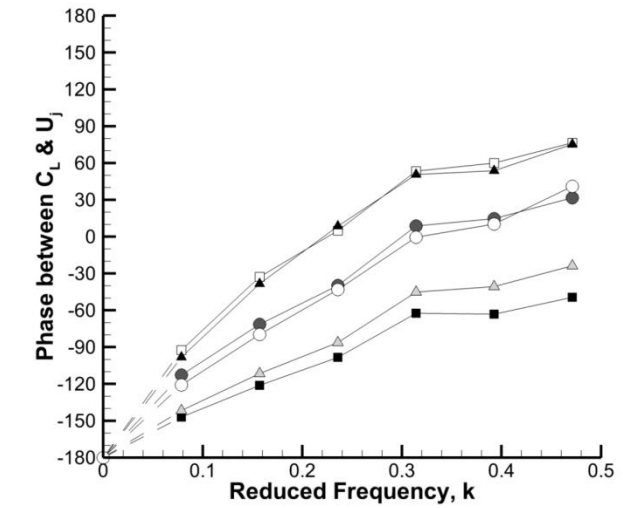

c)

Figure 5.15 - Phase between lift coefficient and jet velocity, showing the effect of varying angle of attack at C_μ = 1.6% for a) x_j/c = 0.95, b) x_j/c = 0.60 & c) x_j/c = 0.08.

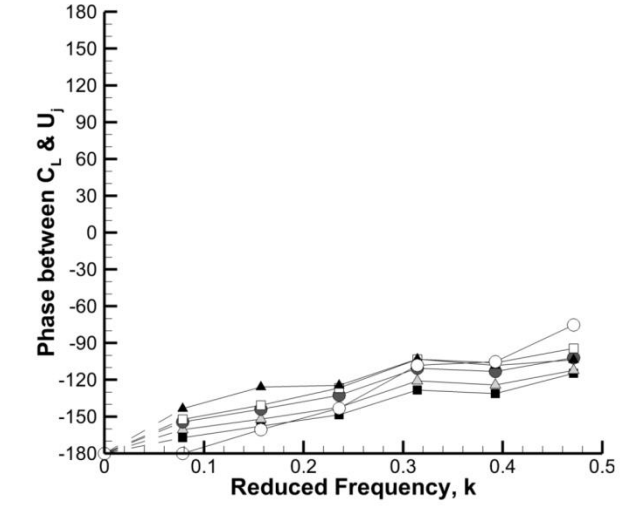

a)

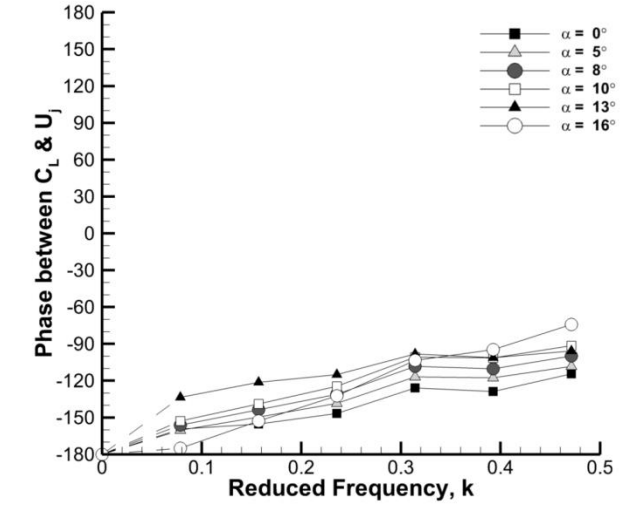

b)

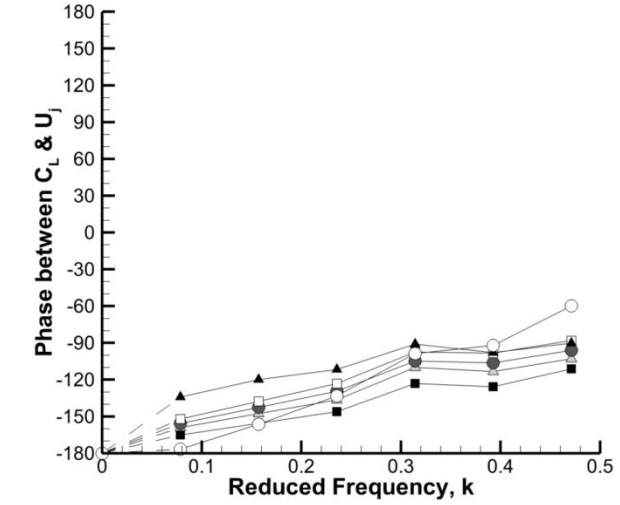

c)

Figure 5.16 - Phase between lift coefficient and jet velocity, showing the effect of varying angle of attack at x_j/c = 0.95 for a) C_μ = 1.6%, b) C_μ = 2.4%, & c) C_μ = 3.2%.

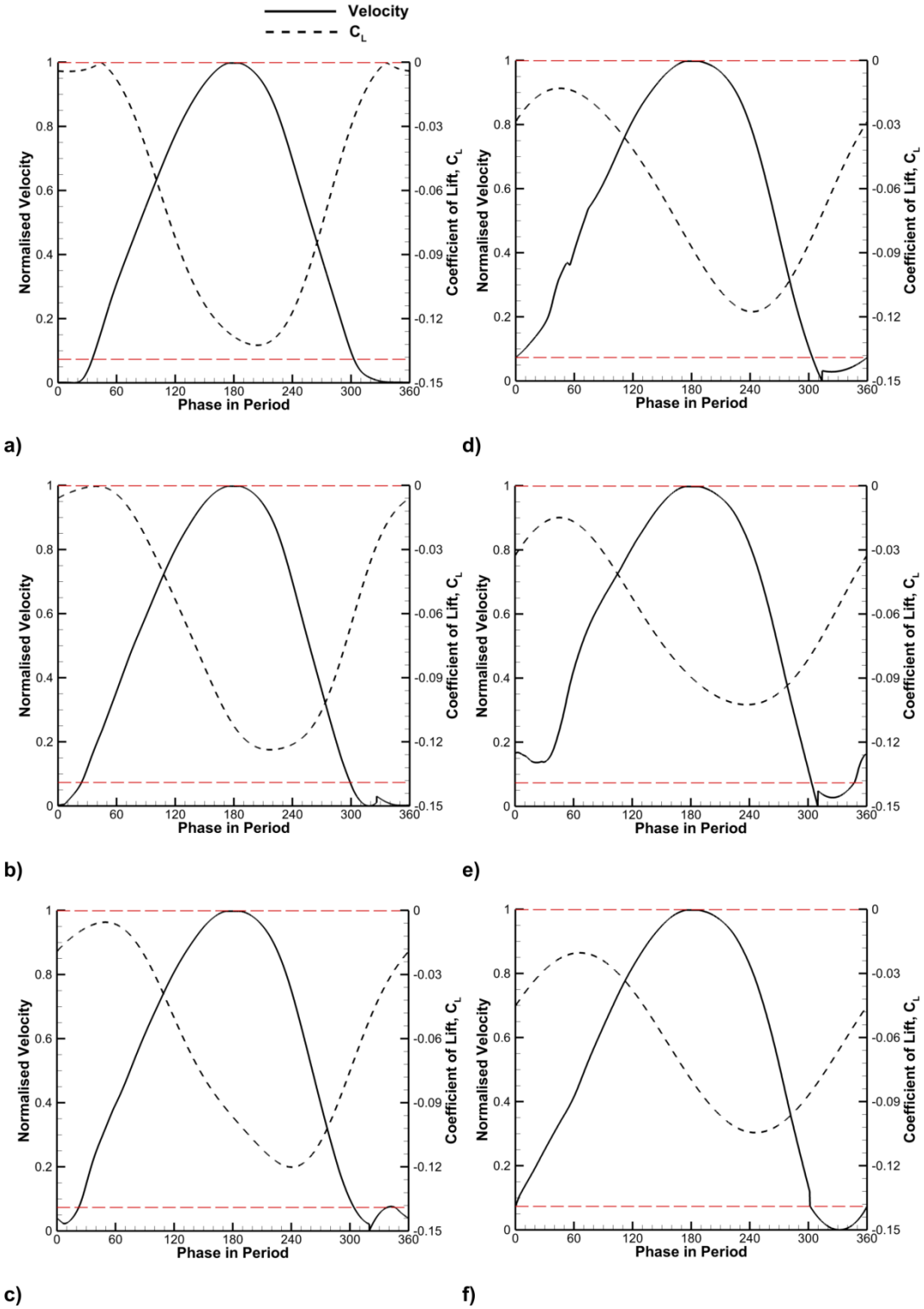

Figure 5.17 - Lift coefficient with phase in period, at α = 0°, x_j/c = 0.95, C_μ = 1.6% for; a) k = 0.079, b) k = 0.157, c) k = 0.236, d) k = 0.314, e) k =0.393, & f) k = 0.471.

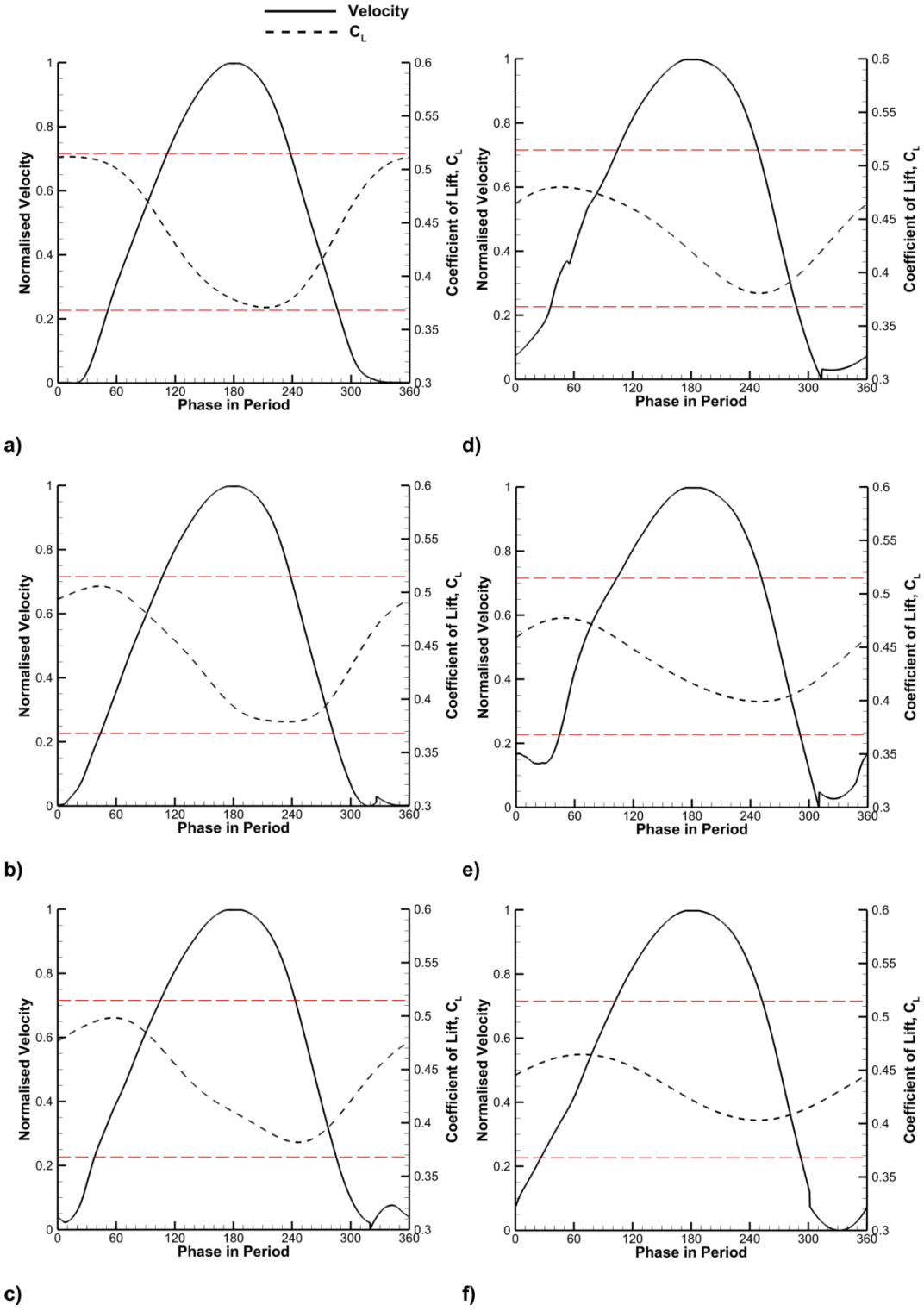

Figure 5.18 - Lift coefficient with phase in period, at α = 5°, x_j/c = 0.95, C_μ = 1.6% for; a) k = 0.079, b) k = 0.157, c) k = 0.236, d) k = 0.314, e) k =0.393, & f) k = 0.471.

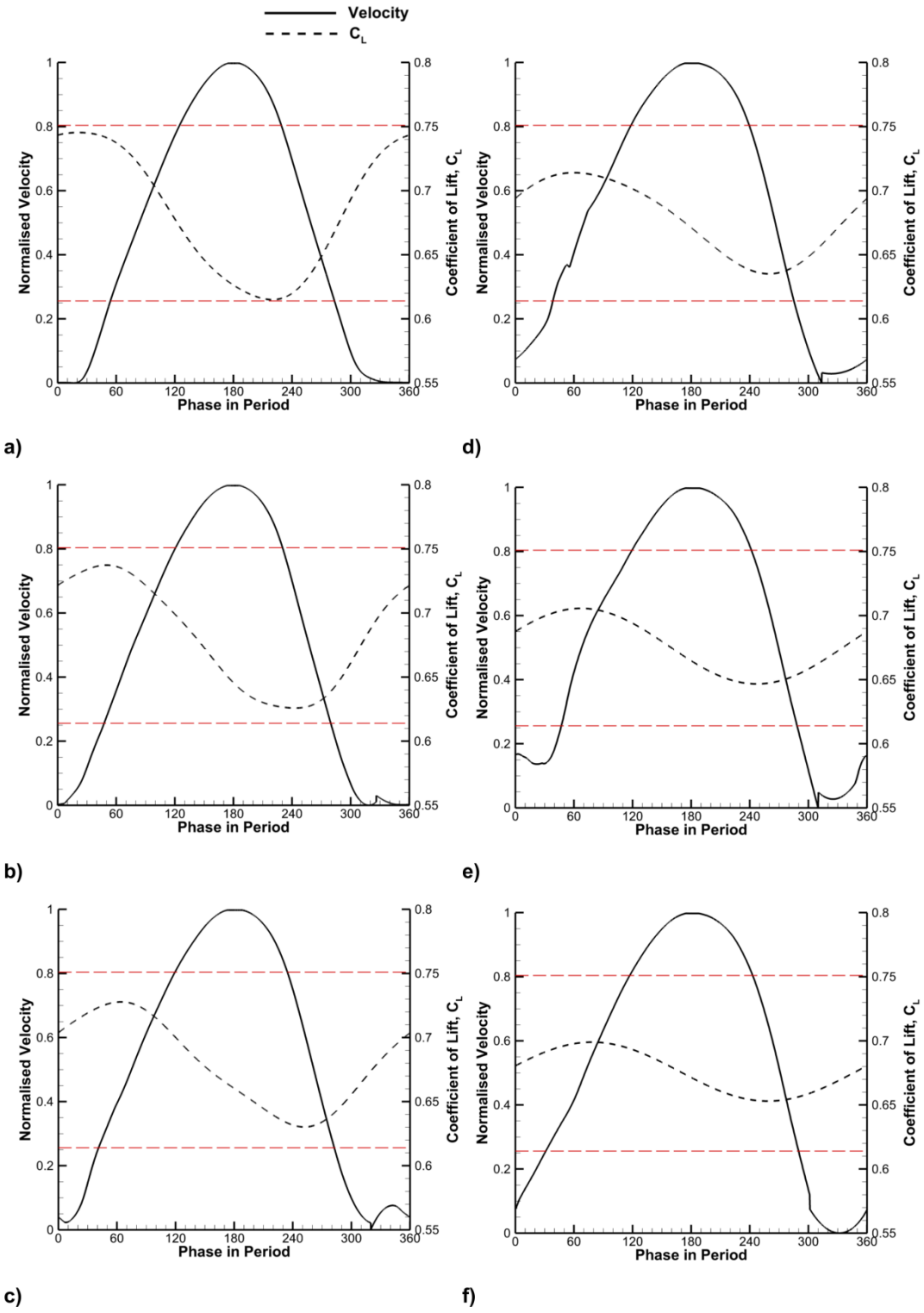

Figure 5.19 - Lift coefficient with phase in period, at α = 8°, x_j/c = 0.95, C_μ = 1.6% for; a) k = 0.079, b) k = 0.157, c) k = 0.236, d) k = 0.314, e) k =0.393, & f) k = 0.471.

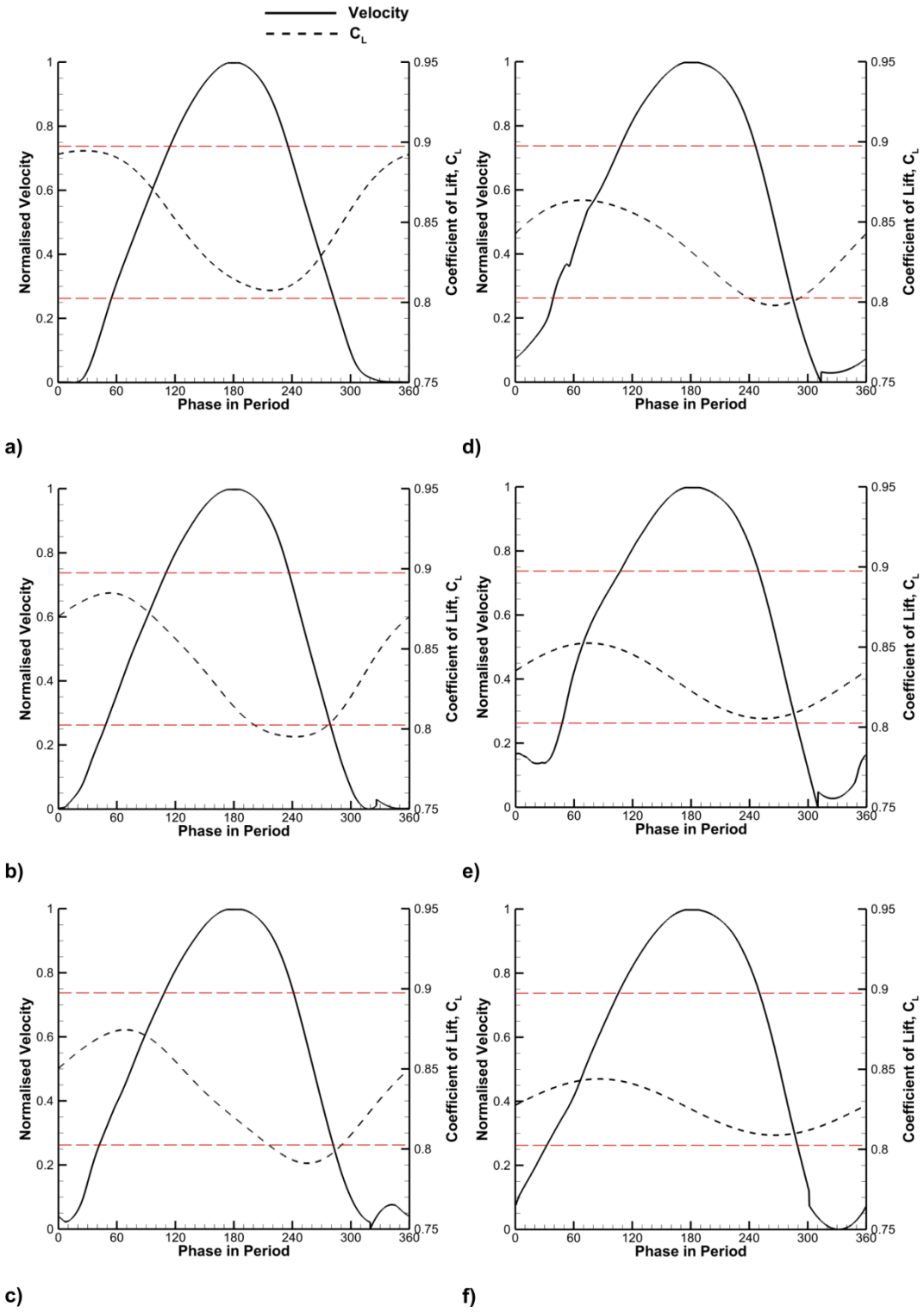

Figure 5.20 - Lift coefficient with phase in period, at α = 10°, x_j/c = 0.95, C_μ = 1.6% for; a) k = 0.079, b) k = 0.157, c) k = 0.236, d) k = 0.314, e) k =0.393, & f) k = 0.471.

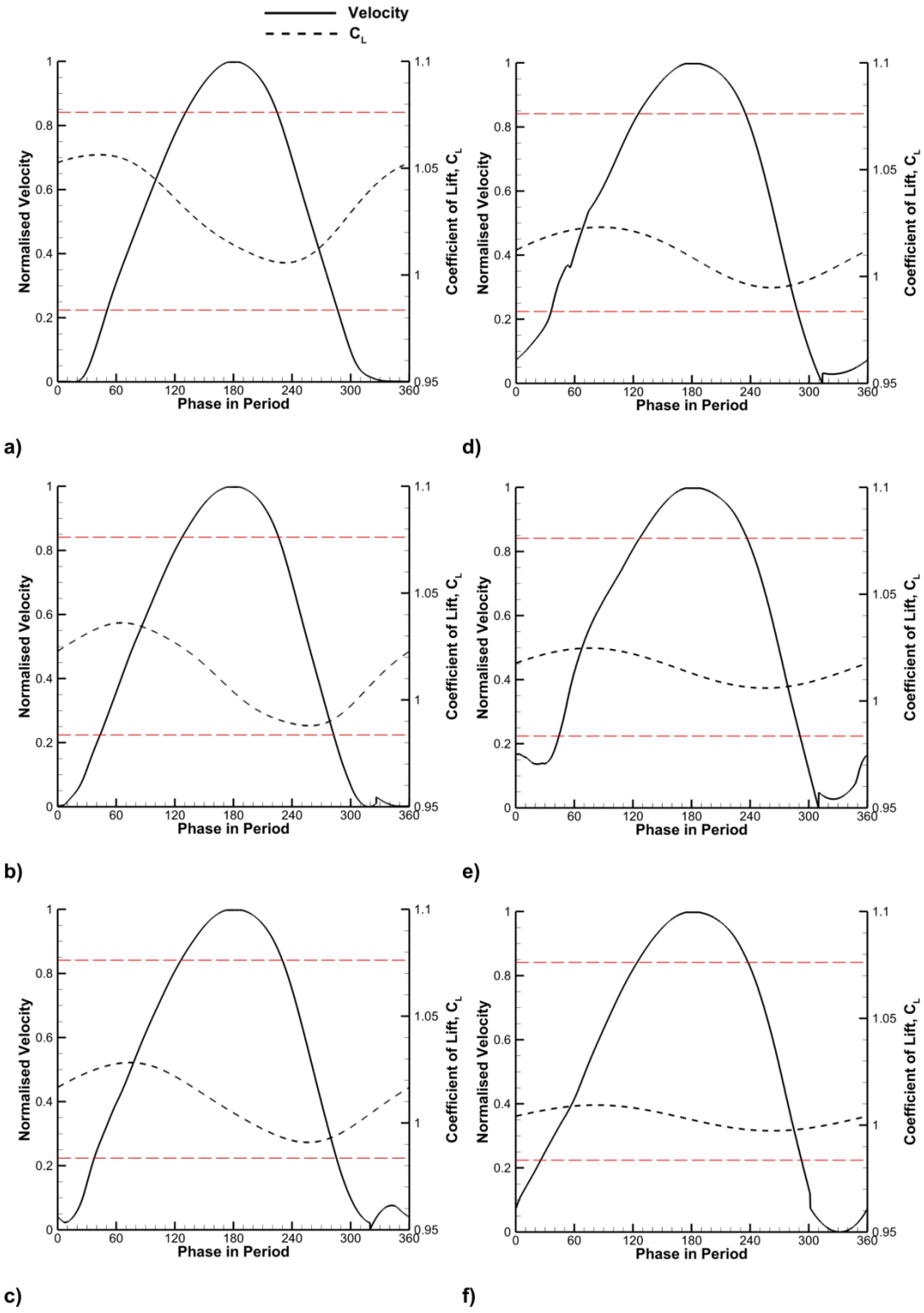

Figure 5.21 - Lift coefficient with phase in period, at α = 13°, x_j/c = 0.95, C_μ = 1.6% for; a) k = 0.079, b) k = 0.157, c) k = 0.236, d) k = 0.314, e) k =0.393, & f) k = 0.471.

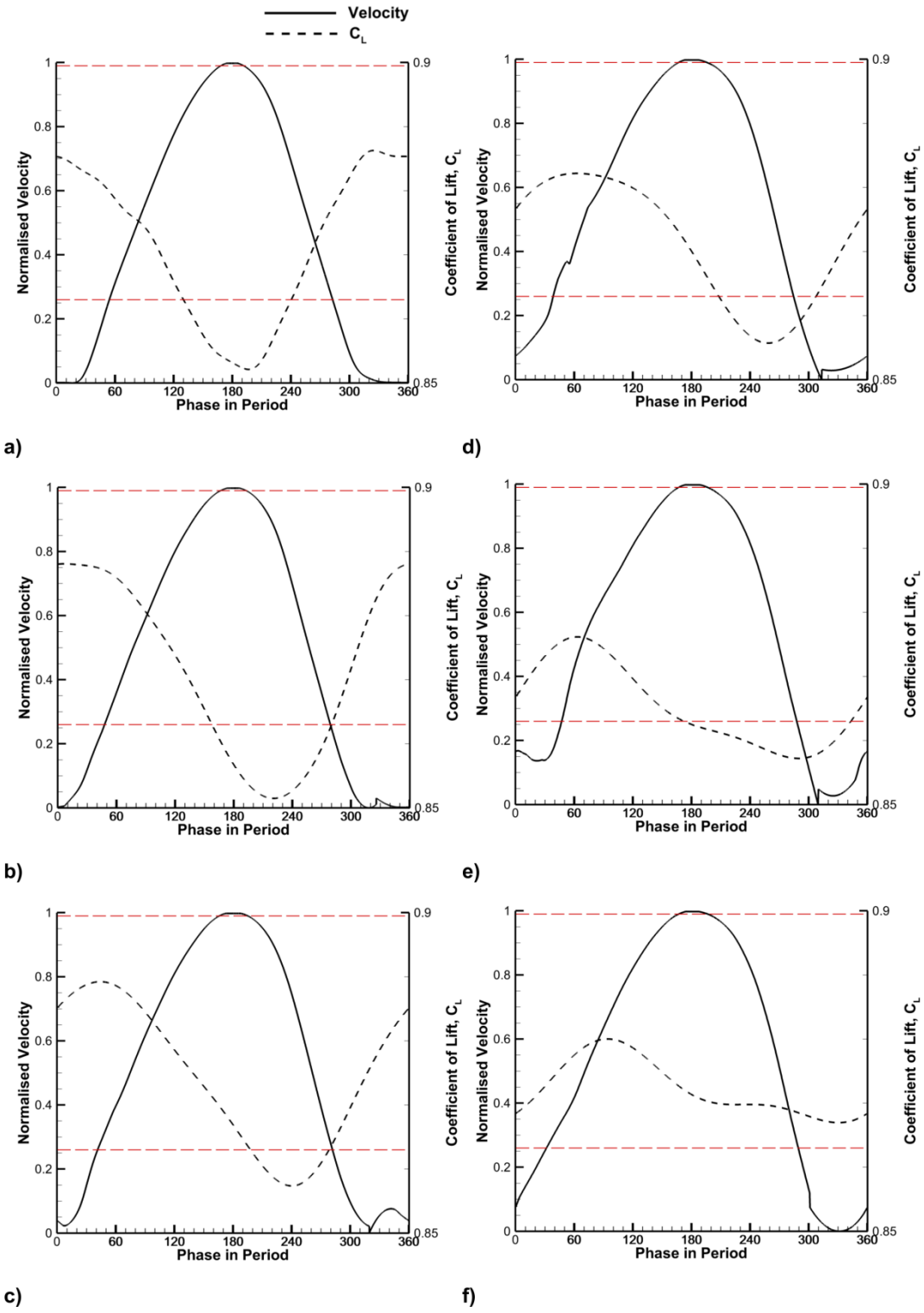

Figure 5.22 - Lift coefficient with phase in period, at α = 16°, x_j/c = 0.95, C_μ = 1.6% for; a) k = 0.079, b) k = 0.157, c) k = 0.236, d) k = 0.314, e) k =0.393, & f) k = 0.471.

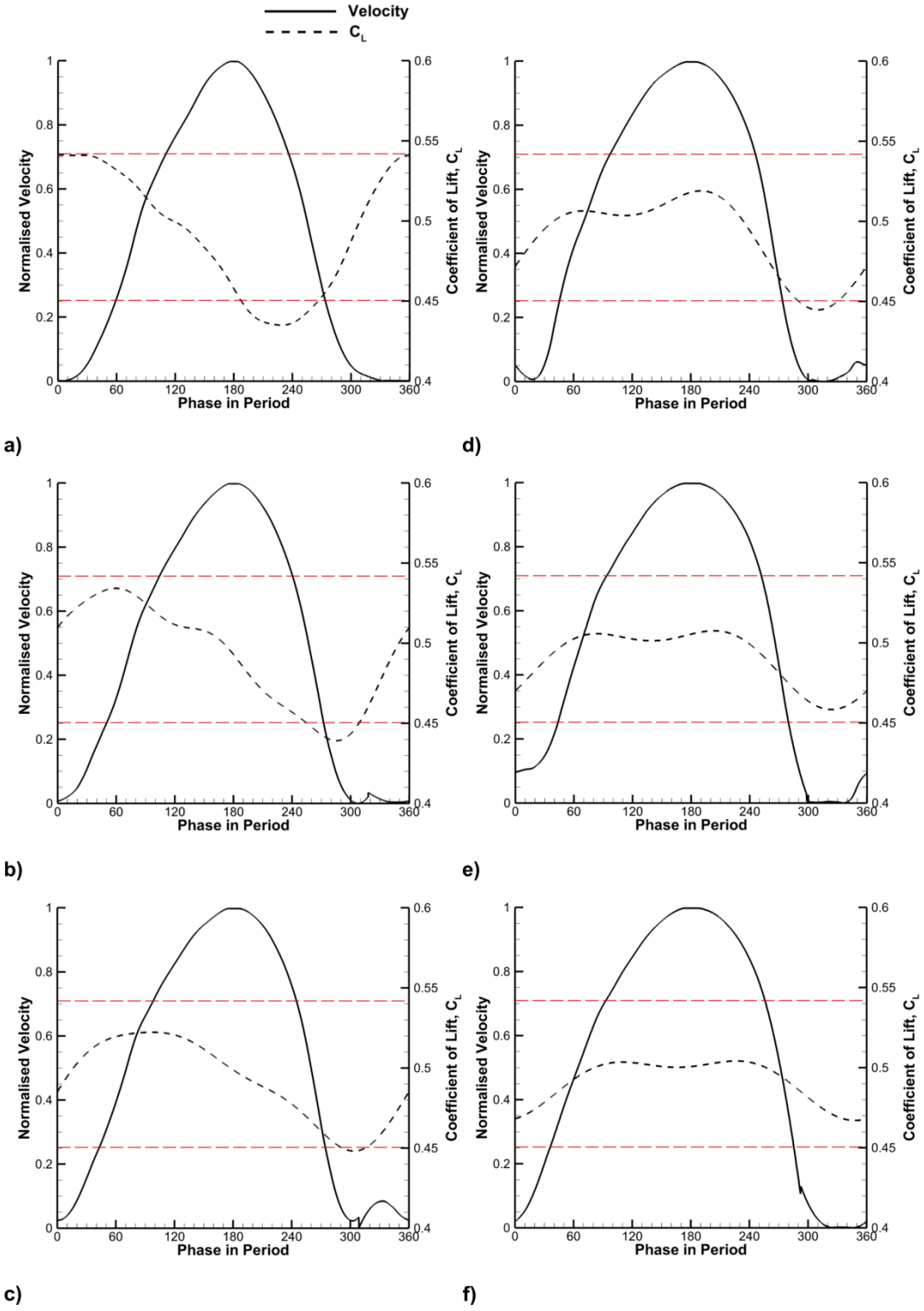

Figure 5.23 - Lift coefficient with phase in period, at α = 5°, x_j/c = 0.60, C_μ = 1.6% for; a) k = 0.079, b) k = 0.157, c) k = 0.236, d) k = 0.314, e) k =0.393, & f) k = 0.471.

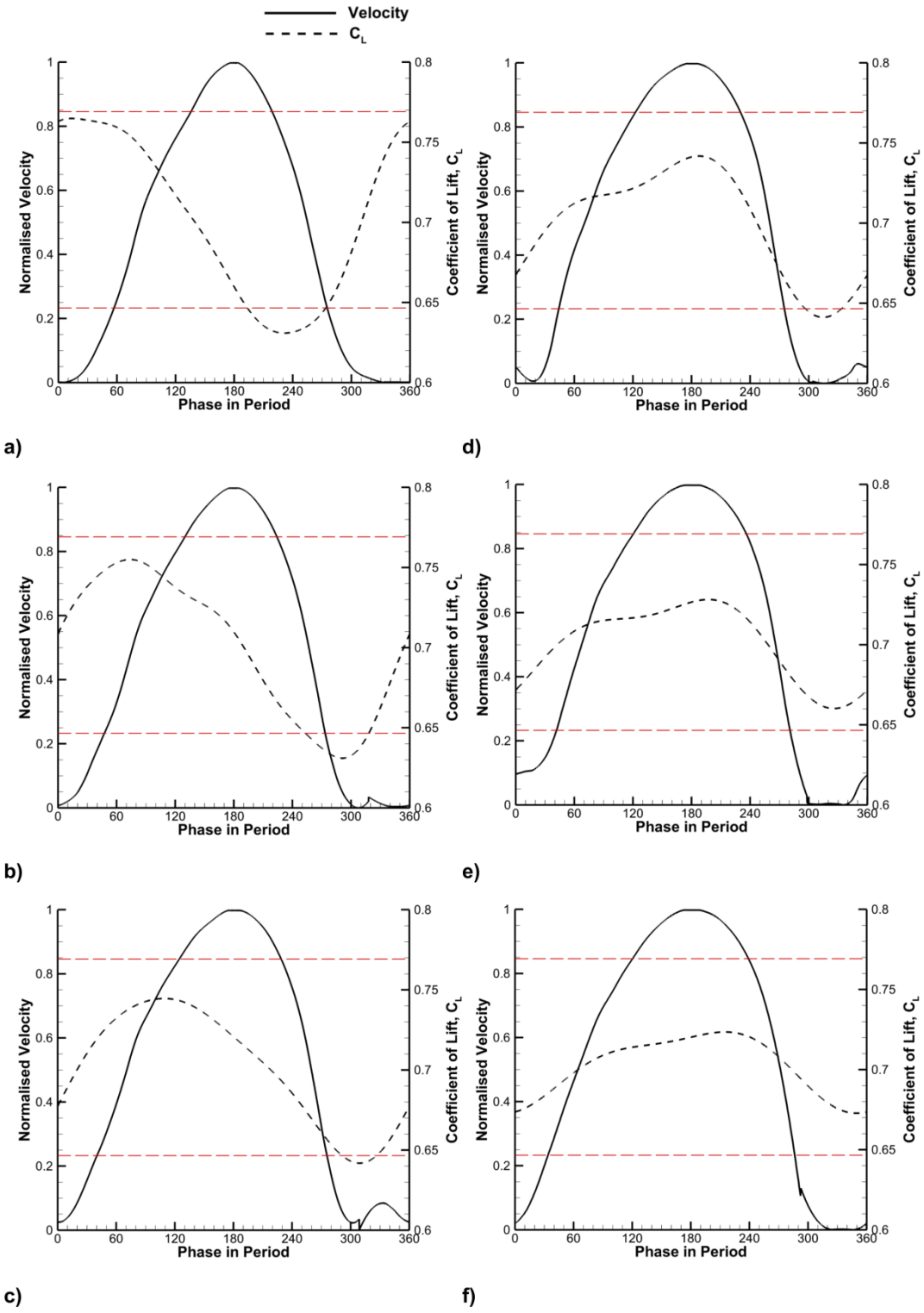

Figure 5.24 - Lift coefficient with phase in period, at α = 8°, x_j/c = 0.60, C_μ = 1.6% for; a) k = 0.079, b) k = 0.157, c) k = 0.236, d) k = 0.314, e) k =0.393, & f) k = 0.471.

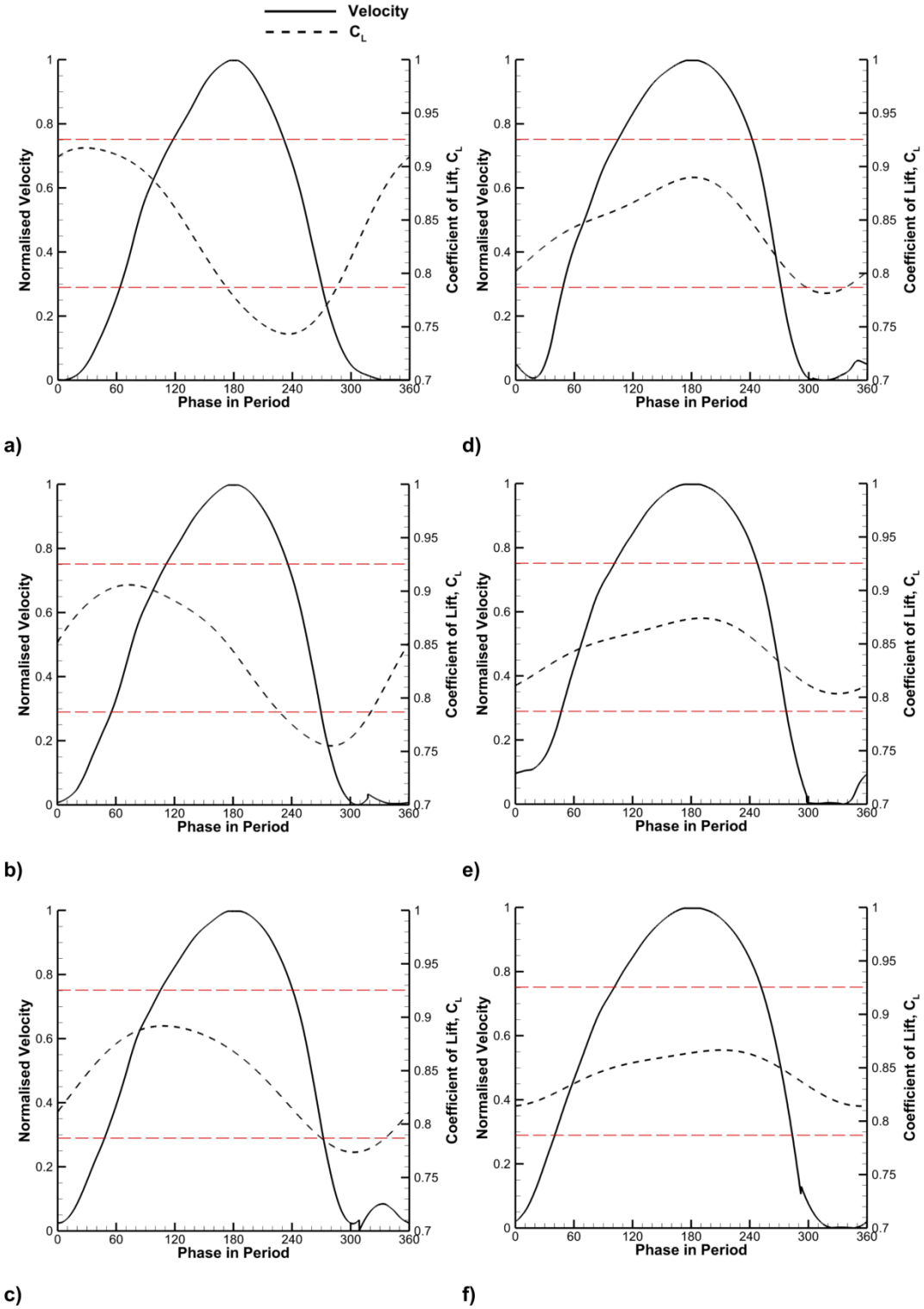

Figure 5.25 - Lift coefficient with phase in period, at α = 10°, x_j/c = 0.60, C_μ = 1.6% for; a) k = 0.079, b) k = 0.157, c) k = 0.236, d) k = 0.314, e) k =0.393, & f) k = 0.471.

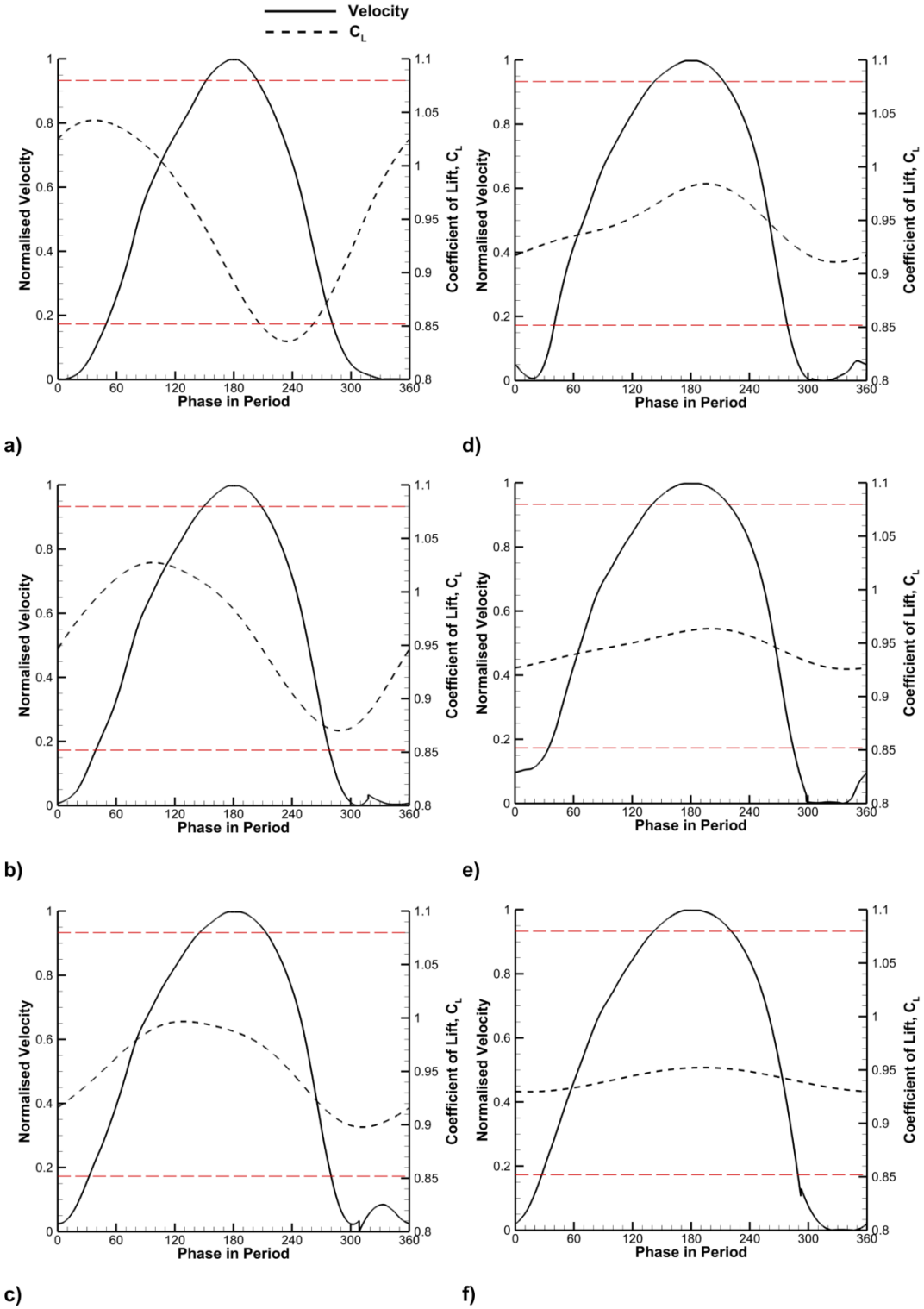

Figure 5.26 - Lift coefficient with phase in period, at α = 13°, x_j/c = 0.60, C_μ = 1.6% for; a) k = 0.079, b) k = 0.157, c) k = 0.236, d) k = 0.314, e) k =0.393, & f) k = 0.471.

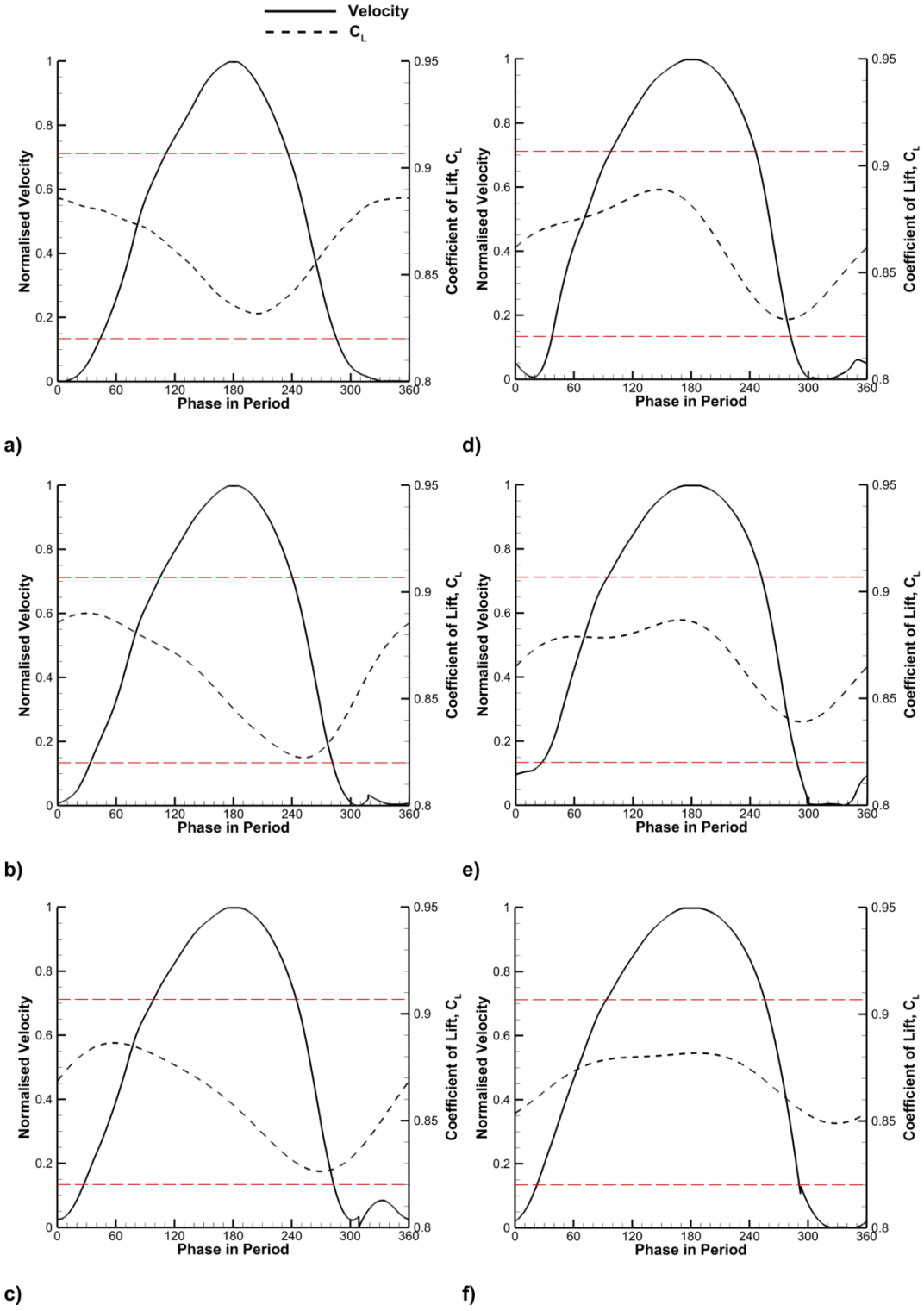

Figure 5.27 - Lift coefficient with phase in period, at α = 16°, x_j/c = 0.60, C_μ = 1.6% for; a) k = 0.079, b) k = 0.157, c) k = 0.236, d) k = 0.314, e) k =0.393, & f) k = 0.471.

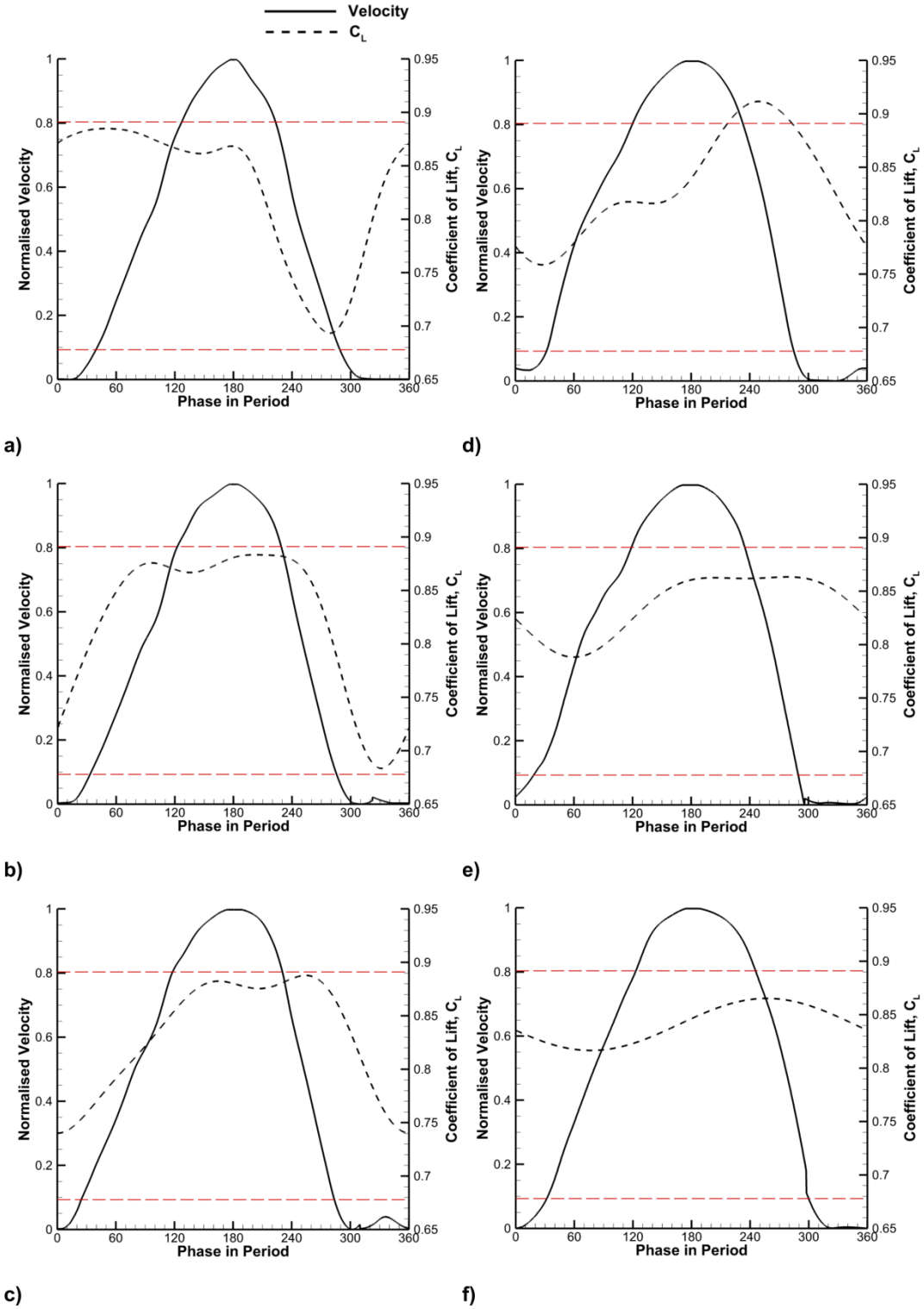

Figure 5.28 - Lift coefficient with phase in period, at α = 10°, x_j/c = 0.08, C_μ = 1.6% for; a) k = 0.079, b) k = 0.157, c) k = 0.236, d) k = 0.314, e) k =0.393, & f) k = 0.471.

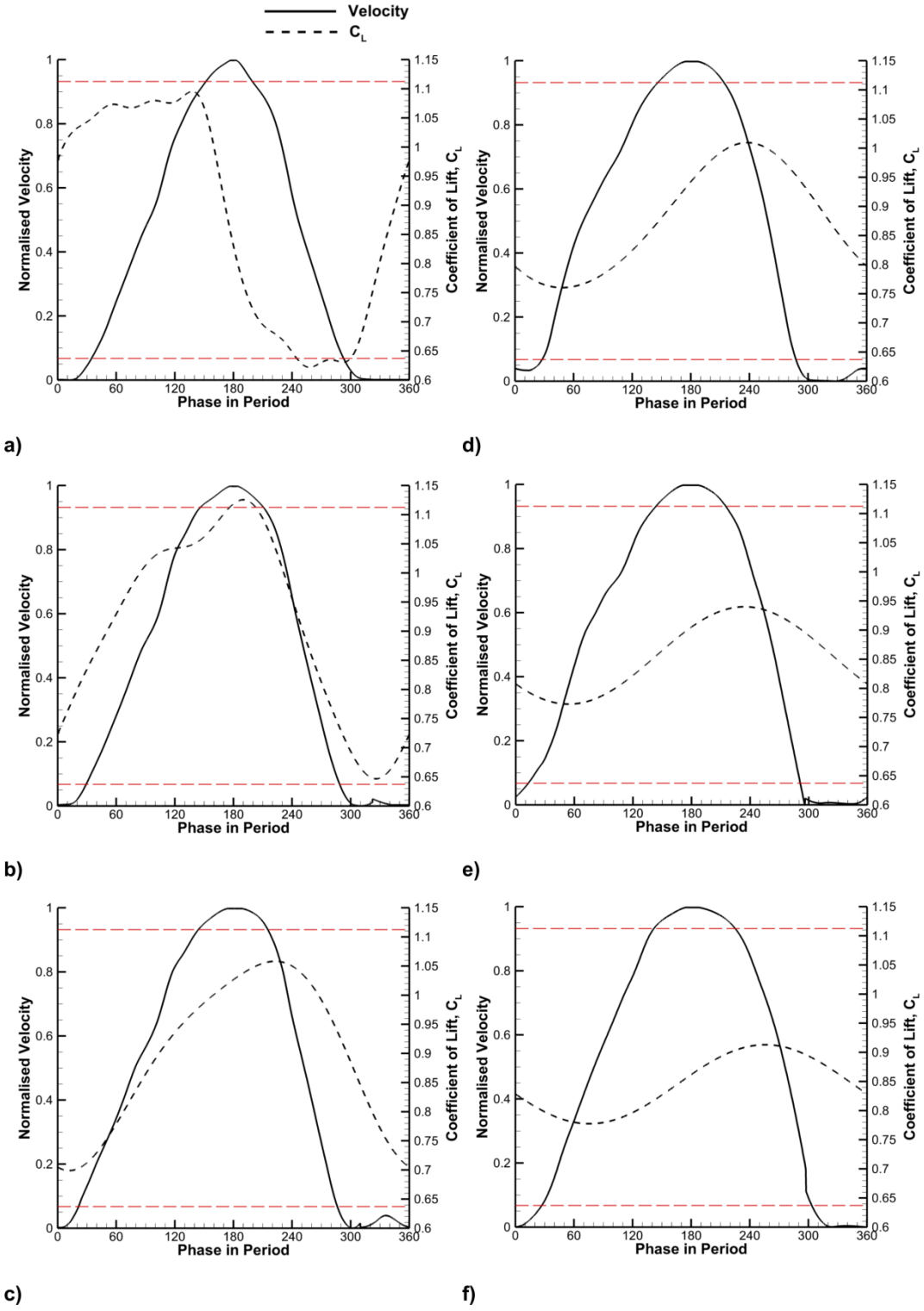

Figure 5.29 - Lift coefficient with phase in period, at α = 13°, x_j/c = 0.08, C_μ = 1.6% for; a) k = 0.079, b) k = 0.157, c) k = 0.236, d) k = 0.314, e) k =0.393, & f) k = 0.471.

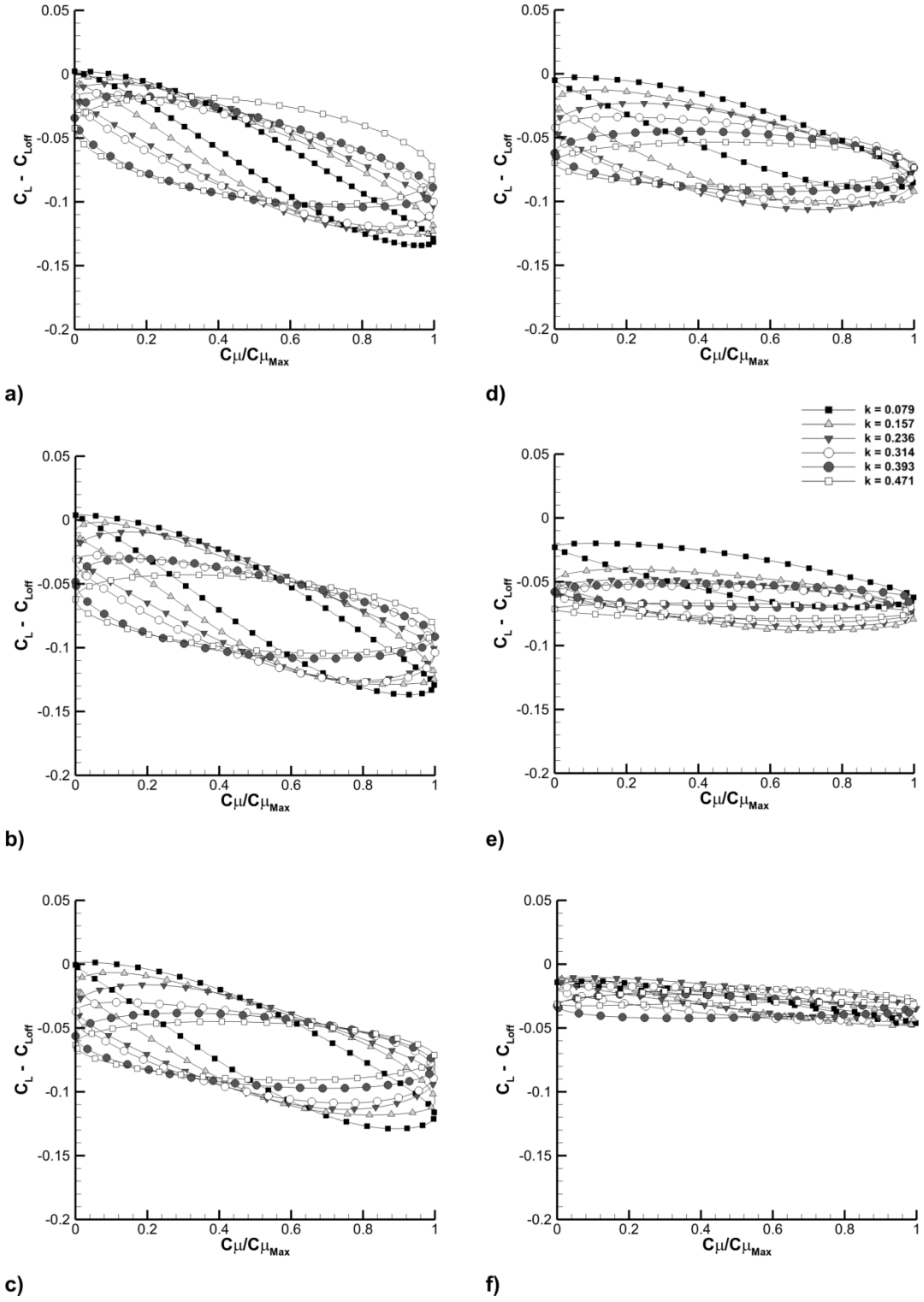

Figure 5.30 - Phase-averaged lift loops with varying reduced frequency for C_μ = 1.6%, x_j/c = 0.95 at a) α = 0°, b) α = 5°, c) α = 8°, d) α = 10°, e) α = 13° & f) α = 16°.

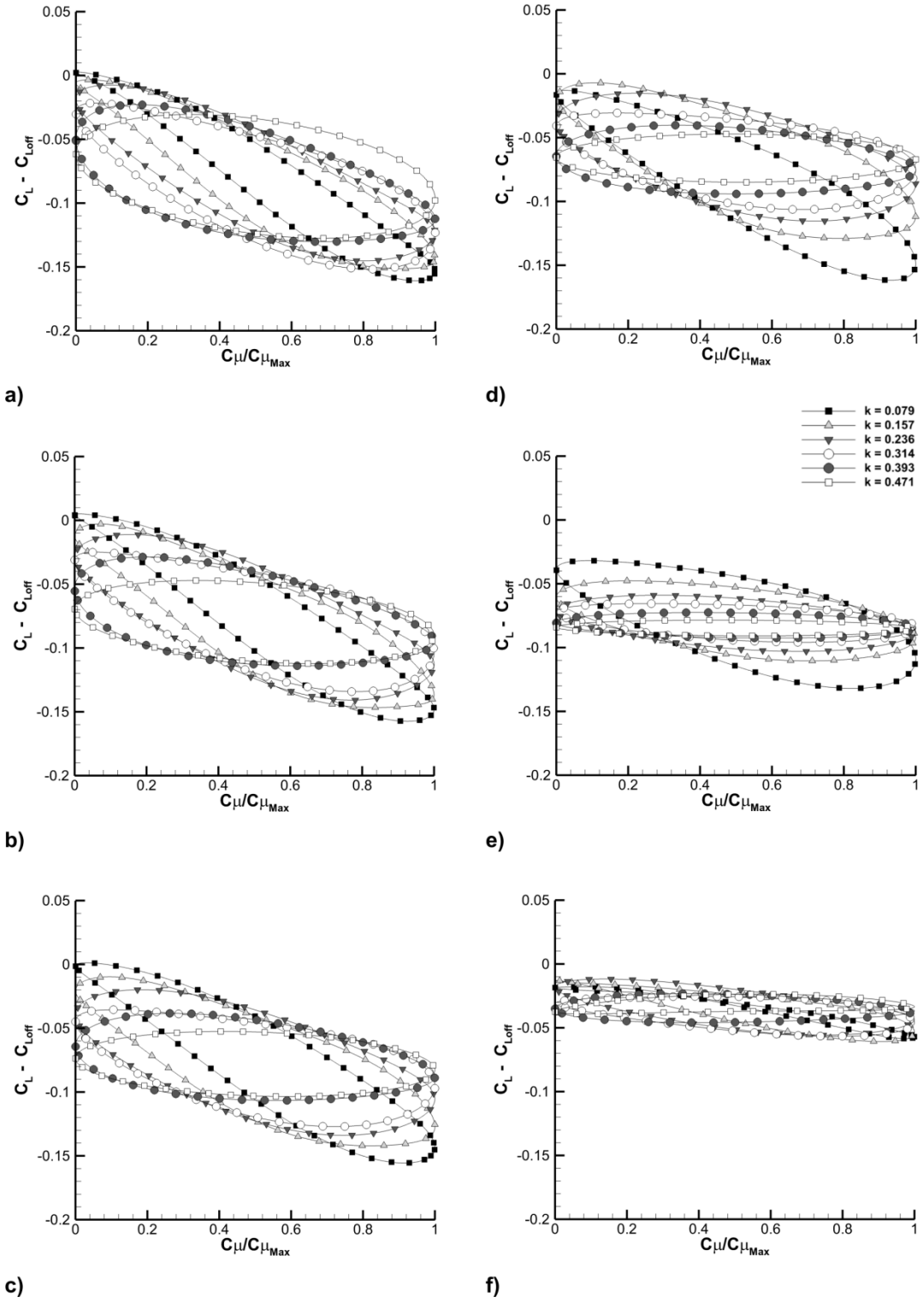

Figure 5.31 - Phase-averaged lift loops with varying reduced frequency for C_μ = 2.4%, x_j/c = 0.95 at a) α = 0°, b) α = 5°, c) α = 8°, d) α = 10°, e) α = 13° & f) α = 16°.

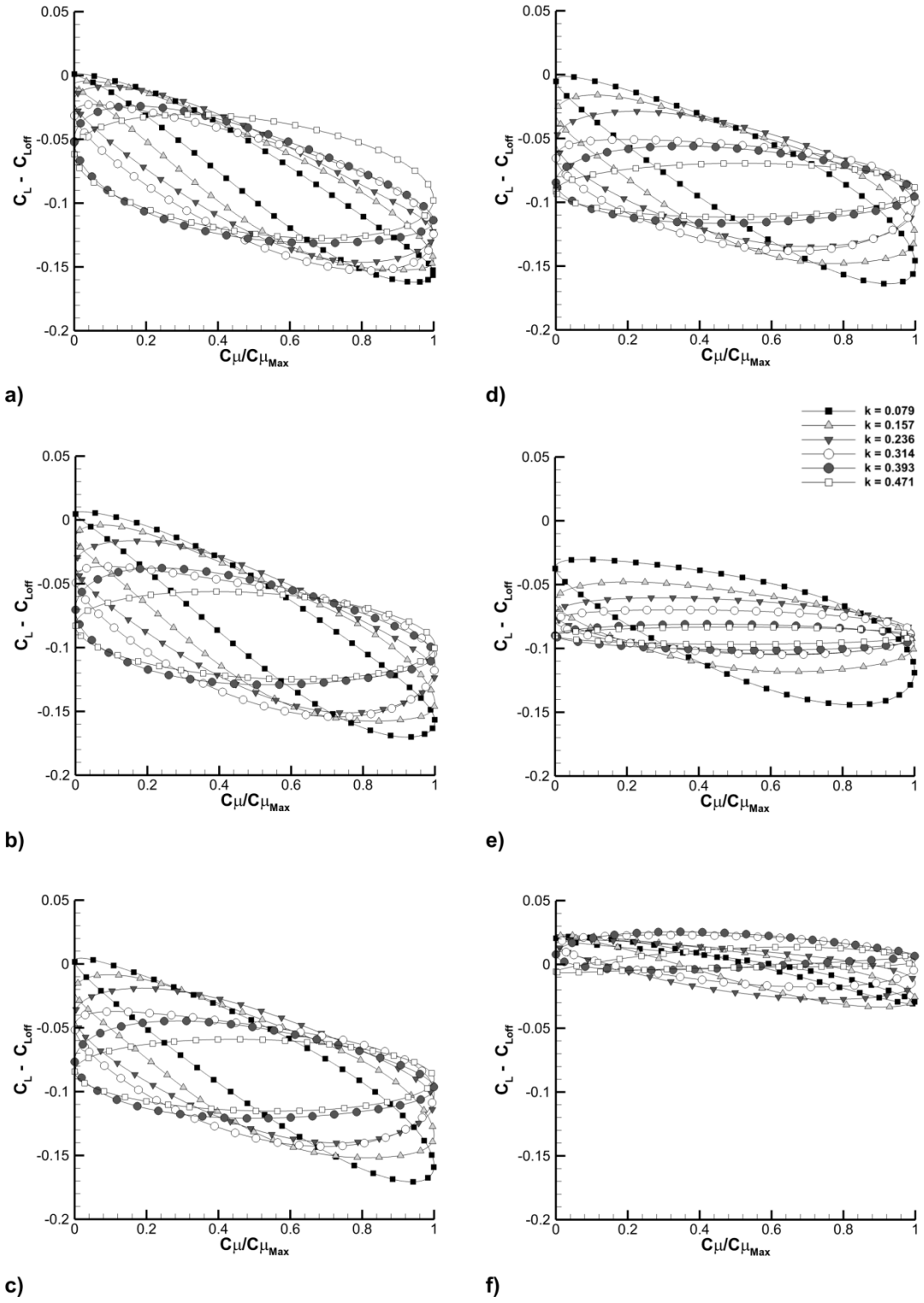

Figure 5.32 - Phase-averaged lift loops with varying reduced frequency for C_μ = 3.2%, x_j/c = 0.95 at a) α = 0°, b) α = 5°, c) α = 8°, d) α = 10°, e) α = 13° & f) α = 16°.

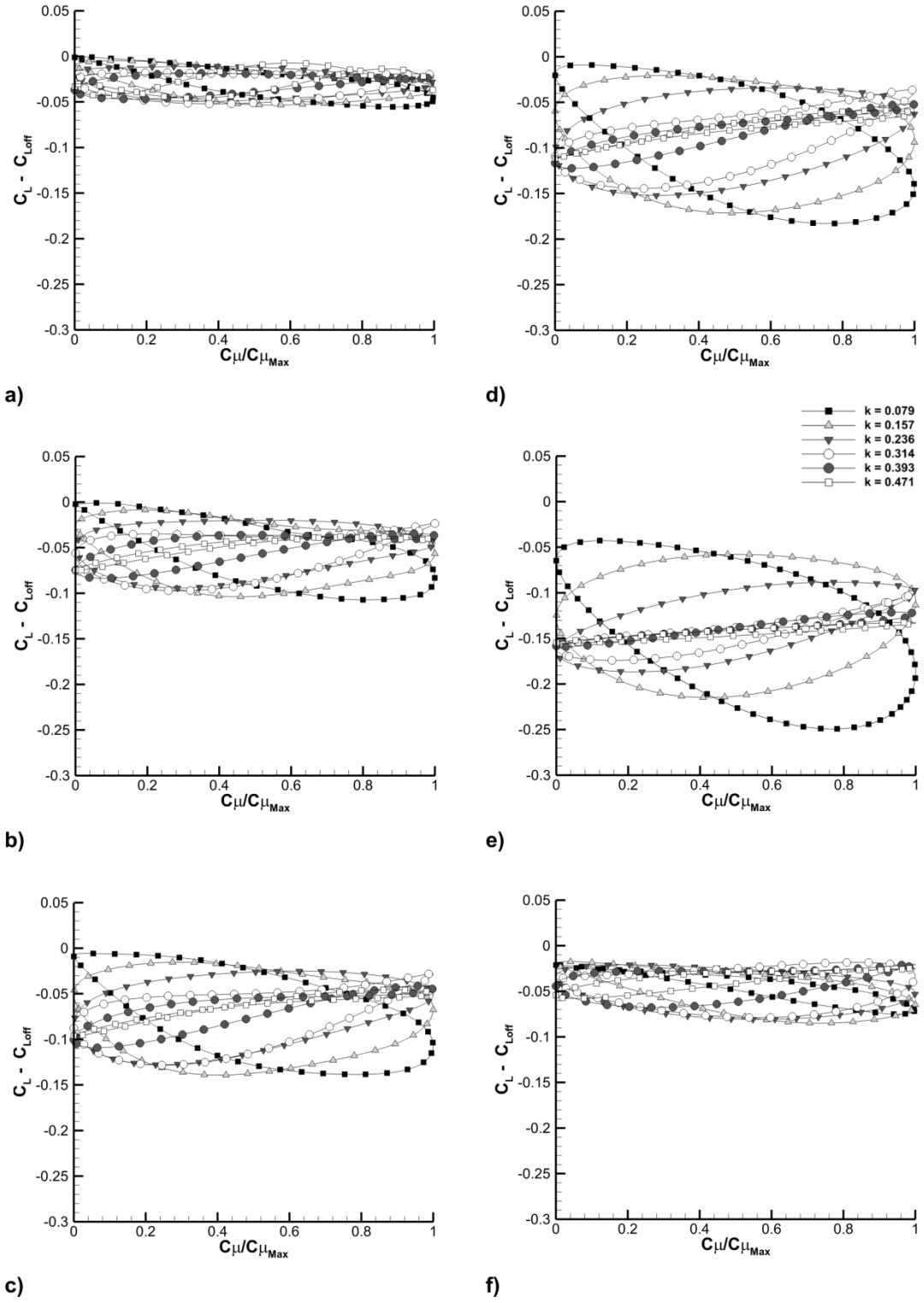

Figure 5.33 - Phase-averaged lift loops with varying reduced frequency for C_μ = 1.6%, x_j/c = 0.60 at a) α = 0°, b) α = 5°, c) α = 8°, d) α = 10°, e) α = 13° & f) α = 16°.

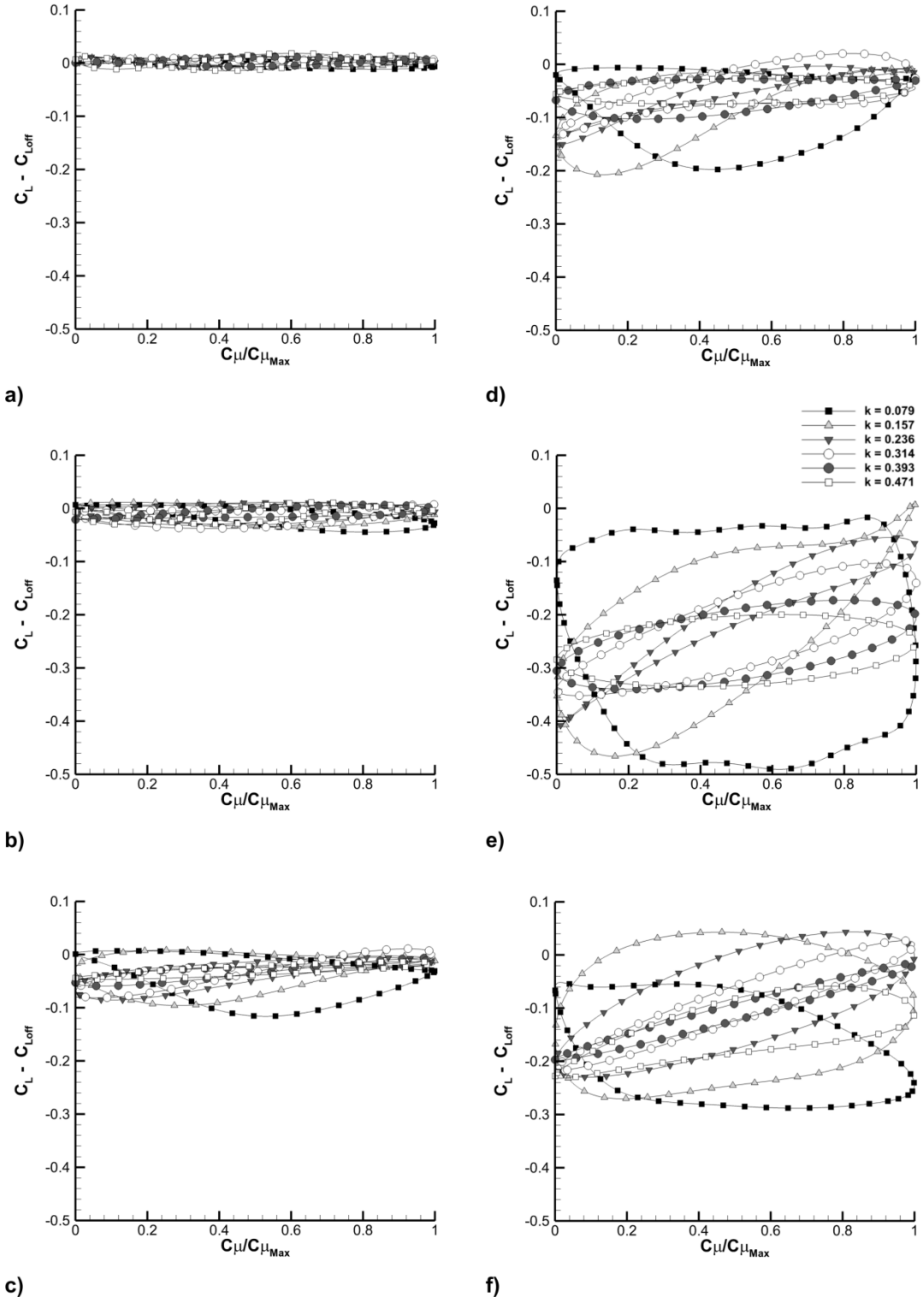

Figure 5.34 - Phase-averaged lift loops with varying reduced frequency for C_μ = 1.6%, x_j/c = 0.08 at a) α = 0°, b) α = 5°, c) α = 8°, d) α = 10°, e) α = 13° & f) α = 16°.

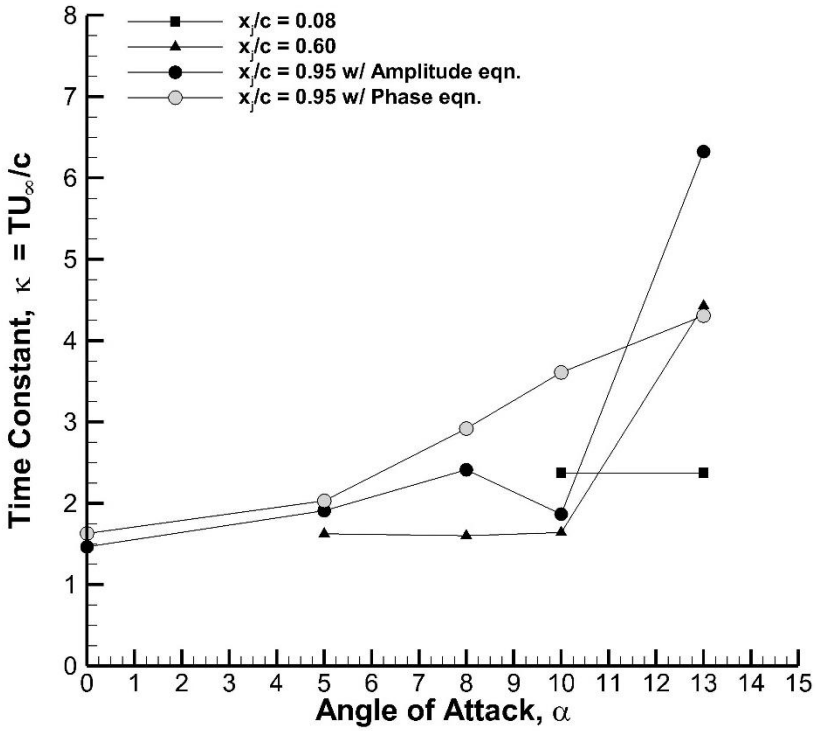

Figure 5.35 - Time constants for periodic deployment at x_j/c =0.08, 0.60 & 0.95.

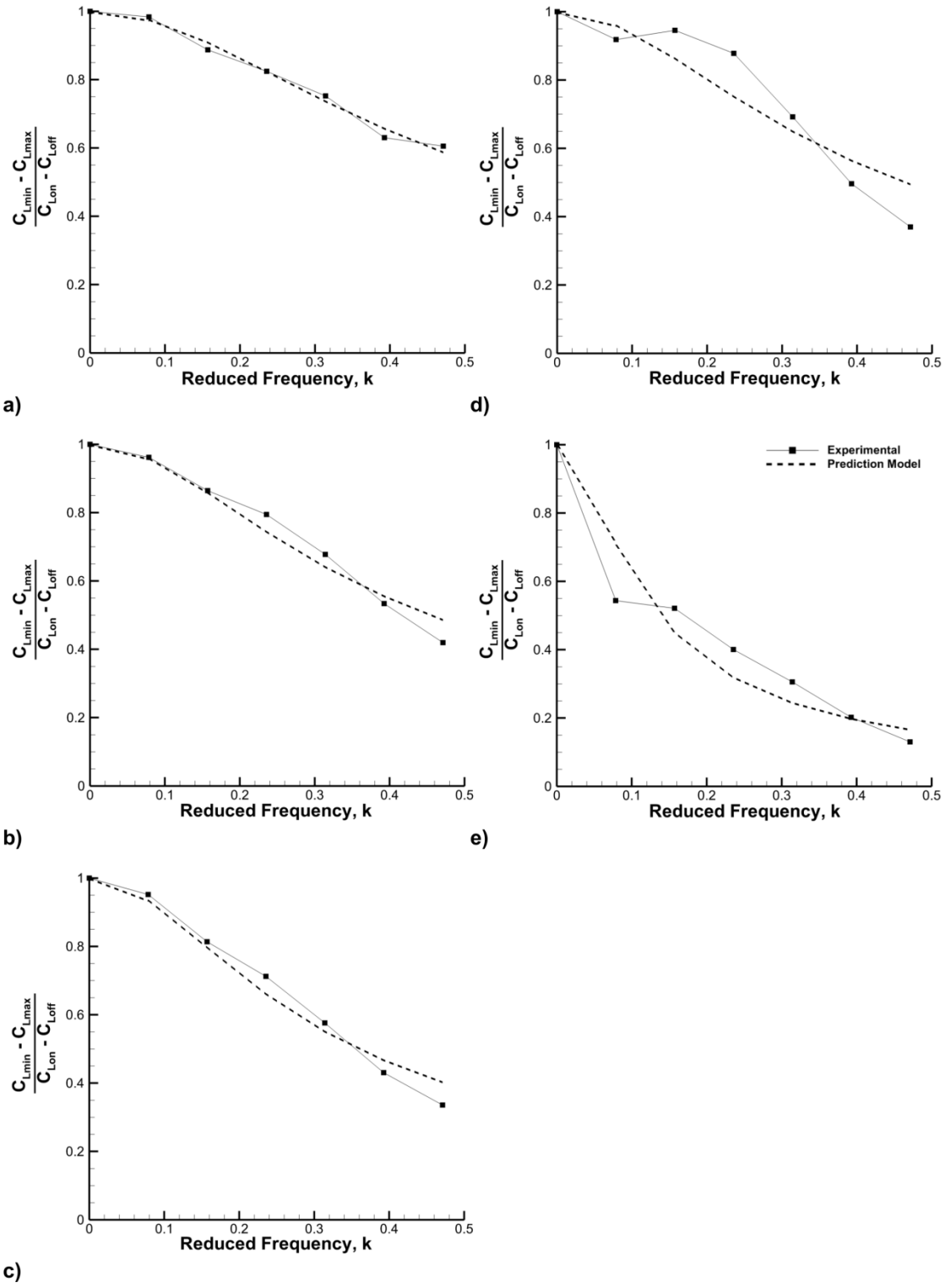

Figure 5.36 - Comparison of model to experimental data for amplitude ratio vs reduced frequency, using κ from Eqn. 5.1, x_j/c = 0.95 at C_μ = 1.6%; a) α = 0°, b) α = 5°, c) α = 8°, d) α = 10° & e) α = 13°.

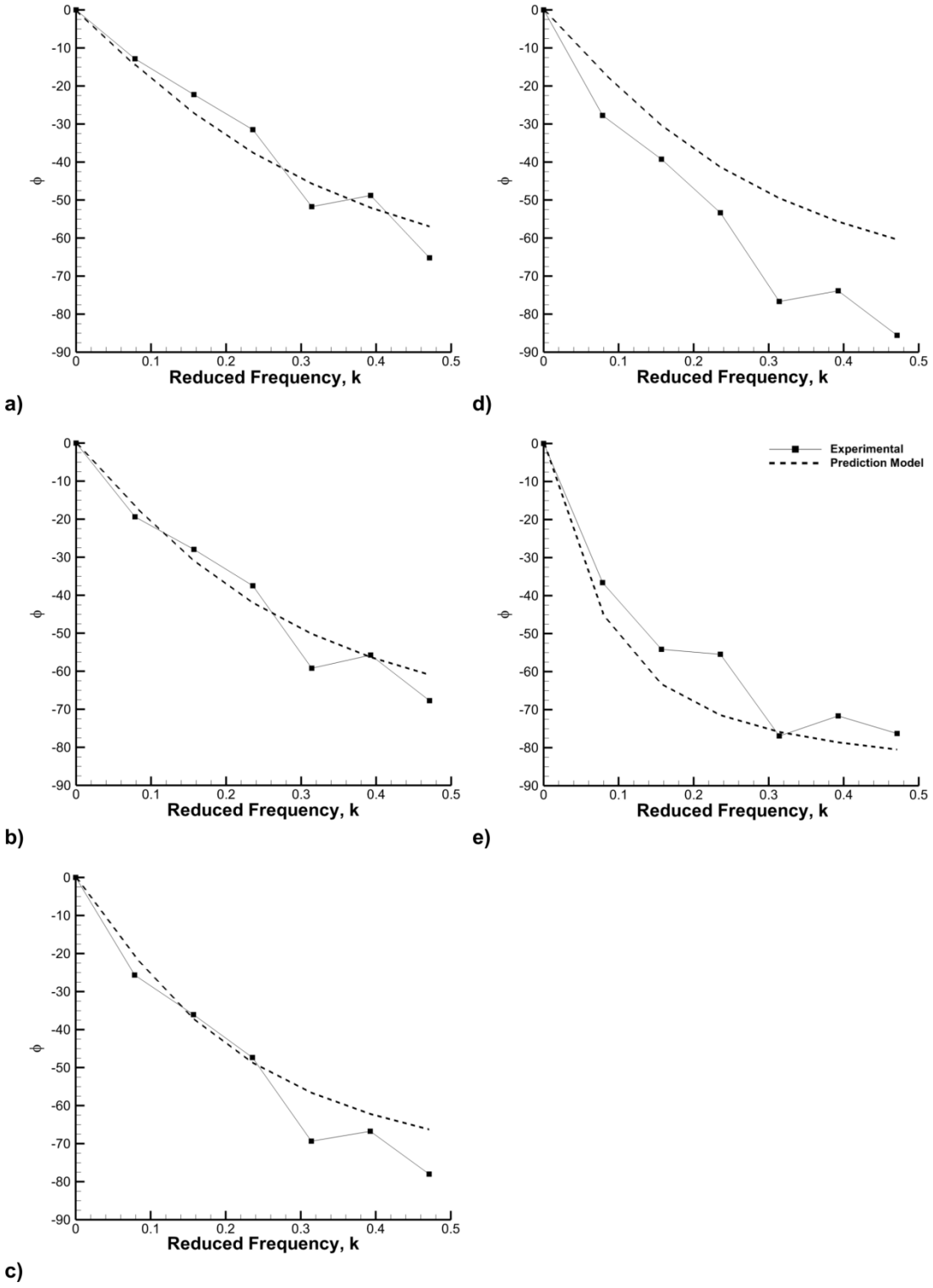

Figure 5.37 - Comparison of model to experimental data for phase angle, using κ from Eqn. 5.1, x_j/c = 0.95 at C_μ = 1.6%; a) α = 0°, b) α = 5°, c) α = 8°, d) α = 10° & e) α = 13°.

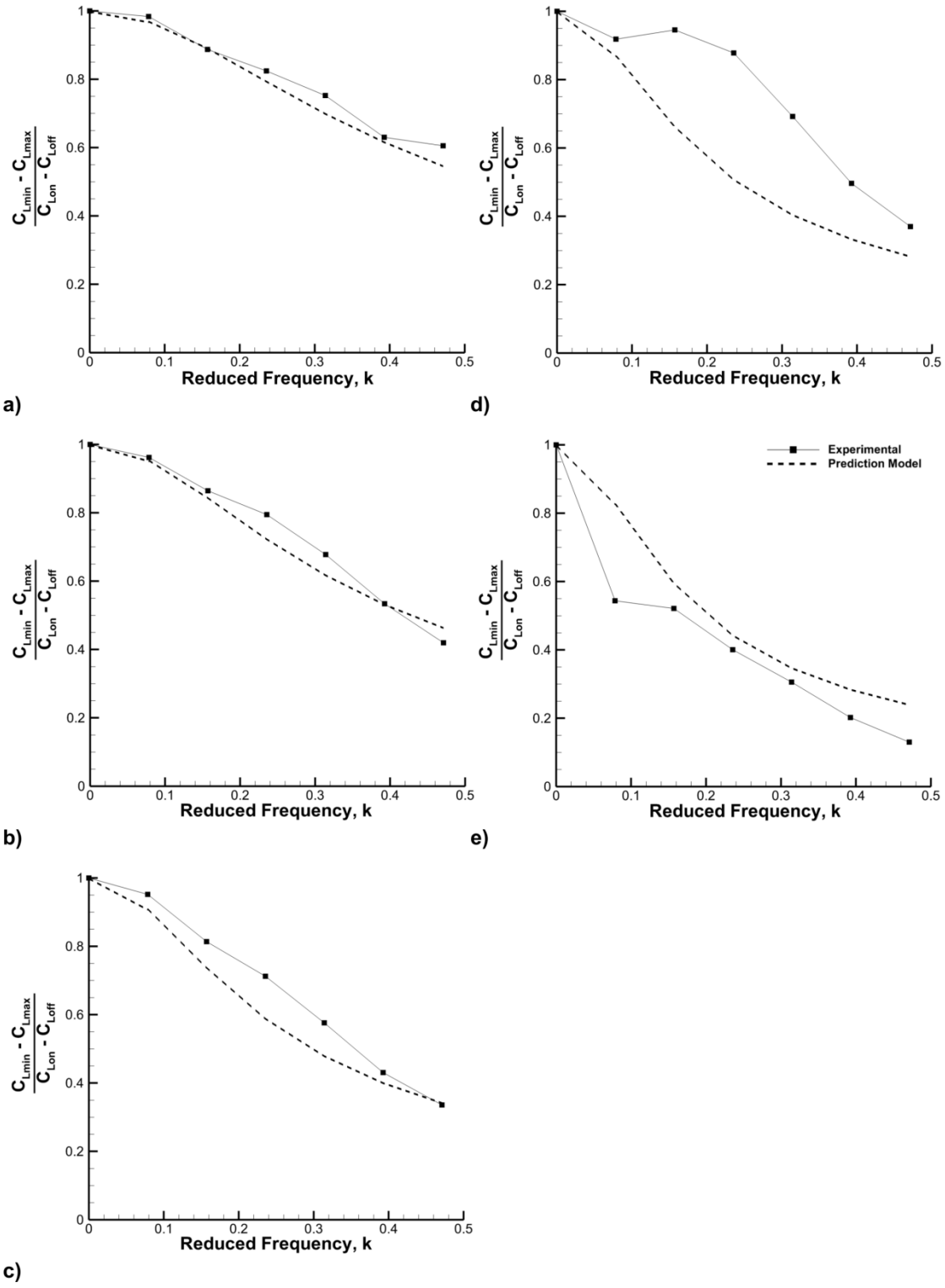

Figure 5.38 - Comparison of model to experimental data for amplitude ratio vs reduced frequency, using κ from Eqn. 5.2, x_j/c = 0.95 at C_μ = 1.6%; a) α = 0°, b) α = 5°, c) α = 8°, d) α = 10° & e) α = 13°.

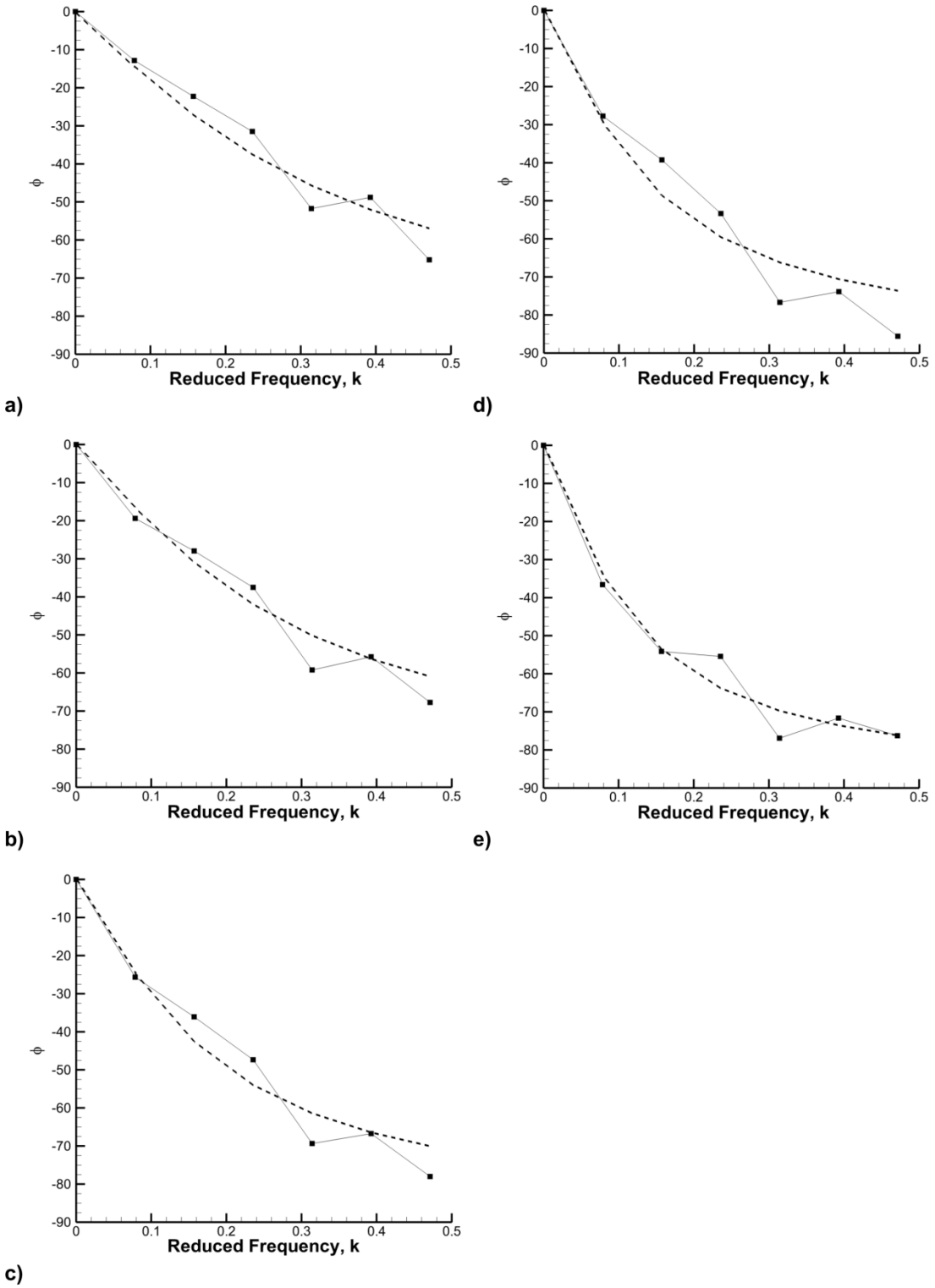

Figure 5.39 - Comparison of model to experimental data for phase angle, using κ from Eqn. 5.2, x_j/c = 0.95 at C_μ = 1.6%; a) α = 0°, b) α = 5°, c) α = 8°, d) α = 10° & e) α = 13°.

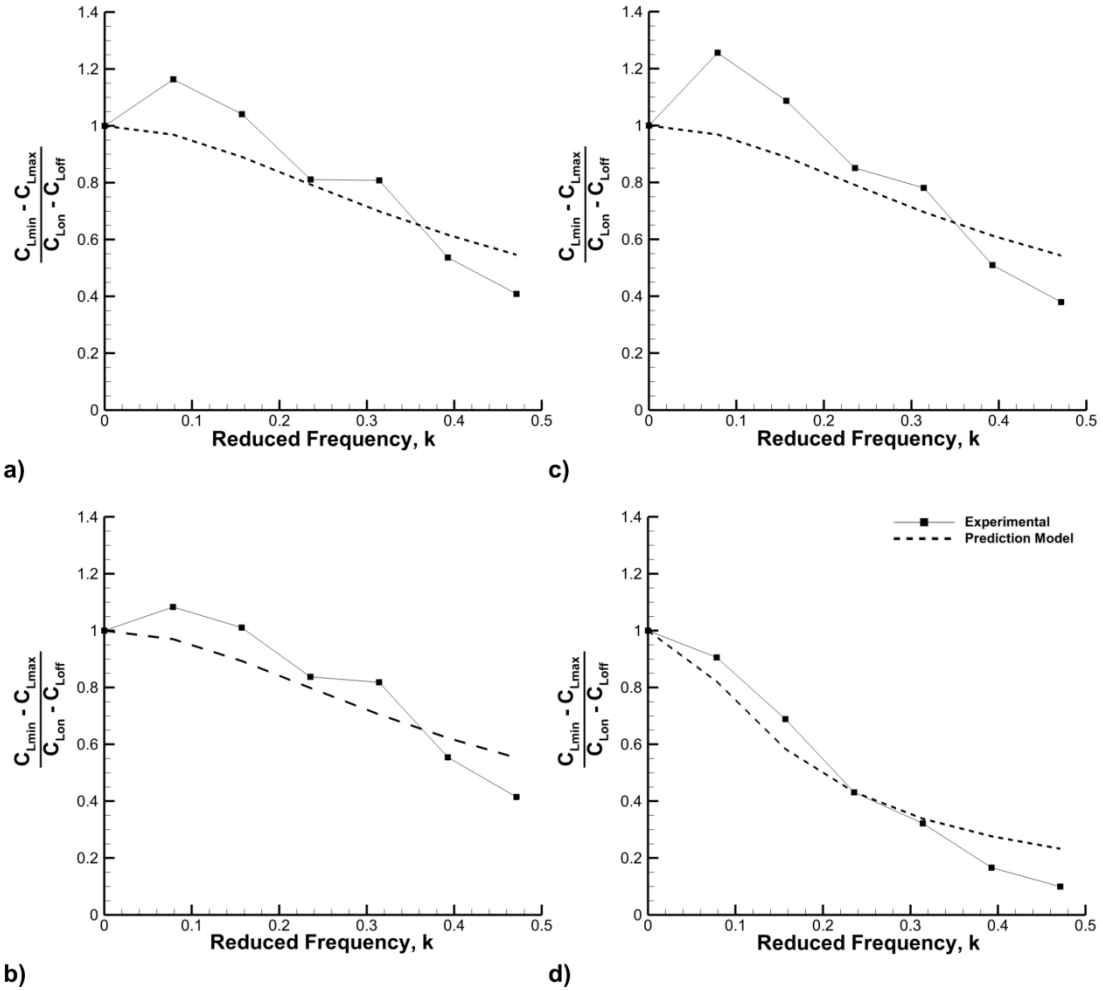

Figure 5.40 - Comparison of model to experimental data for amplitude ratio vs reduced frequency, using κ from Eqn. 5.1, x_j/c = 0.60 at C_μ = 1.6%; a) α = 5°, b) α = 8°, c) α = 10° & d) α = 13°.

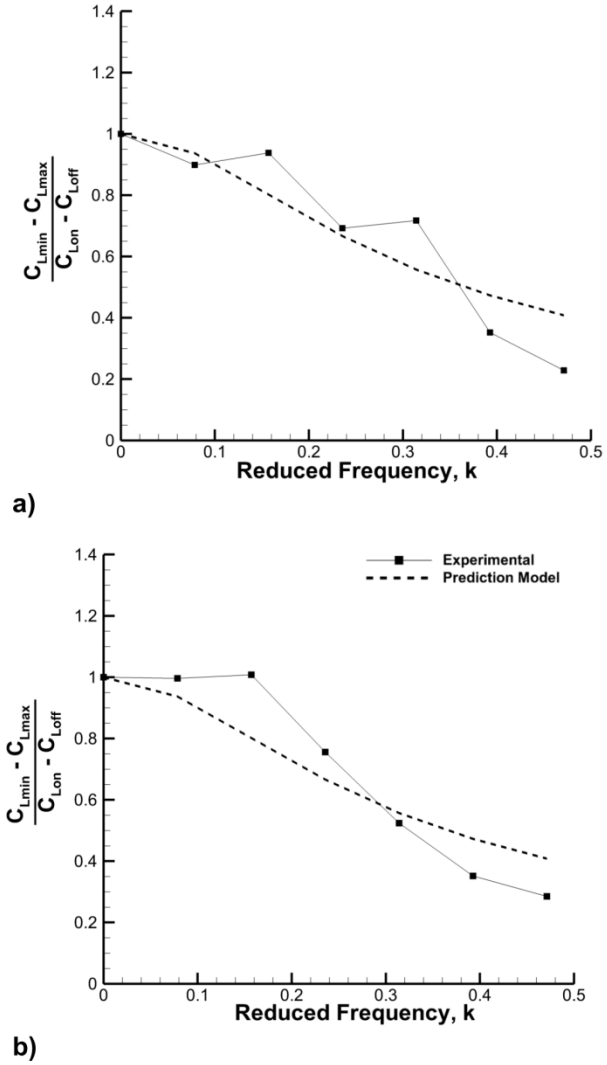

Figure 5.41 - Comparison of model to experimental data for amplitude ratio vs reduced frequency, using κ from Eqn. 5.1, x_j/c = 0.08 at C_μ = 1.6%; a) α = 10° & b) α = 13°.

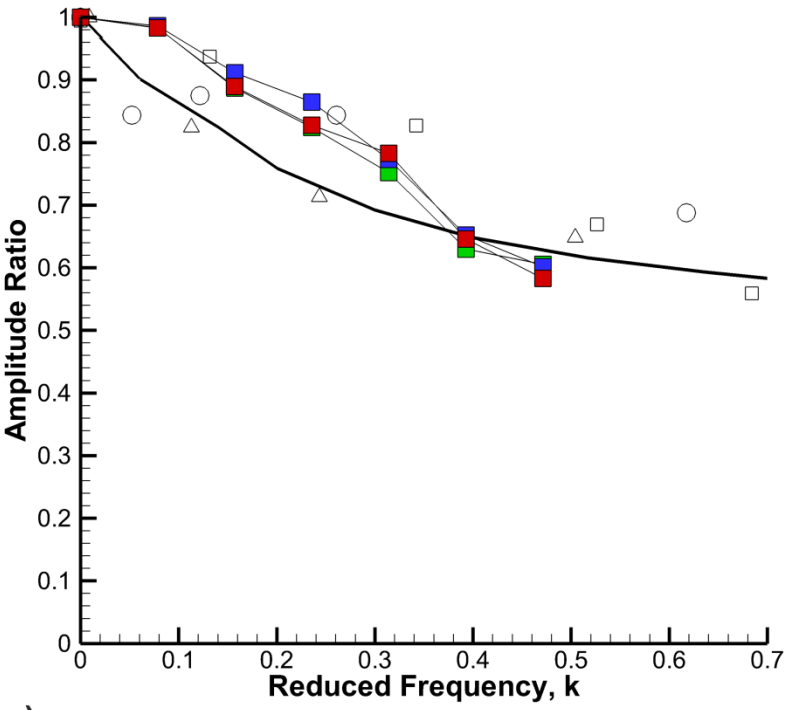

a)

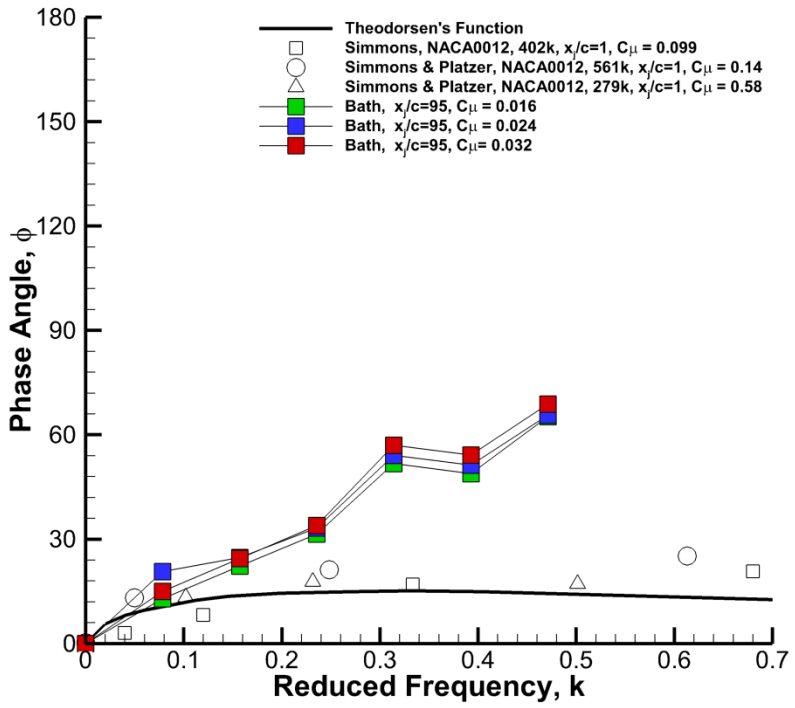

b)

Figure 5.42 - Experimental validation with data from the literature for α = 0°; a) amplitude ratio and b) phase angle.

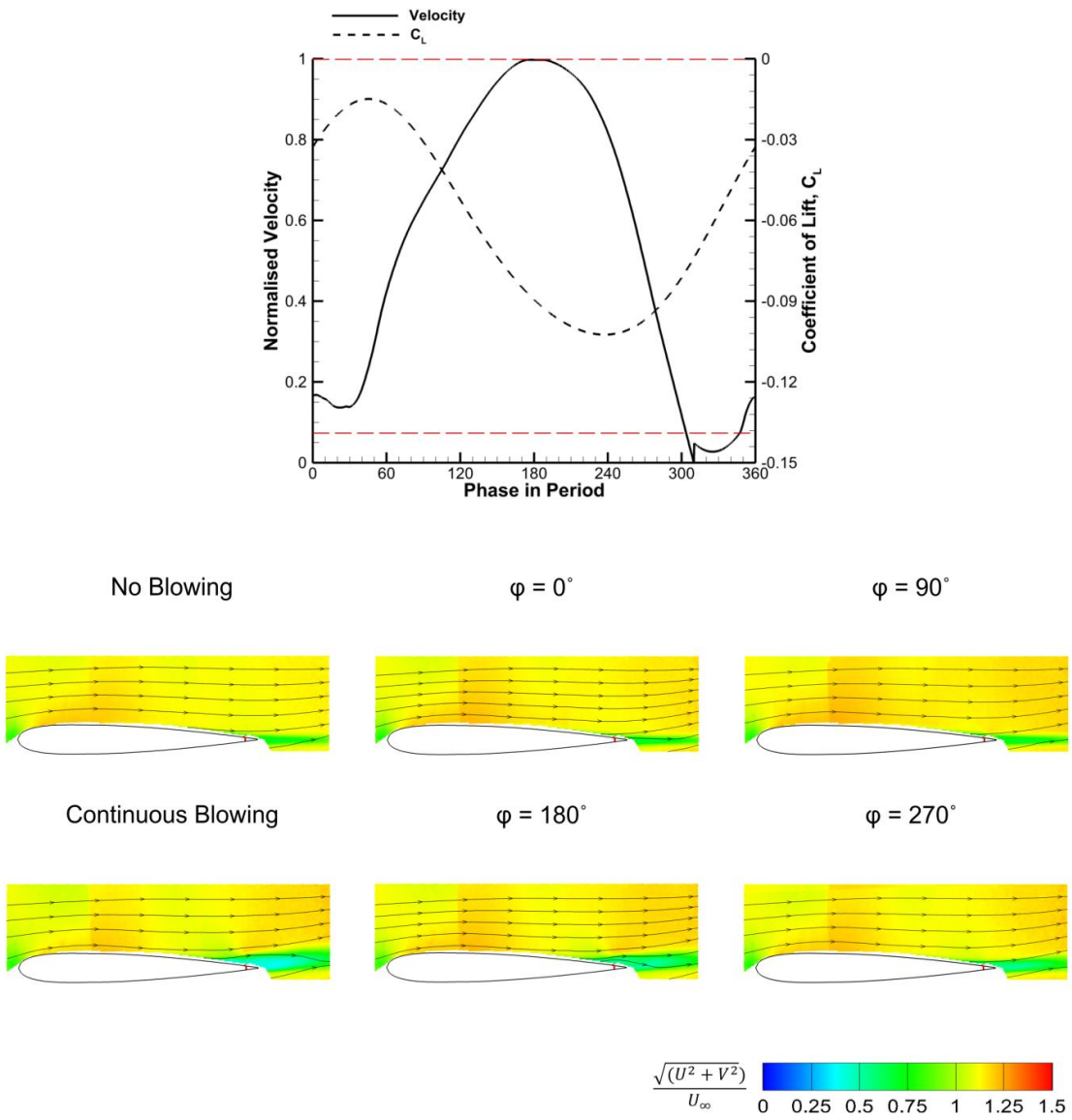

Figure 5.43 - Phase-averaged velocity field data comparing varying phases in k = 0.393 period for x_j/c = 0.95 at α = 0°, C_μ = 1.6%.

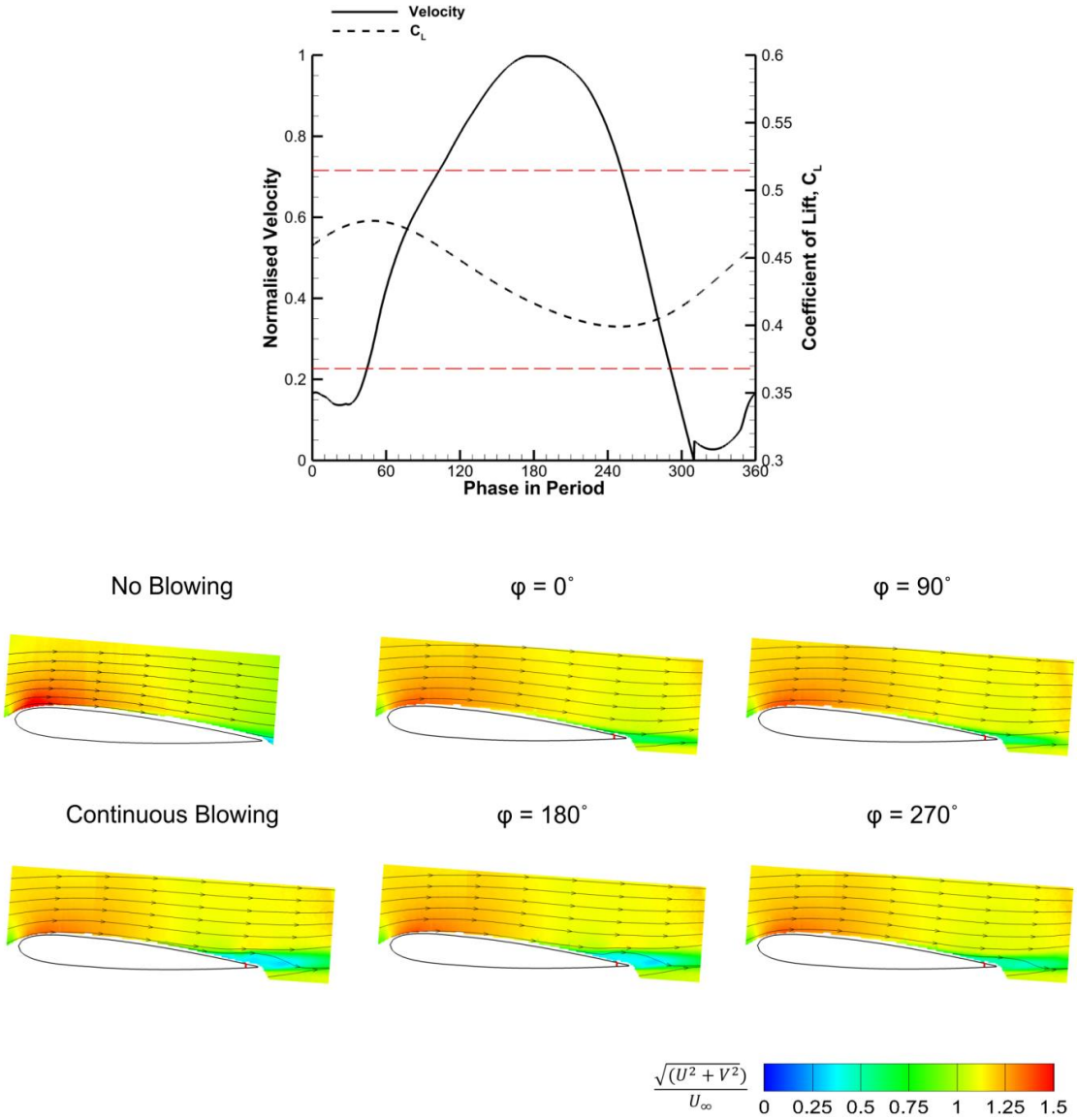

Figure 5.44 - Phase-averaged velocity field data comparing varying phases in k = 0.393 period for x_j/c = 0.95 at α = 5°, C_μ = 1.6%.

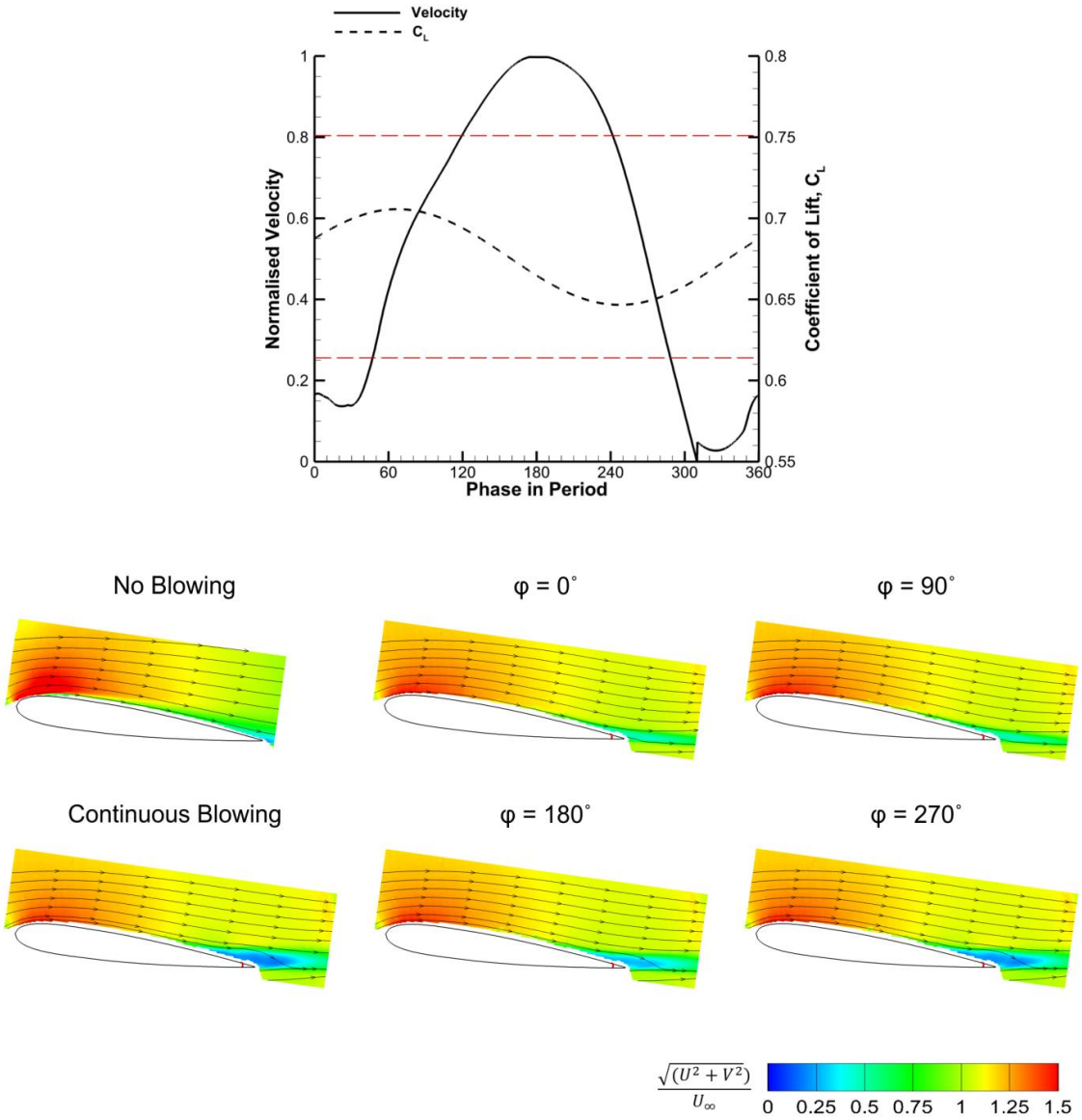

Figure 5.45 - Phase-averaged velocity field data comparing varying phases in k = 0.393 period for x_j/c = 0.95 at α = 8°, C_μ = 1.6%.

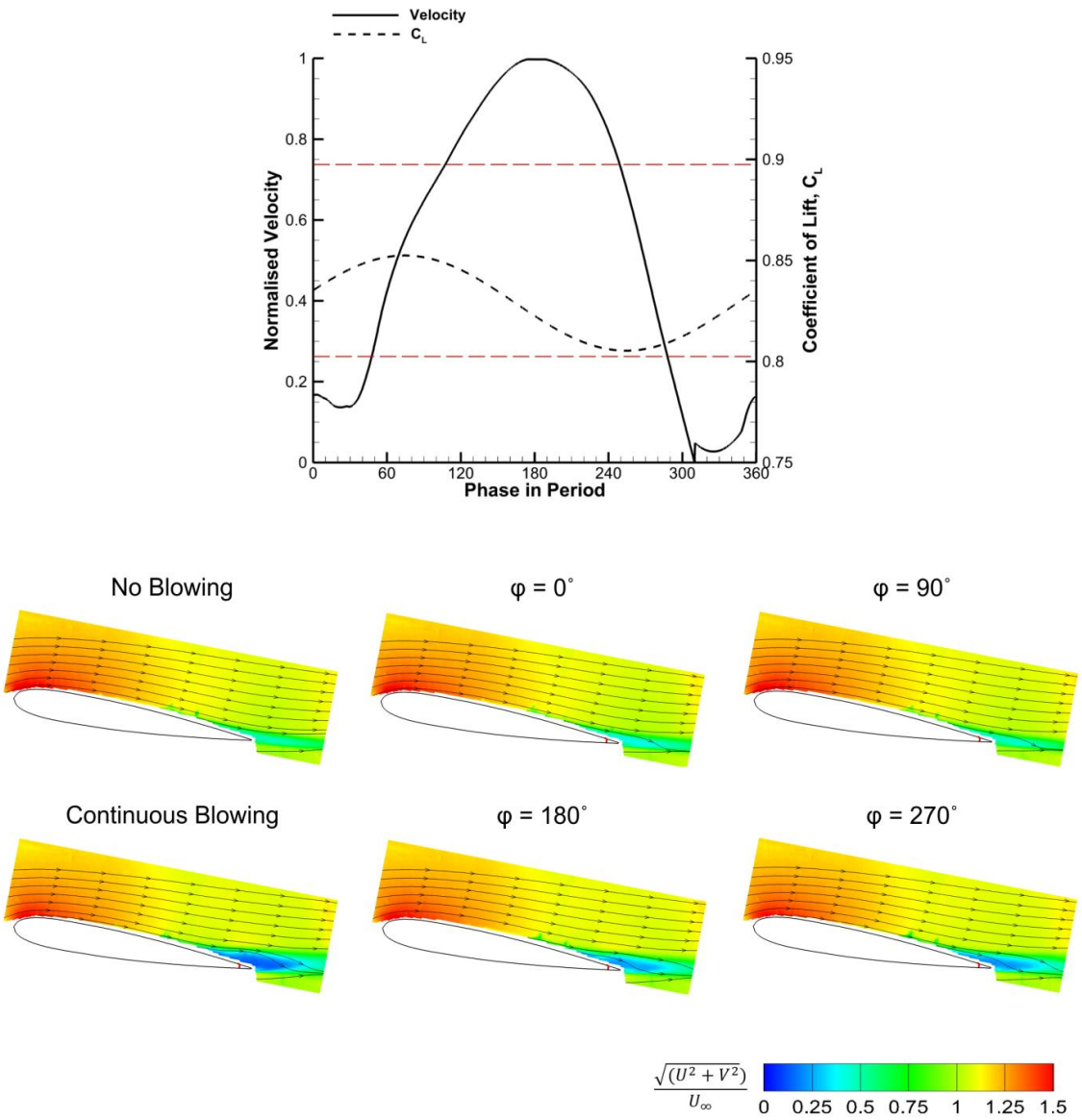

Figure 5.46 - Phase-averaged velocity field data comparing varying phases in k = 0.393 period for x_j/c = 0.95 at α = 10°, C_μ = 1.6%.

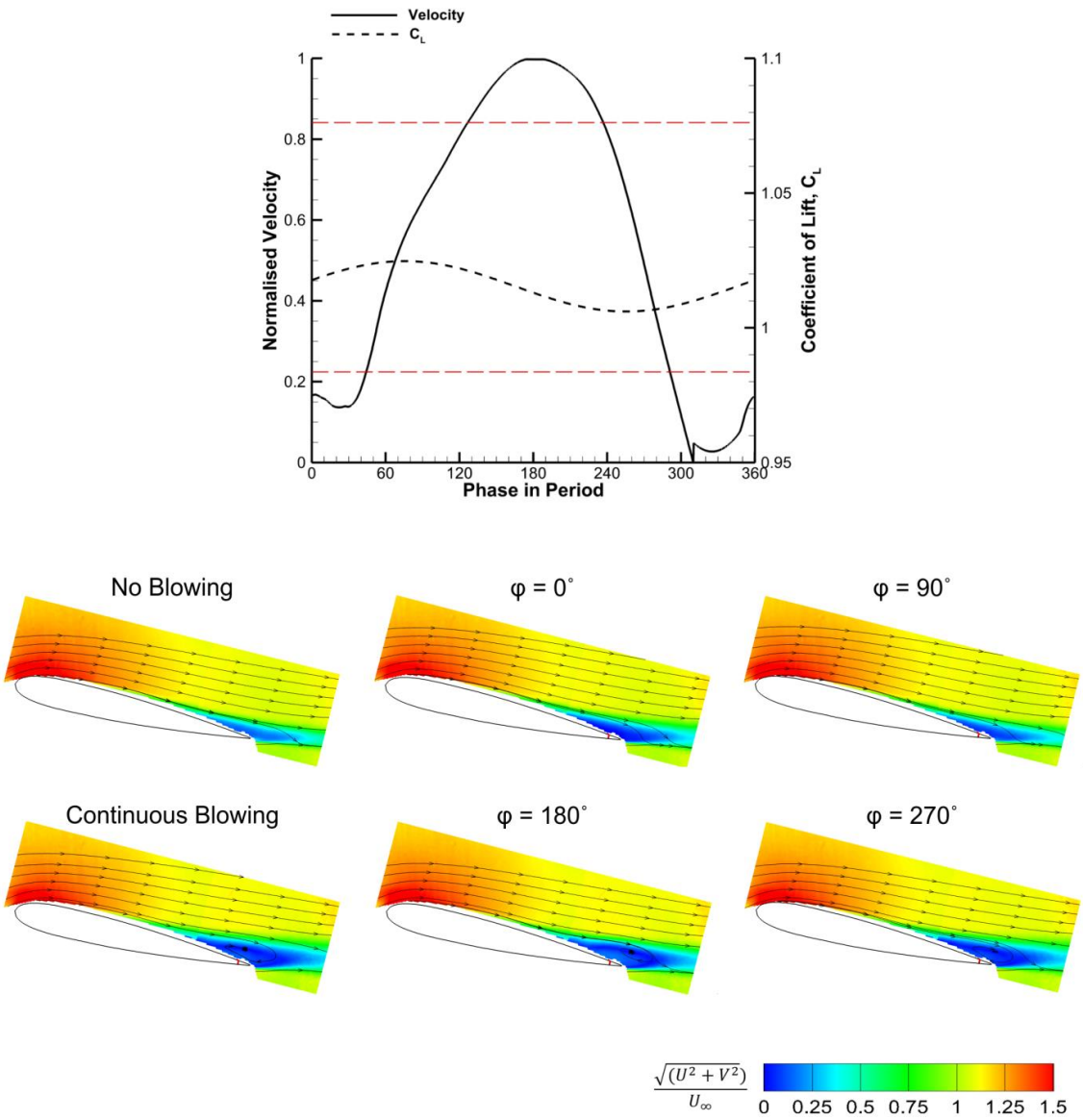

Figure 5.47 - Phase-averaged velocity field data comparing varying phases in k = 0.393 period for x_j/c = 0.95 at α = 13°, C_μ = 1.6%.

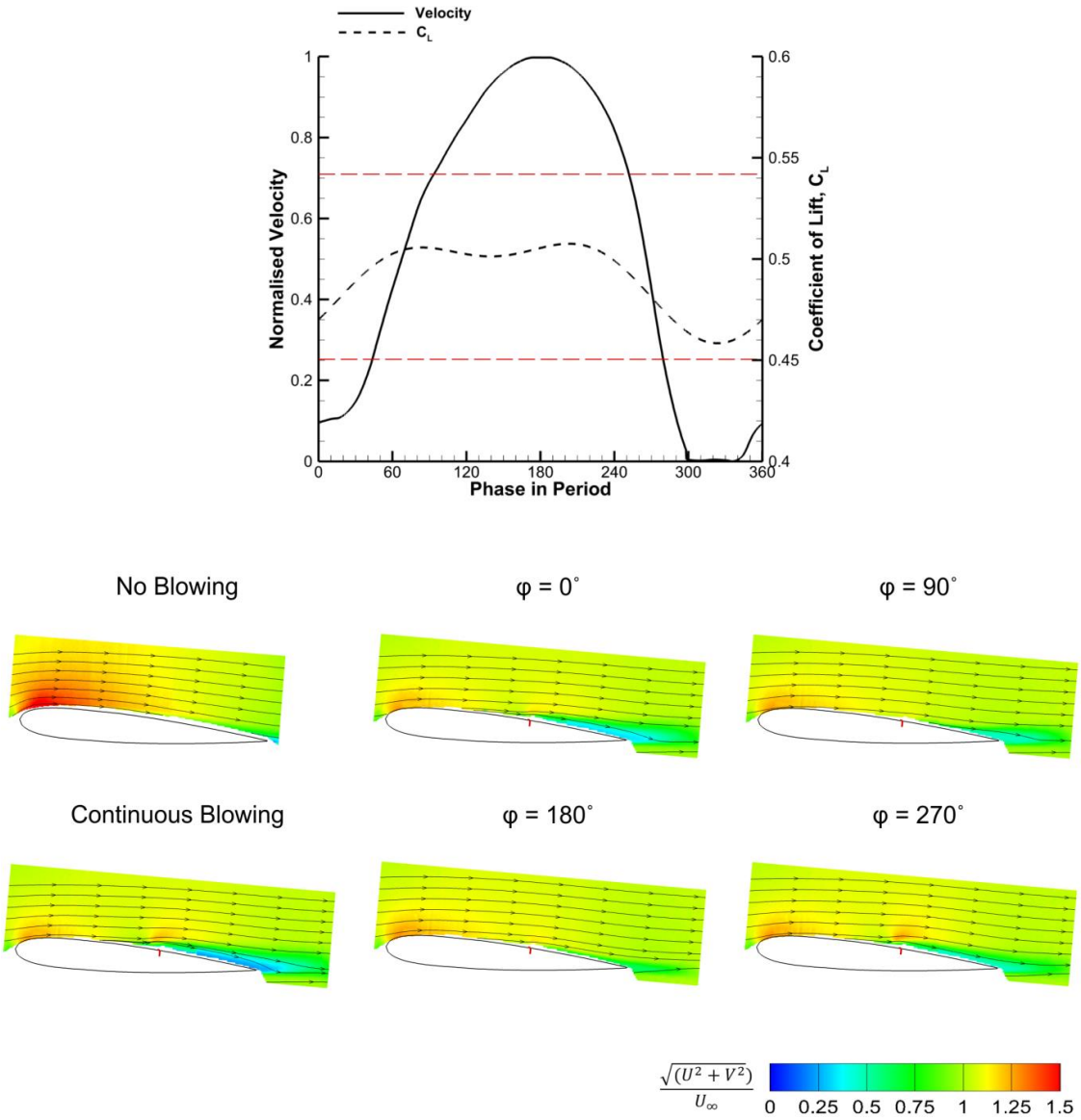

Figure 5.48 - Phase-averaged velocity field data comparing varying phases in k = 0.393 period for x_j/c = 0.60 at α = 5°, C_μ = 1.6%.

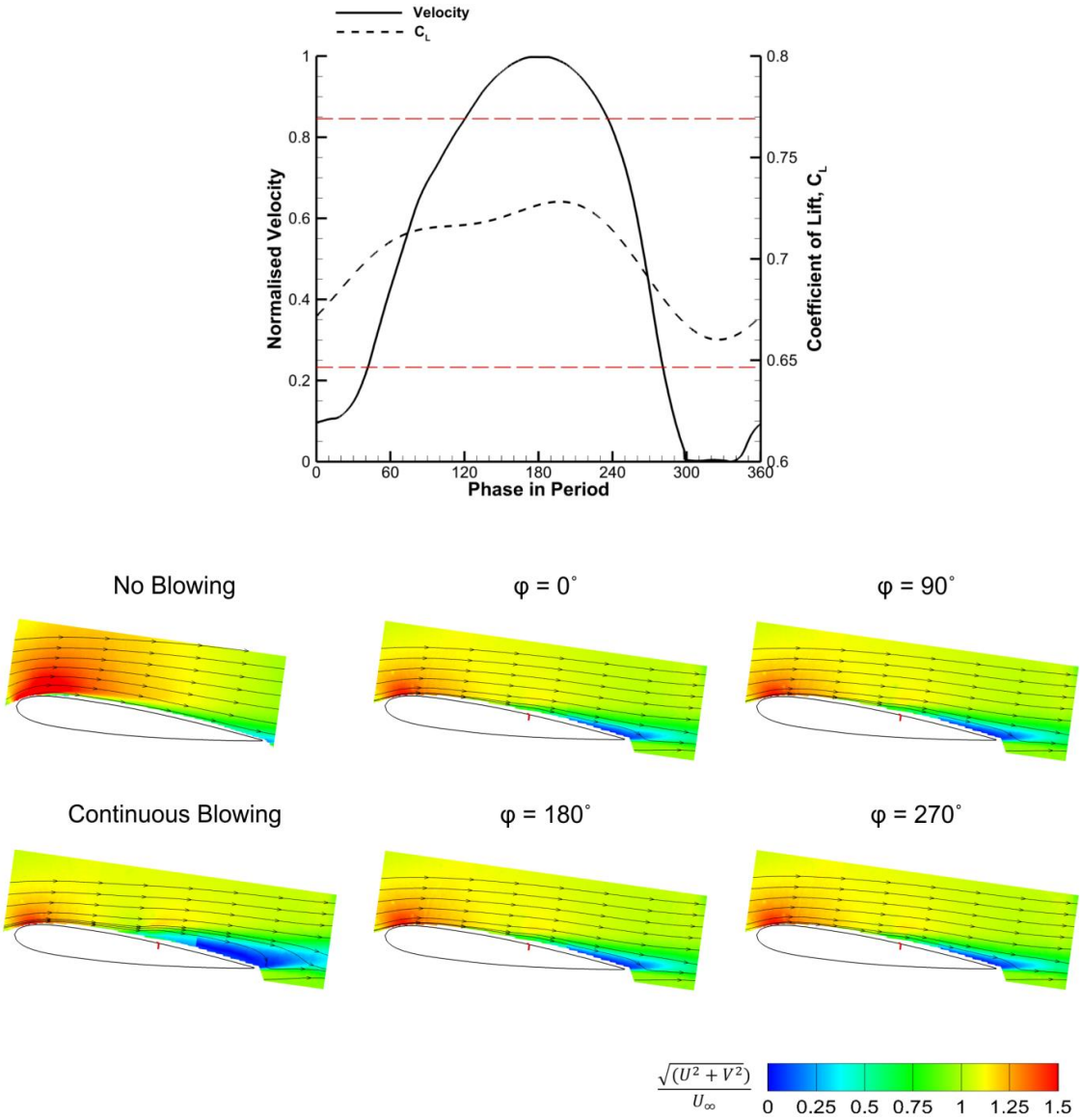

Figure 5.49 - Phase-averaged velocity field data comparing varying phases in k = 0.393 period for x_j/c = 0.60 at α = 8°, C_μ = 1.6%.

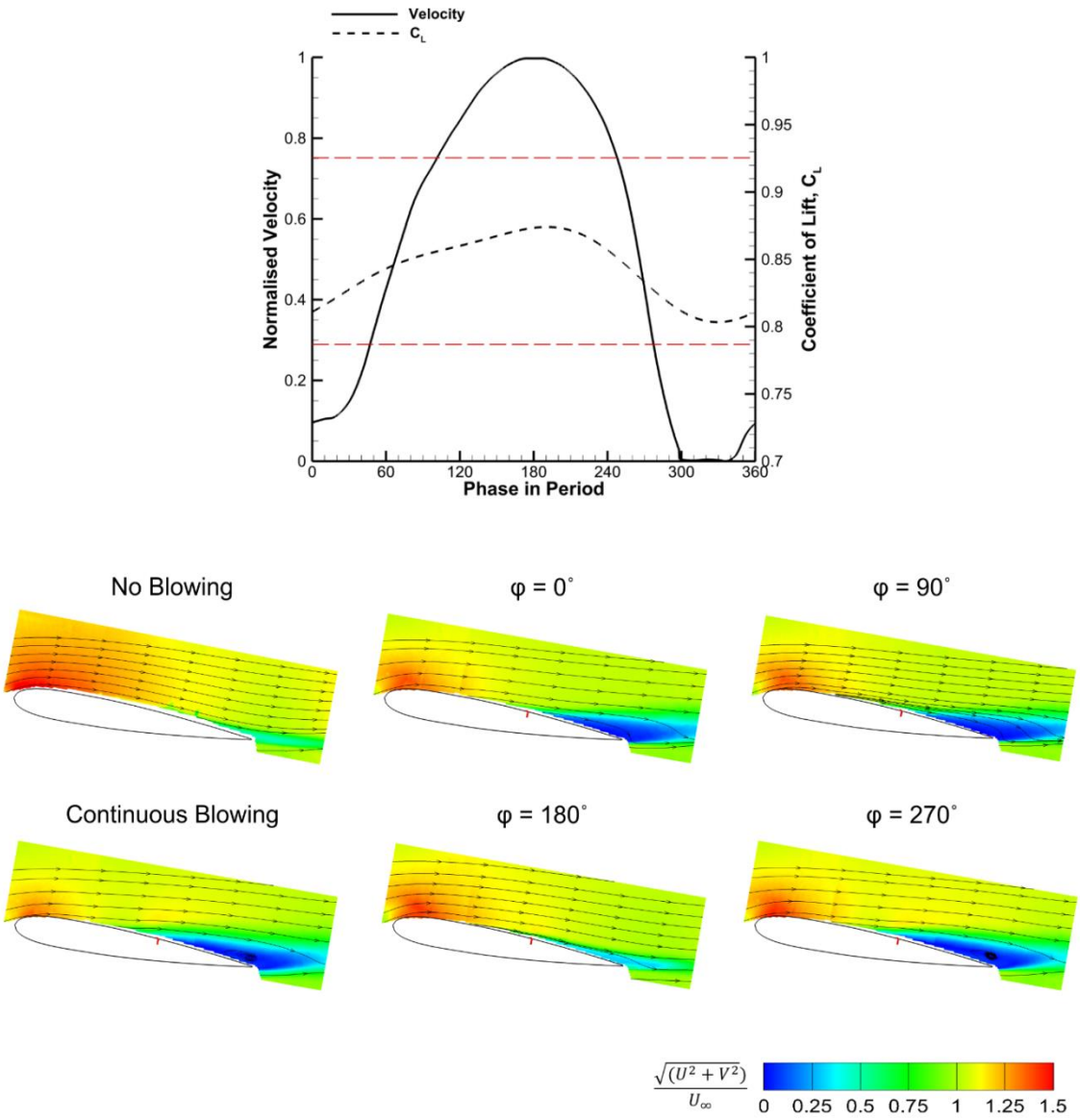

Figure 5.50 - Phase-averaged velocity field data comparing varying phases in k = 0.393 period for x_j/c = 0.60 at α = 10°, C_μ = 1.6%.

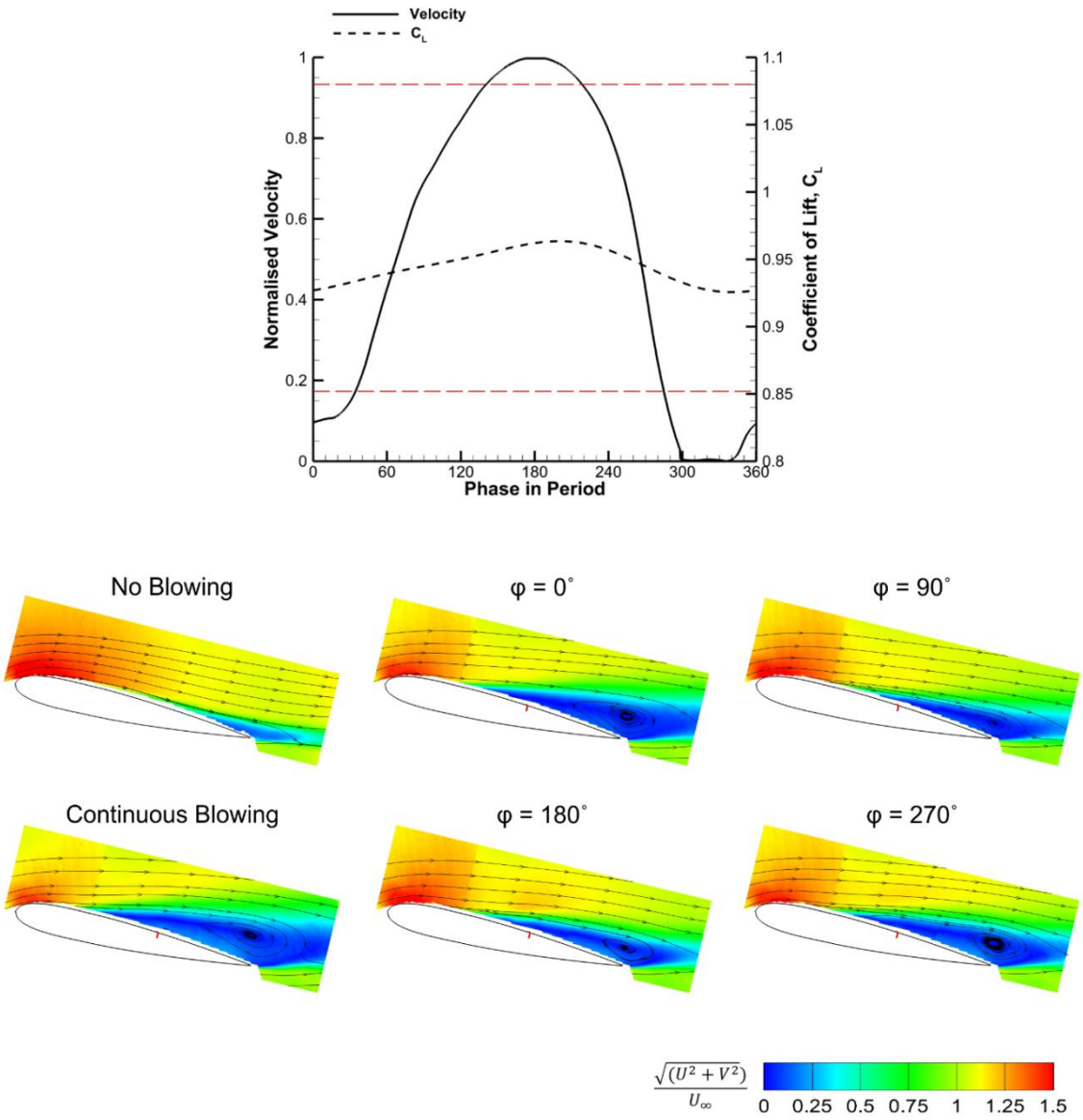

Figure 5.51 - Phase-averaged velocity field data comparing varying phases in k = 0.393 period for x_j/c = 0.60 at α = 13°, C_μ = 1.6%.

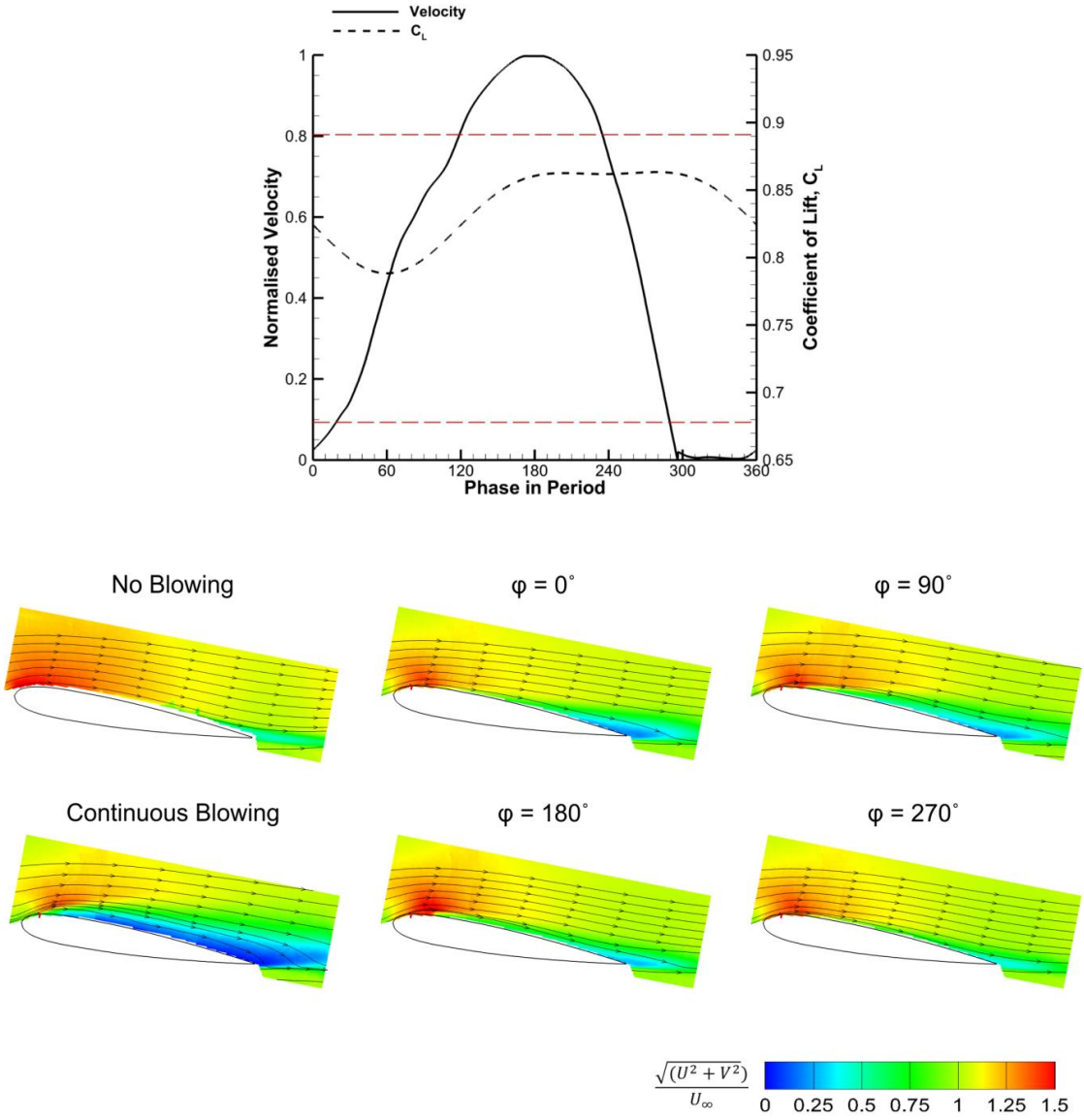

Figure 5.52 - Phase-averaged velocity field data comparing varying phases in k = 0.393 period for x_j/c = 0.08 at α = 10°, C_μ = 1.6%.

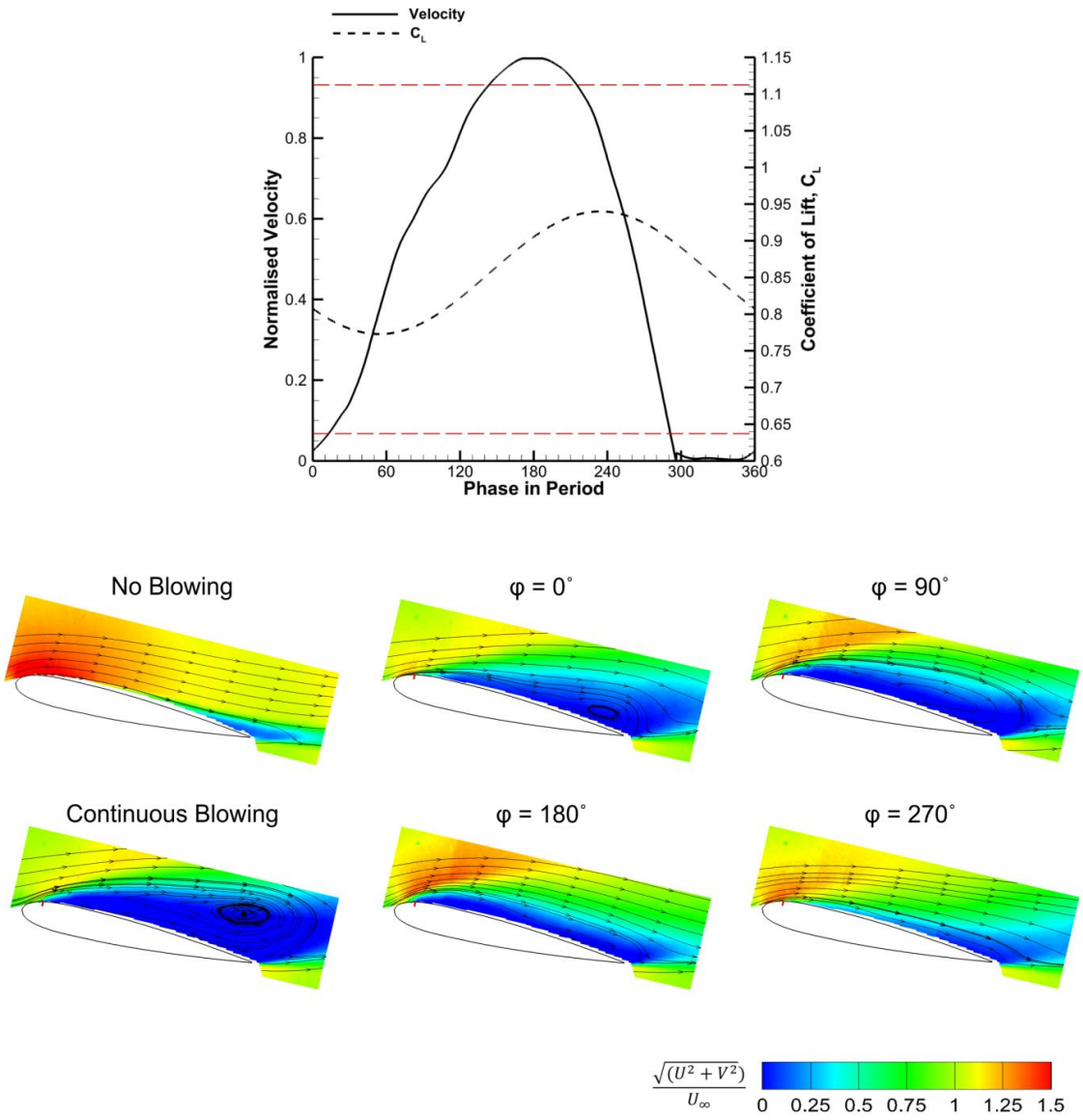

Figure 5.53 - Phase-averaged velocity field data comparing varying phases in k = 0.393 period for x_j/c = 0.08 at α = 13°, C_μ = 1.6%.

Chapter 6 : Transient Measurements

6.1 Force Measurements

Cycle averaged force measurements were performed for all three jet locations to evaluate the response of the upstream blowing jet flap to a step deployment. Measurements are conducted for a range of angles of attack between α = 0° to 16°. In Figs. 6.1 to 6.13, lift response to activation and deactivation of the jet is presented. Cycle hot wire measurements were conducted to measure the velocity input. For the activation phase, the jet velocity begins to rise at a convective time unit of τ = 0, towards a normalised velocity of 1. Similarly, the deactivation phase sees the velocity tend towards a value of 0, starting at τ = 0. For reference each convective time unit of τ = 1 equates to the airfoil travelling one chord length. The dashed line is the lift response to the velocity input, and is read with the right-hand-side axis for lift coefficient, C_L.

When considering the activation phase for the x_j/c = 0.95 jet, lift reacts to the jet velocity change immediately at α = 0°, in Fig. 6.1a. Although, steady-state lift is not attained until τ = 6-8. As shown in Fig. 6.1b, deactivation of the jet incites a similar reaction time towards steady-state. Upon deactivating the jet, oscillations in velocity magnitude are observed which do not cease until τ = 20. It is not fully understood why this oscillatory behaviour occurs. However, when examining the respective lift response, it is clear that these oscillations are not replicated in the force signal. When inclining to α = 5° Fig. 6.2a & b, the response of the jet remains around τ = 8 for both, activation and deactivation. Figures 6.3a & b shows this response becomes slower at α = 8°, as it extends to τ = 10. At α = 10°, 92% of steady-state lift reduction is achieved at τ = 8, seen in Fig. 6.4a. However, the remaining 8% requires a further four convective time units. This behaviour is mirrored during the deactivation phase, in Fig. 6.4b. At stall angle, α = 13°, steady-state lift reduction is much slower to reach than lower angles, Fig. 6.5a. Although significant lift reduction is achieved, $C_L - C_{Loff}$ = -0.104, it takes τ = 28 to manifest. Lift reduction at α = 16° is not as large as earlier angles, additionally, there is some unsteadiness which makes it difficult to accurately determine the time it takes to reach steady-state. When analysing Fig. 6.6a, a step change in lift appears to occur at around τ = 10, indicating a faster response than stall angle.

For x_j/c = 0.60, in Fig. 6.7a & b, the jet responds slower to the trailing edge jet at α = 5°. Change in lift reaches a maximum at approximately τ = 10. However, when comparing jets at x_j/c = 0.60 & 0.95 for α = 8°, Figs. 6.8a & 6.3a, the two jets realise comparable lift reduction of $C_L - C_{Loff} \approx$ -0.13. Furthermore, this change is attained in a similar time, τ = 10. The deactivation phase in Fig. 6.8b is subjected to the same rate for lift change. The time it takes to attain steady-state doubles to τ = 20, when inclining to α = 10°, shown in Fig. 6.9a & b. Just as seen with the trailing edge jet,

the x_j/c = 0.60 jet experiences a larger delay when at α = 13°, consequently reaching τ = 40 for steady-state. The longer time delay could be attributed to the larger lift reduction requiring more time to reach. At α = 16°, the change is large enough to distinguish from the unsteadiness.

For x_j/c = 0.08 at α = 10°, minimum lift coefficient is attained within τ = 20 but is accompanied with a lift reversal at the beginning of the cycle. This lift reversal, although relatively small, introduces a time delay which lasts approximately six convective time units, before lift reduction begins in Fig. 6.11a. This time delay suggests there is a limiting factor to the bandwidth. This is also observed upon jet deactivation. When examining the lift response at α = 13°, the lift reversal is noted once more but does not last as long as it did at α = 10°. This suggests that behaviour is inherent to the leading edge jet. As will be shown in section 6.3, flow visualisation may identify the mechanism provoking this time delay.

6.2 Modelling of Aerodynamic Response

Similar to how the aerodynamic response was modelled for periodic deployment, transient measurements can also be modelled to a first order system. The input profile and lift response both follow a profile akin to a combination of first order ramp and step responses. Equation [6.1] below models the jet velocity profile:

$$I = \frac{1}{\tau_{dep}}\left[\tau \times u(\tau) - \left(\tau - \tau_{dep}\right) \times u\left(\tau - \tau_{dep}\right)\right] \quad [6.1]$$

Equation [6.1] is modelled on the normalised velocity deployment, such that τ_{dep} is the convective time when maximum velocity is reached. The inverse of τ_{dep} represents the gradient towards normalised velocity reaching unity. The $u(\tau)$ denotes the Heaviside unit step function used in MATLAB, and steady-state blowing is attained when convective time reaches the deployment time, $\tau = \tau_{dep}$. The information from the modelled input profile is then used to produce a curve fit to the lift response with the equation below:

$$\frac{C_L - C_{Loff}}{C_{Lon} - C_{Loff}} = \frac{1}{\tau_{dep}}\left[\left(\tau - \kappa\left(1 - e^{-\tau/\kappa}\right)\right)u(\tau) - \left(\left(\tau - \tau_{dep}\right) - \kappa\left(1 - e^{-(\tau-\tau_{dep})/\kappa}\right)\right)u\left(\tau - \tau_{dep}\right)\right] \quad [6.2]$$

Experimental data is normalised so that steady-state lift is unity. As such, Eq. [6.2] includes transient and steady-state terms to model the first order response. Therefore, experimental data from transient measurements is modelled using the curve fit tool in MATLAB, to produce a fit for the left-hand-side of Eq. [6.2]. Figures 6.14 to 6.19 illustrate a good fit to the data with Eq. [6.2]. From the fitted function, a time constant κ is determined to quantify the transient response of the jet. For x_j/c = 0.08, a time delay is introduced to account for the initial reversal. The time constant is determined

for the data presented in section 6.1 for the activation and deactivation phases. Due to the difficulty in observing a distinct step change at α = 16°, the range of angles is reduced to α = 0° to 13°.

Figure 6.20 presents the time constants for all three jet locations. Solid symbols represent time constants for activation phase, while open symbols are for deactivation. From data at x_j/c = 0.95, it is evident that an increase in time constant is proportional to angle of attack. The smallest time constant is at α = 0°, where κ = 1.3 for activating the jet. The proportional relationship holds true at x_j/c = 0.60, where time constants at α = 5° & 8° are similar to those attained for x_j/c = 0.95. However, time constants for the trailing edge do not exceed $\kappa \leq 3$, for angles α < 13°. When comparing performance with location at α = 10°, the activating jet retains a faster transient response at x_j/c = 0.95, while the upstream locations realise time constants between κ = 4 to 4.26. The jet at α = 13°, produces a larger spread in time constant values when varying jet location. Although time constants for the leading edge appear small, one should be reminded of the time delays noted for this location. The time constant does not reflect the associated time delay. Trends noted for activation time constants, are also exhibited with deactivation. Comparison between both phases shows a consistency in time constants.

A comparison between time constants for transient and periodic measurements is presented in Figs. 6.21. All time constants presented are obtained for a maximum momentum coefficient of C_μ = 0.016. When recalling to Chapter 5, two variations of time constants was calculated for x_j/c = 0.95. Despite the difference deployment profiles, time constants are directly proportional to the angle of attack for x_j/c = 0.60 & 0.95. At x_j/c = 0.08, the trend in time constants is consistent between both sets of data. Transient time responses closely match to periodic deployment until α = 13°.

6.3 Flow Field Measurements

To further understand the development of the jet during a step deployment, particle image velocimetry measurements have been completed for the jet at x_j/c = 0.08, 0.60 & 0.95 with C_μ = 0.016. Angles selected for the jet at x_j/c = 0.95, are α = 0°, 10° & 13°, while PIV was conducted at α = 10° only for jets x_j/c = 0.08 & 0.60. Measurements are performed at a number of convective time units within the cycle. Presented in Figs. 6.22 to 6.30 are the cycle averaged velocity flow fields for the selected cases. Also shown are the respective cycle averaged force measurements. PIV is considered for both, the activation and deactivation phases of the cycle.

6.3.1 Jet On

For α = 0°, the airfoil produces a lift coefficient of C_L = 0 due to its symmetrical profile. As shown in Fig. 6.22, flow field measurement at τ = -10 is indicative of an inactive jet. A wake of reduced velocity magnitude follows the trailing edge. As mentioned earlier, the x_j/c = 0.95 jet is fastest at attaining steady-state lift when at lower angles of attack. Once the demand is employed, a disturbance in flow field is noted. As seen at τ = 2, the reduced velocity region commences ahead of the jet now to produce a change in lift of $C_L - C_{Loff}$ = -0.024. As time elapses between τ = 2 to 8, changes in flow field are small. However, the reduced velocity initiates further upstream with time. Aft of the jet, a further reduction in velocity strengthens. This leads to lift reducing by $C_L - C_{Loff}$ = -0.141 by τ = 8. However, 93% of this change in lift is already attained by τ = 6. Beyond τ = 8, force remains relatively constant, and as one would expect, so does the flow field at τ = 22 & 40.

For the activation phase of step deployment, flow field measurements were taken for all three jet locations at α = 10°, with C_μ = 0.016. This elicits a comparison in flow field development among the locations. At a convective time of τ = -10, the jet velocity is zero and is therefore representative of baseline case, in Fig. 6.23. No clear separation is observed at this angle of attack when there is no blowing but a low velocity region near the trailing edge suggests this location is susceptible to separation. Soon after activating the x_j/c = 0.95 jet at τ = 3, also Fig. 6.23, the streamlines have begun to deflect upwards and the velocity region extends further upstream causing $C_L - C_{Loff}$ = -0.042. The separated region continues to grow for τ = 6 to 12 causing greater streamline deflection. At τ = 12, the change in lift coefficient stabilises at approximately its steady-state value, $C_L - C_{Loff}$ = -0.12. This reveals that a third of the steady-state lift change is attained at a quarter of the rise time. In the range τ = 12 to 48 there is a small reduction in velocity magnitude in the separated region but generally the changes are small.

For x_j/c = 0.60, Fig. 6.24, the time taken to reach the steady-state value of $C_L - C_{Loff}$ = -0.158, is τ = 20. Hence, slower than the trailing edge jet by eight convective time units. At τ = 5,

acceleration of flow above the jet and an advancing separation region is observed, rendering a change in lift of $C_L - C_{Loff}$ = -0.04. This separated region continues to grow reaching the jet around τ = 10. The high velocity magnitude region at the leading edge diminishes in size with convective time unit. After τ = 10, the flow field changes are smaller reflecting the lift coefficient.

For x_j/c = 0.08, the lift response is again slower than x_j/c = 0.95 and exhibits unsteadiness, in Fig. 6.25. Within the first five convective time units following activation, reversal in lift is observed. Lift increases by $C_L - C_{Loff}$ = 0.02 at τ = 5. After which lift decreases sharply producing $C_L - C_{Loff}$ = -0.236 at τ = 20. This renders the x_j/c = 0.08 jet to be the most effective location for reducing lift at α = 10°, despite the initial lift augmentation. When referring to the velocity flow fields, trailing edge separation can be seen at τ = 5, with a reduction in velocity magnitude along the airfoil commencing near $x/c \approx 0.19$. Similar behaviour with increased transitory lift, was observed by Darabi & Wygnanski [180] who attributed the lift reversal due to the development of a leading edge vortex analogous to the dynamic stall vortex. The shear layer ostensibly is deflected upwards near the jet at τ = 10 as the jet begin to develop and incite lift reduction. Near the leading edge, magnitude of velocity reduces with time, as separation extends across the entire airfoil. A small increase in deflection angle of the shear layer between τ = 15 & 20 indicates a larger wake size.

In order to understand why the jet at x_j/c = 0.08 is so slow to respond, close-up images accompanied with velocity profiles of local flow to the leading edge jet at τ = -10, 5, 10, 15 & 60 are presented in Fig. 6.26. Velocity profiles were taken at four stations; x/c = 0.025, 0.065, 0.135 & 0.175. The lengths of the arrows represent velocity magnitude. Figure 6.27 shows vorticity plots for these respective cases. Laser reflections render it difficult to capture detail close to the airfoil surface. Figure 6.26a & 6.27a show the initial state of the airfoil prior to the jet activation, with little variation in magnitude observed nearer to the surface and no sign of negative vorticity. For τ = 5, changes in the flow field are observed at x/c = 0.175 where a velocity reduction occurs. Upstream of this station, a local area at $y/c \approx 0.23$ shows a reduction in velocity. This local reduction in velocity coincides with the emergence of vorticity in correspondence to Fig. 6.27b, signifying that the jet has initiated. This indicates that the leading edge jet maintains fast actuation. No change is exhibited near the leading edge and the jet, demonstrating the jet is inhibited from fully actuating. As this time increases to τ = 10, effective upstream blowing appears to be commencing, as shown in Fig. 6.27c, with stations downstream of the blowing jet show velocity profiles are becoming separated, see Fig. 6.26c. It is evident upstream blowing is deflecting the shear layer away, with velocities below the layer reduced. Figure 6.26c shows velocity magnitude at x/c = 0.025 remains unchanged from τ = 5 to τ = 10. However, at τ = 15, the jet reduces the velocity magnitude close to the surface with reduction in velocity more obvious downstream of the jet. Separation from the airfoil occurs further upstream

to what is observed at τ = 10. Due to these flow field changes, a change in lift of $C_L - C_{Loff}$ = -0.22 is realised.

As shown previously, the baseline case at α = 13° can be represented by flow field measurements taken at τ = -10. Prior to jet deployment for x_j/c = 0.95, the airfoil experiences separation from $x/c \approx 0.80$, as seen in Fig. 6.28. Once the jet is activated, this separated region extends forwards to $x/c \approx 0.72$, subsequently enlarging the wake size. Additionally, the entire region above the leading edge is concentrated with high velocity magnitude at τ = -10. With the jet employed, this high velocity magnitude region clearly reduces in size. This causes a reduction in lift of $C_L - C_{Loff}$ = -0.05 at τ = 7. Although jet velocity has attained steady-state at this stage, the lift reduces with a larger lag than what is observed for lower angles of attack for x_j/c = 0.95. At τ = 14, the separated region initiates further upstream at $x/c \approx 0.68$, highlighting the influence the jet has far upstream of its location. Between τ = 14 & 28, streamlines deflect upwards as the recirculation within the separated region intensifies with convective time. From the force measurements in Fig. 6.5a, it could be said steady-state is achieved at τ = 28 where the change in lift from the baseline case is $C_L - C_{Loff}$ = -0.094. This demonstrates that by τ = 7, or 25% of time taken to reach steady-state, over half the change in lift from continuous blowing is obtained. As such, the trailing edge jet retains significant effectiveness despite the high angle of attack.

6.3.2 Jet Off

For load control applications the deactivation phase is as important in maintaining a constant force. Force and PIV measurements for the deactivation phase of the jet at x_j/c = 0.08 & 0.60, with α = 10°, are presented in Fig. 6.29 & 6.30. Hot wire measurements show velocity oscillations occur on deactivation. The magnitude of these oscillations increases in severity towards the trailing edge. As such, the deactivation phase for the trailing edge jet was omitted from PIV consideration. Although it is assumed these oscillations subside when a freestream velocity is introduced and where not observed in the force signal, this cannot be explicitly demonstrated. For x_j/c = 0.60 in Fig. 6.29, lift coefficient during steady-state blowing at τ = -10 is C_L = 0.72. A large recirculation region is observed aft of the jet, with deflected streamlines away from the upper surface. However, once deactivation is instigated at τ = 0, lift does not respond to jet velocity change until τ = 1.5. This means lift has increased by the time it reaches τ = 3, $C_L - C_{Lon}$ = 0.013. This increase is insufficient to create a major change in flow field. Streamlines tend towards the upper surface, as the observed separated region reduces significantly in size at τ = 7. This translates to lift augmenting by $C_L - C_{Lon}$ = 0.111. Flow separates at approximately $x/c \approx 0.75$, with a reduced velocity magnitude following this location. As the airfoil the jet continues to τ = 10, separation is displaced downstream to $x/c \approx 0.80$. At this point in the phase, the airfoil nearly attains the lift of the baseline case, with

$C_L - C_{Loff}$ = -0.016. As it is near the steady-state value, the flow field experiences small changes between τ = 10 & 40. Steady-state lift is achieved at τ = 20, which is the same time it took the activating jet to achieve a steady-state value. Hence, suggesting the jet near the mid-span is equally fast upon activating or deactivating.

Upon deactivation, the x_j/c = 0.08 jet velocity in Fig. 6.30 does not decelerate as fast as it accelerates for the activating jet, as it is seen to take six convective time units to reach negligible velocity. Lift at τ = -10 is akin to that of the τ = 60 in Fig. 6.25,C_L = 0.68. Hence, the flow field presented is similar. Similar to what was observed with the activation phase for x_j/c = 0.08, a force reversal occurs at $\tau \approx 3$ with a change of lift of $C_L - C_{Loff}$ = 0.3. Therefore, instant termination of jet creates a similar effect to the immediate activation for leading edge jets. The velocity flow field shows a ripple on the shear layer directly aft of the jet. Lift rises at τ = 3, and the large separation on the upper surface subsides by τ = 7. The high velocity magnitude expected near the leading edge begins to re-establish, although separation is clear near the trailing edge. Streamlines return closer towards the upper surface, as time rises to τ = 10 as an augmentation in velocity at the leading edge continues to manifest. Lift is still at a deficit in comparison to the baseline case, $C_L - C_{Loff}$ = -0.06. Between τ = 10 & 20, streamlines aft of the trailing edge progress upwards, which contributes to increasing lift by 5%. Once the airfoil has reached a steady state at τ = 40, flow has completely reattached to the upper surface and lift coefficient has returned to the baseline value. The oscillations with jet velocity observed soon after deactivation appear to not have had an effect on the lift response.

6.4 Literature Comparison

As mentioned in section 6.3.1, the lift reversal associated with the leading edge jet was also observed by Darabi & Wygnanski [180], who made use of audio frequencies to incite flow reattachment to an inclined flap. Although the reduced frequency had an effect on how quickly reattachment is obtained, a reduction in force occurs before force augmentation, immediately after actuation. This force reduction is further exacerbated with greater momentum coefficients, but remains constant in the time it is observed at. During the separation process [181], a reversal in force is also noted before force reduction can occur. When considering process time, the reattachment process is completed within a shorter time in comparison to the separation. Through flow visualisation techniques, Darabi & Wygnanski [180] attribute the initial increase in lift to a vortex forming near the leading edge, in a process analogous to dynamic stall vortex. As such, it is required of the vortex to be completely convected beyond the trailing edge before lift reduction can proceed. Therefore, the aerodynamic response to the step deployment is what reduces the bandwidth of control when blowing from the leading edge. This is corroborated by Kerstens *et al.* [118] who notes a time delay associated with leading edge pulsed blowing.

Transient experiments for leading edge blowing at α = 20° have shown to reach a steady-state at around τ = 6 [118]. This is faster than what is observed in the present study, but this could be due to differences in testing conditions, such as jet blowing strength. Furthermore, force measurements for a normal blowing jet at x_j/c = 0.95 on the lower surface have been performed by Blaylock *et al.* [72]. Using a momentum coefficient of C_μ = 0.0029, steady-state lift takes around τ = 10 to reach. Although the deflection angles are dissimilar, this is slower than what is attained in the current study for the upper surface jet by two convective time units. However, the jet velocity achieves a maximum in a similar time to what is noted in the current study.

PIV measurements could be compared to CFD studies, which have been conducted by Blaylock *et al.* [72]. The RANS solver was capable of identifying a growing separation region upon jet activation. The aerodynamic response becomes more responsive when this separated region closes at the trailing edge, as such an alteration in flow field near to the trailing edge realises an augmentation in circulation. Prior to steady-state, a vortex aft of the jet enhances in strength to compel the bubble to ultimately burst. Although close-up images of the transient flow field at α = 0° were not taken within the current study, a reduced velocity magnitude region was observed to propagate upstream with time.

6.5 Conclusions

Force and flow field measurements were taken to evaluate the efficacy of the jet flap with transient deployment. When the jet flap is activated with a step profile, the lift response is always found to lag the input. Despite this, aerodynamic response for x_j/c = 0.95 at α = 0°, is found to reach steady state lift within τ = 8. Deactivation is achieved within a similar convective time. In general, the response becomes slower as angle of attack is increased. As was observed for periodic deployment, displacing the jet to upstream locations incites a greater aerodynamic lag. The leading edge jet experiences a time delay of six convective time units before aerodynamically responding to the input profile. The aerodynamic response was modelled using a first order system, and the jet response was quantified using a time constant. For x_j/c = 0.95 jet at α = 0°, time constant is found to be as low as κ = 1.3 and doesn't exceed κ = 3 for angles below α = 13°. Flow field measurements exhibit minimum lift reduces with increased separation and reduced velocity magnitude near leading edge.

6.6 Figures

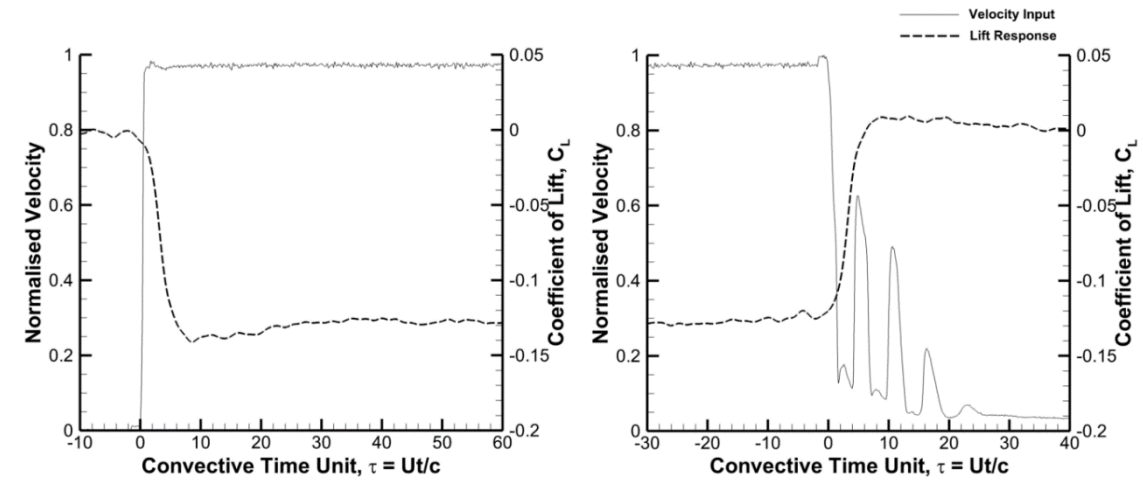

Figure 6.1 - Transient force measurements for x_j/c = 0.95, with $C_\mu = 1.6\%$ at α = 0°; a) activated jet and b) deactivated jet.

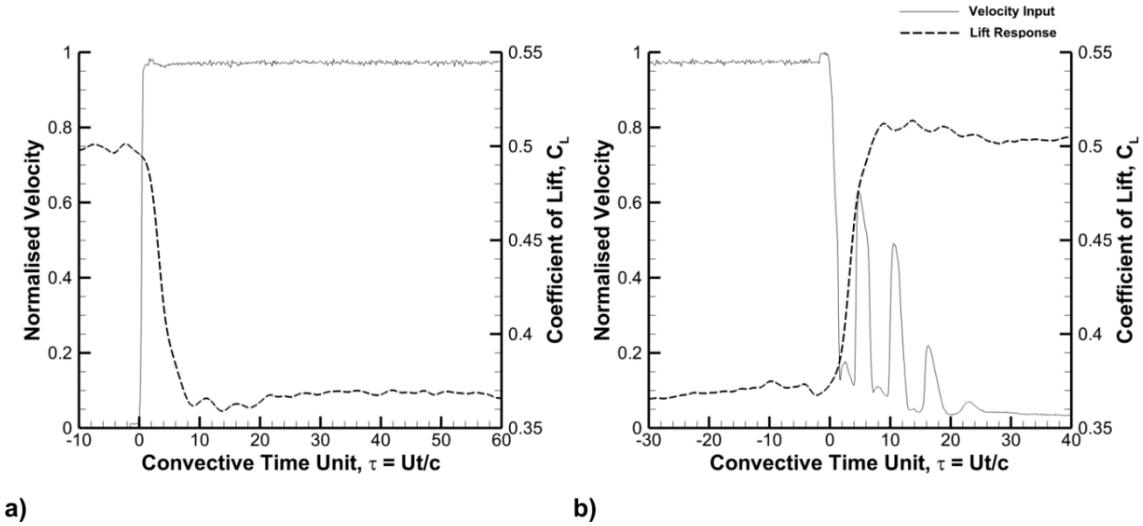

Figure 6.2 - Transient force measurements for x_j/c = 0.95, with $C_\mu = 1.6\%$ at α = 5°; a) activated jet and b) deactivated jet.

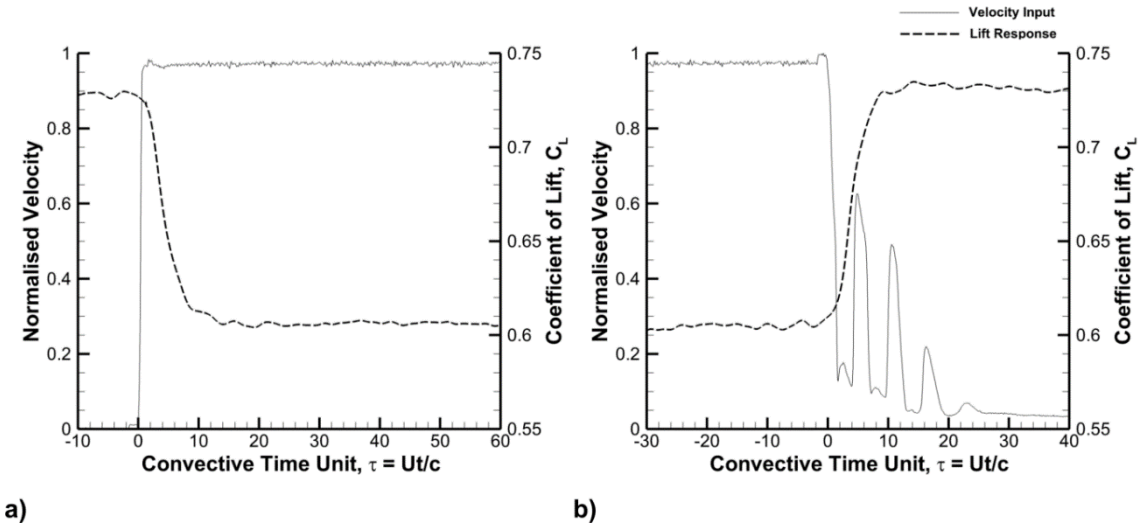

Figure 6.3 - Transient force measurements for x_j/c = 0.95, with $C_\mu = 1.6\%$ at α = 8°; a) activated jet and b) deactivated jet.

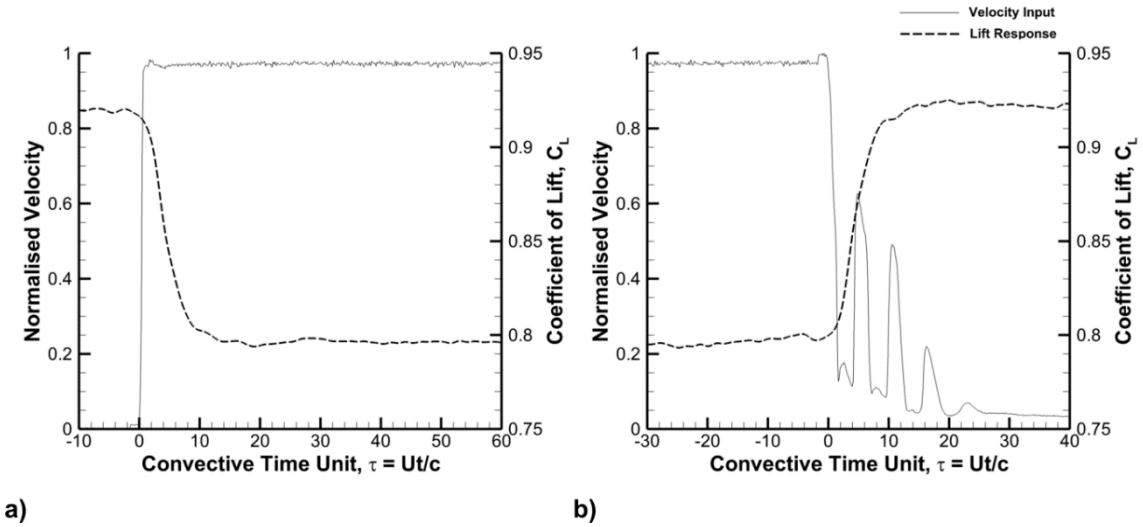

Figure 6.4 - Transient force measurements for x_j/c = 0.95, with $C_\mu = 1.6\%$ at α = 10°; a) activated jet and b) deactivated jet.

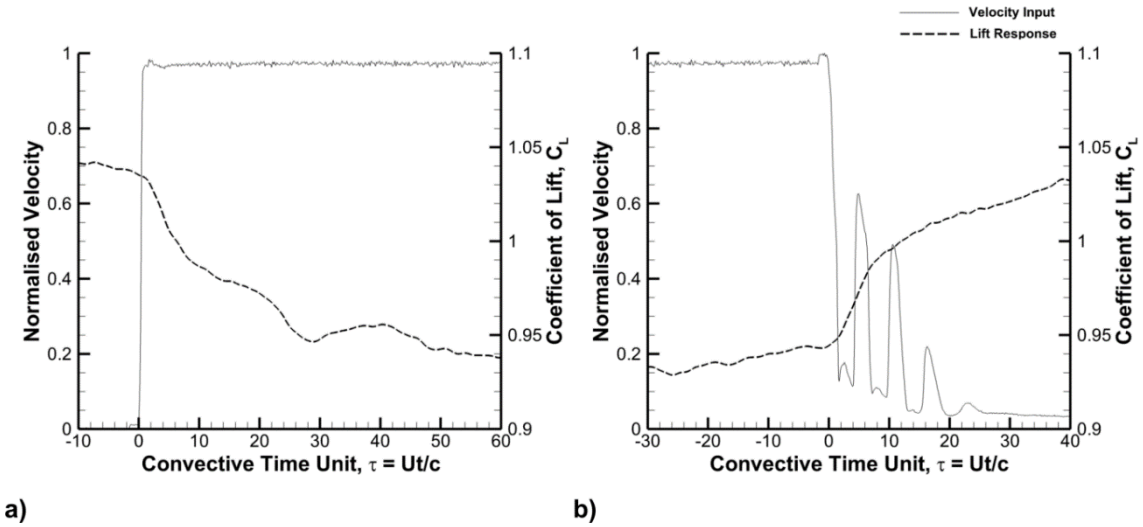

Figure 6.5 - Transient force measurements for x_j/c = 0.95, with $C_\mu = 1.6\%$ at α = 13°; a) activated jet and b) deactivated jet.

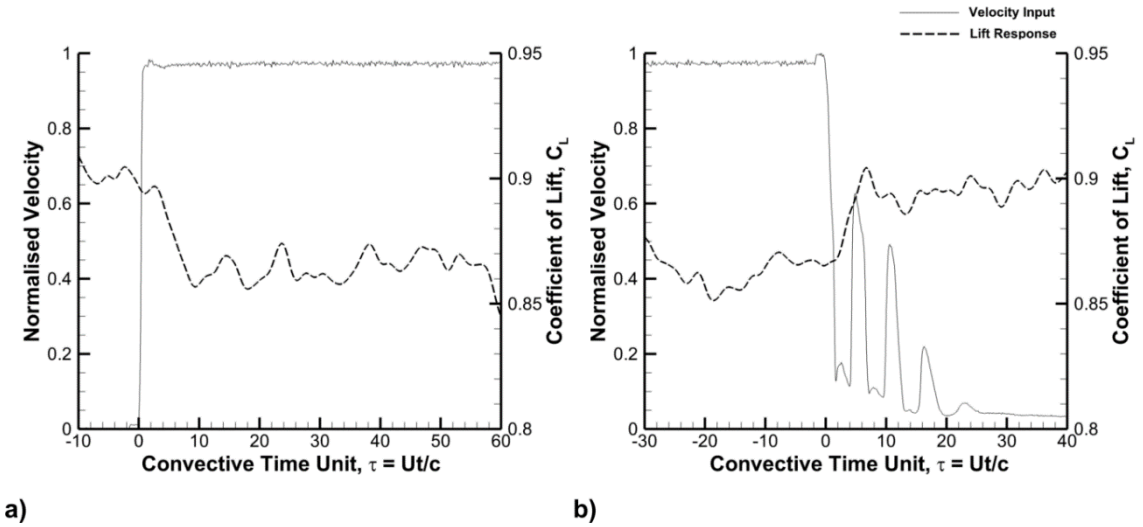

Figure 6.6 - Transient force measurements for x_j/c = 0.95, with $C_\mu = 1.6\%$ at α = 16°; a) activated jet and b) deactivated jet.

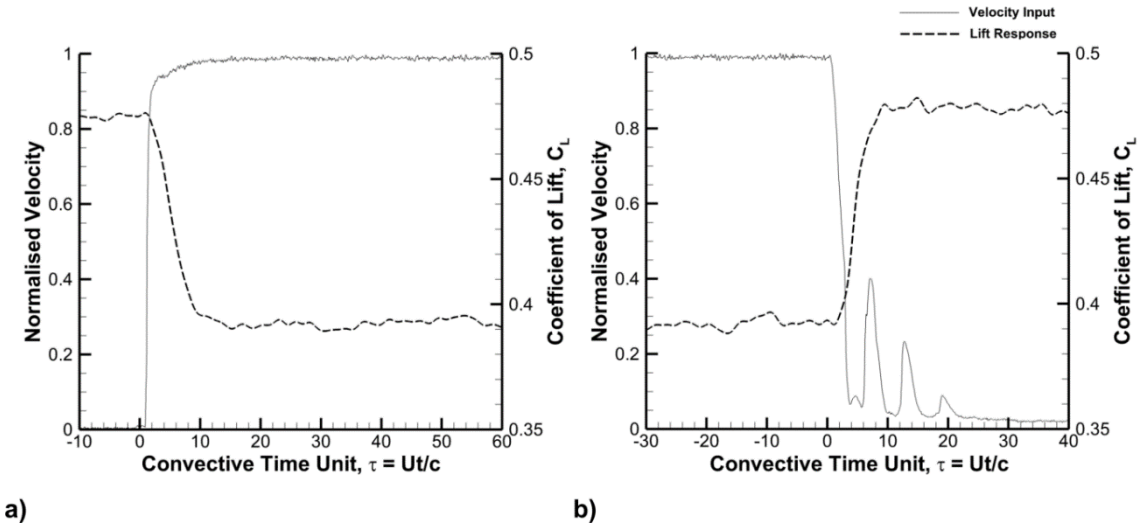

Figure 6.7- Transient force measurements for x_j/c = 0.60, with $C_\mu = 1.6\%$ at α = 5°; a) activated jet and b) deactivated jet.

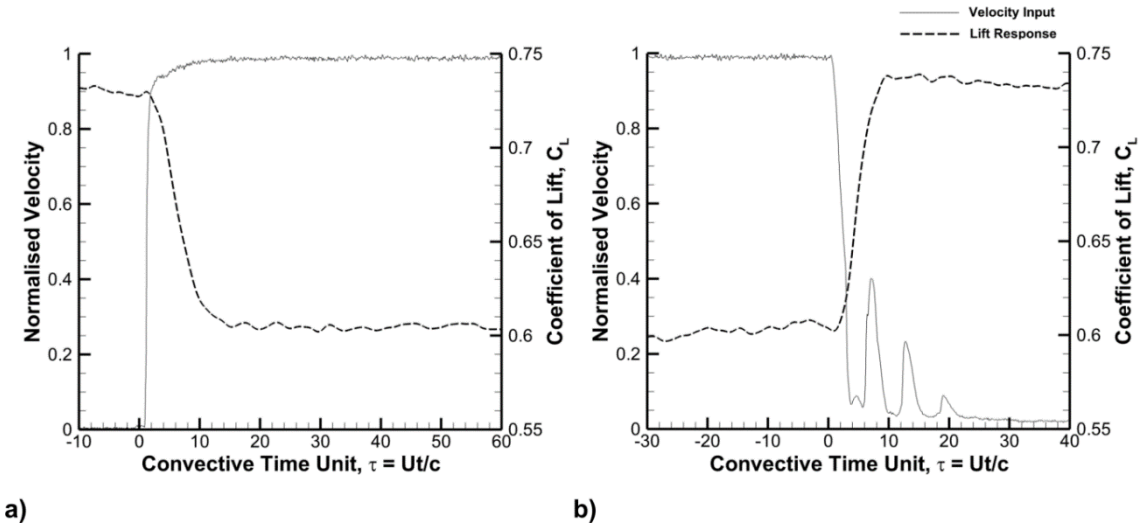

Figure 6.8 - Transient force measurements for x_j/c = 0.60, with $C_\mu = 1.6\%$ at α = 8°; a) activated jet and b) deactivated jet.

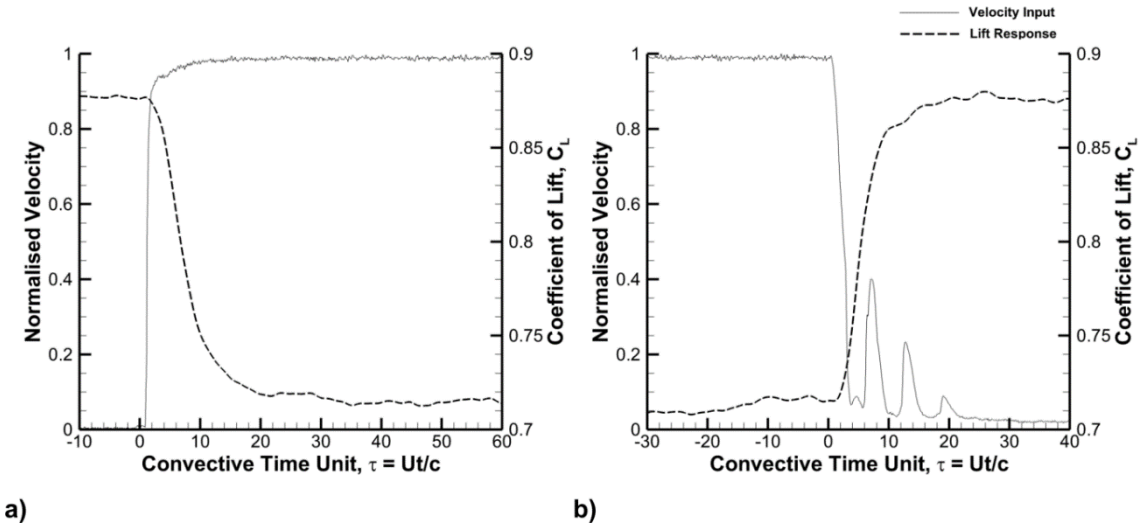

Figure 6.9 - Transient force measurements for x_j/c = 0.60, with $C_\mu = 1.6\%$ at α = 10°; a) activated jet and b) deactivated jet.

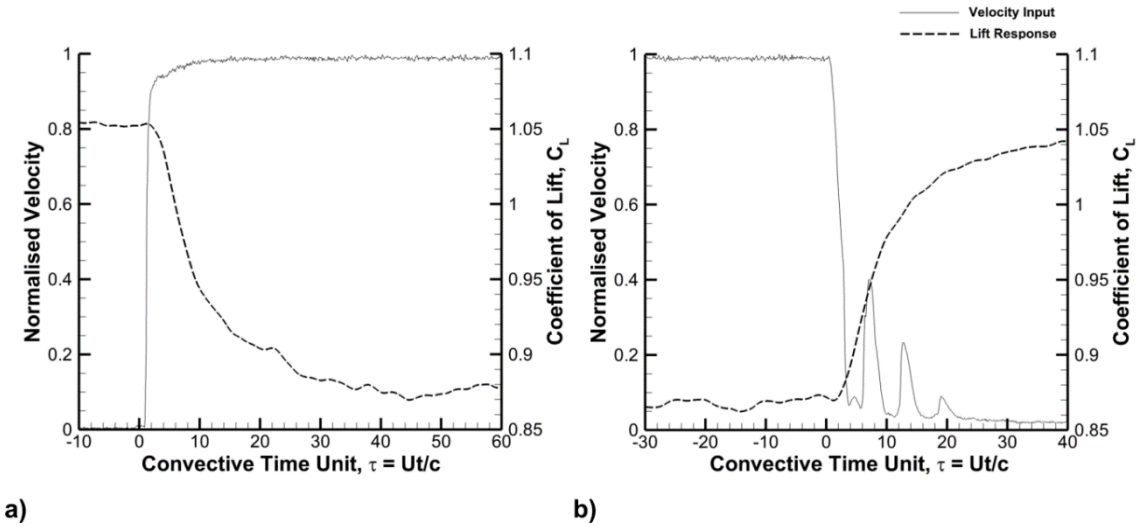

Figure 6.10 - Transient force measurements for x_j/c = 0.60, with $C_\mu = 1.6\%$ at α = 13°; a) activated jet and b) deactivated jet.

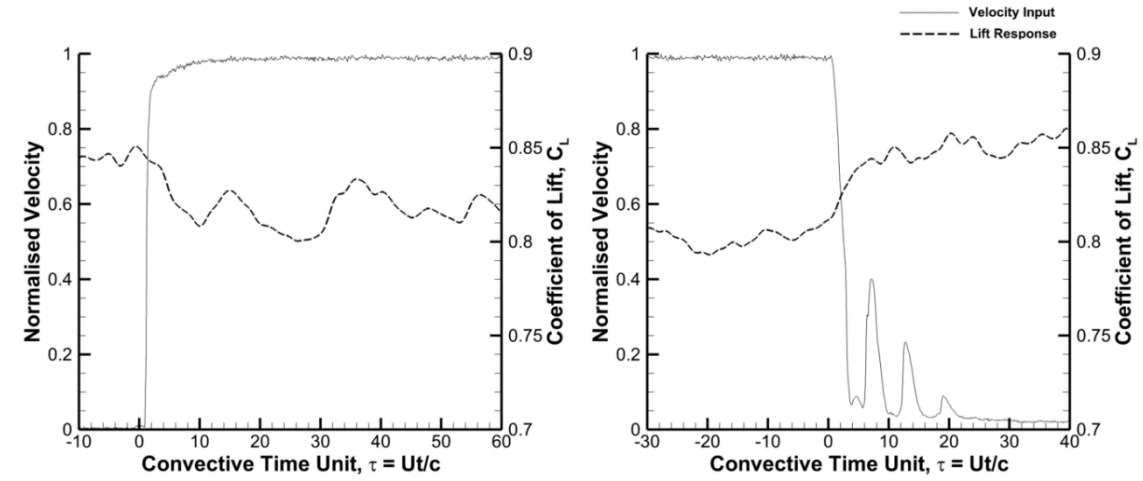

Figure 6.11 - Transient force measurements for x_j/c = 0.60, with $C_\mu = 1.6\%$ at α = 16°; a) activated jet and b) deactivated jet.

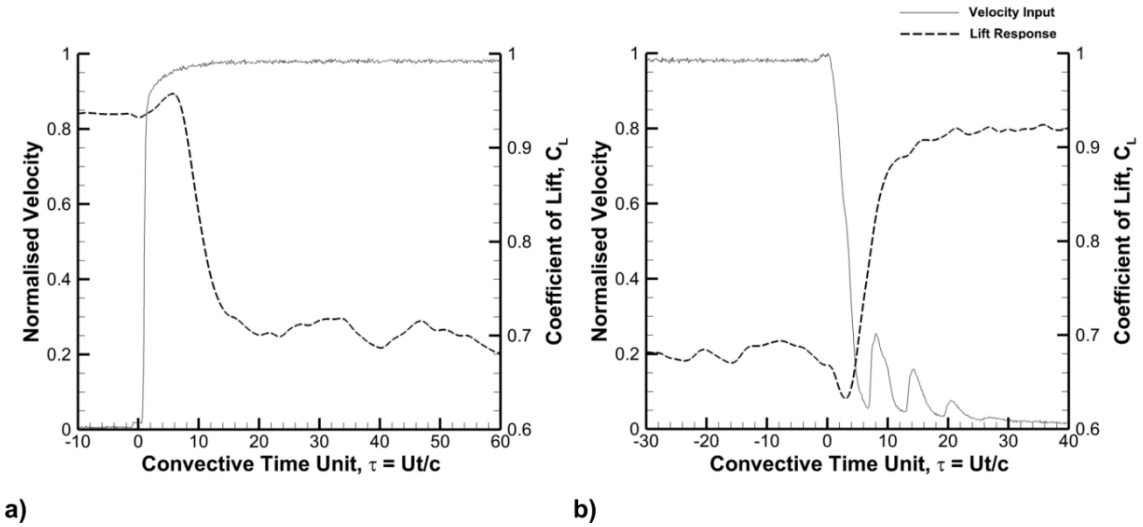

Figure 6.12 - Transient force measurements for x_j/c = 0.08, with $C_\mu = 1.6\%$ at α = 10°; a) activated jet and b) deactivated jet.

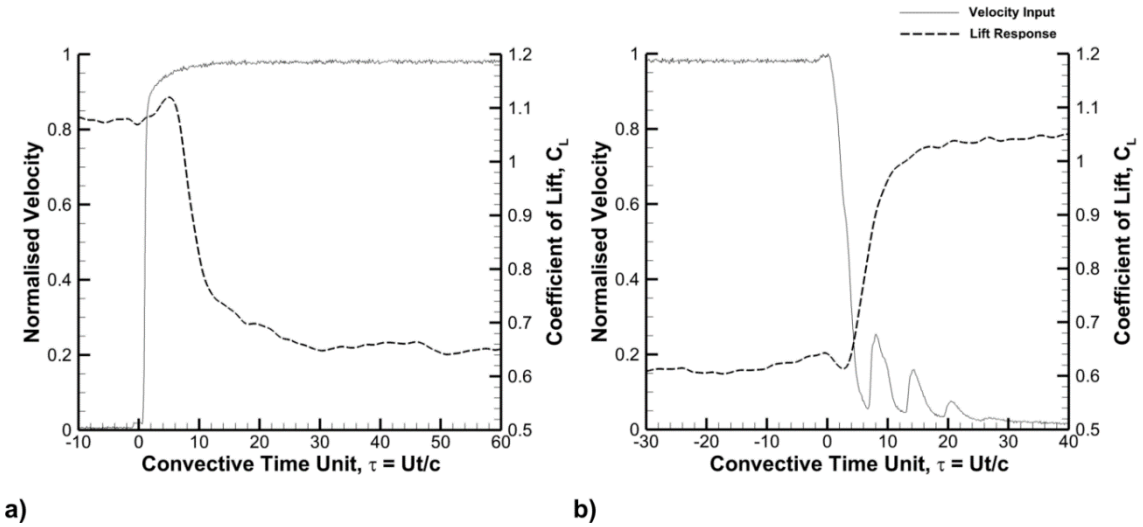

Figure 6.13 - Transient force measurements for x_j/c = 0.08, with $C_\mu = 1.6\%$ at α = 13°; a) activated jet and b) deactivated jet.

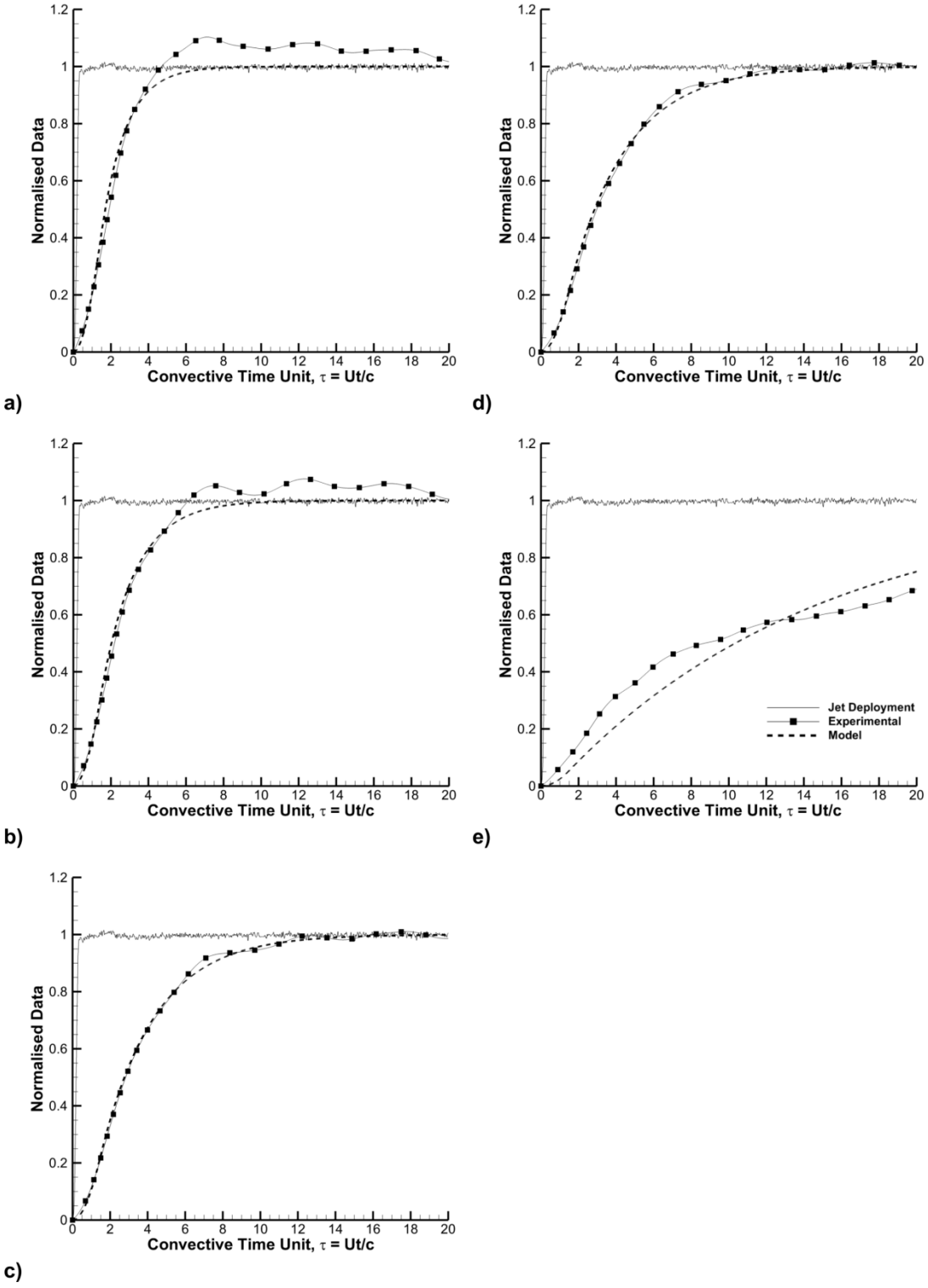

Figure 6.14 - Comparison of model to experimental data for activating jet for x_j/c = 0.95 at C_μ = 1.6%; a) α = 0°, b) α = 5°, c) α = 8°, d) α = 10° & e) α = 13°.

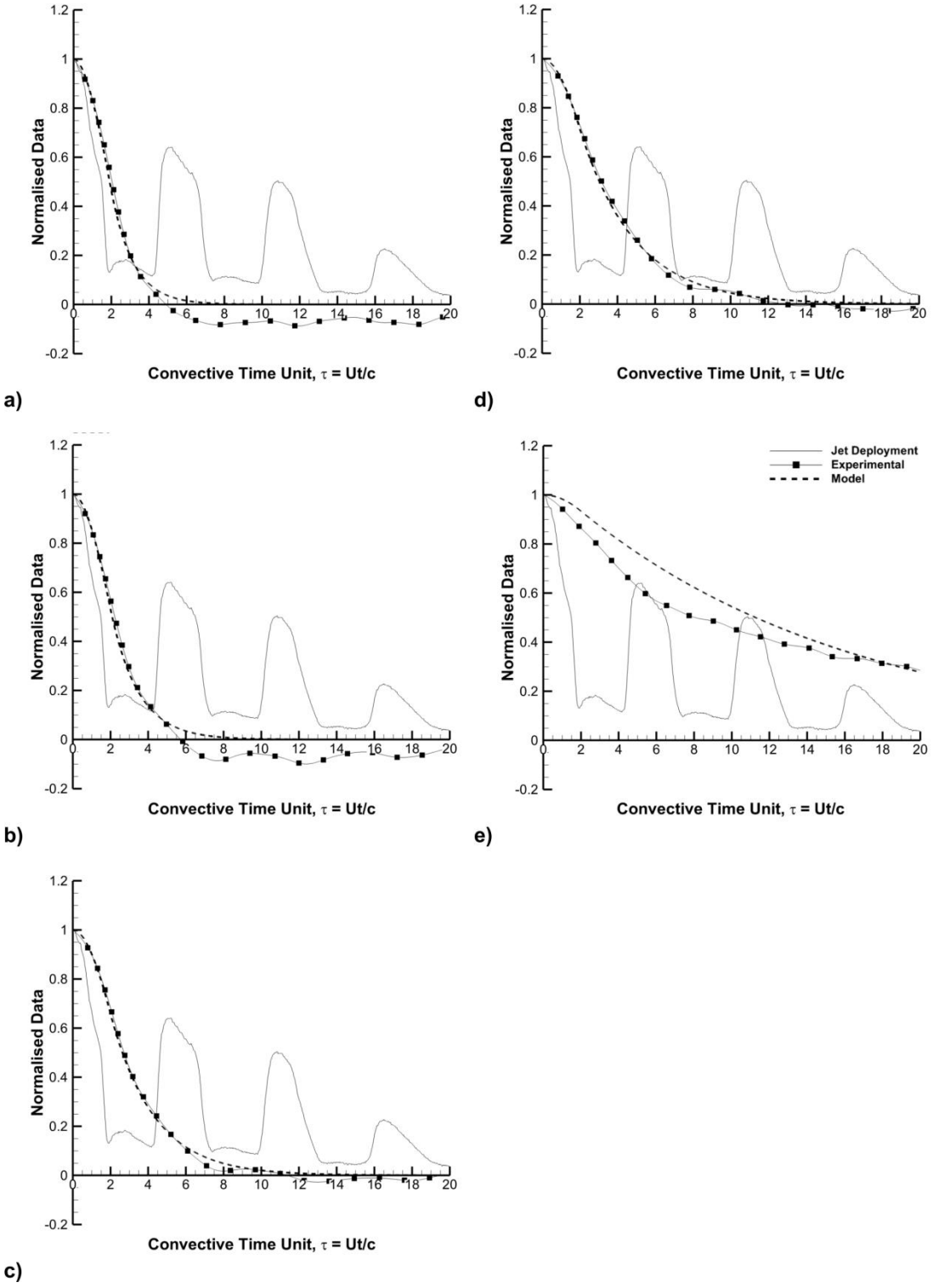

Figure 6.15 - Comparison of model to experimental data for deactivating jet for x_j/c = 0.95 at C_μ = 1.6%; a) α = 0°, b) α = 5°, c) α = 8°, d) α = 10° & e) α = 13°.

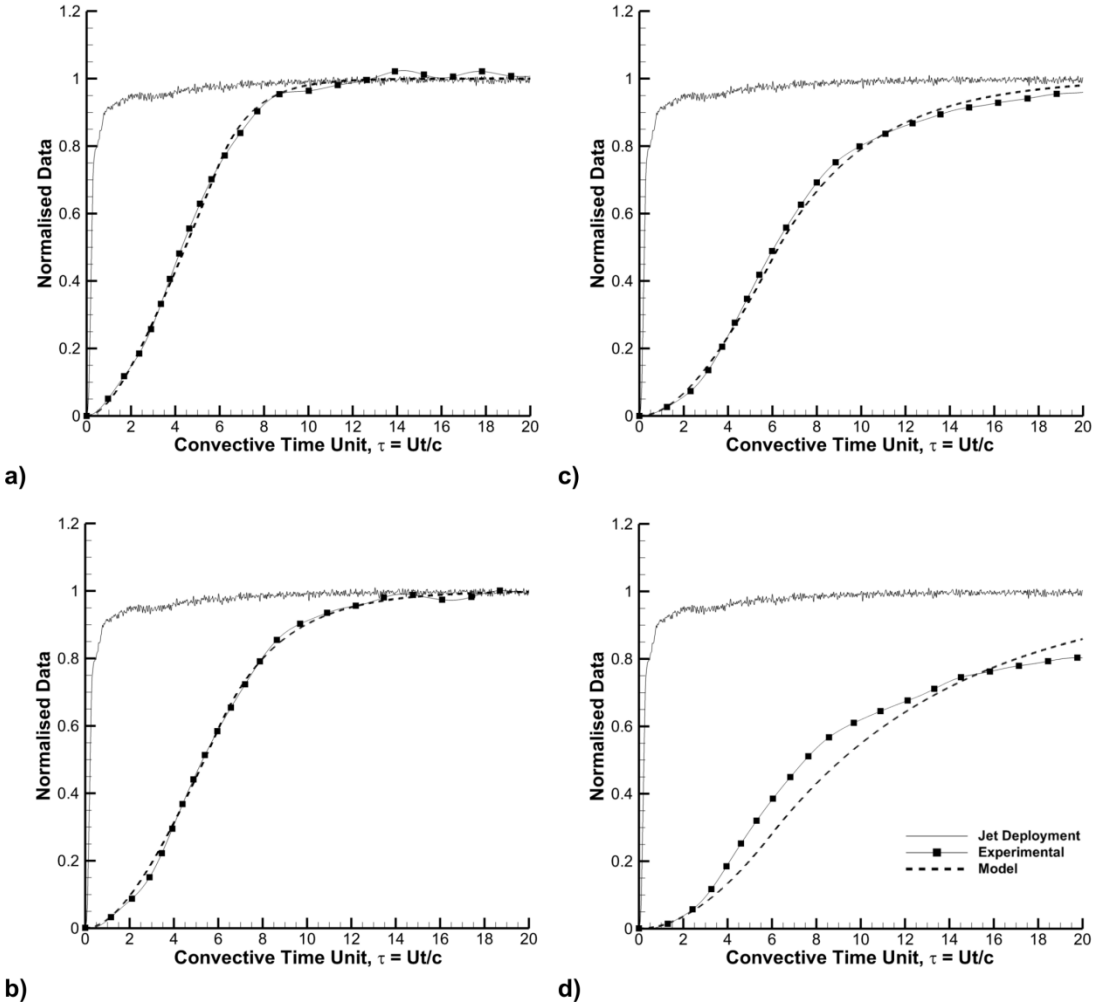

Figure 6.16 - Comparison of model to experimental data for activating jet for x_j/c = 0.60 at C_μ = 1.6%; a) α = 5°, b) α = 8°, c) α = 10° & d) α = 13°.

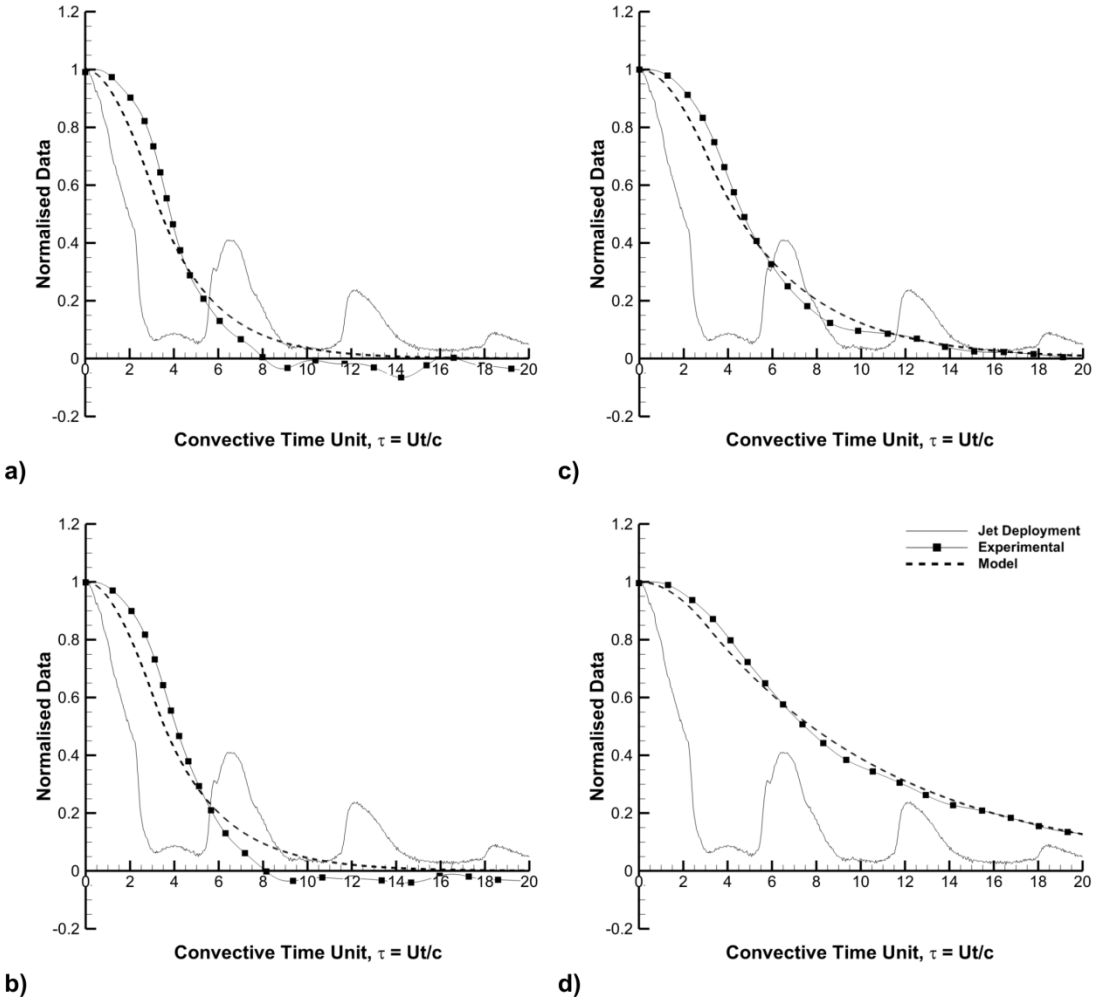

Figure 6.17 - Comparison of model to experimental data for deactivating jet for x_j/c = 0.60 at C_μ = 1.6%; a) α = 5°, b) α = 8°, c) α = 10° & d) α = 13°.

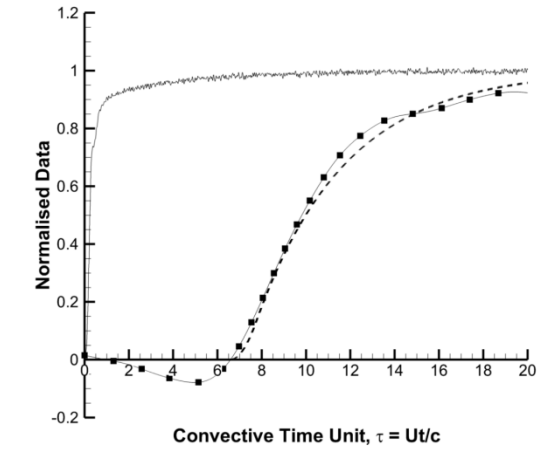

a)

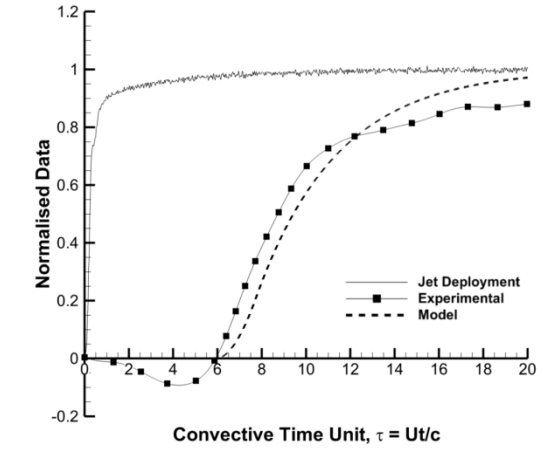

b)

Figure 6.18 - Comparison of model to experimental data for activating jet for x_j/c = 0.08 at C_μ = 1.6%; a) α = 10° & b) α = 13°.

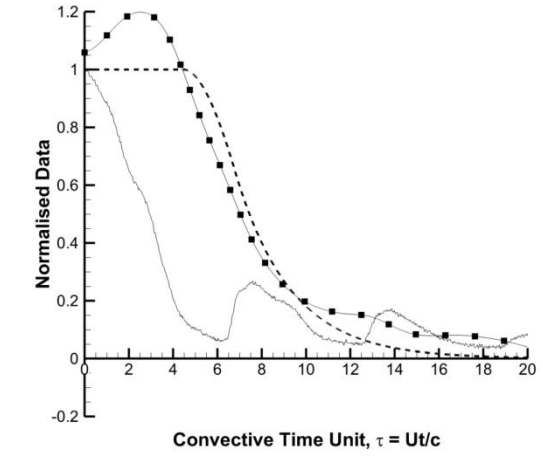

a)

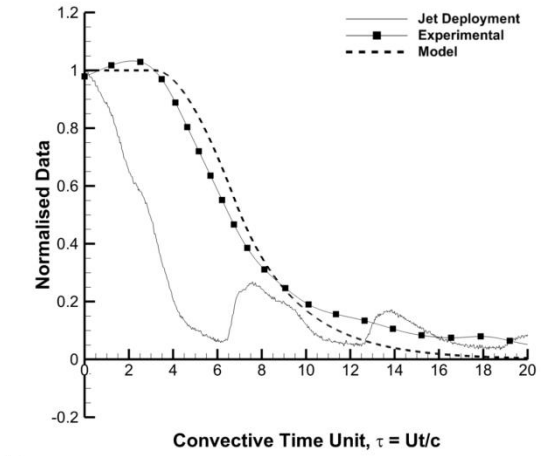

b)

Figure 6.19 - Comparison of model to experimental data for deactivating jet for x_j/c = 0.08 at C_μ = 1.6%; a) α = 10° & b) α = 13°.

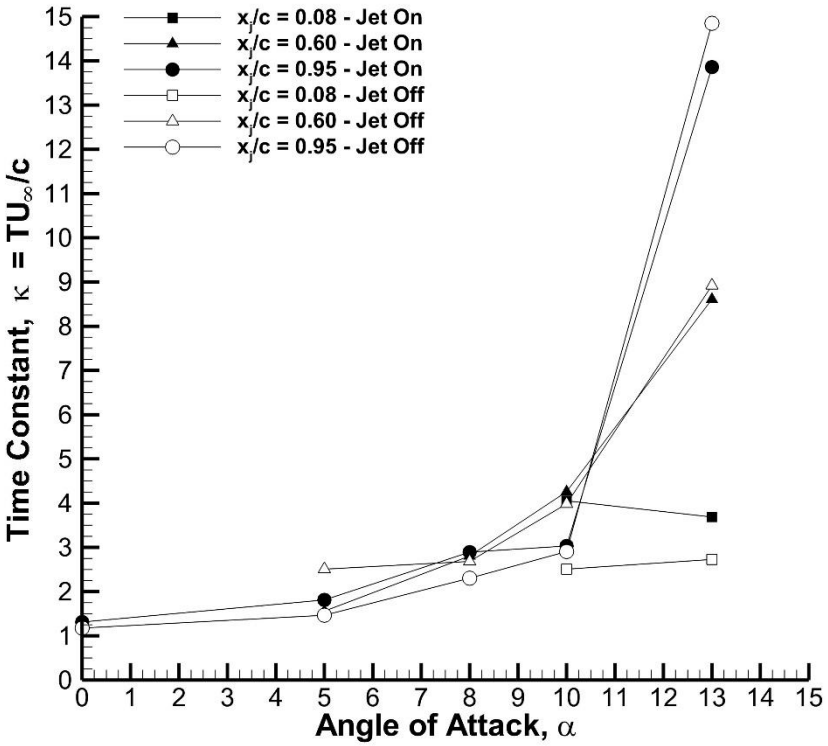

Figure 6.20 - Time constants for x_j/c = 0.08, 0.60 & 0.95.

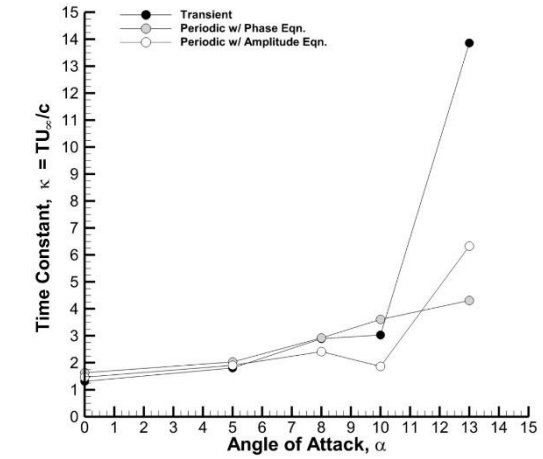

a)

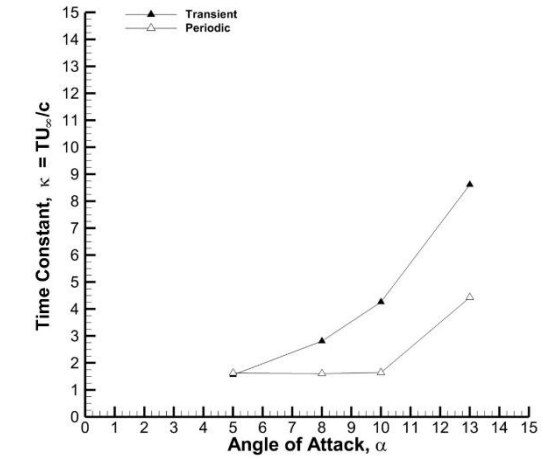

b)

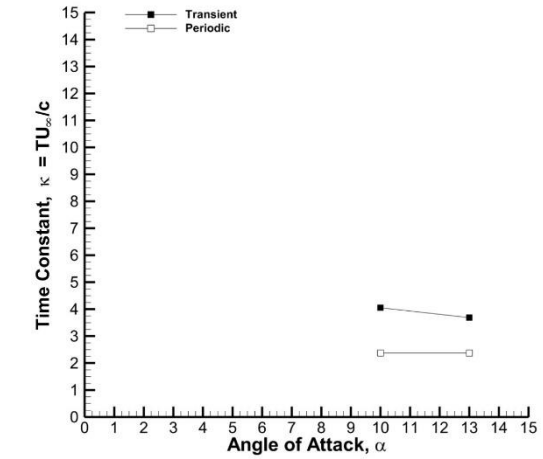

c)

Figure 6.21 – Comparison of time constants for periodic and transient measurements at x_j/c =0.08, 0.60 & 0.95.

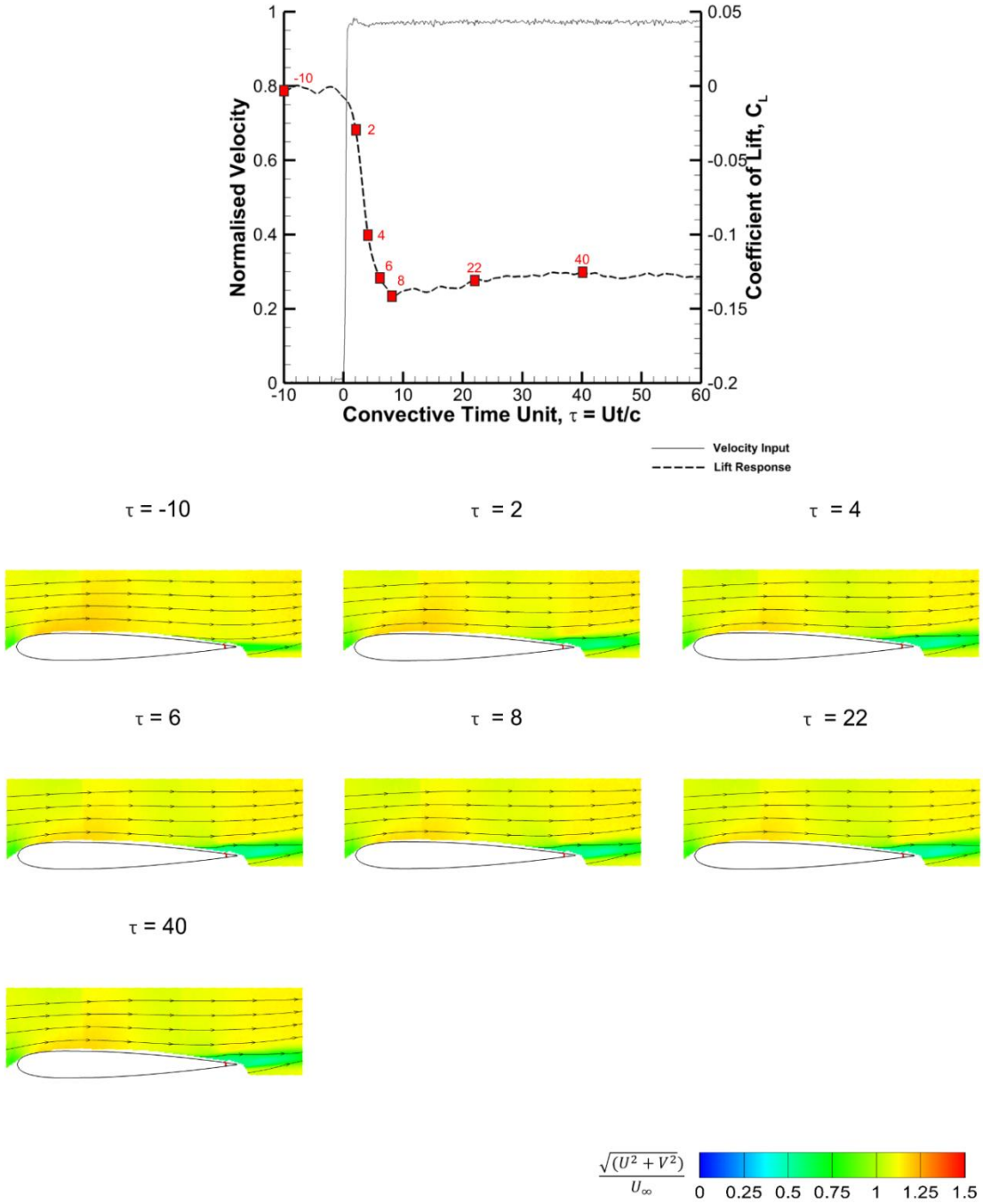

Figure 6.22 - Phase-averaged velocity field data for developing transient jet at x_j/c = 0.95 at α = 0°, C_μ = 1.6%.

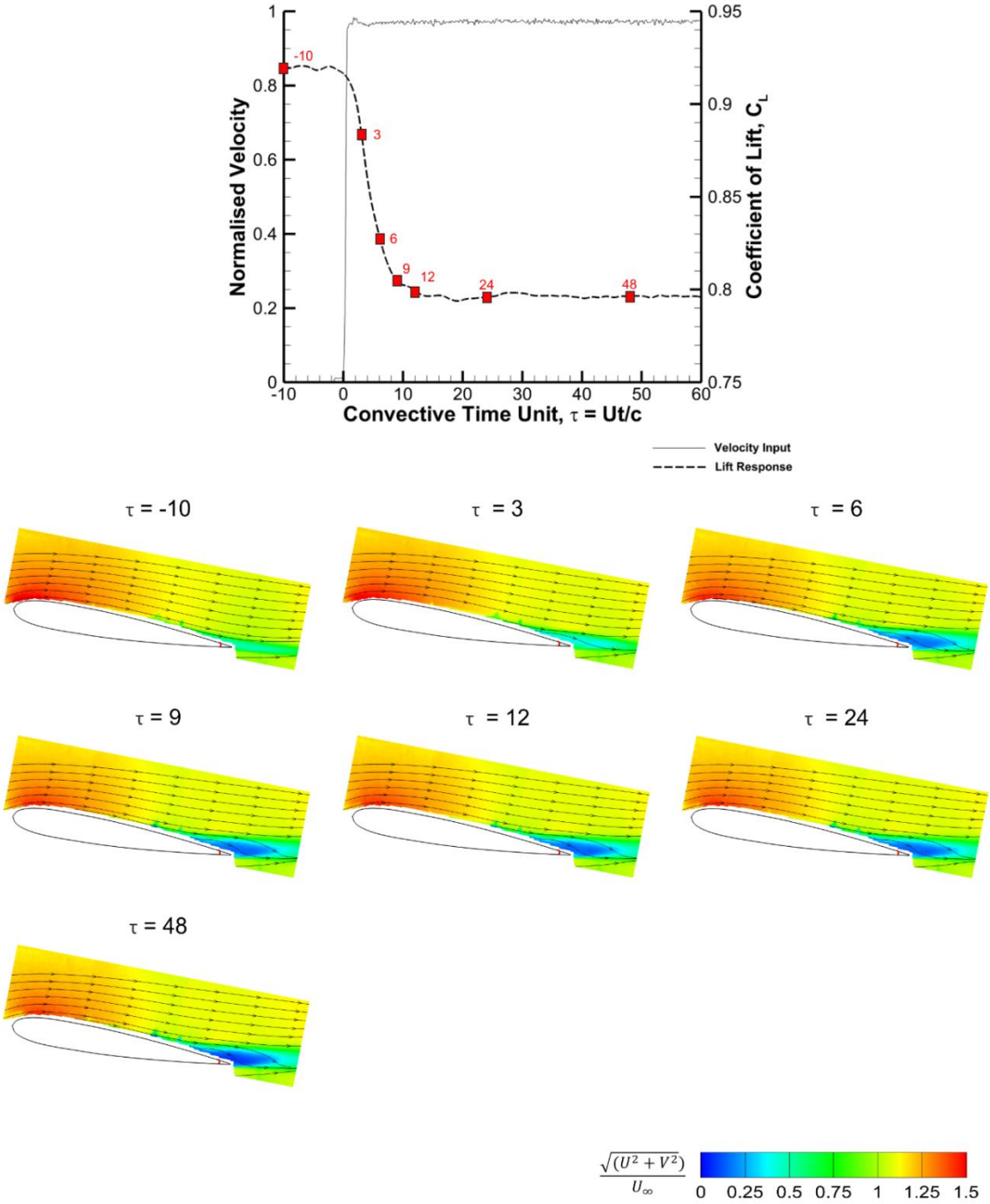

Figure 6.23 - Phase-averaged velocity field data for developing transient jet at x_j/c = 0.95 at α = 10°, C_μ = 1.6%.

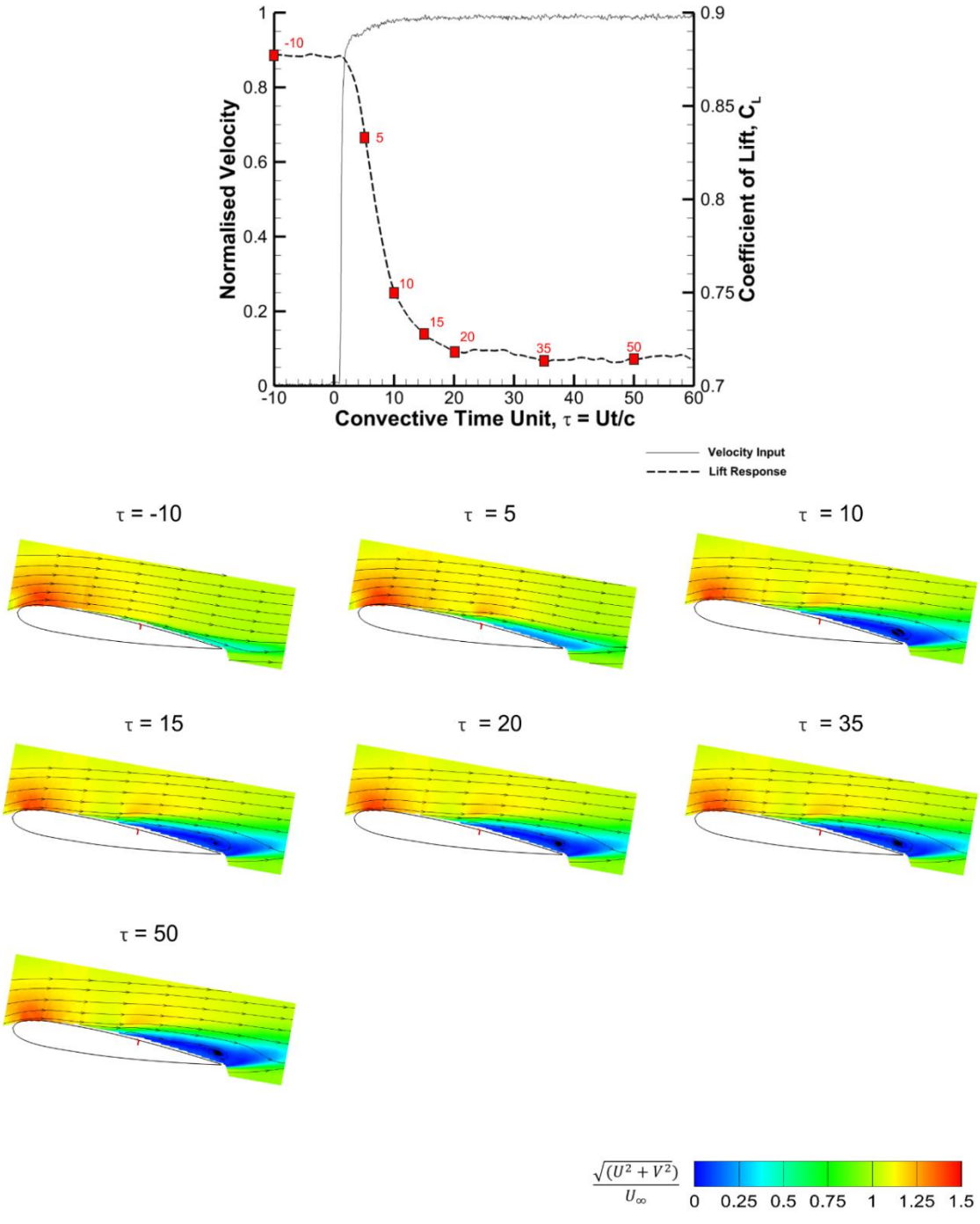

Figure 6.24 - Phase-averaged velocity field data for developing transient jet at x_j/c = 0.60 at α = 10°, C_μ = 1.6%.

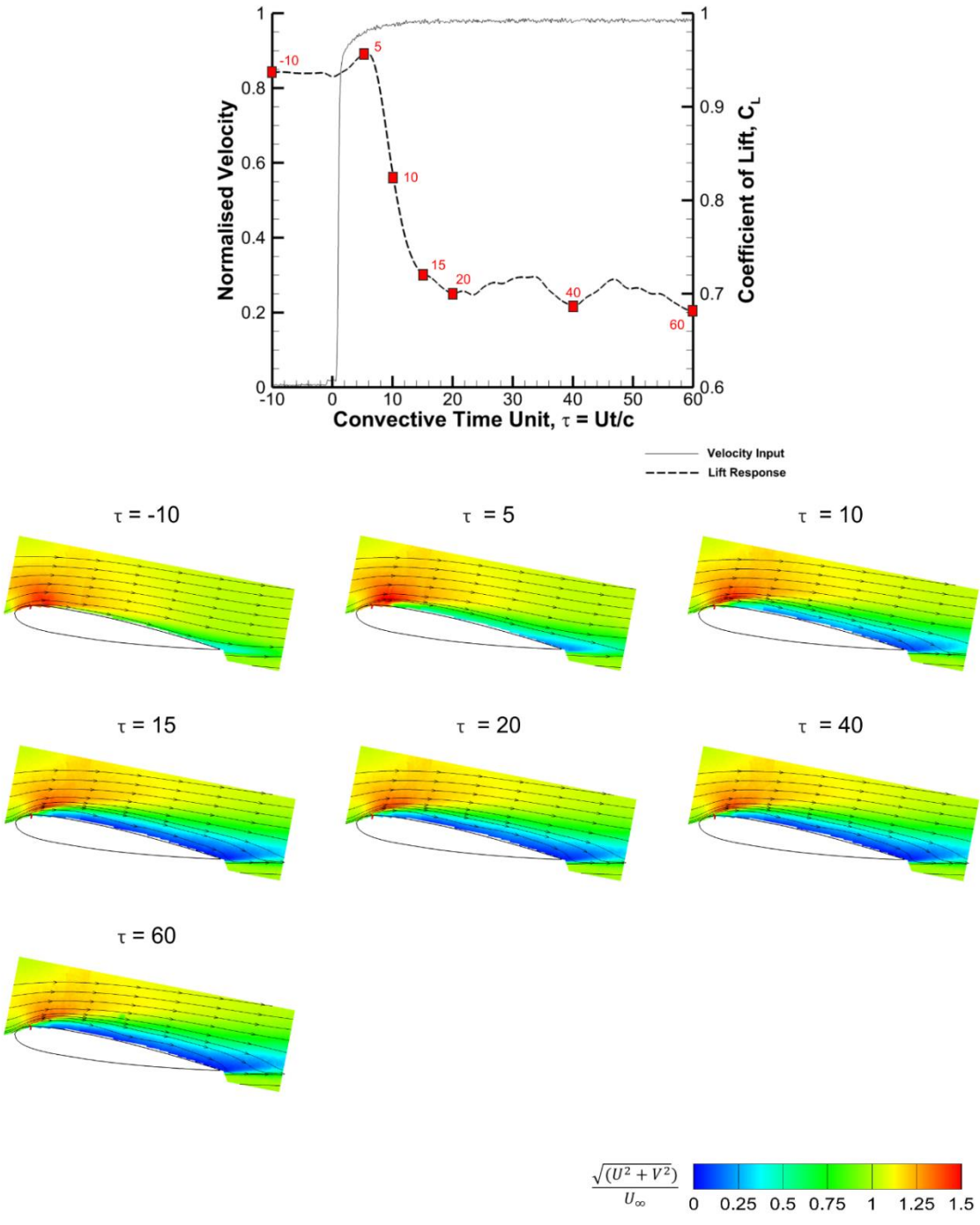

Figure 6.25 - Phase-averaged velocity field data for developing transient jet at x_j/c = 0.08 at α = 10°, C_μ = 1.6%.

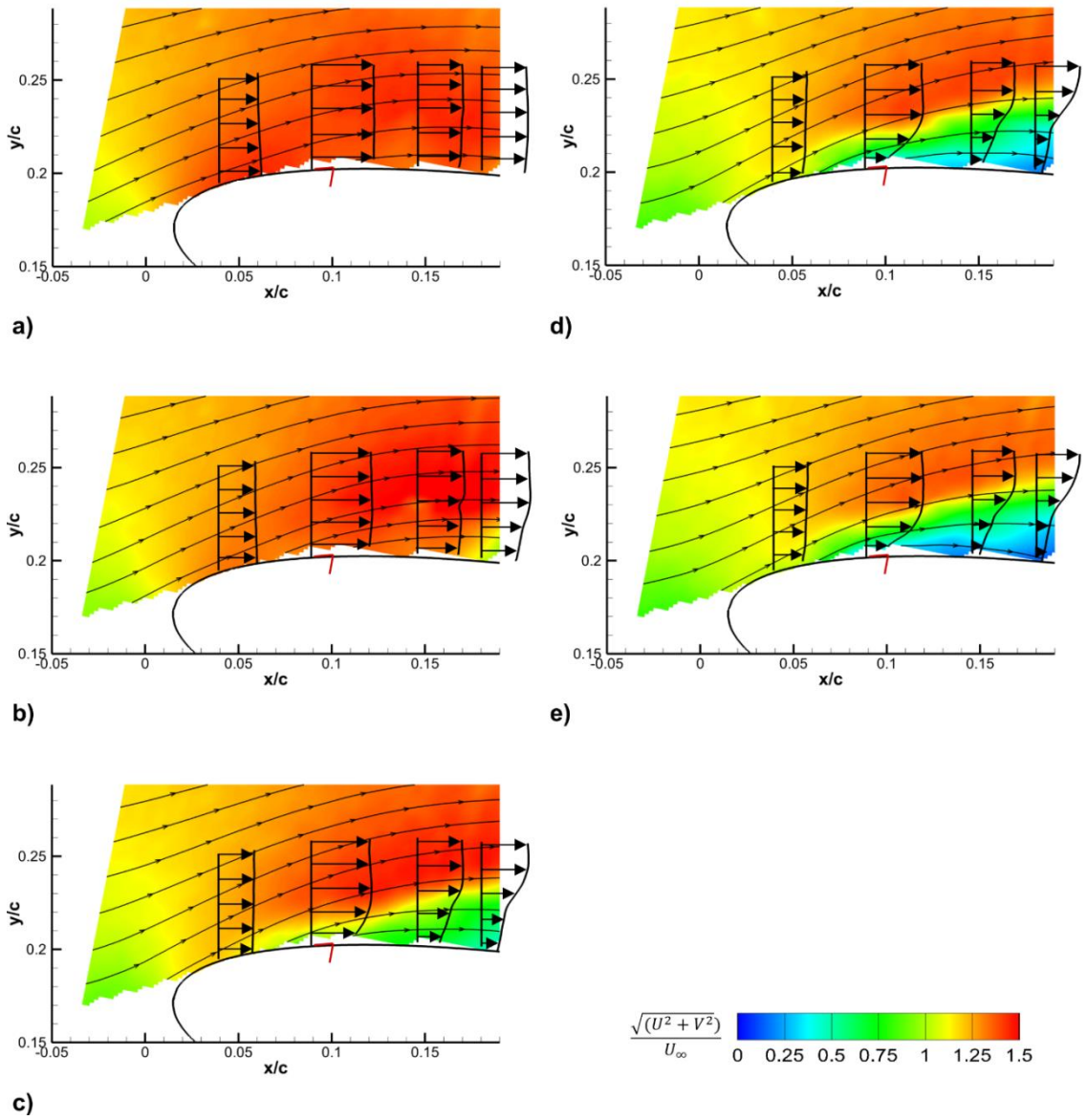

Figure 6.26 - Close up comparison of velocity profiles for x_j/c = 0.08, α = 10° at C_μ = 1.6% for a) τ = -10, b) τ = 5, c) τ = 10, d) τ = 15 & e) τ = 60.

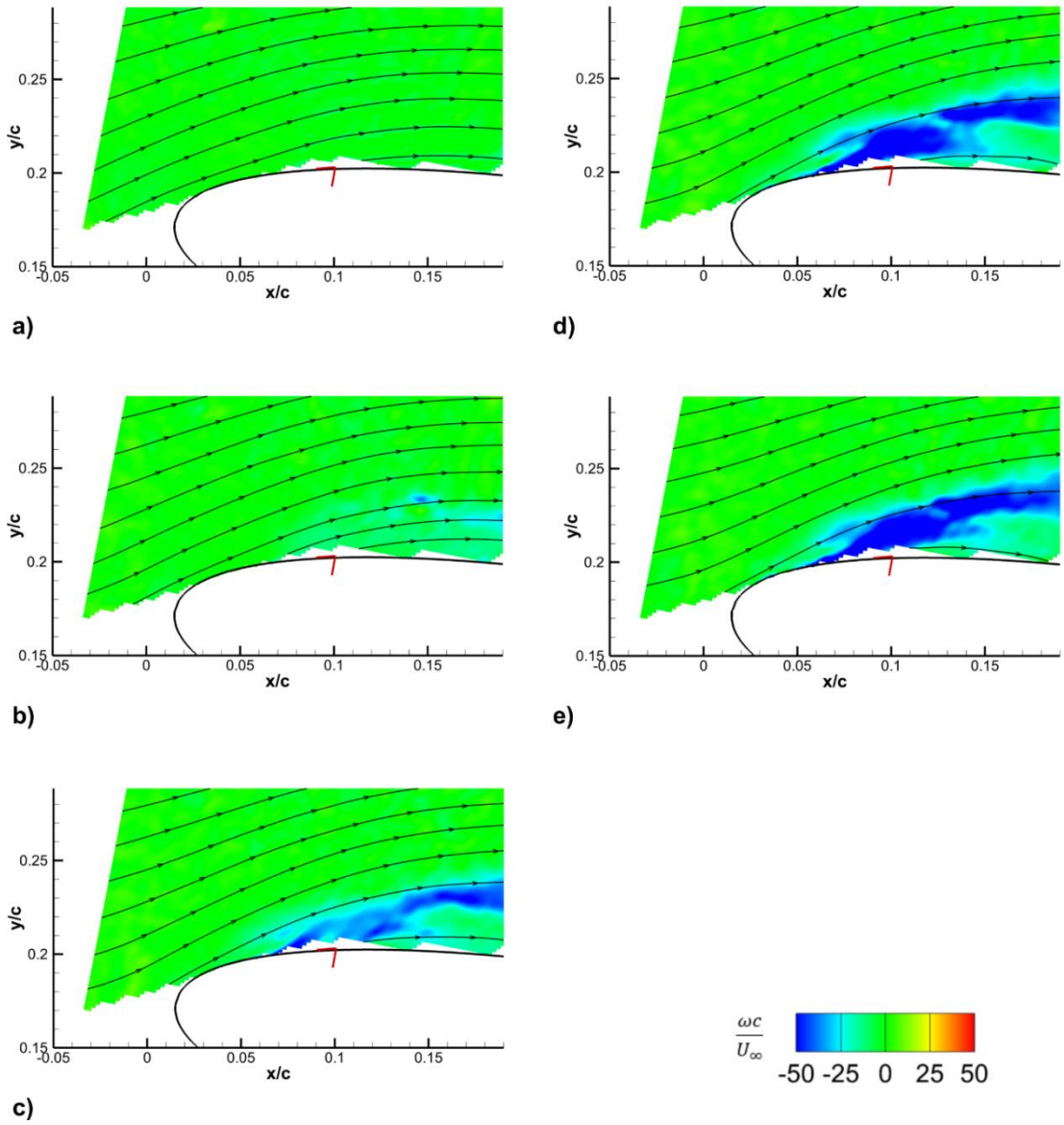

Figure 6.27 - Close up comparison of vorticity profiles for x_j/c = 0.08, α = 10° at C_μ = 1.6% for a) τ = -10, b) τ = 5, c) τ = 10, d) τ = 15 & e) τ = 60

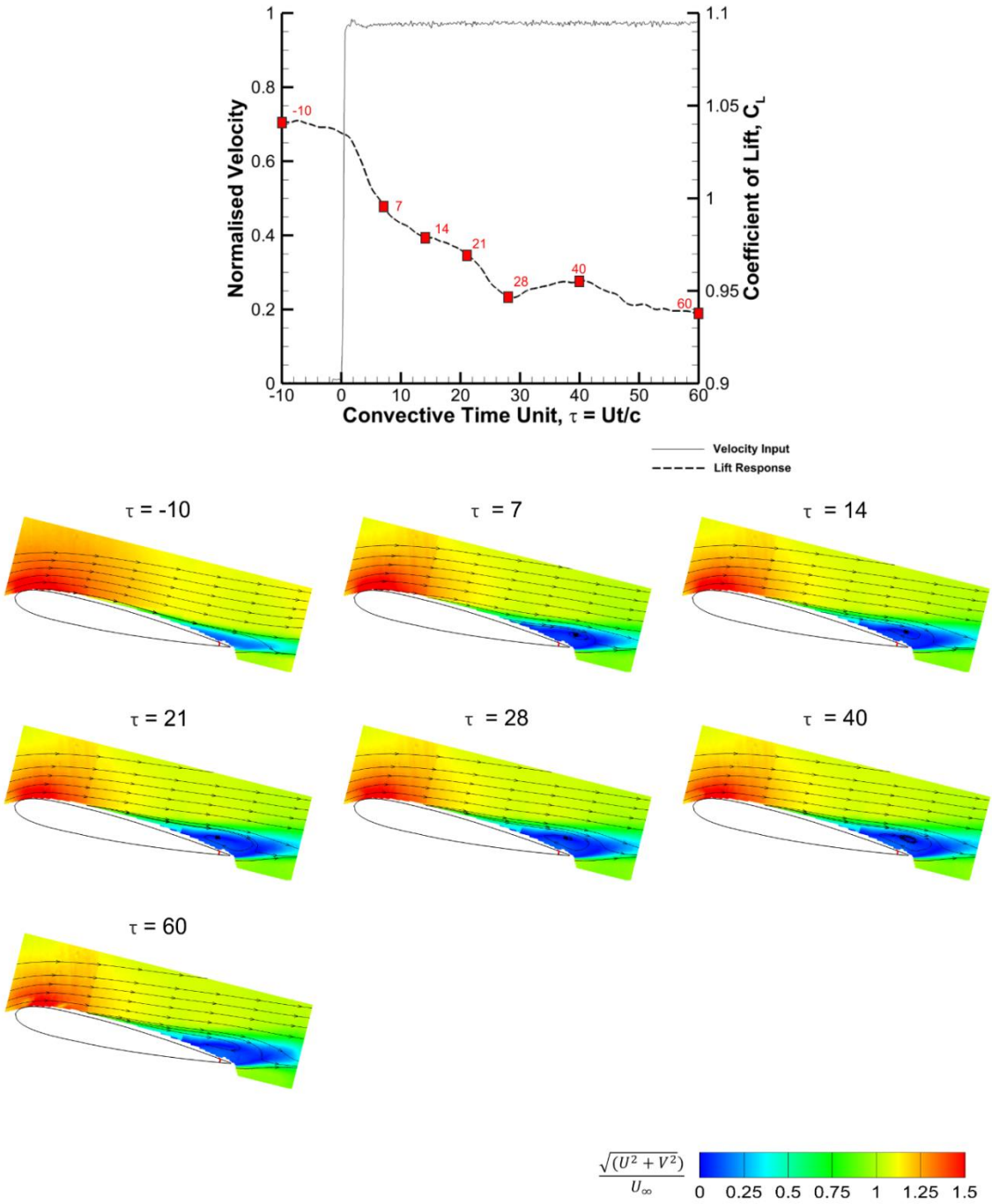

Figure 6.28 - Phase-averaged velocity field data for developing transient jet at x_j/c = 0.95 at α = 13°, C_μ = 1.6%.

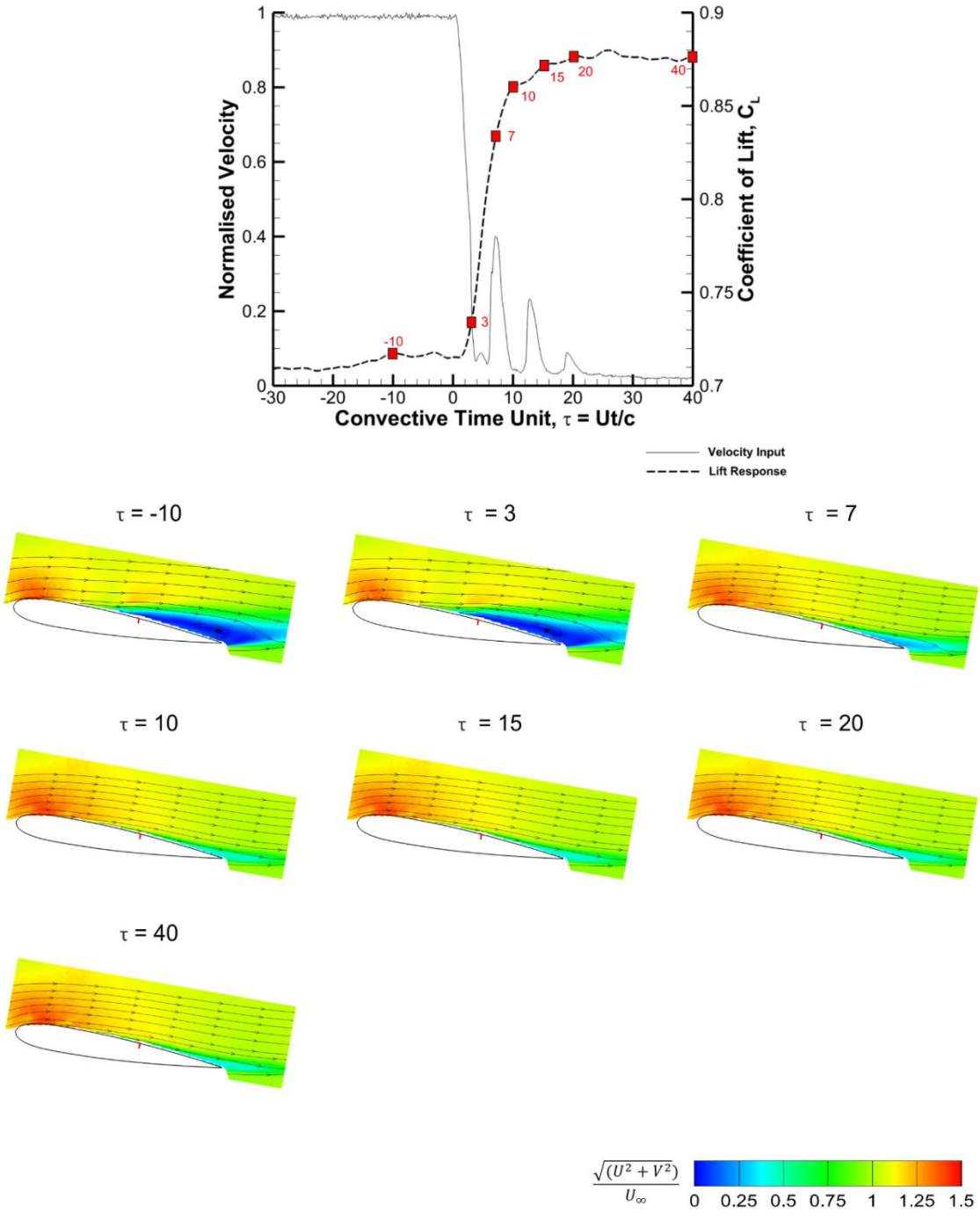

Figure 6.29 - Phase-averaged velocity field data for terminating transient jet at x_j/c = 0.60 at α = 10°, C_μ = 1.6%.

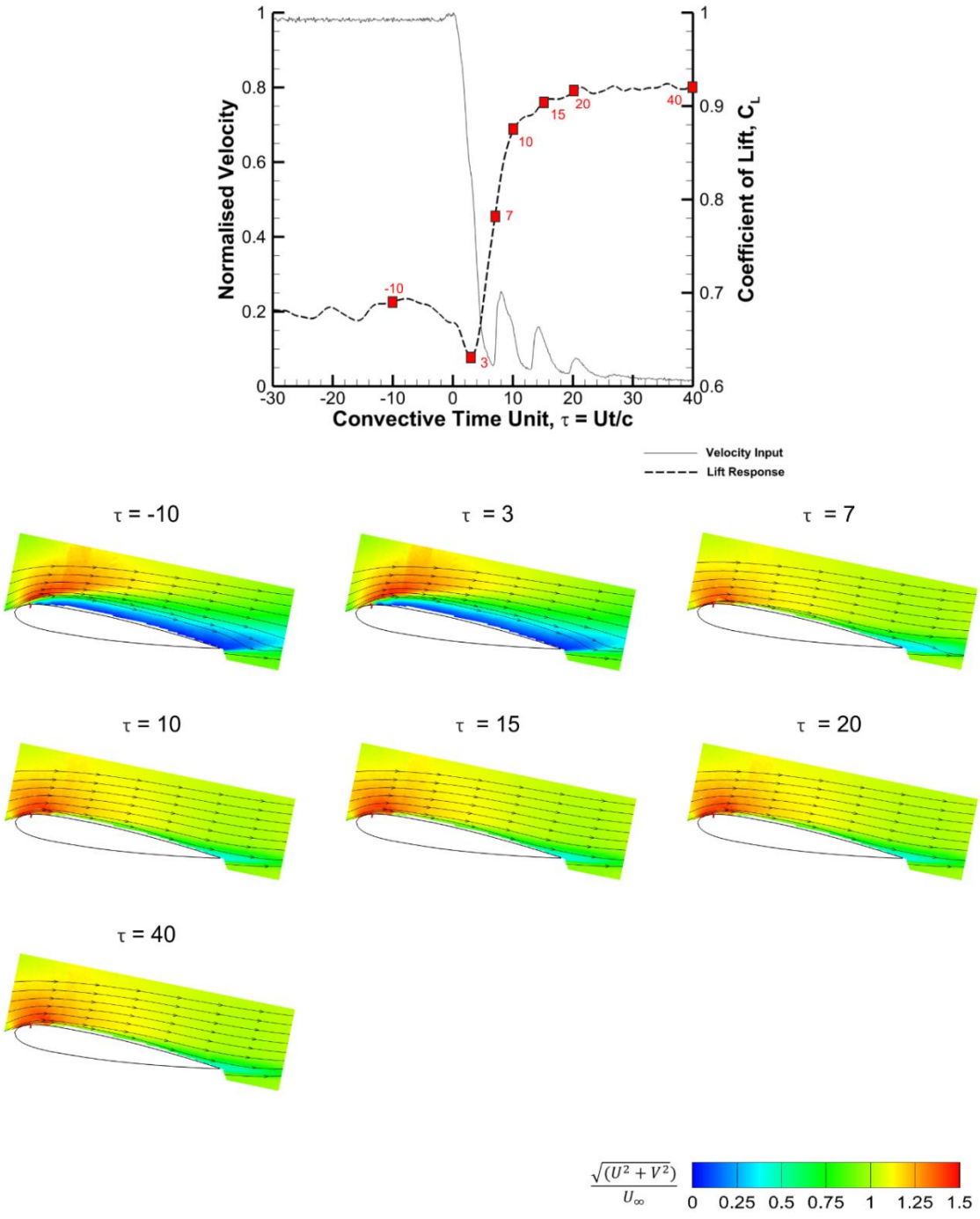

Figure 6.30 - Phase-averaged velocity field data for terminating transient jet at x_j/c = 0.08 at α = 10°, C_μ = 1.6%.

Chapter 7 : Implementation

Chapters 4 to 6 have shown the upstream blowing jet is an effective mechanism for lift reduction. Although the purpose of this current work is to investigate the jet at a fundamental level, the implications for the eventual application, i.e., commercial aircraft, should also be considered. This chapter aims to assess the challenges and limitations associated with scaling the jet to counter vertical gusts at the cruise conditions of commercial aircraft. When scaling to a commercial aircraft there are some dimensionless groups and geometric properties that match with the experiment, eg. momentum coefficient, and can therefore be directly scaled; and others, eg. Reynolds number, that do not and therefore their effect needs to be considered in the context of the available literature. Each of these dimensionless groups and geometric characteristics will be considered in turn in the following sub-sections.

7.1 Reynolds Number

The experiments were performed with a Re = 660,000, whereas the Reynolds number for flight conditions are of the order of 10^7 yielding a difference of 10^2. In the current study the experimental Reynolds number was limited by practical considerations. The freestream velocity and chord length would require a larger or higher velocity wind tunnel facility to achieve along with a very significant increase in the scale of the blowing source. An alternative method is to test with a cryogenic pressurised tunnel [182], which allows models to be tested at transonic speeds. This is achieved through testing with a diatomic gas such as nitrogen, which is cooled and pressurised. Therefore, increasing its density and lowering its viscosity. Airbus currently use the cryogenic European Transonic Wind tunnel (ETW) in Germany, to validate CFD tests on half models [183].

The effect of Reynolds number on the lift coefficient for static airfoils is well established [184], and can be divided into three principle elements:

1. **Laminar-Turbulent Transition**. It is well established that for developed flows the Reynolds number determines whether the flow is laminar or turbulent; and for developing flows it, along with factors like surface roughness, determines where the transition from laminar to turbulent occurs. An aircraft wing will have a free moving transition point. For a non-tripped airfoil, the transition point was found to migrate upstream with an increasing Reynolds number [185]. However, the airfoil used for experiments presented here had a fixed trip location to ensure a transition to turbulence. A transition to a turbulent boundary layer leaves flow less susceptible to separation. This boundary layer height becomes smaller with Reynolds number.

2. **Separation Delay**. The boundary layer for higher Reynolds number flows has a higher momentum, due to the definition of Reynolds number, and is more likely to be turbulent giving a fuller profile. Both of these characteristics mean the flow is less prone to separation and therefore will experience stall at a higher angle of attack.
3. **Stall Type**. As described for low Mach numbers in ESDU 66034, the type of stall (thin airfoil, leading-edge etc) is determined by the Reynolds number and leading-edge curvature. The effect of Reynolds number is due to the interplay of point 1 and 2 above. For a NACA 0012 airfoil ESDU 66034 predicts thin-airfoil stall at $Re = 6.6\text{x}10^5$ and trailing-edge stall at $Re = 10^7$.

The effect of Reynolds number on the lift coefficient for airfoils with blowing is less well understood. The three principle effects of Reynolds number for a 'clean' airfoil would indicate that higher Reynolds number would become less prone to separation. However, the higher Reynolds number would also delay the stall angle and lead to a trailing edge stall. The effect of this on an airfoil with upstream blowing would likely be beneficial, particularly for trailing edge locations, where the separated region will emerge first. The capability of the jet near the trailing edge to remain effective at higher Reynolds numbers is supported by Lawford & Foster [184], who showed an increase in lift by $\Delta C_L = 0.47$ for a blown jet flap at $\text{Re} = 3.78\text{x}10^6$. This is corroborated by Dods, Jr. & Watson [186], who showed blowing with a deflected trailing edge flap at $\delta_f = 70°$, at Reynolds number of $4\text{x}10^6$ can augment the lift produced. Furthermore, it is shown that a higher momentum coefficient of $C_\mu = 0.82$, is required at a lower Reynolds number of $\text{Re} = 2.3\text{x}10^6$ to produce a similar lift curve to $\text{Re} = 4\text{x}10^6$ at $C_\mu = 0.64$ [186]. Blowing at greater Reynold numbers has been tested by Peake *et al*. [187], who showed that an upper surface jet for boundary layer control remains effective at increasing lift at a Reynolds number of $3\text{x}10^7$; $\Delta C_L = 0.15$ for $C_\mu = 0.02$. Despite the lack of studies on the direct effect of Reynolds number on jet performance, it is clear that lift remains dependent on momentum coefficient for a given Reynolds number. This is evident at low Reynolds numbers of $1.6\text{x}10^5$ [83] and high Reynolds numbers of $3\text{x}10^7$ [187].

Based on the evidence available in the literature and established understanding, the effect of scaling from the current experiment at $Re = 6.6\text{x}10^5$ to full-scale aircraft in cruise at $Re \sim 10^7$ is therefore likely to be insignificant. The capability of the jet to perform and manipulate lift at higher Reynolds numbers with small momentum coefficients has been proven. A trailing edge stall is likely to benefit jet locations towards the trailing edge, as this region will be vulnerable to separation. However, effectiveness of leading edge jet locations would likely be impacted as separation near the leading edge is delayed with higher Re. This might require a greater momentum coefficient, and therefore greater energy, to produce a significant change in lift, particularly at low angles of attack.

Although, the leading edge location was shown within Chapters 4 to 6 to be preferable for higher angles of attack. This behaviour is likely to be consistent at higher Reynolds numbers.

7.2 Mach Number

The current experiments were performed in the subsonic region M = 0.06, however an aircraft at cruise would fly within the transonic region, M = 0.83. Performing experiments at higher Mach number is not viable because the wind tunnel available is of a low subsonic tunnel design, and was near maximum velocity for current experiments. A transonic wind tunnel will be required in order to reach cruise Mach number. A transonic wind tunnel differs to a low speed wind tunnel in a number of ways such as the use of compressed air, and a different test section design. The emergence of a shock wave at M = 1, makes the design of a transonic wind tunnel complicated. This shockwave reflects off the walls of the test section and can be problematic if it interacts with the test model. As such, test section walls of transonic wind tunnels include opened slots to alleviate the effect of reflected shockwaves [188].

Increasing the Mach number to within the transonic region leads to the emergence of a shock wave on the upper surface. This shock wave brings about changes to flow properties. Flow across the shock wave experiences an increase in pressure, temperature, density and entropy. However, velocity, Mach number and total pressure all decrease. These changes in flow property lead to the separation of the boundary layer and a sudden increase in drag [189]. However, drag begins to experience an increase before M = 1; this occurs at the 'drag-divergence Mach number'. The effect of Mach number on the lift coefficient of an airfoil is well established and is primarily:

1. **Increased Lift Slope**. The increased Mach number leads to flow becoming considered compressible at M > 0.3. These compressibility effects certainly bring about changes to the pressure distribution over the airfoil. Efforts to correct these compressibility effects were made during the 1930s [189], which gave rise to the Prandtl-Glauert rule shown in Eq. [7.1].

$$C_L = \frac{C_{L,0}}{\sqrt{1 - M_\infty^2}} \qquad [7.1]$$

   The Prandtl-Glauert rule is linear and shows that the lift slope increases with Mach number. If the incompressible lift coefficient, $C_{L,0} = 2\pi\alpha$, it can be seen that at M = 0.65, lift will increase by 31.6% for a given angle of attack.

2. **Decreased $C_{L,max}$**. As the airfoil increases in angle of attack, flow velocity along the upper surface also increases. When increasing Mach number, the angle of attack at which velocity on the upper surface reaches supersonic speed, decreases [190]. A shock wave emerges at

this point and flow consequently separates, leading to what is known as a shock stall. Therefore, the angle at which the shockwave emerges reduces with Mach number. As a result, the maximum lift coefficient possible also reduces. For a NACA 0012, maximum lift coefficient is found to reduce with Mach number [191].

Upstream blowing jets haven't been tested at high Mach numbers for gust load alleviation. The main focus for jets at high subsonic Mach numbers has been to suppress separation. Jet flaps to mitigate shock-induced separation have been tested before and are shown to be effective. Yoshihara & Zonars [192] showed that a trailing edge jet flap at M = 0.8, increased lift by ΔC_L = 0.4 for C_μ = 0.02. Pressure measurements showed that the shockwave, which emerges on the upper surface, was displaced downstream as a result. Delaying the separation has been shown to improve lift-to-drag ratio, with C_μ = 0.003 being enough momentum to increase L/D_{max} by almost 10% at M = 0.78 [193]. Lockwood & Vogler [86] showed that blowing from the upper surface on a rounded trailing edge to use the Coanda effect isn't effective. Lift coefficient reduces with increasing Mach number for this method. However, lower surface jets remain effective during high subsonic Mach numbers. A normal blowing jet on the lower surface increases lift with Mach number when using low momentum coefficient values (C_μ < 0.04).

Based on the evidence available in the literature and established understanding, the effect of scaling from the current experiment at M = 0.06 to full-scale aircraft in cruise at M ~ 0.83 is therefore likely to be significant. When considering the use of the upstream blowing jet within the transonic region, the separated region which appears aft of the shockwave may facilitate the need for a reduction in suction. Thus, enhancing the effectiveness of smaller momentum coefficients. Literature shows that small momentum coefficients have a significant effect at high subsonic Mach numbers. However, if the jet is to be applied during cruise, then angles of attack will be kept low, $3° \leq \alpha \leq 5°$. Where shock-induced separation may be weak or local velocity has yet to reach critical Mach number. If a shock-induced separation was present, it would be advantageous to place the jet aft of the shock location. This would provide a favourable pressure gradient for the jet to exploit and increase the size of the separated region. If the jet is placed near the leading edge, the momentum coefficient required to counter the higher local velocity would need to be significantly increased.

7.3 Sweep Angle

The current experiments used an infinite wing experiment that therefore, for simplicity, specifically excludes the effect of sweep angle. Sweep angle for typical commercial aircraft is in the range of 25° for A320, and 33.5° for A380. As upstream blowing jets have not been tested for gust load alleviation prior to this project, it was crucial to exclude any variables to understand the

effectiveness of the jet as a standalone device. The inclusion of a sweep angle would introduce three-dimensional flow effects, which would likely affect the results.

The sweep angle is often defined at the quarter chord location of the root and tip. Sweep angles below $\Lambda = 15°$ are considered low, while angles above $\Lambda = 30°$ are high [194]. The effect of sweep angle for finite wings is well established. It can be summarised as:

1. **Delayed shock wave**. Along a two-dimensional airfoil, flow moves along the surface parallel to the chord. However, an introduction of a sweep angle will incite flow in the spanwise direction, where air flows along the wing normal to the chord. This reduces the velocity along the upper surface, and therefore delays the critical Mach number [195].
2. **Decreased $C_{L,max}$.** Increasing sweep angle will reduce the maximum lift coefficient attainable [196]. Raymer [196] suggests that for a clean wing (no high lift devices), the maximum lift reduces by a factor of the cosine of the sweep angle, as shown in Eq. [7.2]:

$$C_L = 0.9 C_{L,max} \cos \Lambda \qquad [7.2]$$

The equation is multiplied by a factor of 0.9 to correct the maximum lift coefficient obtained for three dimensional effects.

The effect of sweep angle for finite wings with blowing is not well understood but is likely to have a considerable effect. This is supported by Yoshihara & Zonars [192] who tested the jet flap on wings with a sweep angle within the transonic region. Yoshihara & Zonars [192] showed that a large sweep of $\Lambda = 45°$ reduces the jet flap's ability to move the shockwave downstream and increase lift. Separated flow traverses from the root to the tip, hence disrupting the jet performance near the tip. Testing with a sweep angle of $\Lambda = 25°$, for a jet spanning half of the wing provides similar results to a full span jet.

Based on the evidence available in the literature and established understanding, the effect of scaling from the current experiment at $\Lambda = 0°$ to full-scale aircraft at $\Lambda = 25° - 35°$ is therefore likely to be significant. The jet performance is likely to depend on the position of the jet along the span of the wing. As the boundary layer thickens as flow spans towards the tip, it is likely to be more vulnerable to separation if the jet is placed outboard. As the performance of upstream blowing is dependent on the size of the separated region it incites, then this separated flow from the sweep angle will serve to assist for the purpose of gust load alleviation. This presents the possibility of the jet requiring a smaller momentum coefficient.

7.4 Section Shape

As stated earlier, the airfoil used in this project was a symmetrical NACA 0012 airfoil. This is a typical design that is the most common in fundamental aerodynamic studies. However commercial aircraft fly at transonic Mach numbers and therefore use supercritical design, see a comparison in Fig. 7.1 [197]. This design works effectively to delay the onset of shock-induced boundary layer separation. The supercritical airfoil exhibits a flat upper surface, which has a negative camber. This front portion of the airfoil reduces lift, but the aft cambered design of the airfoil compensates for this reduction at the fore. The flat region also promotes supersonic flow on the upper surface, which leads to a lower critical Mach number. However, the drag-divergence Mach number increases as the shockwave is weakened.

The effect of airfoil design on lift coefficient is well established. The thickness and camber of the airfoil can determine the aerodynamic performance. The aerodynamic performance of an airfoil can be defined mainly by two characteristics [189]:

1. **Lift-to-drag ratio.** The lift-to-drag ratio is an indicator of how efficient an airfoil is. Ideally, the ratio will be large, indicating a high lift gain for a low drag. It is why a supercritical airfoil is desirable at high subsonic Mach numbers, as a conventional airfoil would suffer from greater drag, for the same freestream Mach number. An aircraft with a large lift-to-drag ratio will have a greater range.
2. **Maximum lift coefficient, $C_{L,max}$.** It is ideal to achieve an airfoil design which maximises the highest lift coefficient obtainable. The maximum lift coefficient is inversely proportional to the stall speed, V_{stall}. This means a lower stall speed can be obtained with a larger $C_{L,max}$. To further increase the maximum lift coefficient beyond that the aifoil can naturally attain, will require the addition of high lift devices.

Many different airfoil geometries have been used within the literature for blowing studies, these include elliptical, symmetrical and supercritical airfoils. Despite the differences in shape, the jet flap has been proven to work effectively on thick supercritical wings with a sweep angle of 20.5° [193]. Petrov *et al.* [193] experimentally investigated the benefit of tangentially blowing from x_j/c = 0.70 on a supercritical wing-fuselage combination and found it was capable of increasing L/D at M =0.78. Elliptical airfoils have been tested with jet flaps at various jet deflection angles [81, 82], with normal blowing separating flow. Symmetrical airfoils have also been used to demonstrate the effectiveness of the jet at various deflection angles [172].

Based on the evidence available in the literature and established understanding, the effect of scaling from the current experiment with a NACA 0012 to full-scale aircraft with a supercritical airfoil is therefore likely to have a moderate effect. It would appear that the section shape is not a limiting factor for the jet flap to perform well. However, this is dependent on the jet location. As

supercritical airfoils encourage flow to exceed $M > 1$ over the front portion of the jet, this may limit the jet's ability to perform when located near the leading edge. Therefore, reducing the change in lift obtained during the current experiments. As such, it may be beneficial to place the jet aft of the shock wave location, where pressure is higher and favourable for the jet to act within.

7.5 Coefficient of Momentum

The effect of the coefficient of momentum is covered in detail in Section 2.3.2.1 of the literature and Chapters 4, 5 and 6. In summary, the square root of the change in lift coefficient is found to be proportional to the momentum coefficient. The change in lift was found to increase with blowing strength.

One issue often cited with fluidic actuators is the source for the high velocity air. One potential method is to bleed air from the engine compressor. Compressed air is often bled for air conditioning or cabin pressurisation purposes. However, as the jet is only to be activated during gust encounters, its bleed will be rare and intermittent.

The experimental jet conditions can be scaled to an Airbus A340 using the methods outlined by Crowther [198]. The smallest momentum coefficient used for upstream blowing, C_μ = 0.008, gave an effectiveness of $\Delta C_L/C_\mu \approx 10$ at α = 0°. If we consider the same momentum coefficient at M = 0.82 for an Airbus A340 at cruise, the jet velocity and mass flow rate can be determined. Table [7.1] shows the parameters used to calculate the mass flow rate of the jet, assuming the flow is incompressible. A typical CFM56-5C jet engine for Airbus A340 has a cruise air mass flow rate of approximately 100 kgs^{-1} [199]. The A340 has 4 of these engines, i.e. 2 for each wing. Therefore, giving a total air mass flow rate of 200 kgs^{-1}. The wing area corresponds to the area of one wing for the aircraft. The jet width is maintained at 0.1% of mean aerodynamic chord, while the jet span is limited to approximately 4 m to span an outboard aileron.

At a cruise altitude of 11 km, static pressure and temperature are P = 22.6 kPa and T = 216.5 K, respectively. This gives an air density of ρ_∞= 0.363 kgm^{-3}. As flow is assumed to be incompressible, freestream air density is equal to jet air density, $\rho_\infty = \rho_j$.

Based on the parameters stated in Table 7.1, the jet mass flow rate for a jet velocity of 1234 ms^{-1} is approximately 7.5% of the jet cruise mass flow rate. This requirement is a relatively low amount for bleeding, and is below the acceptable air bleed extraction stated for the CFM56-5C jet engine, which has a bleed limit of 10% of airflow [200]. If gust instances are considered rare, then the infrequent usage should be considered acceptable. To put this into context, the A340 cabin air system draws approximately 1.74 kgs^{-1} [201], or less than 1% of the total air mass flow rate.

Table 7.1 - Parameters used to scale C_μ = 0.008 on A340.

Parameter	Value
Wing Area	219.5 m²
Mean Aerodynamic Chord	8.44 m
Total Air Mass Flow Rate at Cruise	200 kgs^{-1}
Mach Number	0.82
Jet Width	0.00844 m
Jet Span	4 m
Jet Velocity	1234 ms^{-1}
Jet Mass Flow Rate	15.12 kgs^{-1}

The jet velocity for C_μ = 0.008 is evidently large but retains a small mass flow rate. If flow was considered compressible, the jet velocity for a given momentum coefficient would decrease. Compressor pressure ratio for this particular jet engine is 37.5 [199]. Such a high-pressure ratio will have a significant effect on the jet air density and velocity. Supersonic jet velocities are possible, but the design conditions must be met in order to avoid shockwaves appearing. Consequently, numerical simulations by Petrov *et al.* [193] indicate upper surface tangential blowing for boundary layer control with supersonic jet velocities will produce a sudden drop in suction at the jet location, but the pressure recovery aft of the jet compensates for this localised loss in suction.

For the experiments considered in Chapter 4, the momentum coefficient, C_μ = 0.008, gave a jet velocity to freestream velocity ratio of U_j/U_∞ = 2. If the blowing ratio is considered instead of the momentum coefficient, it can be shown that the mass flow rate required will have a significant reduction. When an A340 is cruising at M = 0.82, the freestream velocity at 11 km is approximately U_∞ = 242 ms^{-1}. As such, the jet velocity becomes U_J = 484 ms^{-1}. The mass flow rate for the jet reduces to $\dot{m} = 5.93\ kgs^{-1}$, which equates to approximately 3% of the jet cruise mass flow rate. The momentum coefficient for this jet velocity equates to C_μ = 0.0012.

7.6 Location of Jet

The chordwise and spanwise location of the jet in the aircraft wing is an important consideration from both an aerodynamic and practical standpoint. The experiments considered three jet locations: x_j/c = 0.08 for leading-edge control, x_j/c = 0.60 mimicking a spoiler and the x_j/c = 0.95 jet to mimic an aileron. From the results section, it was shown that placing the jet at x_j/c = 0.60 was effective at reducing lift for both small and large angles of attack. With reference to Fig. 7.2, it can be seen where the fuel tank on an A330 is placed [202]. The fuel tank ends at approximately at x/c = 0.60, hence it would be permissible to place the jet flap aft of this location. Although this location is reserved for the spoiler, it was observed within the literature review that the spoiler is not as responsive when deployed in unsteady conditions. It was shown earlier in the literature review, that under steady state conditions, a spoiler deflected at δ = 30° could reduce lift by approximately $\Delta C_L \approx$ - 0.5 [36]. However, upstream blowing did not reduce lift by as much during steady state measurements. The advantage of using upstream blowing becomes apparent during transient measurements, as it has been documented that lift becomes more positive before reducing for a spoiler [35], as shown in Fig. 2.7. No such force reversal was found for the upstream blowing jet at x_j/c = 0.60. As such, an ideal possibility would be to combine the spoiler and the jet flap to cover both low and high frequency lift control. This would enhance the effectiveness of the mechanical flap, as well as increase the bandwidth the gust load alleviation system could work within.

When considering the internal structure of a civil aircraft wing, as shown in Fig. 7.3 [203], it can be seen how limited available space is for the introduction of a pneumatic actuator. The only space to locate a plenum chamber appears to be beneath the spoiler. However, when inspecting the cross section further towards the wing tip, it becomes apparent that more space is available. The rear spar for an A320 aircraft is located around 65% of chord [204]. When assuming the outboard aileron size is 25% of chord, this gives a space of 10% of chord to install the blowing system. Furthermore, earlier results shown in Chapter 4, showed that the trailing edge location was ideal for low angles of attack, i.e. at cruise angles. It would then be intuitive to place the actuator nearer towards the outer tip of the wing, to combine with outboard ailerons. The lack of fuel tank and other systems near the outboard aileron, ultimately provides further space. Another benefit of placing the jet near the outer tip inherently reduces the root bending moment to a greater degree. The aileron would be utilised for low frequency manoeuvring, while the upstream blowing jets will be deployed for high frequency load control. It was shown that placing the upstream blowing jet flap near the trailing edge led to the fastest transient response times. The time required to reach steady state value for the trailing edge jet was approximately τ = 10. Small ailerons, in the size of 0.01c, reach steady state in a similar time [52]. Due to the larger inertia associated with larger sized ailerons, this rise time can be expected to increase with size. If the rise time of the jet is maintained for a full-sized aircraft, there is an obvious aerodynamic advantage when under unsteady conditions.

7.7 Frequency

As it was mentioned earlier, a discrete gust follows a 1 – *cosine* shape, as defined within the CS-25 document [17]. The document defines the gust velocity, shown in Eq. [2.5], which must be considered when modelling the unsteady behaviour on aircraft structure. The gust velocity is dependent on the gust gradient, H, and the distance travelled within the gust distance, s. It is obvious that the maximum gust velocity is reached when the gust gradient and the distance penetrated are equal. This maximum gust velocity, U_{ds} is obtained with Eq. [2.6]. Maximum gust velocity is dependent on a reference velocity, which varies with altitude. When considering the conditions at cruising altitude for a commercial aircraft, the reference velocity U_{ref}, is found to be equal to 7.76 ms^{-1} [17]. The design gust velocity considers a flight profile alleviation factor, F_g, which will depend on the maximum operating altitude and various weight configurations.

The gust frequency will vary with the gust gradient. As the gust gradient increases for a given cruise speed, the gust velocity will increase. However, the gust velocity could be used to define the change in effective angle of attack. Figure 7.4 shows the effect of increasing gust frequency on the change in effective angle of attack for A320 and A380 aircrafts. This figure defines the envelope the aircraft can operate within. As the CS-25 document recommends the analysis of gust gradients between H = 9 m and 107 m, the differences in gust frequency subjected to each aircraft will be subject to size and cruise speed differences. The A320 and A380 cruise at M = 0.78 and 0.85, respectively. For H = 9 m, the reduced frequency for the A320 is k = 0.764, whereas, k = 2.14 for the A380. From analysing Fig. 7.4, the largest change in effective angle of attack for both aircrafts can be seen at the smallest reduced frequency, k = 0.064 and k = 0.180 for A320 and A380, respectively. At these reduced frequencies, the change in effective angle of attack is $\Delta\alpha_{eff}$ = 1.90° & 1.69° for the A320 and A380, respectively.

Effectiveness for upstream blowing can also be measured with change in effective angle of attack. The change in effective angle of attack is determined with steady state force measurements from Chapter 4 and is shown in Fig. 7.5. This is calculated by finding the change in lift coefficient as a measure of angle of attack for three jet locations at α = 0°. It can be seen that the trailing edge jet maintains a relatively constant change in effective angle of attack throughout the range of angles considered, for all momentum coefficients shown. In comparison to the jets at x_j/c = 0.08 & 0.60, the momentum coefficient needs to increase to C_μ = 0.024 to see similar changes in effective angle of attack at α = 10°. If the jet is to be considered for cruise conditions, i.e. at 3° ≤ α ≤ 5°, then the figure indicates the jet at x_j/c = 0.95 comfortably reaches the change in effective angle of attack required for the conditions determined in Fig. 7.4. The upstream jet locations are not as effective with reducing lift within the range of angles of attack for cruise. Similarly, the results from Chapter

5 for periodic deployment are used to determine the change in effective angle of attack for a reduced frequency. Figure 7.6a shows the change in effective angle of attack for a momentum coefficient of C_μ = 0.016, for the three jet locations. The change in effective angle of attack remains relatively constant throughout the range of frequencies for all three jet locations. In Fig. 7.6b, the change in effective angle of attack is shown to increase with momentum coefficient. However, the difference in change in angle of attack between the smallest and largest momentum coefficients is not large. This behaviour can be related to the Fig. 4.6, where smaller momentum coefficients were more effective at inducing a change in lift. Hence, smaller momentum coefficient values are more efficient.

Results from Fig. 7.4 and 7.6 are combined to draw a better comparison in Fig. 7.7. The absolute value of the change in effective angle of attack is taken, as the gust produces a positive change in angle, whereas the jet produces a negative change. It is obvious that the change in effective angle of attack for jets at x_j/c = 0.08 and 0.60 is not as large as that of trailing edge. However, at approximately k = 0.074, the x_j/c = 0.60 jet produces a change in effective angle of attack of 36% when compared to the change induced on the A320. Such a saving is certainly workable; however, the trailing edge jet can amplify this reduction. From the figure, it would appear that the x_j/c = 0.95 can negate the change in effective angle of attack for both A320 and A380 aircrafts, particularly at the lower frequencies, k ≤ 0.314. Beyond this frequency, the amplitude reduces at a faster rate than the gust amplitude. Regardless, at approximately k = 0.471, the jet reduces load on the A320 and A380 by 72% and 70%, respectively.

The load distribution for an A320 can be approximated with the methods of Schrenk [205, 206] to visualise the effect of blowing along the outboard aileron. This method assumes the wing has a straight elliptical profile, so that the spanwise lift distribution can be estimated. The lift coefficient is determined for an A320 at cruise and is multiplied with Eq. [7.3] to obtain the section lift coefficient c_l:

$$cc_l = \frac{C_L(c + c_e)}{2} \qquad [7.3]$$

Where, c is the chord and is determined with Eq. [7.4] and the chord of the ellipse c_e is obtained with Eq. [7.5]:

$$c = c_R\left[1 - \left(1 - \frac{c_T}{c_R}\right)\frac{2y}{b}\right] \qquad [7.4]$$

Where c_R and c_T are the root and tip chords of the A320, respectively.

$$c_e = \left(\frac{4S}{\pi b}\right)\sqrt{\left[1 - \left(\frac{2y}{b}\right)^2\right]} \qquad [7.5]$$

The result is shown in Fig. 7.8 as the baseline case. The effect of the gust load can be determined using the load factor equation presented in Eq. [2.2]. The lift on the aircraft is multiplied by the load factor. Presented in Fig. 7.8 is the critical case for the A320, where the gust gradient is H = 107 m, or k = 0.064. This produced a change in effective angle of attack of $\Delta\alpha_{eff}$ = 1.90°, for a gust velocity of U_{ds} = 7.65 ms^{-1}. As noted in Fig. 7.7, the trailing edge jet with C_{μ} = 0.032 approximately produced a similar absolute change in effective angle of attack. A value of $\Delta\alpha_{eff}$ = -1.99° is obtained when interpolating the change in angle of attack for k = 0.064. The effective change in angle of attack on the wing can be modelled through Schrenk approximation. The lift distribution is calculated by determining the effect of the change in angle of attack for a wing producing zero lift, which is then added to the sectional lift coefficient determined with Eq. [7.3]. The section lift coefficient for a wing with zero is lift is obtained with Eq. [7.6]:

$$c_l = C_{L\alpha}(\alpha_R - \alpha_0) \quad [7.6]$$

Where $C_{L\alpha}$ is the lift slope per degree, and α_R is the reference angle of attack. In this case, α_R = -1.99° in the region of the jet. The jet spans 3 m on the outboard section. The angle of attack for zero lift α_0 is obtained with Eq. [7.7]:

$$\alpha_0 = \frac{2}{S}\int_0^{b/2} \alpha_R c \, dy \quad [7.7]$$

The reduction in sectional lift is obvious between the gust load and the jet case in Fig. 7.8. An integral of the area underneath gives the shear force on the wing. Further integration of the shear force will approximate the bending moment. From this, the reduction in root bending moment is estimated to be approximately 30%.

7.8 Summary

This chapter has tried to use literature and results from the current study to deduce the effects of scaling dimensionless groups and geometric properties to full scale conditions. Their effect can be summarised in Table 7.2.

Table 7.2 – Summary of the effects of scaling dimensionless groups and geometric properties.

Group	Effect	Description
Reynolds Number	Weak	Higher Re will delay separation, reducing effectiveness, however, due to delayed stall, will also increase the range of angles of attack over which trailing edge locations are effective.
Mach Number	Strong	Higher Mach number will reduce the $C_{L,max}$, and if sufficiently high, will give rise to a shock wave emerging. This reduces the suction in the region, which may be advantageous for the jet.
Sweep Angle	Strong	As separation from the root traverses towards the tip, this may submerge the jet in a separated region. However, this may beneficial for the jet and increase effectiveness of smaller momentum coefficients.
Section Shape	Moderate	The jet has been shown to be effective on various airfoils. However, supercritical airfoils encourage flow to exceed M > 1. This increased velocity may provide more resistance to separation from the jet.

As it was mentioned earlier, a possibility for implementing the jet flap is to make it work in tandem with flaps and for high frequency gusts. For example, if a mechanical flap is being deployed for low frequency gusts, upstream blowing could be deployed at the same time to augment the separation needed to reduce lift. In addition, as mechanical flaps lose their effectiveness with

frequency, it remains a possibility to reserve the jet flap for high frequency gusts. The idea of combining mechanical flaps with jet flaps is not new, and has been studied to prevent separation and increase lift [193]. In addition, the blowing system on an aircraft has been estimated to be relatively small. Petrov *et al*. [193] approximate the addition of a tangential blowing system, shown in Fig. 7.9, would be no more than 0.5% of an aircraft's take-off weight.

Implementation of an upstream blowing jet system on an A320 is shown in Fig. 7.10. Gusts are initially sensed with a Lidar based system for feedforward control, which gives a 300 ms lead to send a signal to employ the jets [33]. A 300 ms lead for an A320 at cruise M = 0.78, gives enough time for the jet to be deployed at a reduced frequency of $k \approx 0.20$. The signal from the sensor is fed through to the flight control computer, which in turn determines the bleed requirement from the engine compressors. Situated near the jet engines are bleed control units, which will consist of a pressure regulator and an electronically controlled butterfly valve to shut off air bleed when not needed. When the jets are required, air is drawn in the pipes positioned aft of the leading edge slats and traversed around the wing towards the outboard section, so as to avoid the fuel tanks. The turning angles of the pipes will have to be kept small and it is imperative that sharp angled pipes are avoided, as they are known to limit the velocity of flow within them [207]. For a length of pipe which spans the wing, the pressure loss must be considered. Prior to the jet, a control valve is controlled for the opening required to achieve a certain momentum coefficient. Beyond this, the jet is expended but must be done so uniformly. In order to achieve this, it may require a porous metal sheet to redistribute pressure along the jet span. In conclusion, there is sufficient space and permissible air bleed capacity to install an upstream blowing jet.

7.9 Figures

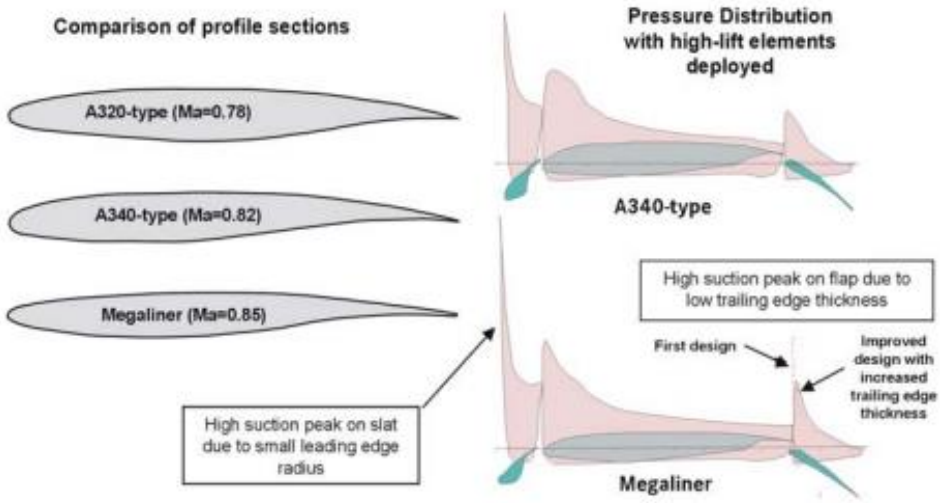

Figure 7.1 - Comparison of profile sections used on commercial aircraft [197].

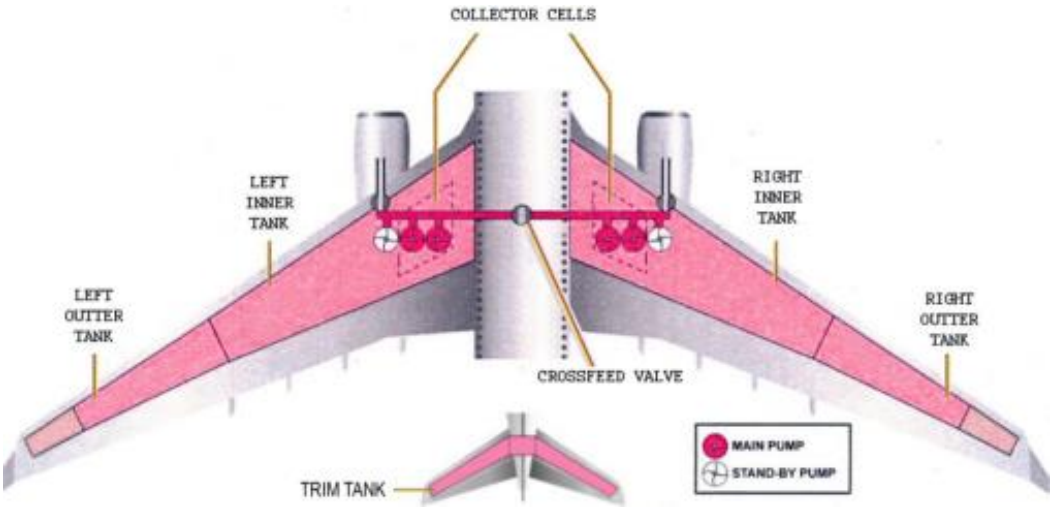

Figure 7.2 – Fuel tank on Airbus A330 [202].

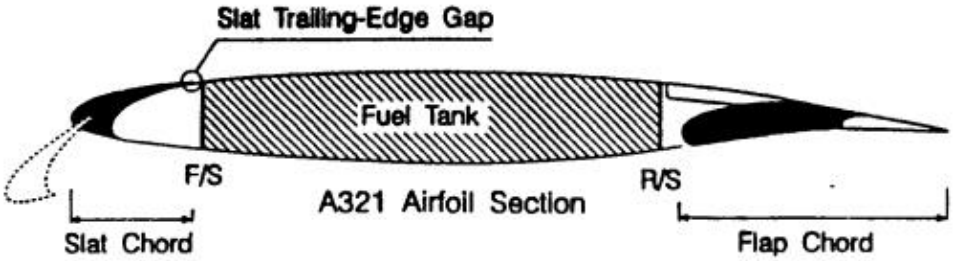

Figure 7.3 – Cross section of A321 wing [203].

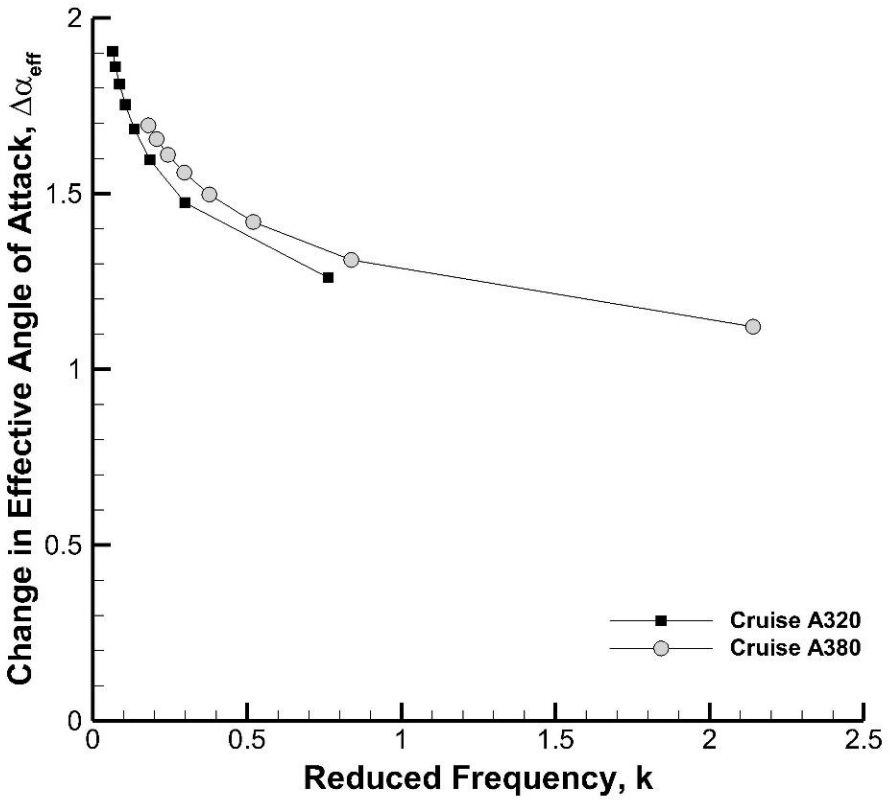

Figure 7.4 – Change in effective angle of attack $\Delta\alpha_{eff}$, with reduced frequency k, for Airbus A320 and A380.

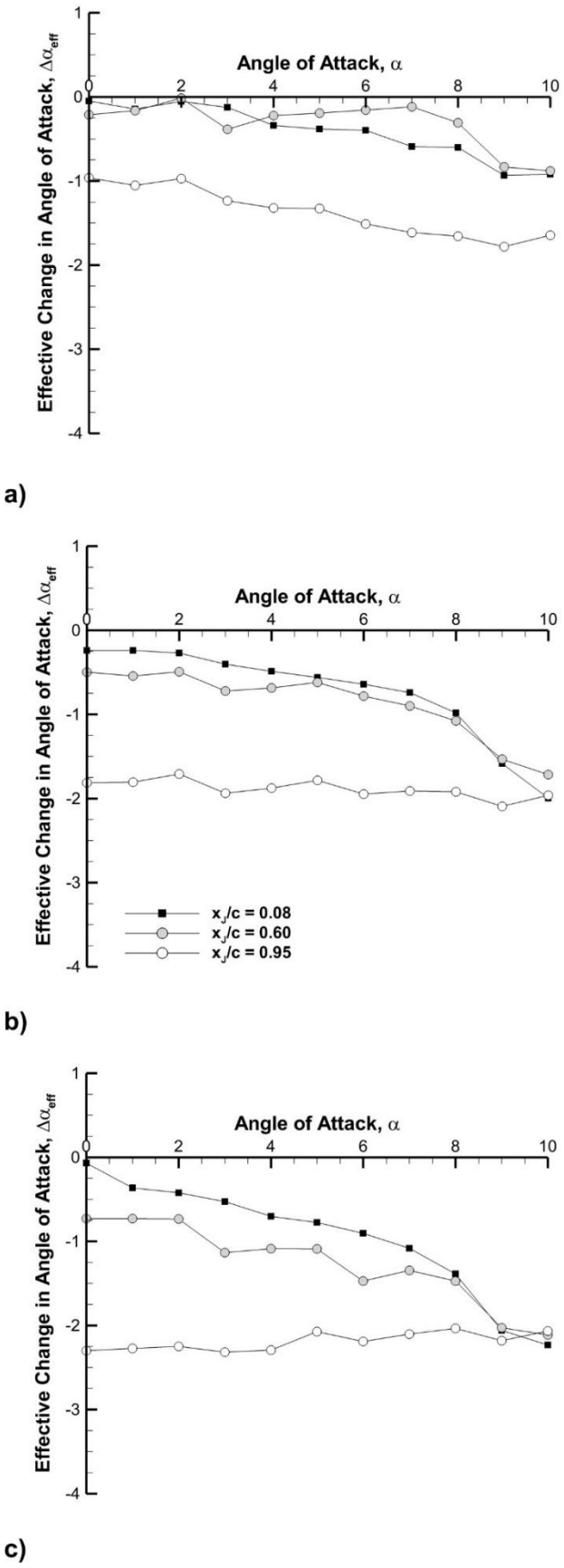

Figure 7.5 - Change in effective angle of attack $\Delta\alpha_{eff}$, with angle of attack α, for steady-state measurements; a) C_μ = 1.6%, b) C_μ = 2.4% & c) C_μ = 3.2%..

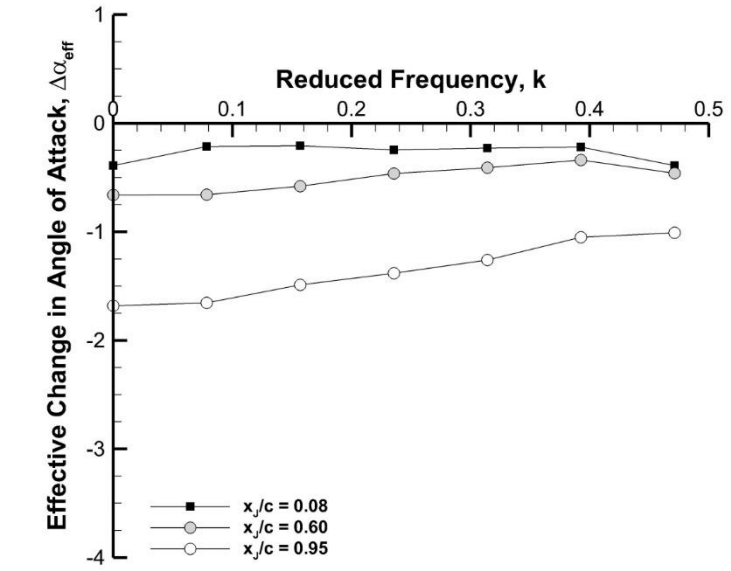

a)

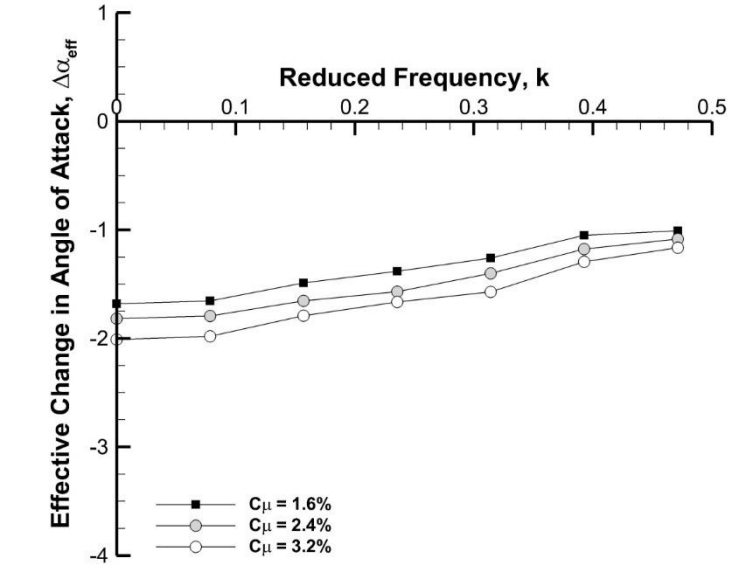

b)

Figure 7.6 - Change in effective angle of attack $\Delta\alpha_{eff}$, with reduced frequency *k*; a) varying jet location with C_μ = 1.6%, b) varying momentum coefficient for x_J/c = 0.95.

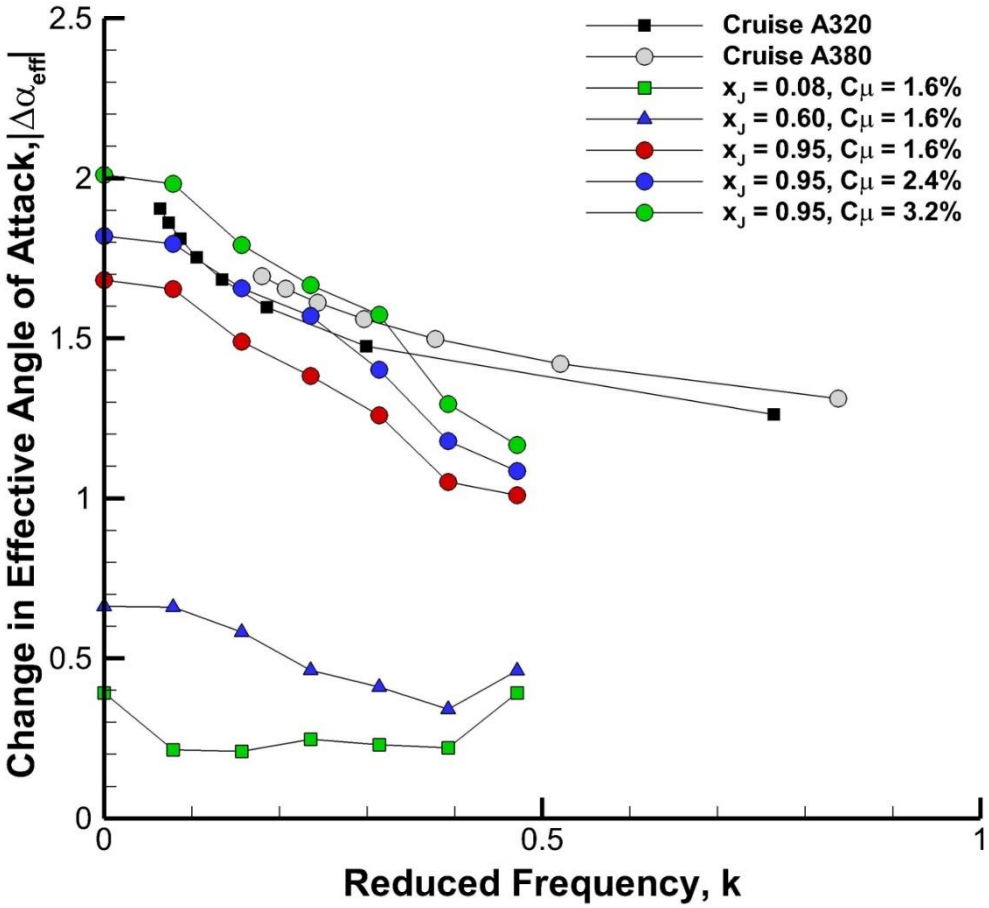

Figure 7.7 - Change in effective angle of attack $\Delta\alpha_{eff}$, with reduced frequency k, for Airbus A320 and A380 compared with results from steady state measurements.

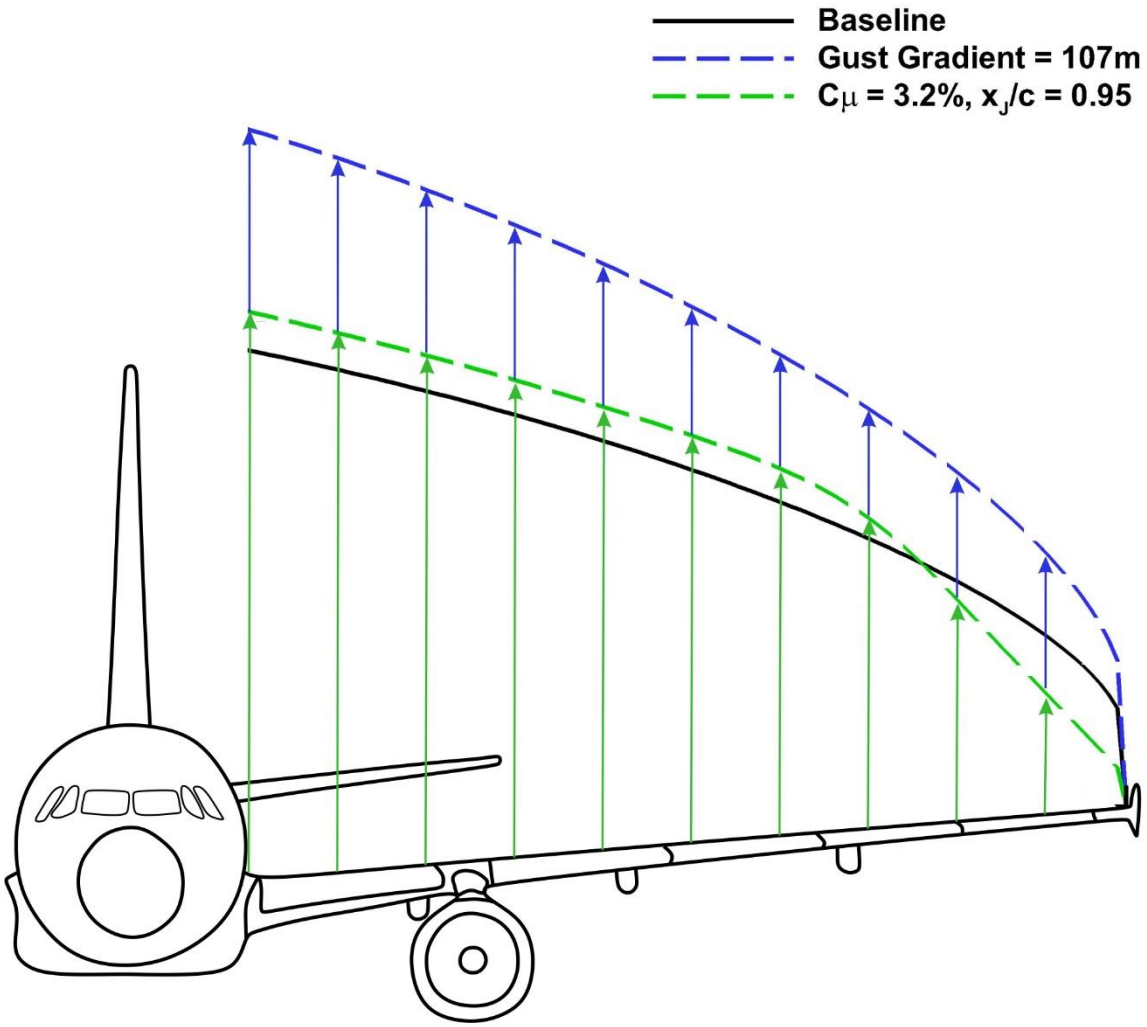

Figure 7.8 -Lift distribution due to gust gradient H = 107 m compared with lift with jet activated.

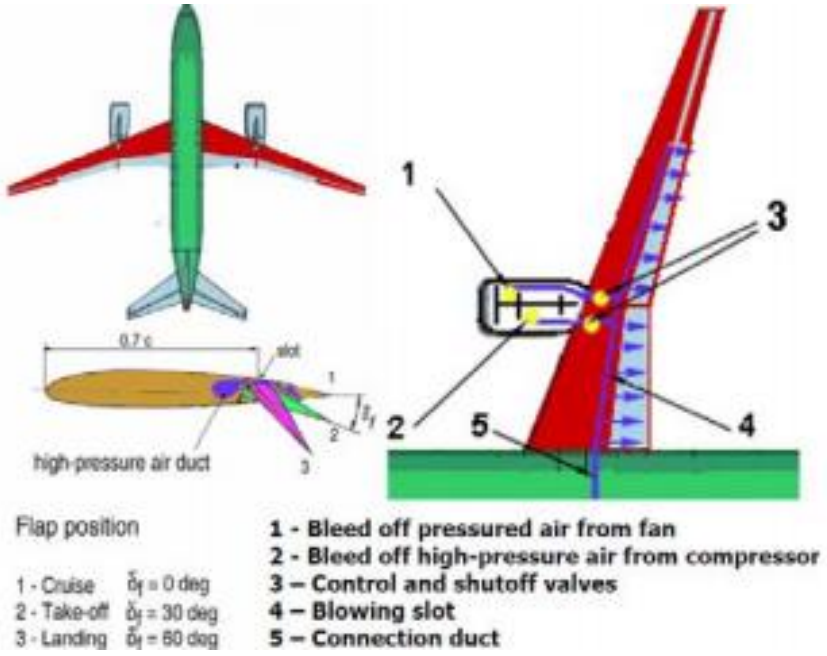

Figure 7.9 – Blowing system used with a trailing edge flap [193].

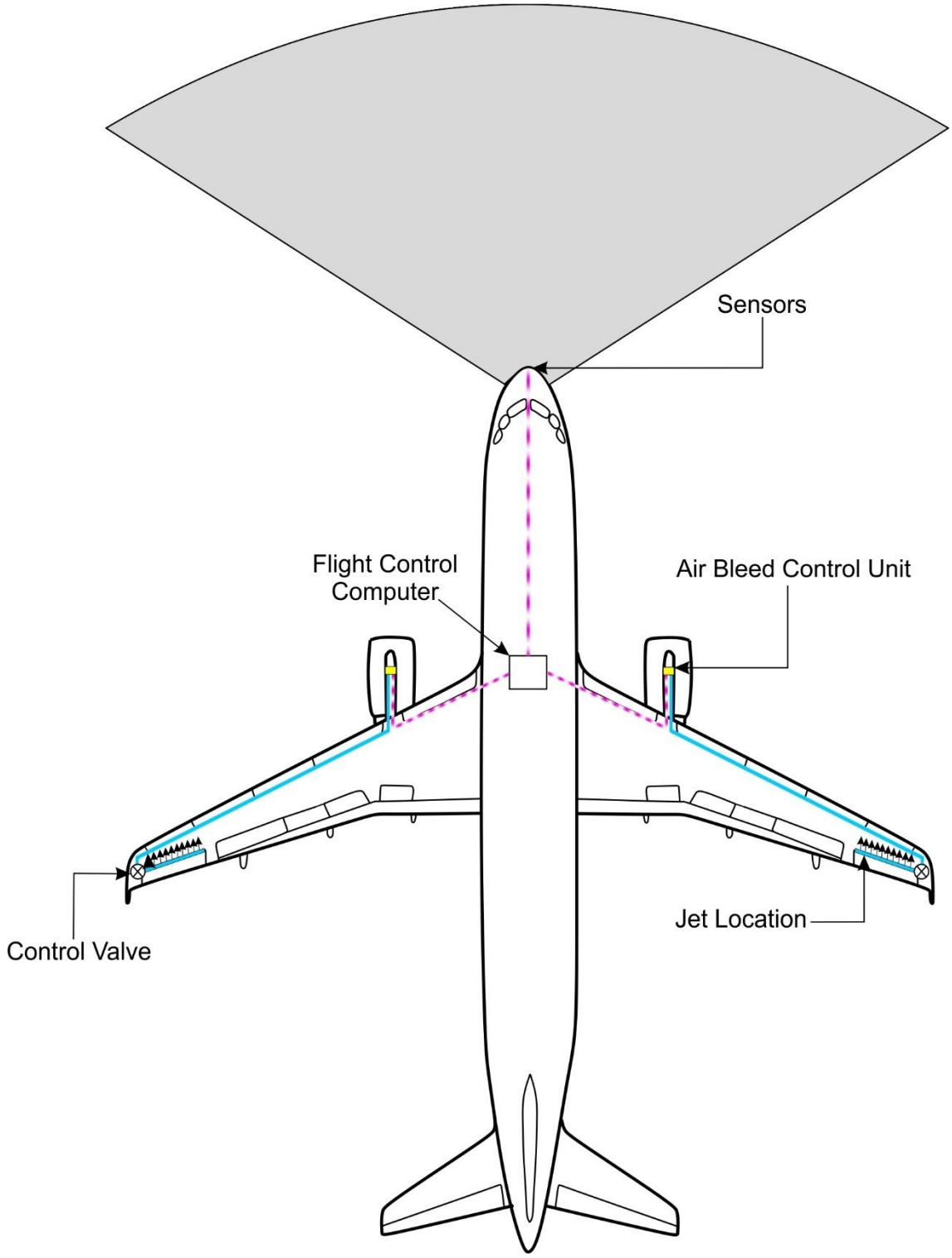

Figure 7.10 – Upstream blowing system implemented on a full scale Airbus A320.

Chapter 8 : Conclusions

Force, pressure, hot wire and two-dimensional PIV measurements were performed to investigate the efficacy and flow mechanisms for steady-state normal and upstream blowing. These results indicate that upstream blowing is more efficient than normal blowing for the same flow rate, normal blowing effectively reduced lift only at x_J/c = 0.95. The flow field measurements indicate that upstream blowing incites the shear layer to detach ahead of the jet location and consequently modify the aerodynamic camber of the airfoil. This behaviour is best demonstrated at x_J/c = 0.60 where the jet momentum impinges with the opposing freestream flow, provoking the freestream flow to deflect away from the airfoil surface. As expected, increasing jet flow rate further reduces lift. The induced camber change causes flow above the shear layer to accelerate which is reflected in the pressure measurements; pressure reduces aft of the jet but increases ahead of the jet. In terms of chordwise location, locations nearer to the trailing edge, x_J/c = 0.95, are preferred for low angles of attack giving an effectiveness of $\Delta C_L/C_\mu$ = 6.24 for C_μ = 0.024 at α = 0°; but locations closer to the leading edge, x_J/c = 0.08, are preferable for higher angles of attack giving an effectiveness of $\Delta C_L/C_\mu$ = 12.20 C_μ = 0.024 at α = 13°.

For periodic deployment with a 1-cos profile, increasing frequency leads to a reduced amplitude and increased phase lag. The phase lag is generally larger when the actuator is placed towards the leading edge. Generally, the amplitude decays faster with increasing angle of attack and with locations nearer the leading-edge. However, retention of lift amplitude is high; for x_J/c = 0.95, amplitude is 80% of steady-state lift for k = 0.236 at α = 5°. Flow fields for periodic deployment at k = 0.393 show that the size of the separated region induced by the jet determines the lift response but never reaches what is observed with continuous blowing. Additionally, the lift response of the jet can be modelled using first order system transfer functions. The time constant of the jet increases with angle of attack.

Transient measurements for a step profile show trailing edge locations incite a faster response, while leading edge locations incur a time delay. Transient PIV measurements demonstrate the separated region incited by jet activation enlarges with convective time until steady-state is established. Flow field measurements show the boundary layer separates from the trailing edge first before the separation point advances ahead of the jet.

These measurements demonstrate that the upstream blowing jet flap is a potential actuator for gust load alleviation but the location of the jet is very important in both steady and unsteady conditions. Scaling of blowing rate shows that a jet with a momentum coefficient of C_μ = 0.008 can be achieved with bleeding just 7.5% of cruise mass flow rate for an A340 engine.

8.1 Suggestions for Future Work

Although the jet flap has been illustrated to be an effective flow control technique, there is a strong dependency on a number of parameters; deflection angle, momentum coefficient, reduced frequency and jet location. However, further work must be performed to better understand its effect before being implemented on commercial aircraft.

The effect of reduced frequency has been studied in this project; however, with the use of an alternative force balance, the range of reduced frequencies tested could be extended towards unity, k =1. This would give a better understanding of the jet flap performance at high frequencies.

As the purpose of this work was to assess the feasibility of the jet flap for gust load alleviation, it would be beneficial to create a gust generating system. This system would subject the wing with a 1 – cos gust in the wind tunnel test section. The control performance of the jet flap would then be examined initially with open-loop control. Thereafter, this work could be extended to test the response within a closed-loop system, by utilising feedback control. It would be interesting to determine if the phase lag seen with leading edge locations, would be too large for effective load control.

Additional parameters could be introduced for investigation, such as the Mach number and sweep angle of the wing. The sweep angle should be varied for a continuous blowing jet flap, before being tested with unsteady blowing. The sweep angle could be combined with other parameters, such as momentum coefficient and varying chordwise location.

Methods of implementing the jet flap on aircraft should also be studied. This could be done by producing a feasible system in order to source air and actuate the jet flap, whilst maintaining a light weight.

List of Publications

Journal Articles

- Al-Battal, N. H., Cleaver, D. J., Gursul, I., "Lift Reduction by Counter Flowing Wall Jets," *Aerospace Science and Technology*, Vol. 78, 2018, pp. 682-695.
- Al-Battal, N. H., Cleaver, D. J., Gursul, I., "Aerodynamic Load Control through Jet Flap Excitation," *in prepartion*.

Conference Papers

- Al-Battal, N. H., Cleaver, D. J., Gursul, I., "Aerodynamic Load Control through Blowing," 54th AIAA Aerospace Sciences Meeting, AIAA 2016-1820, 2016.

References

[1] - Lee, D. S., Fahey, D. W., Forster, P. M., Newton, P. J., Wit, R. C.N., Lim, L. L., Owen, B., and Sausen, R., "Aviation and global climate change in the 21st century," *Atmospheric Environment*, Vol. 43, 2009, pp. 3520-3537.

[2] – "FAA Aerospace Forecast: Fiscal Years 2011-2031," Federal Aviation Administration, 2011.

[3] – Waitz, I.A., Townsend, J., Cutcher-Gershenfeld, J., Greitzer, E. M., and Kerrebrock, J. L., "Aviation and the Environment: A National Vision Statement, Framework for Goals and Recommended Actions," Report to the United States Congress, on behalf of the U.S. DOT, FAA and NASA, December 2004.

[4] – "Flightpath 2050 – Europe's Vision for Aviation," Directorate-General for Research and Innovation and Directorate General for Mobility and Transport, European Commission, Luxembourg, 2011.

[5] – Wright, J. R., and Cooper, J. E., "Aircraft Design and Certification," *Introduction to Aircraft Aeroelasticity and Loads,* 1st ed., Wiley, 2007, pp. 419-427.

[6] – Bieniawski, S. R., and Kroo, I. M., "Flight Control with Miniature Trailing Edge Effectors," *25th International Congress of Aeronautical Sciences*, ICAS, Hamburg, 2006.

[7] – Xu, J., and Kroo, I., "Aircraft Design with Active Load Alleviation and Natural Laminar Flow," *Journal of Aircraft,* Vol. 51, No. 5, 2014, pp. 1532-1545.

[8] – Leishman, G. J., "Unsteady Airfoil Behavior," *Principles of Helicopter Aerodynamics with CD Extra,* 2nd ed., Cambridge University Press, 2006, pp. 423-519.

[9] – "Aviation Safety And Pilot Control: Understanding and Preventing Unfavorable Pilot-Vehicle Interactions," National Research Council, 1997.

[10] – Moulin, B., and Karpel, M., "Gust Loads Alleviation Using Special Control Surfaces," *Journal of Aircraft,* Vol. 44, No. 1, 2007, pp. 17-25.

[11] – Hoblit, F. M., *Gust Loads on Aircraft: Concepts and Applications*, AIAA, 1988.

[12] – *Source book to the Forecaster's Reference Book*, Meteorological Office, 1997.

[13] – Wilson, E. B., "Theory of an Aeroplane Encountering Gusts," *Proceedings of the National Academy of Sciences of the United States of America*, Vol. 2, No. 5, 1916, pp. 294-297.

[14] – Donely, P., and Shufflebarger, C. C., “Tests of a Gust-Alleviating Flap in the Gust Tunnel,” NACA-TN-745, 1940.

[15] – Pratt, K. G., “A Revised Formula for the Calculation of Gust Loads,” NACA-TN-2964, January 1953.

[16] – Lomax, T. L., *Structural Loads Analysis for Commercial Transport Aircraft*, AIAA, 1996.

[17] – “Certification Specifications for Large Aeroplanes CS-25,” European Aviation Safety Agency, 2007.

[18] – Von Karman, T., “Progress in the statistical theory of turbulence,” *Proceedings of the National Academy of Sciences*, Vol. 34, No. 11, 1948, pp. 530-539.

[19] – Press, H., “Atmospheric Turbulence Environment with Special Reference to Continuous Turbulence,” AGARD Report No. 115, April-May 1957.

[20] – Liepmann, H. W., “On the Application of Statistical Concepts to the Buffeting Problem,” *Journal of the Aeronautical Sciences*, Vol. 19, No. 12, 1952, pp. 793-800.

[21] – Rhyne, R. H., and Steiner, R., “Power spectral measurement of atmospheric turbulence in severe storms and cumulus clouds,” NASA-TN-D-2469, 1964.

[22] – Gad-el-Hak, M., *Flow Control: Passive, Active, and Reactive Flow Management*, Cambridge University Press, 2000.

[23] – Gad-el-Hak, M., “Control of Low-Speed Airfoil Aerodynamics,” *AIAA Journal*, Vol. 28, No. 9, 1990, pp. 1537-1552.

[24] – Lin, J.C., Robinson, S. K., McGhee, R. J., and Valarezo, W. O., “Separation Control on High-Lift Airfoils via Micro-Vortex Generators,” *Journal of Aircraft*, Vol. 31, No. 6, 1994, pp. 1317-1323.

[25] – Cattafesta III, L. N., and Sheplak, M., “Actuators for Active Flow Control,” *Annual Review of Fluid Mechanics*, Vol. 43, 2011, pp. 247-272.

[26] – Rowley, C.W., and Batten, B. A., “Dynamic and Closed-Loop Control,” *Fundamentals and Applications of Modern Flow Control*, edited by R. D. Joslin, and D. N. Miller, Vol. 231, Progress in Astronautics and Aeronautics, AIAA, 2009, pp. 115-148.

[27] – “OECD Factbook 2007: Economic, Environmental and Social Statistics,” OECD Publishing, 2007.

[28] – Gilyard, G., and Martin, E., “On the Use of Controls of Subsonic Transport Performance Improvement: Overview and Future Directions,” NASA-TM-4605, 1994.

[29] – Disney, T. E., “The C-5A Active Load Alleviation System,” Aircraft Systems and Technology Meeting, Aircraft Design and Technology Meeting, Los Angeles, 1975.

[30] – Johnston, J. F., “Accelerated Development and Flight Evaluation of Active Controls Concepts for Subsonic Transport Aircraft. Volume 1: Load Alleviation/Extended Span Development and Flight Tests,” NASA-CR-159097, 1979.

[31] – Sensburg, O., Becker, J., Lusebrink, H., and Weiss, F., “Gust Load Alleviation on Airbus A300,” 13th Congress of the International Council of the Aeronautical Sciences, ICAS-82-2.1.1, August 1982.

[32] – Payne, B. W., “Designing a Load Alleviation System for a Modern Civil Aircraft,” 15th Congress of the International Council of the Aeronautical Sciences, ICAS-86-5.2.3, September 1986.

[33] – Rabadan, G. J., Schmitt, N. P., Pistner, T., and Rehm, W., “Airborne Lidar for Automatic Feedforward Control of Turbulent In-Flight Phenomena,” *Journal of Aircraft,* Vol. 47, No, 2, 2010, pp. 392-403.

[34] – “FAST A380 Special Edition,” Airbus, November 2016.

[35] – Consigny, H., Gravelle, A., and Molinaro, R., “Aerodynamic Characteristics of a Two-Dimensional Moving Spoiler in Subsonic and Transonic Flow,” *Journal of Aircraft,* Vol. 21, No. 9, 1984, pp. 687-693.

[36] – McLachlan, B. G., Karamcheti, K., and van Leynseele, F., “Experimental Study of the Flowfield of an Airfoil with Deflected Spoiler,” 20th Aerospace Sciences Meeting, Aerospace Sciences Meetings, AIAA, 1982.

[37] – Maskell, E. C., “Pressure Distributions Illustrating Flow Reattachment behind a Forward Mounted Flap,” ARC-CP-211, 1955.

[38] – McLachlan, B. G., Karamcheti, K., Ayoub, A., and Hadjidakis, G., “A Study of the Unsteady Flow Field of an Airfoil with Deflected Spoiler,” 10th Atmospheric Flight Mechanics Conference Guidance, Navigation, and Control and Co-located Conferences, AIAA, 1983.

[39] – Kim, J. H., and Rho, O. H., “Numerical Simulation of Flowfield Around Airfoil with Stationary or Oscillating Spoiler,” *Journal of Aircraft,* Vol. 35, No. 5, 1998, pp. 704-711.

[40] – Croom, D. R., Shufflebarger, C. C., Huffman, J. K., "An Investigation of Forward-Located Fixed Spoilers and Deflectors as Gust Alleviators on an Unswept-wing Model," NACA-TN-3705, June 1956.

[41] – Lang, J. D., and Francis, M. S., "Interaction of an Oscillating Control Surface with an Unsteady Separated Region," *Journal of Aircraft*, Vol. 13, No. 9, 1976, pp. 687-694.

[42] – Francis, M. S., Keesee, J. E., Lang, J. D., Sparks Jr, G. W., and Sisson, G. E., "Aerodynamic Characteristics of an Unsteady Separated Flow," *AIAA Journal*, Vol. 17, No. 12, 1979, pp. 1332-1339.

[43] – Costes, M., Gravelle, A., Philippe, J., Vogel, S., and Triebstein, H., "Investigation of Unsteady Subsonic Spoiler and Flap Aerodynamics," *Journal of Aircraft*, Vol. 24, No. 9, 1987, pp. 629-637.

[44] – Choi, S.W., Chang, K.S., and Ok, H., "Parametric Study of Transient Spoiler Aerodynamics with Two-Equation Turbulence Models," *Journal of Aircraft*, Vol. 38, No. 5, 2001, pp. 888-894.

[45] – Abbott, I. H., and von Doenhoff, A. E., *Theory of Wing Sections: Including a Summary of Airfoil Data*¸ Dover Publications, Inc., New York, 1959.

[46] – Anderson, J. D., *Fundamentals of Aerodynamics*, 5th ed.. McGraw-Hill Education, New York, 2011.

[47] – Jacobs, E. N., and Pinkerton, R. M., "Pressure Distribution Over a Symmetrical Airfoil Section with Trailing Edge Flap," NACA-TR-360, January 1931.

[48] – Bak, C., Gaunaa, M., Andersen, P. B., Buhl, T., Hansen, P., and Clemmensen, K., "Wind Tunnel Test on Airfoil Risø-B1-18 with an Active Trailing Edge Flap," *Wind Energy*, Vol. 13, No. 2-3, 2010, pp. 207-219.

[49] – Frederick, M., Kerrigan, E. C., and Graham, J. M. R., "Gust alleviation using rapidly deployed trailing-edge flaps," *Journal of Wind Engineering and Industrial Aerodynamics*, Vol. 98, No. 12, 2010, pp. 712-723.

[50] – Leishman, G. J., "Unsteady Lift of a Flapped Airfoil by Indicial Concepts," *Journal of Aircraft*, Vol. 31, No. 2, 1994, pp. 288-297.

[51] – Buhl, T., Gaunaa, M., and Bak, C., "Potential Load Reduction Using Airfoils with Variable Trailing Edge Geometry," *Journal of Solar Energy Engineering*, Vol. 127, No. 4, 2005, pp. 503-516.

[52] – Chow, R., and van Dam, C. P., "On the temporal response of active load control devices," *Wind Energy*, Vol. 13, No. 2-3, 2010, pp. 135-149.

[53] – Patil, S. K. R., and Terry Ng, T., "Control of Separation Using Spanwise Periodic Porosity," *AIAA Journal*, Vol. 48, No. 1, 2010, pp. 174-187.

[54] – Han, Y. O., and Leishman, G. J., "Investigation of Helicopter Rotor-Blade-Tip-Vortex Alleviation Using a Slotted Tip," *AIAA Journal*, Vol. 42, No. 3, 2004, pp. 524-535.

[55] – Filippone, A., "Inverted Jet Spoilers for Aerodynamic Control," *Journal of Aircraft*, Vol. 46, No. 4, 2009, pp. 1240-1252.

[56] – Kearney, J. M., and Glezer, A., "Aero-Effected Flight Control Using Distributed Active Bleed," 41st AIAA Fluid Dynamics Conference and Exhibit, AIAA 2011-3099, Honolulu, June 2011.

[57] – Patel, M. P., DiCocco, J. M., Prince, T. S., and Ng, T. T., "Flow Control Using Reconfigurable Porosity," 21st AIAA Applied Aerodynamics Conference, AIAA 2003-3665, June 2003.

[58] – Ho, S., Nassef, H., Pornsinsirirak, N., Tai, Y.C., and Ho, C.M., "Unsteady aerodynamics and flow control for flapping wing flyers," *Progress in Aerospace Sciences*, Vol. 39, No. 8, 2003, pp. 635-681.

[59] – Tinetti, A., Kelly, J., Bauer, S., and Thomas, R., "On the use of surface porosity to reduce unsteady lift," 15th AIAA Computational Fluid Dynamics Conference, AIAA 2001-2921, 2001.

[60] – Liebeck, R. H., "Design of Subsonic Airfoils for High Lift," *Journal of Aircraft*, Vol. 14, No. 9, 1978, pp. 547-561.

[61] – Tang, D., and Dowell, E. H., "Aerodynamic Loading for an Airfoil with an Oscillating Gurney Flap," *Journal of Aircraft*, Vol. 44, No. 4, 2007, pp. 1245-1257.

[62] – Liu, T., and Montefort, J., "Thin-Airfoil Theoretical Interpretation for Gurney Flap Lift Enhancement," Vol. 44, No. 2, 2007, pp. 667-671.

[63] – Heathcote, D. J., Gursul, I, and Cleaver, D. J., "An Experimental Study of Mini-Tabs for Aerodynamic Load Control," 54th AIAA Aerospace Sciences Meeting, AIAA 2016-0325, January 2016.

[64] – Bieniawski, S., and Kroo, I, M., "Flutter Suppression Using Micro-Trailing Edge Effectors," 44th AIAA Structures, Structural Dynamics, and Materials Conference, AIAA 2003-1941, Norfolk, VA, April 2003.

[65] – Matalanis, C. G., and Eaton, J. K., "Wake Vortex Alleviation Using Rapidly Actuated Segmented Gurney Flaps," *AIAA Journal*, Vol. 45, No. 8, 2007, pp. 1874-1884.

[66] - Heathcote, D. J., Gursul, I, and Cleaver, D. J., "Frequency Response of Aerodynamic Load Control through Mini-tabs," 55th AIAA Aerospace Sciences Meeting, AIAA 2017-0947, 2017.

[67] – Kinzel, M. P., Maughmer, M. D., and Duque, E. P. N., "Numerical Investigation on the Aerodynamics of Oscillating Airfoils with Deployable Gurney Flaps," *AIAA Journal*, Vol. 48, No. 7, 2010, pp. 1457-1469.

[68] – Korbacher, G. K., and Sridhar, K., "A Review of The Jet Flap," University of Toronto Press, UTIA Review No. 14, 1960.

[69] Sobey, I. J., "Coanda Effect," *Introduction to Interactive Boundary Layer Theory*, Oxford University Press, 2000, pp. 284-298.

[70] Seifert, A., Bachar, T., Koss, D., Shepshelovich, M., and Wygnanski, I., "Oscillatory Blowing: A Tool to Delay Boundary-Layer Separation," *AIAA Journal*, Vol. 31, No. 11, 1993, pp. 2052-2060.

[71] – Traub, L. W., Miller, A. C., and Rediniotis, O., "Comparisons of a Gurney and Jet-Flap for Hinge-Less Control," *Journal of Aircraft*, Vol. 41, No. 2, 2004, pp. 420-423.

[72] – Blaylock, M., Chow, R., Cooperman, A., and van Dam, C. P., "Comparison of pneumatic jets and tabs for Active Aerodynamic Load Control," *Wind Energy*, Vol. 17, No. 9, 2014, pp. 1365-1384.

[73] – Wong, C., and Kontis, K., "Flow Control by Spanwise Blowing on a NACA 0012," *Journal of Aircraft*, Vol. 44, No. 1, 2007, pp. 337-340.

[74] – Tavella, D. A., Lee, C. S., Wood, N. J., and Roberts, L., "The jet spoiler as a yaw control device," 4th Applied Aerodynamics Conference, AIAA 86-1806, San Diego, CA, 1986.

[75] – Bamber, M. J., "Wind tunnel tests on airfoil boundary layer control using a backward-opening slot," NACA-TR-385, 1931.

[76] – Bowman, M., Vogelsang, M., *Lockheed F-104 Starfighter*, The Crowood Press Ltd, 2000.

[77] – Tooley, M. Filippone, A., Megson, T.H.G., Cook, M., Carpenter, P. W., Houghton, E. L., Wyatt, D., Jenkinson, L. R., Marchman, J., De Florio, F., Wakinson, J., Gurfil, P., and Curtis, H., "Flight Dynamics," *Aerospace Engineering e-Mega Reference*, Butterworth-Heinemann, 2009, pp. 223-517.

[78] – "Jet Flap in the Air," *Flight International*, Vol. 83, No. 2821, 1963, pp. 454-455.

[79] – Reckzeh, D., "Aerodynamic design of the high-lift-wing for a Megaliner aircraft," *Aerospace Science and Technology*, Vol. 7, No. 2, 2003, pp. 107-119.

[80] – Spence, D. A., "The lift coefficient of a thin, jet-flapped wing," *Proceedings of the Royal Society A,* Vol. 238, No. 1212, 1956, pp. 46-68.

[81] – Dimmock, N. A., "An Experimental Introduction to the Jet Flap," A.R.C., C.P. 344, 1957.

[82] – Dimmock, N. A., "Some Further Jet Flap Experiments," A.R.C., C.P. 345, 1957.

[83] – Traub, L. W., and Agarwal, G., "Aerodynamic Characteristics of a Gurney/Jet Flap at Low Reynolds Numbers," *Journal of Aircraft,* Vol. 45, No. 2, 2008, pp. 424-429.

[84] – McLachlan, B. G., "Study of a Circulation Control Airfoil with Leading/Trailing-Edge Blowing," *Journal of Aircraft,* Vol. 26, No. 9, 1989, pp. 817-821.

[85] – Tuck, A., and Soria, J., "Separation control on a NACA 0015 airfoil using a 2D micro ZNMF jet," *Aircraft Engineering and Aerospace Technology,* Vol. 80, No. 2, pp. 175-180.

[86] – Lockwood, V. E., and Vogler, R. D., "Exploratory wind-tunnel investigation at high subsonic and transonic speeds of jet flaps on unswept rectangular wings," NACA-TN-4353, August 1958.

[87] – Sasson, B., and Greenblatt, D., "Effect of Leading-Edge Slot Blowing on a Vertical Axis Wind Turbine," *AIAA Journal,* Vol. 49, No. 9, 2011, pp. 1932-1942.

[88] – Boeije, C. S., de Vries, H., Cleine, I., van Emden, E., Zwart, G. G. M., Stobbe, H., Hirschberg, A., and Hoeijmakers, H. W. M., "Fluidic Load Control for Wind Turbine Blades," 47th AIAA Aerospace Sciences Meeting Including The New Horizons Forum and Aerospace Exposition, AIAA 2009-684, Orlando, FL, January 2009.

[89] – Bevilaqua, P. M., Schum, E. F., and Woan, C. J., "Progress towards a theory of jet-flap thrust recovery," *Journal of Fluid Mechanics,* Vol. 141, 1984, pp. 347-364.

[90] – Goodarzi, M., Rahimi, M., and Fereidouni, R., "Investigation of Active Flow Control over NACA0015 Airfoil Via Blowing," *International Journal of Aerospace Sciences,* Vol. 1, No. 4, 2012, pp. 57-63.

[91] – Lowry, J. G., and Vogler, R. D., "Wind-tunnel investigation at low speeds to determine the effect of aspect ratio and end plates on a rectangular wing with jet flaps deflected 85 degrees," NACA-TN-3863, December 1956.

[92] – Bradbury, L. J. S., and Riley, J., "The spread of a turbulent plane jet issuing into a parallel moving airstream," *Journal of Fluid Mechanics,* Vol. 27, No. 2, 1967, pp. 381-394.

[93] – Simmons, J. M., Platzer, M. F., and Smith, T. C., "Velocity measurements in an oscillating plane jet issuing into a moving air stream," *Journal of Fluid Mechanics*, Vol. 84, No. 1, 1978, pp. 33-53.

[94] - Weston, R. P., and Thames, F. C., "Properties of Aspect-Ratio-4.0 Rectangular Jets in a Subsonic Crossflow," *Journal of Aircraft*, Vol. 16, No. 10, 1979, pp. 701-707.

[95] – Fearn, R., and Weston, R. P., "Vorticity Associated with a Jet in a Cross Flow," *AIAA Journal*, Vol. 12, No. 12, 1974, pp. 1666-1671.

[96] – Krothapalli, A., and Leopold, D., "A study of flow past an airfoil with a jet issuing from its lower surface," NASA-CR-166610, June 1984.

[97] – Yousefi, K., and Saleh, R., "The effects of trailing edge blowing on aerodynamic characteristics of the NACA 0012 airfoil and optimization of the blowing slot geometry," *Journal of Theoretical and Applied Mechanics*, Vol. 52, No. 1, 2014, pp. 165-179.

[98] – Mikolowsky, W., and McMahon, H., "An Experimental Investigation of a Jet Issuing from a Wing in Crossflow," *Journal of Aircraft*, Vol. 10, No. 9, 1973, pp. 546-553.

[99] – Huang, L., Huang, P. G., LeBeau, R. P. and Hauser, T., "Numerical Study of Blowing and Suction Control Mechanism on NACA0012 Airfoil," *Journal of Aircraft*, Vol. 41, No. 5, 2004, pp. 1005-1013.

[100] – Sasson, B., and Greenblatt, D., "Effect of Steady and Unsteady Slot Blowing on a Vertical Axis Wind Turbine," 28th AIAA Applied Aerodynamics Conference, AIAA 2010-4406, Chicago, IL, June-July 2010.

[101] – Scholz, P., Ortmanns, J., Kähler, C. J., and Radespiel, R., "Leading-Edge Separation Control by Means of Pulsed Vortex Generator Jets," *AIAA Journal*, Vol. 46, No. 4, 2008, pp. 837-846.

[102] – Bobonea, A., "Impact of pulsed blowing jet on aerodynamic characteristics of wind turbine airfoils," 9th International Conference on Mathematical Problems in Engineering, Aerospace and Sciences, AIP Conference Proceedings, Vol. 1493, No. 1, July 2012, pp. 170-174.

[103] – Zhou, P., Wang, Y., Wang, J., and Sha, Y., "Blowing momentum and duty cycle effect on aerodynamic performance of flap by pulsed blowing," *Journal of Physics: Conference Series*, Vol. 822, 2017.

[104] – Petz, R., Nitsche, W., Schatz, M., and Thiele, F., "Increasing Lift by Means of Active Flow Control on the Flap of a Generic High-Lift Configuration," New Results in Numerical and

Experimental Fluid Mechanics V. Notes on Numerical Fluid Mechanics and Multidisciplinary Design, Vol. 92, Springer, Berlin, Heidelberg, 2006.

[105] – Lockwood, R. M., "Pulse reactor lift-propulsion system development program," Advanced Research ARD-308, March 1963.

[106] – Bremhorst, K., and Hollis, P. G., "Velocity Field of an Axisymmetric Pulsed, Subsonic Air Jet," *AIAA Journal*, Vol. 28, No. 12, 1990, pp. 2043-2049.

[107] – Johari, H., "Scaling of Fully Pulsed Jets in Crossflow," *AIAA Journal*, Vol. 44, No. 11, 2006, pp. 2719-2725.

[108] – Johari, H., Zhang, Q., Rose, M. J., and Bourque, S. M., "Impulsively Started Turbulent Jets," *AIAA Journal*, Vol. 35, No. 4, 1997, pp. 657-662.

[109] – Johari, H., and Rixon, G. S., "Effects of Pulsing on a Vortex Generator Jet," *AIAA Journal*, Vol. 41, No. 12, 2003, pp. 2309-2315.

[110] – Johari, H., Pacheco-Tougas, M., Hermanson J. C., "Penetration and Mixing of Fully Modulated Turbulent Jets in Crossflow," *AIAA Journal*, Vol. 37, No. 7, 1999, pp. 842-850.

[111] – Hermanson, J. C., Wahba, A., and Johari, H., "Duty-Cycle Effects on Penetration of Fully Modulated, Turbulent Jets in Crossflow," *AIAA Journal*, Vol. 36, No. 10, 1998, pp. 1935-1937.

[112] – Wu, J. M., Vakili, A. D., and Yu, F. M., "Investigation of the Interacting Flow of Nonsymmetric Jets in Crossflow," *AIAA Journal*¸ Vol. 26, No. 8, 1988, pp. 940-947.

[113] - M'Closkey, R. T. M., King, J. M., Cortelezzi, L., and Karagozian, A. R., *Journal of Fluid Mechanics*, Vol. 452, 2002, pp. 325-335.

[114] – Scholz, P., Casper, M., Ortmanns, J., Kähler, C. J., and Radespiel, R., "Leading-Edge Separation Control by Means of Pulsed Vortex Generator Jets," *AIAA Journal*, Vol. 46, No. 4, 2008, pp. 837-846.

[115] – Hipp, K. D., Walker, M. M., Benton, S. I. and Bons, J. P., "Control of Poststall Airfoil Using Leading-Edge Pulsed Jets," *AIAA Journal*, Vol. 55, No. 2, 2017, pp. 365-376.

[116] – Woo, G. T. K., Crittenden, T. M., and Glezer, A., "Transitory Control of a Pitching Airfoil using Pulse Combustion Actuation," 4th Flow Control Conference, AIAA 2008-4324, Washington, June 2008.

[117] – Wong, C., and Kontis, K., "Experimental Studies on Unsteady Lateral Blowing on a NACA 0012," *Journal of Aircraft*, Vol. 44, No. 6, 2007, pp. 2080-2083.

[118] – Kerstens, W., Pfeiffer, J., Williams, D., King, R., and Colonius, T., "Closed-Loop Control of Lift for Longitudinal Gust Suppression at Low Reynolds Numbers," *AIAA Journal*, Vol. 49, No. 8, 2011, pp. 1721-1728.

[119] – Williams, D., Kerstens, W., Buntain, S., Quach, V., Pfeiffer, J., King, R., Tadmor, G., and Colonius, T., "Closed-Loop Control of a Wing in an Unsteady Flow," 48th AIAA Aerospace Sciences Meeting Including the New Horizons Forum and Aerospace Exposition, AIAA 2010-358, Orlando, FL, January 2010.

[120] – Amitay, M., Smith, D. R., Kibens, V., Parekh, D. E., and Glezer, A., "Aerodynamic Flow Control over an Unconventional Airfoil Using Synthetic Jet Actuators," *AIAA Journal*, Vol. 39, No. 3, 2001, pp. 361-370.

[121] – Smith, B. L., and Glezer, A., "The formation and evolution of synthetic jets," *Physics of Fluids*, Vol. 10, No.9, 1998, pp. 2281-2297.

[122] – Ingård, U. and Labate, S., "Acoustic Circulation Effects and the Nonlinear Impedance of Orifices," *The Journal of the Acoustical Society of America*, Vol. 22, No. 2, 1950, pp. 211-218.

[123] – Chang, R. C., Hsiao, F. -B, and Shyu, R. –N., "Forcing Level Effects of Internal Acoustic Excitation on the Improvement of Airfoil Performance," *Journal of Aircraft*, Vol. 29, No. 5, 1992, pp. 823-829.

[124] – Hao, L. S., and Qiao, Z. D., "An Experimental and Analytical Investigation of Aerodynamic Flow Control Using Synthetic Jet Technology," 25th Internation Congress of the Aeronautical Sciences, ICAS 2006-P2.3, 2006.

[125] – Xu, X., Zhu, X., Zhou, Z., and Fan, R., "Application of Active Flow Control Technique for Gust Load Alleviation," *Chinese Journal of Aeronautics*, Vol. 24, No. 4, 2011, pp. 410-416.

[126] – Goodfellow, S. D., Yarusevych, S., and Sullivan, P. E., "Momentum Coefficient as a Parameter for Aerodynamic Flow Control with Synthetic Jets," *AIAA Journal*, Vol. 51, No. 3, 2013, pp. 623-631.

[127] – Whitehead, J., and Gursul, I., "Interaction of Synthetic Jet Propulsion with Airfoil Aerodynamic at Low Reynolds Numbers," *AIAA Journal*, Vol. 44, No. 8, 2006, pp. 1753-1766.

[128] – Smith, B. L., and Swift, G. W., "A comparison between synthetic jets and continuous jets," *Experiments in Fluids*, Vol. 34, No. 4, 2003, pp. 467-472.

[129] – Gordon, M., and Soria, J., "PIV measurements of a zero-net-mass-flux jet in cross flow," *Experiments in Fluids*, Vol. 33, No. 6, 2002, pp. 863-872.

[130] – Amitay, M., and Glezer, A., "Role of Actuation Frequency in Controlled Flow Reattachment over a Stalled Airfoil," *AIAA Journal*, Vol. 40, No. 2, 2002, pp. 209-216.

[131] – Wang, L., Xia, Z.-X., Luo, Z.,-B., and Chen, J., "Three-Electrode Plasma Synthetic Jet Actuator for High-Speed Flow Control, *AIAA Journal*, Vol. 52, No. 4, 2014, pp. 879-882.

[132] – An, X., Williams, D. R., Eldredge, J. D., and Colonius, T., "Modeling Dynamic Lift Response to Actuation," 54th AIAA Aerospace Sciences Meeting, AIAA SciTech Forum, AIAA 2016-0058, San Diego, CA, January 2016.

[133] – Amitay, M., and Glezer, A., "Flow transients induced on a 2D airfoil by pulse-modulated actuation," *Experiments in Fluids*, Vol. 40, No. 2, 2006, pp. 329-331.

[134] – Duvigneau, R., Hay, A., and Visonneau, M., "Optimal Location of a Synthetic Jet on an Airfoil for Stall Control," *Journal of Fluids Engineering*, Vol. 129, No. 7, 2007, pp. 825-833.

[135] – Widjanarko, S. M. D., Geesing, I. J. A. K., de Vries, H., and Hoeijmakers, H. W. M., "Experimental/Numerical Investigation Airfoil with Flow Control by Synthetic Jets," 28th Congress of the International Council of the Aeronautical Sciences, ICAS 2012-3.7.5, 2012.

[136] – Stolk, M., Patel, D., O'Donnell, K., Marcozza, P., De Breuker, R., Abdalla, M., Nicolini, E., and Gürdal, Z., "Active Flow and Aeroelastic Control of Lifting Surfaces Using Synthetic Jet Actuators," SAE Technical Paper 2007-01-3920, 2007.

[137] – O'Donnell, K., Schober, S., Stolk, M., Marcozza, P., De Breuker, R., Abdalla, M., Nicolini, E., and Gürdal, Z., "Active Aeroelastic Control Aspects of an Aircraft Wing by Using Synthetic Jet Actuators: Modeling, Simulations, Experiments," The 14th International Symposium on: Smart Structures, and Materials & Nondestructive Evaluation and Health Monitoring, SPIE 6523-8, San Diego, CA, March 2007.

[138] – Simmons, J. M., and Platzer, M. F., "Experimental Investigation of Incompressible Flow Past Airfoils with Oscillating Jet Flaps," Vol. 8, No. 8, 1971, pp. 587-592.

[139] – Spence, D. A., "The Flow Past a Thin Wing with an Oscillating Jet Flap," *Philosophical Transactions of the Royal Society A: Mathematical, Physical and Engineering Sciences*, Vol. 257, No. 1085, 1965, pp. 445-477.

[140] – Viets, H., "Flip-Flop Jet Nozzle," *AIAA Journal*, Vol. 13, No. 10, 1975, pp. 1375-1379.

[141] – Platzer, M. F., Simmons, J. M., and Bremhorst, K., "Entrainment Characteristics of Unsteady Subsonic Jets," *AIAA Journal*, Vol. 16, No. 3, 1978, pp. 282-284.

[142] – Simmons, J. M., “Measured Pressure Distributions on an Airfoil with Oscillating Jet Flap,” *AIAA Journal*, Vol. 14, No. 9, 1976, pp. 1297-1302.

[143] – Simmons, J. M., and Platzer, M. F., “A Quasisteady Theory for Incompressible Flow Past Airfoils with Oscillating Jet Flaps,” *AIAA Journal*, Vol. 16, No. 3, 1978, pp. 237-241.

[144] – Simmons, J. M., “Aerodynamic Measurements for an Oscillating Two-Dimensional Jet-Flap Airfoil,” *AIAA Journal*, Vol. 14, No. 6, 1976, pp. 741-748.

[145] – Seifert, A., Darabi, A., and Wygnanski, I., “Delay of Airfoil Stall by Periodic Excitation,” *Journal of Aircraft*, Vol. 33, No. 4, 1996, pp. 691-698.

[146] – Seifert, A., and Pack, L. G., “Oscillatory Control of Separation at High Reynolds Numbers,” *AIAA Journal*, Vol. 37, No. 9, 1999, pp. 1062-1071.

[147] – Hites, M., Nagib, H., Bachar, T., and Wygnanski, I., “Enhanced Performance of Airfoils at Moderate Mach Numbers Using Zero-Mass Flux Pulsed Blowing,” 39th Aerospace Sciences Meeting and Exhibit, AIAA 2001-734, Reno, NV, 2001.

[148] – Sunneechurra, K., and Crowther, W. J., “Problems with Leading-Edge Flow Control Experiments,” *Journal of Aircraft*, Vol. 44, No. 3, 2007, pp. 1052-1055.

[149] – Greenblatt, D., and Wygnanski, I., “Effect of Leading-Edge Curvature on Airfoil Separation Control,” *Journal of Aircraft*, Vol. 40, No. 3, 2003, pp. 473-481.

[150] – Huang, R. F., and Lin, C. L., “Vortex Shedding and Shear-Layer Instability of Wing at Low Reynolds Numbers,” *AIAA Journal*, Vol. 33, No. 8, 1995, pp. 1398-1403.

[151] – Ekaterinaris, J. A., Chandrasekhara, M. S., and Platzer, M. F., “Analysis of Low Reynolds Numbers Airfoil Flows,” *Journal of Aircraft*, Vol. 32, No. 3, 1995, pp. 625-630.

[152] – Rinoie, K., and Takemura, N., “Oscillating behaviour of laminar separation bubble formed on an aerofoil near stall,” *The Aeronautical Journal*, Vol. 108, No. 1081, 2004, pp. 153-163.

[153] – Shan, H., Jiang, L., and Liu, C., “Direct numerical simulation of flow separation around a NACA 0012 airfoil,” *Computers & Fluids*, Vol. 34, No. 9, 2005, pp. 1096-1114.

[154] – Mittal, S., and Saxena, P., “Hysteresis in flow past a NACA 0012 airfoil,” *Computer Methods in Applied Mechanics and Engineering*, Vol. 191, No. 19-20, 2002, pp. 2207-2217.

[155] – Barlow, J. B., Rae, W. H., and Pope, A., *Low-Speed Wind Tunnel Testing*, 3rd ed., John Wiley & Sons, 1999.

[156] – Pankhurst, R. C., and Holder, D. W., *Wind-Tunnel Technique: an Account of Experimental Methods in Low-and High-Speed Wind Tunnels*, Sir Isaac Pitman & Sons, 1952.

[157] – Mendelsohn, R. A., and Polhamus, J. F., "Effect of the tunnel-wall boundary layer on test results of a wing protruding from a tunnel wall," NACA-TN-1244, Washington, April 1947.

[158] – Liebeck, R. H., "Laminar separation bubbles and airfoil design at low Reynolds numbers," 10th Applied Aerodynamics Confrence, AIAA-92-2735-CP, 1992.

[159] – Tani, I., Hama, R., and Mituisi, S., "On the Permissible Roughness in the Laminar Boundary Layer," Aeronautical Research Institute, Tokyo Imperial University Report 199, 1940, pp. 417-428.

[160] – Sheldahl, R. E., and Kilmas, P. C., "Aerodynamic Characteristics of Seven Symmetrical Airfoil Sections Through 180-Degree Angle of Attack for Use in Aerodynamic Analysis of Vertical Axis Wind Turbines," Sandia National Laboratories energy report SAND80-2114, March 1981.

[161] – Jacobs, E. N., and Sherman, A., "Airfoil section characteristics as affected by variations of the Reynolds number," NACA-TR-586, 1937.

[162] – Kundu, A. K., *Aircraft Design*, Cambridge University Press, 2010.

[163] – Gould, R. W. F., "Pitot-Stem Blockage Corrections in Uniform and Non-Uniform Flow," Aeronautical Research Council, ARC-CP-1175, 1971.

[164] – Collis, D. C., and Williams, M. J., "Two-dimensional convection from heated wires at low Reynolds numbers," *Journal of Fluid Mechanics*, Vol. 6, No. 3, 1959, pp. 357-384.

[165] – Kumme, R., "Dynamic force measurement in practical applications," XVI IMEKO World Congress, Vienna, September 2000.

[166] – Moffat, R. J., "Contributions to the Theory of Single-Sample Uncertainty Analysis," *Journal of Fluids Engineering*, Vol. 104, No. 2, 1982, pp. 250-258.

[167] – Moffat, R. J., "Describing the uncertainties in experimental results," *Experimental Thermal and Fluid Science*, Vol. 1, No. 1, 1988, pp. 3-17.

[168] – Prasad, A. K., "Particle image velocimetry," *Current Science*, Vol. 79, No. 1, 2000, pp. 51-60.

[169] – Charonko, J. J., and Vlachos, P. P., "Estimation of uncertainty bounds for individual particle image velocimetry measurements from cross-correlation peak ratio," *Measurement Science and Technology*¸ Vol. 24, No. 6, 2013, pp. 1-16.

[170] – Bearman, P. W., Harvey, J. K., and Stewart, J. N., "Two and three component velocity measurements in a wind tunnel using PIV," *The Aeronautical Journal,* Vol. 103, No. 1021, 1999, pp. 167-173.

[171] - Cooperman, A. M., "Wind Tunnel Testing of Microtabs and Microjets for Active Load Control of Wind Turbine Blades," Ph.D. Dissertation, Mechanical and Aeronautical Engineering Dept., University of California, Davis, 2005.

[172] - Al-Battal, N. H., Cleaver, D. J., Gursul, I., "Lift Reduction by Counter Flowing Wall Jets," *Aerospace Science and Technology*, Vol. 78, 2018, pp. 682-695.

[173] - Hopkins, D.F. and Robertson, J.M., "Two-Dimensional Incompressible Fluid Jet Penetration", *Journal of Fluid Mechanics,* vol. 29, 1967, pp. 273-287.

[174] - Chen, C., Seele, R., and Wygnanski, I., "Flow Control on a Thick Airfoil Using Suction Compared to Blowing", *AIAA Journal,* vol. 51, 2013, pp. 1462-1472.

[175] - Wang, Z. and Gursul, I., "Lift Enhancement of a Flat-Plate Airfoil by Steady Suction", *AIAA Journal,* vol. 55, 2017, pp. 1355-1372.

[176] – Horton, H. P., "A Semi-Empirical Theory for the Growth and Bursting of Laminar Separation Bubbles," Aeronautical Research Council, ARC-CP-1073, 1967.

[177] - Mahesh, K., "The Interaction of Jets with Crossflow", *Annual Review of Fluid Mechanics,* vol. 45, 2013, pp. 379-407.

[178] - Balachandar, R., Robillard, L. and Ramamurthy, A.S., "Some Characteristics of Counter Flowing Wall Jets", *Journal of Fluids Engineering Transactions of the ASME,* vol. 114, 1992, pp. 554-558.

[179] – Theodorsen, T., "General theory of aerodynamic instability and the mechanism of flutter," NACA-TR-496, January 1949.

[180] – Darabi, A., and Wygnanski, I., "Active management of naturally separated flow over a solid surface. Part 1. The forced reattachment process," *Journal of Fluid Mechanics*, Vol. 510, 2004, pp. 105-129.

[181] – Darabi, A., and Wygnanski, I., "Active management of naturally separated flow over a solid surface. Part 2. The separation process," *Journal of Fluid Mechanics*, Vol. 510, 2004, pp. 131-144.

[182] – Goodyer, M. J., "The Cryogenic Wind Tunnel," *Progress in Aerospace Sciences*, Vol. 29, No. 3, 1992, pp. 193-220.

[183] – Reckzeh, D., and Hansen, H., "High Reynolds-Number Windtunnel Testing for the Design of Airbus High-Lift Wings," *New Results in Numerical and Experimental Fluid Mechanics V. Notes on Numerical Fluid Mechanics and Multidisciplinary Design (NNFM)*, Vol. 92, 2006, pp. 1-8.

[184] – Lawford, J. A., and Foster, D. N., "Low-Speed Wind-Tunnel Tests on a Wing Section with Plain Leading- and Trailing-Edge Flaps having Boundary-Layer Control by Blowing," Aeronautical Research Council, R. & M. No. 3639, 1970.

[185] – Pires, O., Munduate, X., Ceyhan, O., Jacobs, M., and Snel, H., "Analysis of High Reynolds Numbers Effects on a Wind Turbine Airfoil Using 2D Wind Tunnel Test Data," *Journal of Physics: Conference Series*, Vol. 753, 022047, 2016.

[186] – Dods, Jr. J. B., and Watson, E. C., "The Effects of Blowing Over Various Trailing-Edge Flaps on an NACA 0006 Airfoil Section, Comparisons with Various Types of Flaps on Other Airfoil Sections, and an Analysis of Flow and Power Relationships for Blowing Systems," National Aeronautics and Space Administration, NASA TN D-8293, August 1976.

[187] – Peake, D.J., Bowker, A.J., Mokry, M., Yoshihara, H., and Magnus, R., "Transonic Lift Augmentation of Two-Dimensional Supercritical Aerofoils by Means of Aft Camber, Slot Blowing and Jet Flaps, in High Reynolds Number Flow," *Proceedings of the 9th Congress of the International Council of the Aeronautical Sciences*¸ ICAS, Haifa, 1974.

[188] – Goffert, B., Ortega, M. A., and Pessoa, J. B., "Numerical Study of Wall Ventilation in a Transonic Wind Tunnel," *Journal of Aerospace Technology and Management*, Vol. 7, No. 1, 2015, pp. 81-92.

[189] – Anderson, J. D., *Fundamentals of Aerodynamics*¸ 3rd ed, McGraw-Hill Education, New York, 2001.

[190] – Ahrens, G., Dellmann, T., Gies, S., Hecht, M., Hefazi, H., Henke, R., Pischinger, S., Schaufele, R., and Tegel, O., "Transport Systems," *Springer Handbook of Mechanical Engineering*, Vol. 10, Springer Bering Heidelberg, Heidelberg, 2009, pp. 1011-1148.

[191] – Kirk, F. N., "Effects of Mach Number on Maximum Lift," Royal Aircraft Establishment, RAE TN Aero 1867, 1947.

[192] – Yoshihara, H., and Zonars, D., "The Transonic Jet Flap - A Review of Recent Results," *SAE Transactions*, Vol. 84, 1975, pp. 3055-3063.

[193] – Petrov, A. V., Bokser, V. D., Sudakov, G. G., and Savin, P. V., "Application of Tangential Jet Blowing for Suppression of Shock Induced Flow Separation at Transonic Speeds," *27th Congress of International Council of the Aeronautical Sciences*, ICAS, Nice, 2010.

[194] – Paraschivoiu, I., "Finite Span Wing," *Subsonic Aerodynamics*, Ecole Polytechnique de Montreal, Montreal, 2003, pp. 213-272.

[195] – Anderson, J. D., "Aerodynamics in the Age of the Jet Airplane," A History of Aerodynamics: And Its Impact on Flying Machines, Cambridge University Press, Cambridge, 1999, pp. 370-446.

[196] – Raymer, D. P., "Wing Geometry," Aircraft Design: A Conceptual Approach, 2nd ed., AIAA, Washington, DC, 1992, pp. 47–65.

[197] – Reckzeh, D., "Aerodynamic Design of Airbus High-lift Wings in a Multidisciplinary Environment," *European Congress on Computational Methods in Applied Sciences and Engineering ECCOMAS, Jyväskylä, 2004.*

[198] – Crowther W. J., "Separation Control on a Trailing-Edge Flap Using Air Jet Vortex Generators," *Journal of Aircraft,* Vol. 43, No. 5, 2006, pp. 1589-1593.

[199] – El-Sayed, A. F., "Turbofan Engines," *Aircraft Propulsion and gas turbine engines*, CRC Press, 2008, pp. 215-306.

[200]– "Type-Certificate Data Sheet for CFM56-5B and CFM56-5C series engines," European Aviation Safety Agency, 2017

[201] – Carlile, D., "Cabin Air Comfort," *FAST Airbus Technical Digest*, No. 19, 1996, pp. 4-11.

[202] – "In-Flight Fuel Feed Failure Resulting in Engine Fuel Starvation," Transportation Safety Board of Canada, A08Q0082, April 2008.

[203] – Rudolph, P. K. C., "High-Lift Systems on Commercial Subsonic Airliners," National Aeronautics and Space Administration, NASA Contractor Report 4746, September 1996.

[204] – Sensmeier, M. D., and Samareh, J. A., "A Study of Vehicle Structural Layouts in Post-WWII Aircraft," 45th AIAA/ASME/ASCE/AHS/ASC Structures, Structural Dynamics & Materials Conference, AIAA 2004-1624, Palm Springs, CA, April 2004.

[205] – Schrenk, O., "A Simple Approximation Method for Obtaining the Spanwise Lift Distribution," National Advisory Committee for Aeronautics, TM No. 948, 1940.

[206] – Gatewood, B. E., "Appendix B/ External forces on flight vehicles," *Virtual Principles in aircraft Structures,* 1st ed, Vol. 1, Kluwer Academic Publishers, 1989, pp. 279-316.

[207] – Haider, N., "Prediction of Compressible Flow Pressure Losses in 30 – 150 Deg Sharp Cornered Bends," *Journals of Fluids Engineering*, Vol. 117, No. 4, 1995, pp. 589-592.